Ph.D. Thesis

Sampled-Data Analysis and Control of DC-DC Switching Converters

by Chung-Chieh Fang

Ph.D. 97-5

Sponsored by
the National Science Foundation
Engineering Research Center Program,
the University of Maryland,
Harvard University,
and Industry

ABSTRACT

Title of Dissertation: SAMPLED-DATA ANALYSIS AND CONTROL OF DC-DC SWITCHING CONVERTERS

Chung-Chieh Fang, Doctor of Philosophy, 1997

Dissertation directed by: Professor Eyad H. Abed
Department of Electrical Engineering

A unified sampled-data method is proposed for the analysis and control of DC-DC switching converters. Two types of DC-DC converters are considered in this dissertation: PWM converters and load-resonant converters. Numerous examples are given to illustrate the results.

In the study of PWM converters, general nonlinear sampled-data models are developed. Conditions are obtained for existence and local orbital stability of periodic solutions. The stability of the bifurcated solutions of a reduced model is also investigated. The input filter instability problem is studied using the Neimark-Sacker bifurcation. Audio-susceptibility and output impedance are also analyzed using the developed models. Several schemes are proposed for stabilizing unstable periodic solutions in PWM converters. Among these, washout filter-based designs are introduced to provide robust stability without reliance on knowledge of the nominal operating condition. In addition, gain-scheduling

is used to enlarge the operating range. The power stage of the PWM converter is analyzed to facilitate control design. New results are obtained on the open-loop zeros of the power stage. New control designs are proposed to achieve line and load regulations as well as a faster transient response. These designs include state feedback with or without feedforward terms, state feedback through washout filters, dynamic state feedback and dynamic output feedback. These control laws can be applied to both voltage and current regulations.

These results are extended to the study of load-resonant converters. The developed methods are more concise and unified than traditional methods used to analyze load-resonant converters. Analytical conditions are obtained for the existence and local orbital stability of periodic solutions is derived. Analytical formulae are derived for audio-susceptibility, output impedance, and half-cycle dynamics. Integral control is applied to this type of converter to achieve line and load regulation.

SAMPLED-DATA ANALYSIS AND CONTROL OF DC-DC SWITCHING CONVERTERS

by

Chung-Chieh Fang

Dissertation submitted to the Faculty of the Graduate School of the
University of Maryland in partial fulfillment
of the requirements for the degree of
Doctor of Philosophy
1997

Advisory Committee:

Professor Eyad H. Abed, Chairman/Advisor
Assistant Professor Balakumar Balachandran
Professor David L. Elliott
Professor William S. Levine
Professor Robert W. Newcomb
Professor Edward Ott

DEDICATION

To my late brother, Chung-Yi,

for his love and companionship

ACKNOWLEDGEMENTS

I would like to express my deepest gratitude to my advisor Dr. Abed for his expert guidance and encouragement during my doctoral studies.

I am also very grateful to Dr. Elliott and Dr. Levine for many helpful comments on the first draft of the dissertation when my advisor was on sabbatical.

Acknowledgments are also due to the other members of my advisory committee, Dr. Balachandran, Dr. Ott and Dr. Newcomb for their reading of the dissertation and providing comments.

I would also like to thank my friends Mr. Craig Lawrence and Mr. Jia-Bin Chen for many helpful discussions.

I would like to thank Dr. P.T. Krein and Dr. F.C. Lee for sending useful references on power electronics.

Thanks are also due to my family members, Dr.D.C. Liaw, Dr. J.-H. Fu and Dr. D. Hamill for encouragement.

TABLE OF CONTENTS

LIST OF TABLES

LIST OF FIGURES

Chapter 1

Introduction

1.1 Motivation and Background

DC-DC converters are widely used in industrial, aerospace and consumer products. A good DC-DC converter should satisfy the following three types of requirements:

1. Economic requirements:

   The circuit should be energy efficient, small in size, light in weight, and low in cost.

2. Steady-state performance requirements:

   The output voltage, output current, and AC ripple should be within the specified range.

3. Dynamic performance requirements:

   The circuit should be stable and the output voltage should be kept within the specified range under disturbances at the source voltage and the load (i.e., the converter should have good line and load regulations).

There are two main types of DC-DC converters: linear and switch-mode. In general, linear DC-DC converters are not energy efficient and are very large, while switch-mode DC-DC converters can meet the three requirements previously mentioned. In switching converters, lossless elements such as efficient switches, inductors, capacitors, and transformers are used to store energy temporarily and transmit it to the load. By properly choosing the switching frequency, inductance, and capacitance values, the converter can be of small size and light weight, and can filter out large AC ripples, so that the steady-state performance requirements are met. By using feedback control, the dynamic performance requirements can also be met. Despite all the advantages of switches, they also make the circuits nonlinear and difficult to analyze.

Switching DC-DC converters can be classified into two categories, pulse width modulated (PWM) converters and soft-switched converters, which are also called resonant converters. In PWM converters, there is a small loss of power during switching because of the finite values of voltage and current during the switching transient. So the switching frequency and corner frequency $(1/\sqrt{LC})$ can not be increased much, and therefore the size and weight cannot be reduced. Another drawback of these converters is the high electromagnetic interference (EMI) during switching. Using soft-switching techniques, switching loss can be reduced so that the switching frequency can be increased, and therefore the size and weight can be reduced. At the same time, soft-switched converters have less EMI because of their smooth state trajectories. The main disadvantage of soft-switched converters is the increased peak current or voltage for the same output voltage.

Analysis, control, and stabilization are the main issues in switching converters. To facilitate the analysis and design of these converters, a good analysis method is needed. The most popular analysis method is the state space averaging method by Middlebrook and Ćuk [61]. Generally the switching frequency is so high that the state trajectories have small switching ripples. The state space averaging method approximates the original circuits by continuous-time autonomous systems, thus smoothing out these small ripples and capturing the basic dynamics. At the same time, continuous-time design methods are well known, so the feedback compensation is easy to design.

However, it has gradually been found that the averaging method does not work well when the converters are operating in current mode control [10, 73, 90], and cannot accurately predict subharmonic instability [10], chaotic phenomena [16, 31, 15, 97], and steady-state DC offset [51]. This has led to many efforts devoted to modify the averaging theory as applied to DC-DC converters [79, 78, 102, 76, 43, 50].

The sampled-data method [48, 40, 58, 103, 39, 18, 3, 4, 22] is another method for analyzing switching circuits. Of the cited studies, Lee et al. [48], Verghese et al. [103] and Lutz et al. [58] are the most commonly cited sources on sampled-data modeling of DC-DC converters. In PWM converters, this method was used under the assumption that the switching frequency is fast enough so that *approximate* discrete models can be used. It is shown in [68] that these models could be inaccurate both quantitatively and qualitatively. In soft-switched converters, this method was applied either numerically, thus offering little insight, or using tedious notion and formalism, thus making it not very useful for design. In summary, the power of the sampled-data method has not been fully exploited

in the modeling , analysis and control design of DC-DC converters.

Other modeling methods are the extended describing function method [109, 110], which is useful for resonant converters, the switch-model method [106, 100, 104, 105], and the state-plane method [11, 66, 86, 65], which is useful only for low-dimensional circuits.

Regarding control methods, many are available: voltage mode control, current mode control, average current mode control [92], sliding mode control [101, 84], charge control [93], one-cycle control [88], hysteretic control [57], boundary control [65], LQR optimal control [95, 52, 26], robust control [107, 54, 53], adaptive control [98, 85, 81], function control [55, 56], Lyapunov-based control [77, 36], nonlinear control [80, 82, 32, 83], digital control [19, 38, 91] and other methods [67, 12]. These control methods are generally either based on an averaged model, which is an approximate model; or based on an approximate sampled-data model; or based on a detailed sampled-data model, thus it is difficult to use it for design.

About the stabilization issue, when a designed converter turns out to be unstable, traditionally it is redesigned or fitted with an additional circuit which is predetermined and fixed, instead of using state feedback. Recently, a targeting method [71, 72] has been used to stabilize unstable periodic orbits in chaotic switching converters, but the stabilization algorithm is complicated.

Some other stability issues have been considered and analyzed separately. For example, it is known that adding an input filter will sometimes result in instability [59]. Impedance analysis are used for this instability problem [60, 47, 20, 41, 33].

There is a serious need for a unified method for analyzing the switching converters of a variety of configurations. In this study, we will show the efficacy of the sampled-data approach is the best method in addressing the issues noted above. In summary, this dissertation addresses the following issues: analysis (stability, performance, bifurcation), design, stabilization, and control of PWM and load-resonant converters. These issues are studied for the following configurations: voltage/current mode control, fixed/variable frequency, continuous/discontinuous conduction mode, and with/without input filter.

1.2 Summary of Contributions

Below is a summary of the contributions in this dissertation:

- Proposed a unified method for different issues/converters/configurations of DC-DC converters.
- Derived analytical conditions for stability and bifurcation of limit cycles arising in DC-DC converters.
- Derived analytical formulae for audio-susceptibility and output impedance of DC-DC converters.
- Explained input filter instability by Neimark-Sacker bifurcation.
- Discovered the possibility of saddle-node bifurcation in DC-DC converters.
- Calculated the stability coefficient for period-doubling bifurcation in a one-dimensional switching converter.

- Determined the period-doubling bifurcation point by harmonic balance method.
- Derived stabilizability conditions and designed digital or analog stabilizers for unstable PWM converters.
- Designed robustification of stabilization of PWM converters.
- Proposed a new continuous-time model of power stage.
- Found new results about open-loop zeros in PWM converters
- Simplified the analysis of load-resonant converters.
- Designed several new digital control schemes for DC-DC converters.
- Designed dynamic output feedback controllers for DC-DC converters that don't require sensing the current.
- Designed a state observer for the buck converter.

1.3 Organization of the Dissertation

The organization of this dissertation is as follows. In Chapter 2, basic background for the dissertation is reviewed. In Chapter 3, stability and bifurcation analysis of PWM converters in voltage/current mode control and continuous/discontinuous conduction mode are presented. A general sampled-data model of PWM converters is developed. Analytical conditions on the existence of periodic solutions and asymptotic orbital stability are derived. Analytical formulae for audio-susceptibility and output impedance are obtained. The stability of bifurcated

solutions in a reduced system is also investigated. The input filter instability problem is explained by Neimark-Sacker bifurcation.

When these controlled converters are unstable, digital or analog stabilization schemes are developed in Chapter 4. Conditions for stabilizability are derived. Washout filters are introduced to make the system robust without knowing the equilibrium point. The operating range is extended by a gain-scheduling method.

Then we turn tha attention to the power stage only. In Chapter 5, a sampled-data model of power stage in continuous/discontinuous conduction mode is derived. Also a new continuous-time model of power stage is derived from this sampled-data model. In Chapter 6, some new findings about the zero in sampled-data model of power stage are obtained. Once a good model of the power stage is derived, many digital/analog static/dynamic and state/output feedback control methods for PWM converters are developed in Chapter 7.

Soft-switched DC-DC conversion is becoming popular because of its efficiency and high power density. One class of soft-switched converters, the load-resonant converter, is analyzed in Chapter 8. Despite their complexity, load-resonant converters have similar structures to PWM converters. A more concise and unified method than the traditional one to analyze this type of converter is developed. Analytical conditions on the existence of periodic solutions and asymptotic orbital stability are derived. Analytical formulae of audio-susceptibility, output impedance and half-cycle dynamics are also derived. Integral control is applied to this type of converter and is shown to have good line/load regulation. To help the readers to understand the whole picture of this dissertation, a schematic diagram of the problems considered in this dissertation is shown in Fig. 1.1.

Finally, the conclusions of this dissertation and suggestions for the future

research are given in Chapter 9.1.

1.4 Acronyms and Symbols

Acronyms

CCM	continuous conduction mode
DCM	discontinuous conduction mode
TEM	trailing-edge modulation
LEM	leading-edge modulation
FFC	fixed-frequency control
VFC	variable-frequency control
SRC	series resonant converter
PRC	parallel resonant converter
SRPC	series-parallel resonant converter
RHP	right half plane
LHP	left half plane
PWM	pulse-width modulation
ESR	equivalent series resistance
EMI	electromagnetic interference
S	sampled-data method
SC	a method converting ("lifting") sample-data dynamics to a consistent continuous-time dynamic model

Symbols

v_s	source voltage

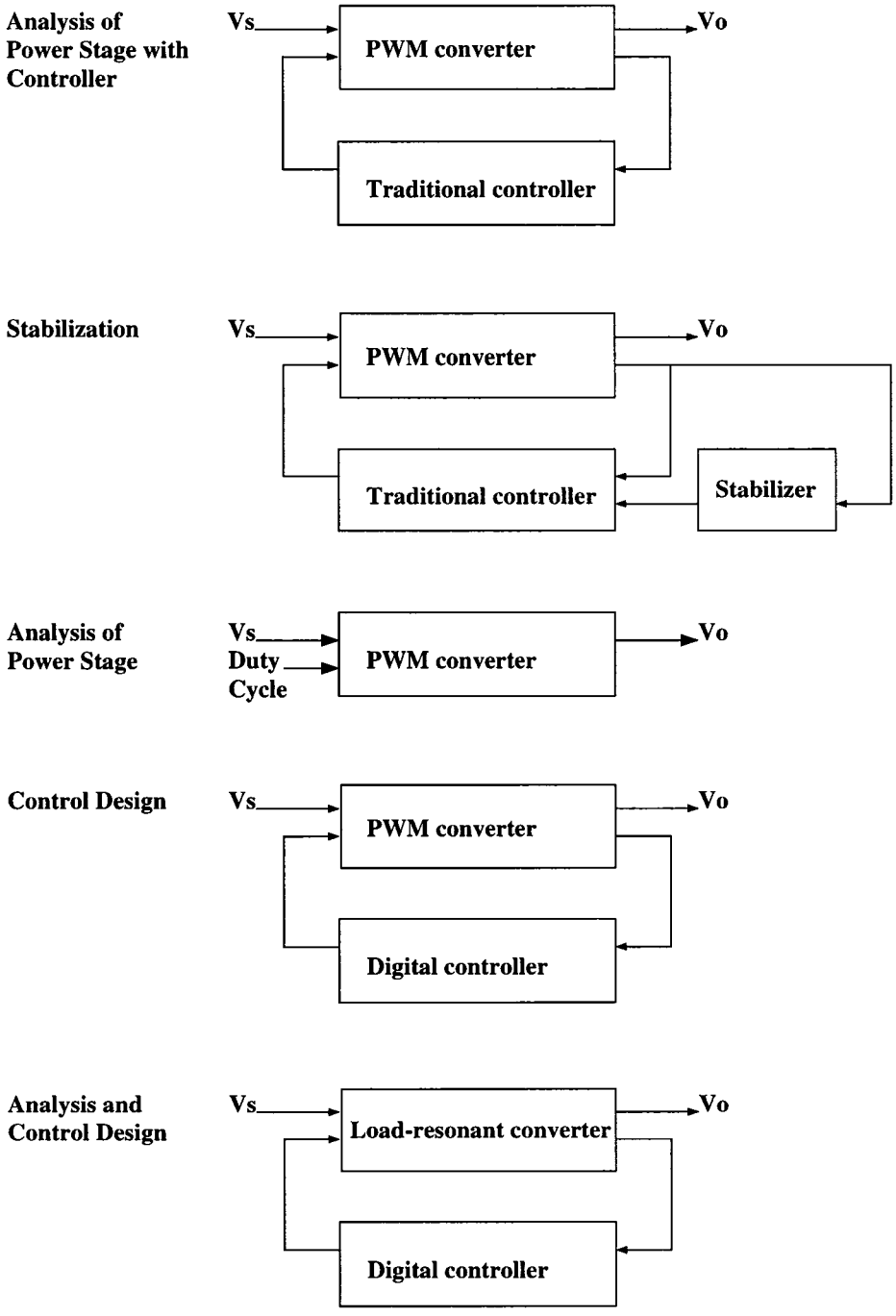

Figure 1.1: Problems considered in the dissertation

$V_{s,*}$	critical value of source voltage
v_o	output voltage
v_C	capacitor voltage
v_d	voltage across the diode
$h(t)$	Compensating ramp in current mode control or PWM triangular wave in voltage mode control
V_h	$h(T^-)$
V_l	$h(0^+)$
V_{SET}	set-point (nominal) output voltage
i_L	inductor current
V_r	reference signal (voltage or current), usually constant unless modulated in a control scheme
f_s	switching frequency
T	$\frac{1}{f_s}$, period of a cycle
ω_s	$2\pi f_s$, angular switching frequency
D_c	duty cycle
d, d_1, etc.	switching instant in a cycle
$x^0(t)$	nominal steady-state orbit
$\hat{x}_n$	$x_n - x^0(0)$
v_{sn}	$v_s(nT)$, source voltage sampled at clock time
$\hat{v}_{sn}$	$v_{sn} - V_s$
$T_{oc}(z)$	control-to-output transfer function derived from sample-data method
$T_{os}(z)$	audio-susceptibility transfer function derived from sample-data method
$T_{oo}(z)$	output impedance transfer function derived from sample-data method
A'	transpose of matrix A

$\sigma[A]$	the set of eigenvalues (or spectrum) of matrix A
$\lvert\sigma[A]\rvert$	the set of magnitudes of the eigenvalues of matrix A
$\mathrm{tr}[A]$	trace of matrix A
$\det[A]$	determinant of matrix A
$\ln[x]$	natural logarithms of x

Chapter 2

Preliminaries

In this chapter, some basic concepts necessary for this dissertation will be reviewed. Results on discrete-time linear system will be presented in Sec. 2.1. Basic bifurcation theory of discrete-time systems will be discussed in Sec. 2.2. Some background materials about DC-DC converters will be reviewed in Sec. 2.3.

2.1 Results on Discrete-Time Linear Systems

2.1.1 Stability Theorems

Theorem 2.1 *[34] The following statements are equivalent:*

(i) The fixed point 0 of the system $x_{n+1} = \Phi x_n$ *is asymptotically stable.*

(ii) $|\sigma(\Phi)| < 1$.

(iii) There exists a real, symmetric, and positive definite matrix P *such that* $(\Phi^T P \Phi - P)$ *is negative definite.*

Theorem 2.2 *The following statements are equivalent:*

(i) The fixed point 0 of the system $x_{n+1} = \Phi x_n$ *is stable.*

(ii) There exists a real, symmetric, and positive definite matrix P *such that*

$(\Phi^T P \Phi - P)$ is negative semidefinite.

2.1.2 Frequency Response of Discrete-Time Systems

Suppose a stable linear discrete-time system has a transfer function $H(z)$ in the z-domain. Let the input be $\cos(\omega nT)1(n)$, where $1(n)$ is the discrete-time unit step function. Then the steady-state output is $|H(e^{j\omega T})|\cos(\omega nT + \angle H(e^{j\omega T}))$. (For a proof, see [25].) This frequency response is valid for a band-limited continuous-time input, which has an angular frequency spectrum from 0 to $2\pi/T$. For an input with angular frequency higher than $2\pi/T$, the aliasing effect will occur because the sampling frequency is not high enough. For example, a continuous-time input with angular frequency frequency $\omega + 2\pi l/T$ will have the same samples as that with angular frequency frequency ω when the sampling period is T.

2.1.3 Discretizing a Continuous-Time System Through a Zero-Order-Hold

Consider a linear continuous-time system,

$$\begin{aligned} \dot{x} &= Ax + Bu \\ y &= Ex \end{aligned} \tag{2.1}$$

where $A \in \mathbf{R}^{n\times n}$, $B \in \mathbf{R}^{n\times 1}$, $E \in \mathbf{R}^{1\times n}$, $x \in \mathbf{R}^n$, and $y, u \in \mathbf{R}$.

We can transform this continuous-time system to a discrete-time system through a zero-order-hold as shown in Fig. 2.1.

The discrete-time system has the dynamics

$$\begin{aligned} x_{n+1} &= \Phi x_n + \Gamma u_n \\ y_n &= Ex_n \end{aligned} \tag{2.2}$$

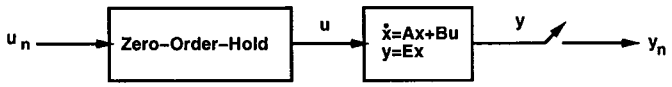

Figure 2.1: Discretizing a continuous-time system through a zero-order-hold

where

$$\Phi = e^{AT} \tag{2.3}$$

$$\Gamma = \int_0^T e^{A\sigma} d\sigma B \tag{2.4}$$

The following is a useful fact to help in the conversion between the continuous-time pair (A, B) and the discrete-time pair (Φ, Γ).

Fact 2.1

$$\begin{bmatrix} \Phi & \Gamma \\ 0 & 1 \end{bmatrix} = \exp\left(\begin{bmatrix} A & B \\ 0 & 0 \end{bmatrix} T \right)$$

The input-to-output transfer function in the continuous-time domain is

$$E(sI - A)^{-1}B \tag{2.5}$$

The input-to-output transfer function in the discrete-time domain is

$$E(zI - \Phi)^{-1}\Gamma \tag{2.6}$$

Given the discrete-time dynamics (2.2), we can obtain the continuous-time transfer function (2.5) by using Fact 2.1. This procedure will be used to obtain continuous-time audio-susceptibility, output impedance, and control-to-output transfer functions in the dissertation. Since we transform the discrete-time (sampled-data) dynamics to continuous-time dynamics, we will refer to this as the SC method.

d	Z_d
1	1
2	$z+1$
3	z^2+4z+1

Table 2.1: Polynomials Z_d, for d =1, 2 and 3

Next, we review the relation of the poles and zeros of the continuous-time transfer function (2.5) with those of the discrete-time transfer function (2.6). For details, the reader is referred to [5, 2].

Assume the continuous-time transfer function (2.5) has n poles, namely, $p_1, \ldots, p_n$, and $n-d$ zeros: $z_1, \ldots, z_{n-d}$. Then the the discrete-time transfer function (2.6) will have n poles: $e^{p_1 T}, \ldots, e^{p_n T}$, and $n-1$ zeros. The extra $d-1$ zeros are due to sampling. For small T, $n-d$ of the $n-1$ of the discrete-time transfer function zeros are close to $e^{z_1 T}, \ldots, e^{z_{n-d} T}$. The other $d-1$ zeros will go to the zeros of the polynomials Z_d, shown in Table 2.1 for the case d =1, 2 and 3.

2.1.4 Orbital Stability

Definition 2.1 *[37] Denote by γ the closed orbit generated by the periodic solution $x^0(t)$. Then $x^0(t)$ is asymptotically orbitally stable if there is δ such that*

$$\text{dist}[x(0), \gamma] < \delta \Rightarrow \lim_{t \to \infty} \text{dist}[x(t), \gamma] = 0$$

where $\text{dist}[z, \gamma]$ *is defined as the smallest distance between the point z and any point on γ.*

2.2 Basic Bifurcation Theory of Discrete-Time Systems (Mappings)

In this section we recall the basic bifurcation theory that will be used in this dissertation. Most of the material presented is from [45]. For details, the reader is referred to [45, 29, 108].

Consider a discrete-time parameter-dependent mapping

$$x \mapsto f(x, \alpha), \quad x \in \mathbf{R}^n, \quad \alpha \in \mathbf{R} \tag{2.7}$$

Suppose a bifurcation happens at $\alpha = \alpha_*$. For convenience, below we take $\alpha_* = 0$. Assume $x = 0$ is a fixed point for $\alpha = 0$. Let $A(\alpha) = f_x(0, \alpha)$. The fixed point $x = 0$ is called a *hyperbolic* fixed point if $A(\alpha)$ has no eigenvalues on the unit circle in the complex plane. As α passes through 0, there are three ways in which the hyperbolicity condition can be violated depending on the eigenvalue λ (sometimes called multiplier) of $A(\alpha)$.

Definition 2.2

1. The bifurcations associated with the appearance of $\lambda = 1$:

(a) When the mapping has a unique curve of fixed points in the x-α plane passing through $(0, 0)$ and locally lying on one side of $\alpha = 0$, a saddle-node bifurcation is said to occur.

(b) When the mapping has two curves of fixed points in the x-α plane passing through $(0, 0)$ and locally lying on both sides of $\alpha = 0$, a transcritical bifurcation is said to occur.

(c) When the mapping has two curves of of fixed points in the x-α plane passing through $(0, 0)$ with one curve locally lying lying on both sides of $\alpha = 0$ and another

curve locally lying on one side of $\alpha = 0$, it is called a pitchfork bifurcation.

2. The bifurcation associated with the appearance of $\lambda = -1$: When the mapping has a curve of fixed point in the x-α plane on both sides of $\alpha = 0$ and a curve of period-two points on one side of $\alpha = 0$ intersecting with the first curve at $\alpha = 0$, then a period-doubling bifurcation is said to occur.

3. The bifurcation associated with the appearance of a complex-conjugated pair of eigenvalues crosses the unit circle away from the real axis, a Neimark-Sacker bifurcation can occur, leading to the emergence of a small-amplitude "invariant circle" around the fixed-point on one side of $\alpha = 0$.

Among these bifurcations, the transcritical and pitchfork bifurcations are not generic [29] and they will not be discussed further in this dissertation. In discrete-time systems, these bifurcations are sometimes called by different names. The saddle-node bifurcation is also called a fold bifurcation or tangent bifurcation; the period-doubling bifurcation is also called a flip bifurcation or subharmonic bifurcation; the Neimark-Sacker bifurcation is also called a secondary Hopf bifurcation.

We first study low-dimensional ($n = 1$ or 2) mappings.

Theorem 2.3 *[45] (Topological normal form for the saddle-node bifurcation) Consider a one-dimensional system*

$$x \mapsto f(x, \alpha), \quad x \in \mathbf{R}, \quad \alpha \in \mathbf{R} \tag{2.8}$$

with smooth f, $f(0,0) = 0$ and let $\lambda = f_x(0,0) = 1$.

Assume that the following nondegeneracy conditions are satisfied:

(A.1) $f_{xx}(0,0) \neq 0$;

(A.2) $f_\alpha(0,0) \neq 0$.

Then this system is locally topologically equivalent near the origin to one of the the following normal forms (i.e., with either the + or − sign chosen):

$$\eta \mapsto \beta + \eta \pm \eta^2$$

Theorem 2.4 *[45] (Topological normal form for the period-doubling bifurcation) Consider a one-dimensional system*

$$x \mapsto f(x, \alpha), \quad x \in \mathbf{R}, \quad \alpha \in \mathbf{R} \tag{2.9}$$

with smooth f, $f(0,0) = 0$ and let $\lambda = f_x(0,0) = -1$.

Assume that the following nondegeneracy conditions are satisfied:

(B.1) $a \stackrel{\text{def}}{=} \frac{1}{2}(f_{xx}(0,0))^2 + \frac{1}{3}f_{xxx}(0,0) \neq 0$;

(B.2) $f_{x\alpha}(0,0) \neq 0$.

Then this system is locally topologically equivalent near the origin to the following normal form:

$$\eta \mapsto -(1+\beta)\eta + \text{sign}(a)\eta^3$$

Thus, the period-doubling bifurcation is supercritical if $a > 0$; subcritical if $a < 0$. In [1], the authors relate the period-doubling bifurcation to stationary bifurcation in continuous-time systems and obtain

$$\beta_2 = -2a \tag{2.10}$$

where β_2 is a coefficient in a Taylor series expression of the eigenvalue of the period-doubled solution.

Theorem 2.5 *[45] (Generic Neimark-Sacker bifurcation)*

For any generic two-dimensional one-parameter system

$$x \mapsto f(x, \alpha), \quad x \in \mathbf{R}^2, \quad \alpha \in \mathbf{R} \tag{2.11}$$

having at $\alpha = 0$ the fixed point $x_0 = 0$ with complex multipliers $\lambda_{1,2} = e^{\pm i\theta_0}$, there is a neighborhood of x_0 in which a unique closed invariant curve bifurcates from x_0 as α passes through zero.

So far, we have studied bifurcations of fixed points in generic one-parameter discrete-time systems having the minimum possible dimensions. In the following we will show that for generic n-dimensional systems, the bifurcations occur in essentially the same way.

Assume that in system (2.7) there are n_0 eigenvalues of $A(0)$ on the unit circle and n_- eigenvalues of $A(0)$ inside the unit circle. Let the eigenspace corresponding to the n_0 eigenvalues on the unit circle be T^c.

Theorem 2.6 *[45] (Center Manifold Theorem)*
There is a locally defined smooth n_0-dimensional invariant manifold $W^c(0)$ of system (2.7) that is tangent to T^c at $x=0$.

Moreover, there is a neighborhood U of $x_0 = 0$, such that if $f^k(x) \in U$ for all $k \geq 0$, then $f^k(x) \to W^c(0)$ as $k \to +\infty$.

The manifold W^c is called the *center manifold* and can be locally represented as the graph of a smooth function:

$$W^c = \{(u, v) : v = V(u)\}$$

where $u \in \mathbf{R}^{n_0}$, $v \in \mathbf{R}^{n_-}$, and the function $V : \mathbf{R}^{n_0} \to \mathbf{R}^{n_-}$ with $V(u) = O(\| u \|^2)$.

Theorem 2.7 *[45] (Reduction Principle)*
System (2.7) is locally topologically equivalent near the origin to the system

$$\begin{pmatrix} u \\ v \end{pmatrix} \mapsto \begin{pmatrix} Bu + g(u, V(u)) \\ Cv \end{pmatrix} \tag{2.12}$$

where $u \in \mathbf{R}^{n_0}$, $v \in \mathbf{R}^{n-}$, $B \in \mathbf{R}^{n_0 \times n_0}$ *with all of its eigenvalues on the unit circle,* $C \in \mathbf{R}^{n- \times n-}$ *with all of its eigenvalues inside the unit circle, and function g has Taylor expansion starting with quadratic or higher order terms.*

We can see that the mappings for u and v are uncoupled and the stability of (2.7) is determined by the mapping of u only.

2.3 DC-DC Switching Converters

DC-DC switching converters are classified as pulse-width modulated (PWM) converters and soft-switched converters. In this dissertation, we also have occasion to refer to what may be called the "dimension" of a converter, which will refer to the order of the associated continuous-time dynamical model. Usually, this agrees with the number of energy storage elements.

In the PWM converter, a square-wave pulse is used to achieve voltage regulation. These coverters are very popular because of their simplicity and their technological maturity. Many control ICs for PWM converters are available at low cost. Nonzero voltage and current during switching result in a power loss. Therefore there is a limit on the switching frequency. Since the size of the converter is inversely proportional to the switching frequency, the size cannot be further decreased. Also there is an electromagnetic interference (EMI) problem because of the square wave nature of the voltage and current.

There are four basic types of PWM converters: buck (Fig. 2.2), boost (Fig. 2.3), buck-boost (Fig. 2.4) and Cuk (Fig. 2.5) converters. In the figures, an equivalent series resistor (ESR) R_c is shown for each converter, although this is not always done in the literature. The ESR has an impact on the form of the general

models that we obtain for converter circuits. The buck converter is also called a step-down converter because the output voltage is always less than the input voltage. The boost converter is also called a step-up converter because the output voltage is always greater than the input voltage. The buck-boost converter or Ćuk converter has negative output voltage with magnitude either greater or less than the input voltage depending on the duty cycle. One main feature of the Ćuk converter is its non-pulsating current both at the input and output, whereas the currents in the other three converters pulsate.

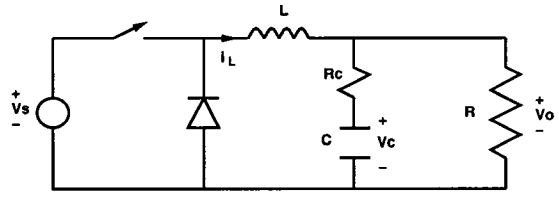

Figure 2.2: Buck converter with source voltage and resistive load

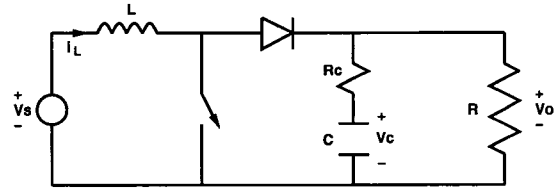

Figure 2.3: Boost converter with source voltage and resistive load

A PWM converter includes a controlled switch and a diode. Generally the circuit topology is designed to prevent the switch and the diode from being on together and the switch is turned on and off once in one switching cycle. Thus there are at most three stages (controlled switch on and diode off, off-on, and off-off) in one switching cycle. (Here we assume the circuit is in normal operation.

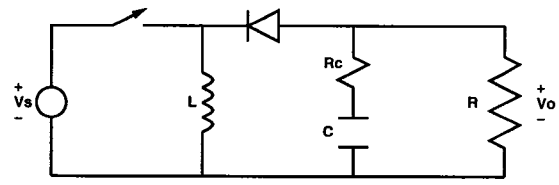

Figure 2.4: Buck-boost converter with source voltage and resistive load

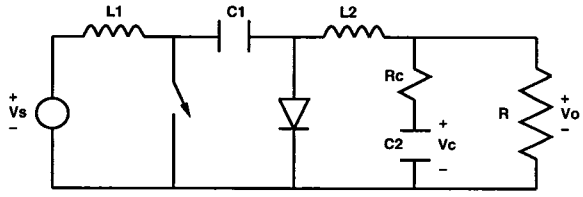

Figure 2.5: Cuk converter with source voltage and resistive load

For other irregular on-off patterns and the associated phenomena, the reader is referred to [24, 6].) In continuous conduction mode (CCM), the inductor current never drops to zero, so the switch and the diode are never off together and there are only two stages in one switching cycle. In discontinuous conduction mode (DCM), the inductor current drops to zero and remains zero until the next cycle begins. There are therefore three stages in this mode. These two modes of a buck converter are shown in Fig. 2.6.

Generally when the switching frequency is high, the value of the output voltage can be estimated from the values of the source voltage and duty cycle. Next, we will show this using an example of a buck converter (Fig. 2.2 with $R_c = 0$) operated in CCM. When the switch is on, the current flows from the source, through the switch and the inductor, then to the load. Let the state $x = (i_L, v_C)$. The system dynamics (state dynamics plus output equation) while

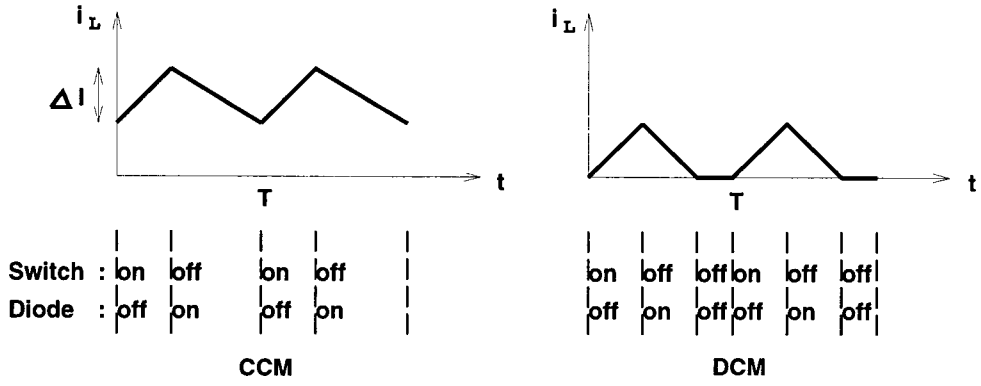

Figure 2.6: Inductor current waveforms and the operation of the switch and diode of a buck converter in CCM or DCM

the switch is on is

$$\begin{aligned} \dot{x} &= \begin{bmatrix} 0 & \frac{-1}{L} \\ \frac{1}{C} & \frac{-1}{RC} \end{bmatrix} x + \begin{bmatrix} \frac{1}{L} \\ 0 \end{bmatrix} v_s \\ &\stackrel{\text{def}}{=} A_{\text{ON}} x + B_{\text{ON}} v_s \end{aligned} \tag{2.13}$$

$$\begin{aligned} v_o &= \begin{bmatrix} 0 & 1 \end{bmatrix} x \\ &\stackrel{\text{def}}{=} E_{\text{ON}} x \end{aligned} \tag{2.14}$$

When the switch is turned off, the current flows through the diode and inductor, then to the load. The system dynamics while the switch is off is

$$\begin{aligned} \dot{x} &= \begin{bmatrix} 0 & \frac{-1}{L} \\ \frac{1}{C} & \frac{-1}{RC} \end{bmatrix} x + \begin{bmatrix} 0 \\ 0 \end{bmatrix} v_s \\ &\stackrel{\text{def}}{=} A_{\text{OFF}} x + B_{\text{OFF}} v_s \end{aligned} \tag{2.15}$$

$$\begin{aligned} v_o &= \begin{bmatrix} 0 & 1 \end{bmatrix} x \\ &\stackrel{\text{def}}{=} E_{\text{OFF}} x \end{aligned} \tag{2.16}$$

(For DCM, there is a third interval in a cycle, where both the switch and

	Buck	Boost	Buck-boost	Cuk
$\frac{V_o}{V_s}$	D_c	$\frac{1}{1-D_c}$	$\frac{-D_c}{1-D_c}$	$\frac{-D_c}{1-D_c}$

Table 2.2: Input and output voltage relationship of PWM converters in CCM

diode are off. The system matrices are denoted by A_{FF}, B_{FF} and E_{FF}.)

From the system dynamics during the on (Eq. (2.13)) and off interval (Eq. (2.15)), we can estimate the output voltage from the input voltage and the duty cycle D_c. Assume that $v_s = V_s$ and the average output is V_o. During the on interval, we have

$$L\frac{di_L}{dt} \approx L\frac{\Delta I}{D_c T} = V_s - V_o \tag{2.17}$$

while in the off interval, we have

$$L\frac{di_L}{dt} \approx L\frac{-\Delta I}{(1-D_c)T} = -V_o \tag{2.18}$$

From Eqs. (2.17) and (2.18), we have

$$\frac{V_o}{V_s} = D_c \tag{2.19}$$

Therefore different output voltages can be achieved by varying the duty cycle.

The input-output voltage relationships of other PWM converters can be obtained in a similar fashion and are shown in Table 2.2.

In PWM converters, duty cycle or switching frequency can be used as control variables. The situation in which the the switching frequency is fixed and the duty cycle is controlled is called fixed-frequency control (FFC). On the other hand, variable-frequency control (VFC) involves fixing the on-time or the off-time while controlling the the switching frequency. FFC is generally preferred because it presents a less significant EMI problem.

In trailing-edge modulation (TEM), the switch is designed to be on first in a cycle. In leading-edge modulation (LEM) the switch is designed to be off first in a cycle. These two designs are illustrated in Fig. 2.7.

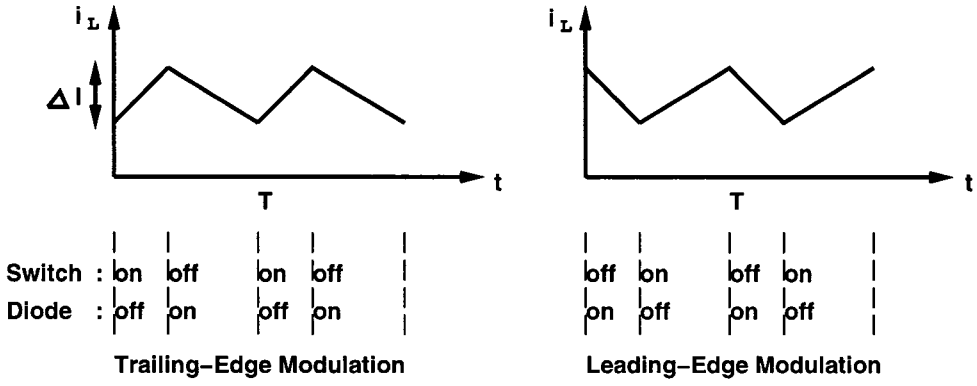

Figure 2.7: Trailing-edge and leading-edge modulations

The amplitude of the voltage and current ripple can also be estimated. Using Eq. (2.19) in Eq. (2.17) gives

$$\Delta I = \frac{V_s(1 - D_c)D_cT}{L} \tag{2.20}$$

So the current ripple is determined by the system parameters (V_s, T, D_c, L) of the power stages. Similarly the voltage ripple can be proved to be determined by the system parameters of the power stages. Thus the steady-state requirements can be satisfied by properly choosing the parameters of the power stage. The dynamic performance requirements can be met by using an appropriate controller.

The two most popular control set-ups are voltage mode control and current mode control. These set-ups are flexible in that we can modify them by including an additional control loop. This will be presented in Chapter 4. A buck converter under the two control methods is shown in Fig. 2.8 and Fig. 2.9, respectively. In

voltage mode control, the output voltage is measured and input into the error amplifier, together with a reference voltage V_r. The output signal from the error amplifier is compared with a ramp signal to decide when to turn the switch on or off. In current mode control, an extra measurement of the inductor current is made and input to the comparator.

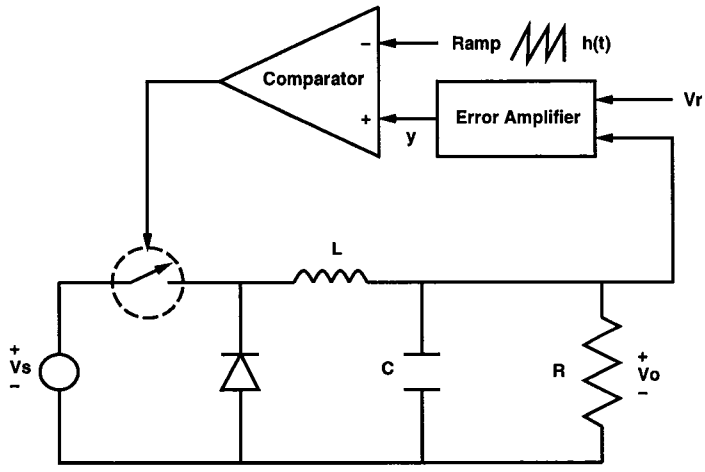

Figure 2.8: Buck converter with voltage mode control

The states can be scaled without affecting the dynamics. Let the state of the converter be

$$x = (\sqrt{L}i_L, \sqrt{C}v_C) \tag{2.21}$$

Then $\frac{x'x}{2}$ is the energy stored in the inductor and capacitor. Introduce the following notation:

$$f_s = \frac{1}{T} \quad \text{(switching frequency)} \tag{2.22}$$

$$\omega_s = 2\pi f_s \quad \text{(angular switching frequency)} \tag{2.23}$$

$$\omega_0 = \frac{1}{\sqrt{LC}} \quad (LC \text{ resonant frequency}) \tag{2.24}$$

$$\omega_l = \frac{R_c}{L} \tag{2.25}$$

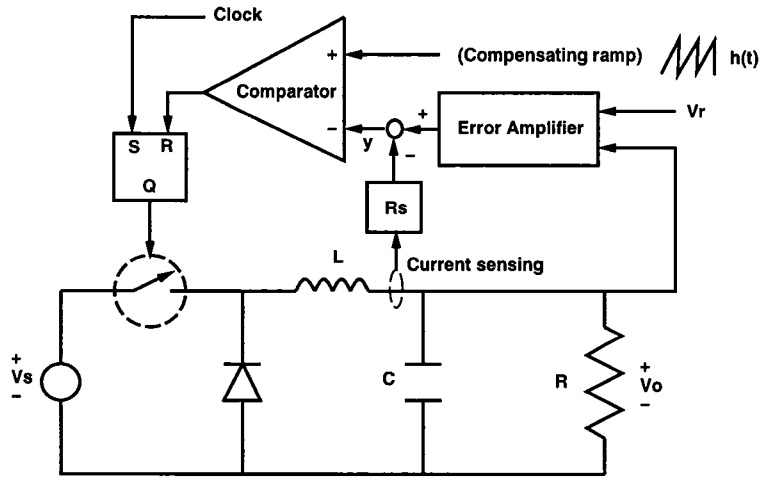

Figure 2.9: Buck converter with current mode control

$$\omega_c = \frac{1}{RC} \tag{2.26}$$

$$\omega_e = \frac{1}{R_c C} \tag{2.27}$$

$$\omega = \sqrt{\omega_0^2 - (\frac{\omega_c - \omega_l}{2})^2} \tag{2.28}$$

$$\kappa = \frac{R}{R + R_c} \tag{2.29}$$

(here we assume $\omega_0 > |\omega_c - \omega_l|/2$).

Then the state equation matrices for the buck converter (Fig. 2.2) using the state (2.21) are

$$A_{\text{ON}} = \kappa \begin{bmatrix} -\omega_l & -\omega_0 \\ \omega_0 & -\omega_c \end{bmatrix} \tag{2.30}$$

$$B_{\text{ON}} = \begin{bmatrix} \frac{1}{\sqrt{L}} \\ 0 \end{bmatrix} \tag{2.31}$$

$$E_{\text{ON}} = \kappa \begin{bmatrix} \frac{R_c}{\sqrt{L}} & \frac{1}{\sqrt{C}} \end{bmatrix} \tag{2.32}$$

$$A_{\text{OFF}} = A_{\text{ON}} \tag{2.33}$$

$$B_{\text{OFF}} = \begin{bmatrix} 0 \\ 0 \end{bmatrix} \tag{2.34}$$

$$E_{\text{OFF}} = E_{\text{ON}} \tag{2.35}$$

$$A_{\text{FF}} = \kappa \begin{bmatrix} 0 & 0 \\ 0 & -\omega_c \end{bmatrix} \tag{2.36}$$

$$B_{\text{FF}} = B_{\text{OFF}} \tag{2.37}$$

$$E_{\text{FF}} = E_{\text{ON}} \tag{2.38}$$

Similarly, Then the state equation matrices for the boost converter (Fig. 2.3) using the state (2.21) are

$$A_{\text{ON}} = \kappa \begin{bmatrix} 0 & 0 \\ 0 & -\omega_c \end{bmatrix} \tag{2.39}$$

$$B_{\text{ON}} = \begin{bmatrix} \frac{1}{\sqrt{L}} \\ 0 \end{bmatrix} \tag{2.40}$$

$$E_{\text{ON}} = \kappa \begin{bmatrix} 0 & \frac{1}{\sqrt{C}} \end{bmatrix} \tag{2.41}$$

$$A_{\text{OFF}} = \kappa \begin{bmatrix} -\omega_l & -\omega_0 \\ \omega_0 & -\omega_c \end{bmatrix} \tag{2.42}$$

$$B_{\text{OFF}} = B_{\text{ON}} \tag{2.43}$$

$$E_{\text{OFF}} = \kappa \begin{bmatrix} \frac{R_c}{\sqrt{L}} & \frac{1}{\sqrt{C}} \end{bmatrix} \tag{2.44}$$

$$A_{\text{FF}} = A_{\text{ON}} \tag{2.45}$$

$$B_{\text{FF}} = \begin{bmatrix} 0 \\ 0 \end{bmatrix} \tag{2.46}$$

$$E_{\text{FF}} = E_{\text{ON}} \tag{2.47}$$

In the soft-switched converter, the voltage or the current is zero at the switching instant. Therefore power loss is reduced and the switching frequency can be

increased. At high switching frequency, the input energy is "chopped" into small packet, the size of the inductor and capacitor can be decreased. To achieve zero current or voltage switching, some form of LC resonance is generally required and these converters are also called resonant converters. Because of the smoother waveform of current and voltage, resonant converters have less electromagnetic interference (EMI) than PWM converters.

There are four main classes of soft-switched converters [64]: load-resonant converters, resonant-switch converters, resonant-dc-link converters and high-frequency-link integral-half-cycle converters. Among these soft-switched converters, only the load-resonant converters are studied in this dissertation. There are three main configurations of load-resonant converters: the series resonant converter (SRC), the parallel resonant converter (PRC) and the series-parallel resonant converter (SPRC, also called LCC-type PRC because of having similar structure as PRC). An SPRC is shown in Fig. 2.10. It is an SRC if C_p is open-circuited and L_f is short-circuited; it is a PRC if C_s is short-circuited. The SRC is suitable for high-output-voltage low-output-current applications; the PRC is suitable for low-output-voltage high-output-current applications [89]. The SPRC combines the advantage of the SRC and the PRC, and can operate over a wide range of loads.

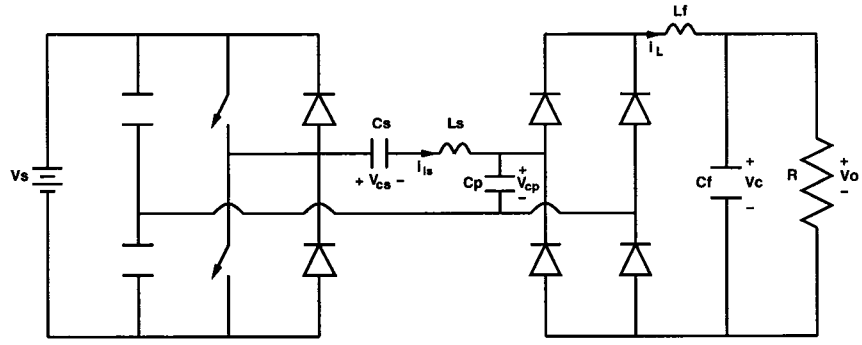

Figure 2.10: Series-parallel resonant converter with source voltage and resistive load

Chapter 3

Sampled-Data Modeling and Analysis of PWM DC-DC Converter Dynamics

This is the first of five chapters focusing on PWM DC-DC converters. In this chapter, stability, bifurcation, and performance analysis of closed-loop PWM converters are considered.

There are many different PWM converters and they can operated in different control modes. These converters all have similar structures. This motivates us to model them in a unified way. In Sec. 3.1 and Sec. 3.2, we propose a general sampled-data model for PWM converters in continuous conduction mode (CCM) with fixed-frequency control (FFC). This work builds on the model of of Lee et al. [48], Verghese et al. [103] and Lutz et al. [58]. Since switching converters are meant to be operated in periodic mode, we analyze the existence of periodic solutions in Sec. 3.3. In Sec. 3.4, we study the linearized sampled-data dynamics. In Sec. 3.5, we study the local orbital stability of periodic solutions of the non-linear model. In Sec. 3.6, we derive formulae for audio-susceptibility and output impedance to determine the effects of line and load disturbances. In Sec. 3.7, we determine a coefficient β_2 that can be used to determine the stability of a

bifurcated limit cycle that emerges from the nominal periodic solution through a period-doubling bifurcation. In Sec. 3.8 and Sec. 3.9, we perform similar analysis assuming discontinuous conduction mode (DCM) and variable-frequency control (VFC), respectively. Because of the inherently special structure of the buck converter, an alternative method, harmonic balance method, can be applied. This is presented in Sec. 3.10. In Sec. 3.11, we illustrate the results of this chapter using numerous examples taken from the literature.

3.1 Modeling PWM Converter in CCM with FFC

In this section, we try to model a general DC-DC PWM converter in CCM with FFC. The switch and the diode are assumed to be ideal that there is no voltage drop when they are on. In FFC, the switching frequency f_s is fixed, so is the cycle of the period T. In CCM, the switch is generally on and off once in a cycle.

A general switching circuit in CCM and FFC can be modeled by the system blocks shown in Fig. 3.1, where $A_1, A_2 \in \mathbf{R}^{n\times n}$, $B_1, B_2 \in \mathbf{R}^{n\times 1}$, $C, E_1, E_2 \in \mathbf{R}^{1\times n}$, and $D \in \mathbf{R}$ are constant, $x \in \mathbf{R}^n$, $y \in \mathbf{R}$ are the state and the measured output respectively. The source and output voltages are v_s and v_o respectively. The voltage (or current) reference is v_r, which is assumed to be time-varying here although it is constant in most applications. The associated switching decision for voltage mode and current mode control is shown in Fig. 3.2 and Fig. 3.3 respectively. The external signal $h(t)$ is generally a T-periodic function. For example, in current mode control, $h(t)$ is an external compensating ramp. In voltage mode control, $h(t)$ is a PWM triangular wave.

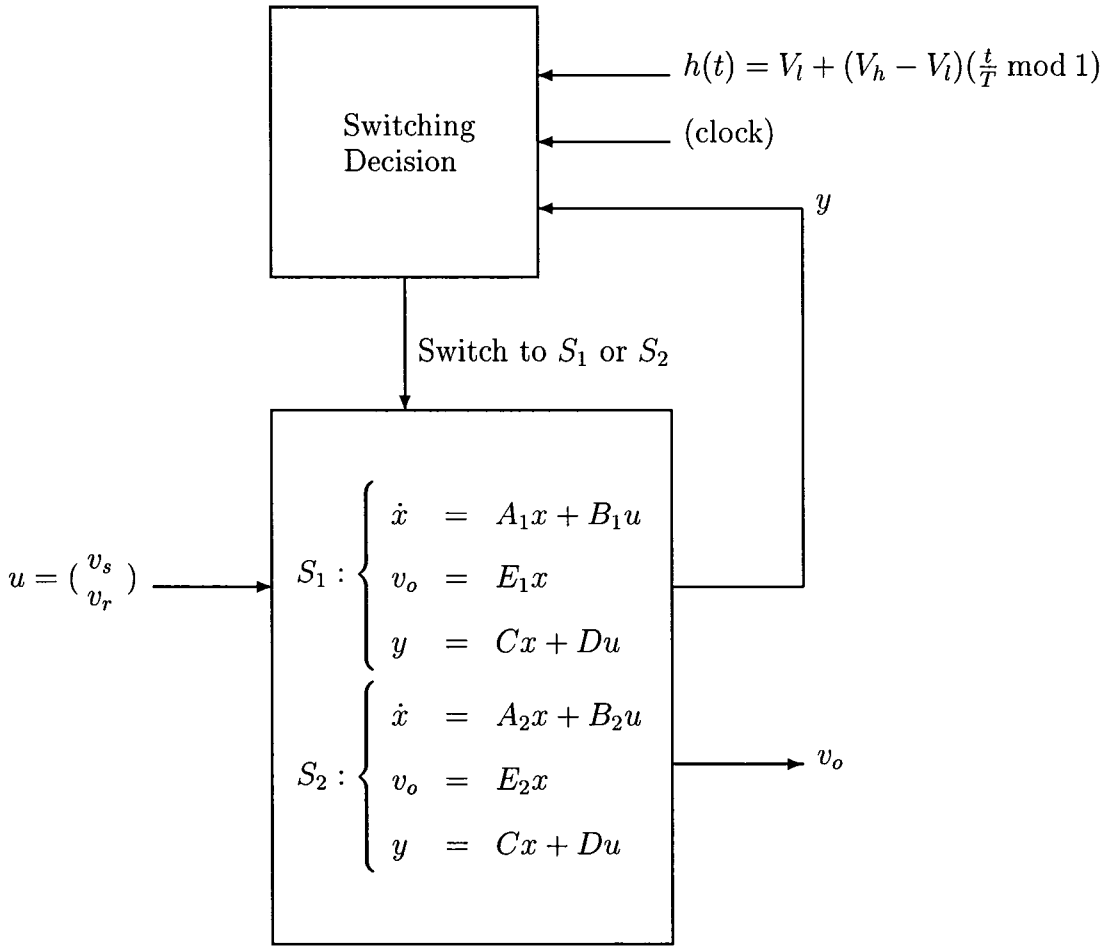

Figure 3.1: A general model for switching converters in current/voltage mode

Generally the operating condition switches back and forth between S_1 and S_2 once per clock cycle. The signals $y(t)$ and $h(t)$ in current mode control are shown in Fig. 3.4. The operating condition is switched to S_1 when a clock pulse occurs, and switched to S_2 when $y(t) = h(t)$. The signals $y(t)$ and $h(t)$ in voltage mode control are shown in Fig. 3.5. The circuit is in S_1 when $y(t) > h(t)$ and in S_2 when $y(t) \leq h(t)$.

In CCM there are two stages depending on whether the controlled switch is

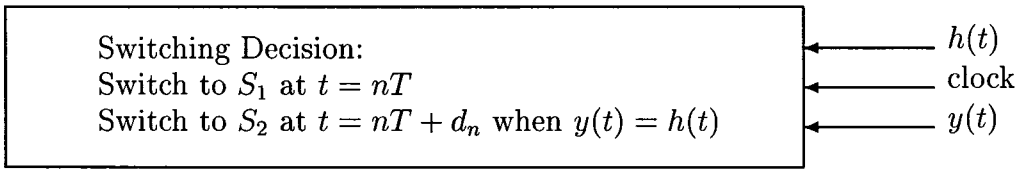

Figure 3.2: Switching decision in current mode control

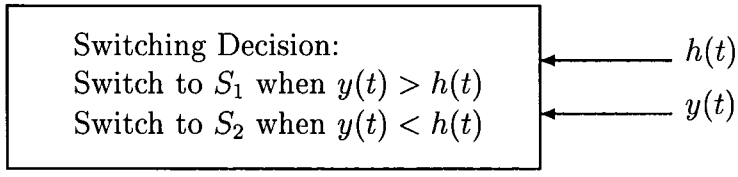

Figure 3.3: Switching decision in voltage mode control

on or off:

$$S_1 \ : \ \begin{cases} \dot{x} &= A_1 x + B_1 u \\ v_o &= E_1 x \end{cases} \tag{3.1}$$

$$S_2 \ : \ \begin{cases} \dot{x} &= A_2 x + B_2 u \\ v_o &= E_2 x \end{cases} \tag{3.2}$$

In the trailing-edge design, the controlled switch is on in S_1. In the leading-edge design, the controlled switch is off in S_1.

Here E_1 need not be the same as E_2. Thus v_o can be discontinuous. The boost converter in Fig. 2.3, for example, has $E_1 \neq E_2$ if the equivalent series resistance (ESR) $R_c \neq 0$. A typical output voltage waveform of a boost converter with ESR is shown in Fig. 3.6. In most applications, the output voltage of interest is the peak, minimum, or average voltage. So in the following, we will use E to denote E_1, E_2, or $(E_1 + E_2)/2$.

A main difference between the modeling here and the presentation in [48, 103] is that our model accurately refers the effect of the external signal $h(t)$. This

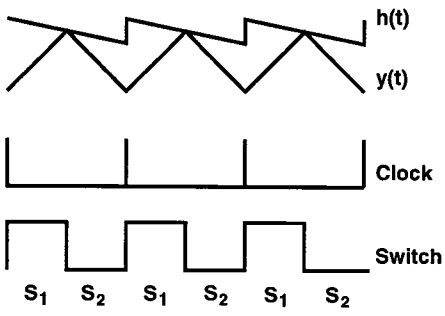

Figure 3.4: Waveforms of a PWM converter in current mode control

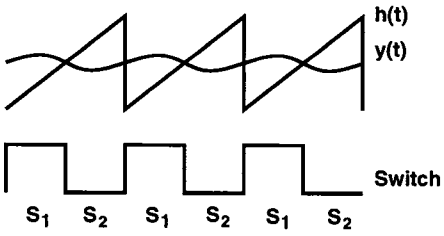

Figure 3.5: Waveforms of a PWM converter in voltage mode control

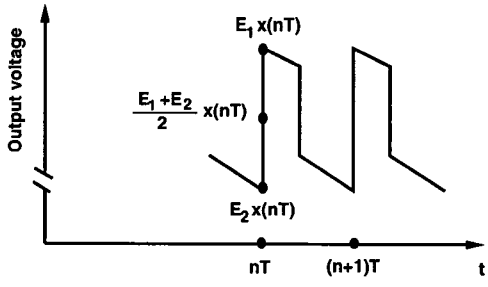

Figure 3.6: A typical output voltage waveform of a boost converter with ESR

model is sufficiently general to address many PWM converters under different configurations. In this chapter, we concentrate on voltage and current mode control. The same modeling approach can be applied to other configurations, such as average current mode control [92], charge control [93], and one-cycle control [88].

3.2 General Sampled-Data Model of the PWM Converter in CCM with FFC

Generally in the PWM converter, the switching frequency is very high that there is little variation in v_s and v_r in a cycle. So $u = (v_s, v_r)$ can be assumed to be constant in a cycle.

Assume we sample the state at the clock time, $x_n = x(nT)$. Let $u_n = (v_{sn}, v_{rn})$ be constant in a cycle. We try to develop the sampled-data dynamics mapping x_n to x_{n+1}, which is shown in Fig. 3.7.

In the $(n+1)$-th cycle, let the instant when the signals $y(t)$ and $h(t)$ intersects be $nT + d_n$. We have $y(nT + d_n) = h(nT + d_n)$, which places a constraint on the dynamics. So the PWM converter in CCM with FFC has the following sampled-data dynamics:

$$\begin{aligned} x_{n+1} &= f(x_n, u_n, d_n) \\ &= e^{A_2(T-d_n)}(e^{A_1 d_n} x_n + \int_0^{d_n} e^{A_1(d_n-\sigma)} d\sigma B_1 u_n) \\ &\quad + \int_{d_n}^{T} e^{A_2(T-\sigma)} d\sigma B_2 u_n \qquad (3.3) \\ g(x_n, u_n, d_n) &= y(nT + d_n) - h(nT + d_n) \\ &= C(e^{A_1 d_n} x_n + \int_0^{d_n} e^{A_1(d_n-\sigma)} d\sigma B_1 u_n) + D u_n - h(d_n) \end{aligned}$$

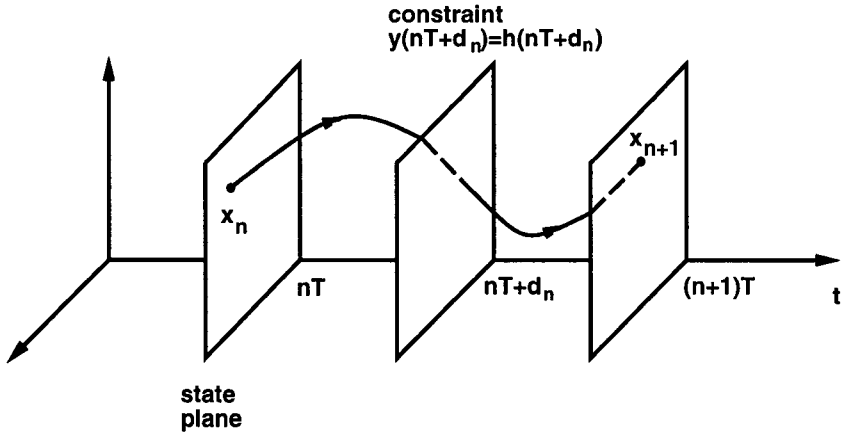

Figure 3.7: Illustration of sampled-data dynamics of PWM converter in CCM with FFC

$$= 0 \tag{3.4}$$

$$v_{on} = Ex_n \tag{3.5}$$

3.3 Existence and Analysis of Periodic Solutions in PWM converter

We first show a lemma related to the invertibility of a matrix, which will be used for proof of existence of periodic solutions.

3.3.1 A Preliminary Lemma

The following assumptions will be used in the dissertation.

(A1) $\mathrm{Re}[\sigma(A_1)] \leq 0$, $\mathrm{Re}[\sigma(A_2)] \leq 0$.

(A2) $\mathrm{Re}[\sigma(A_1)] \leq 0$, $\mathrm{Re}[\sigma(A_2)] < 0$.

(or $\mathrm{Re}[\sigma(A_1)] < 0$, $\mathrm{Re}[\sigma(A_2)] \leq 0$.)

(A3) $\mathrm{Re}[\sigma(A_1)] < 0$, $\mathrm{Re}[\sigma(A_2)] < 0$.

Throughout the dissertation, (A1) is assumed implicitly. In some cases, (A2) or (A3) is assumed.

Generally the circuit will dissipate energy due to the inherent resistance, so all of the eigenvalues of A_1 and A_2 are in the open left half of the complex plane (LHP). (None can be in the right half of the complex plane since the circuit is a single RLC circuit between switching instants.) If some of the resistances in the circuit are not modeled, then A_1 or A_2 may have some eigenvalues on the imaginary axis. We need to assume (A2) to prove over stability results. The stored energy in the circuit in either stage is given by the same formula, which involves capacitor voltages and inductor currents ($\frac{1}{2}\sum(L_i i_{Li}^2 + C_i v_{Ci}^2)$). From Theorem 2.1 and 2.2, there exists a real, symmetric, and positive definite matrix $P \in \mathbf{R}^{n\times n}$ such that $e^{A_1^T t_1} P e^{A_1 t_1} - P$ is negative semidefinite and the matrix $e^{A_2^T t_2} P e^{A_2 t_2} - P$ is negative definite.

The following lemma is related to the open-loop stability and stabilizability of PWM converters, which will be discussed in Chapter 5.

Lemma 3.1 *Assume that there exists a real, symmetric, and positive definite matrix $P \in \mathbf{R}^{n\times n}$ such that for any $t_1, t_2 > 0$, $e^{A_1^T t_1} P e^{A_1 t_1} - P$ is negative semidefinite and $e^{A_2^T t_2} P e^{A_2 t_2} - P$ is negative definite. Then all of the eigenvalues of $e^{A_2 t_2} e^{A_1 t_1}$ are inside the unit circle.*

Proof:

$$\begin{aligned} & e^{A_1^T t_1} e^{A_2^T t_2} P e^{A_2 t_2} e^{A_1 t_1} - P \\ = \; & e^{A_1^T t_1} e^{A_2^T t_2} P e^{A_2 t_2} e^{A_1 t_1} - e^{A_1^T t_1} P e^{A_1 t_1} + e^{A_1^T t_1} P e^{A_1 t_1} - P \\ = \; & e^{A_1^T t_1} (e^{A_2^T t_2} P e^{A_2 t_2} - P) e^{A_1 t_1} + e^{A_1^T t_1} P e^{A_1 t_1} - P \end{aligned}$$

which is negative definite. So all of the eigenvalues of $e^{A_2 t_2} e^{A_1 t_1}$ are inside the unit circle. □

3.3.2 Existence of Fixed Points in Sampled-Data Dynamics

From the circuit operations depicted in Figs. (3.1, 3.2, 3.3), we can deduce necessary and sufficient conditions for the existence of a T-periodic solution. These are given next.

There exists a periodic solution of the system in Fig. 3.1 if and only if there exist $x^0(t)$, $(y^0(t) = Cx^0(t) + Du)$ and a constant $d \in [0, T]$, , such that the following hold:

(i) In current mode control:

$$y^0(d) = h(d) \tag{3.6}$$

$$\dot{x}^0(t) = A_1 x^0(t) + B_1 u \quad \text{for } t \in [0, d) \tag{3.7}$$

$$\dot{x}^0(t) = A_2 x^0(t) + B_2 u \quad \text{for } t \in [d, T) \tag{3.8}$$

(ii) In voltage mode control:

$$y^0(d) = h(d) \tag{3.9}$$

$$y^0(T^-) = h(T^-) \tag{3.10}$$

$$y^0(t) > h(t) \quad \text{for } t \in (0, d) \tag{3.11}$$

$$y^0(t) < h(t) \quad \text{for } t \in (d, T) \tag{3.12}$$

$$\dot{x}^0(t) = A_1 x^0(t) + B_1 u \quad \text{for } t \in [0, d) \tag{3.13}$$

$$\dot{x}^0(t) = A_2 x^0(t) + B_2 u \quad \text{for } t \in [d, T) \tag{3.14}$$

To find the solution $x^0(t)$ and d, we can try to find the fixed point in the sampled-data dynamics (3.3)-(3.5). Since we sample at the clock time, the periodic solution $x^0(t)$ is sampled as $x^0(0)$. Let the fixed point in the sampled-data dynamics (3.3)-(3.5) be $(x_n, u_n, d_n) = (x^0(0), u, d)$, where $u = (V_s, V_r)'$. Then this fixed point satisfies

$$x^0(0) = f(x^0(0), u, d) \tag{3.15}$$

$$g(x^0(0), u, d) = 0 \tag{3.16}$$

where the functions $f(\cdot)$ and $g(\cdot)$ are given in Eqs. (3.3) and (3.4). Thus we have $(n+1)$ nonlinear equations, Eqs. (3.15) and (3.16), in $(n+1)$ unknowns, $x^0(0)$ and d. We can use Newton's method to solve for $x^0(0)$ and d [48].

These $(n+1)$ nonlinear equations can be further reduced to one equation. From Eq. (3.15), we can express $x^0(0)$ as

$$\begin{aligned} x^0(0) = {} & (I - e^{A_2(T-d)}e^{A_1 d})^{-1} e^{A_2(T-d)} \int_0^d e^{A_1(d-\sigma)} d\sigma B_1 u \\ & + \int_d^T e^{A_2(T-\sigma)} d\sigma B_2 u \end{aligned} \tag{3.17}$$

Similarly we can express $x^0(d)$ as a function of d, denoted as $X_d(d)$:

$$\begin{aligned} X_d(d) = {} & (I - e^{A_1 d}e^{A_2(T-d)})^{-1} (e^{A_1 d} \int_d^T e^{A_2(T-\sigma)} d\sigma B_2 u \\ & + \int_0^d e^{A_1(d-\sigma)} d\sigma B_1 u) \end{aligned} \tag{3.18}$$

where the function $X_d(\cdot)$ has the following property (assuming here that all of the eigenvalues of A_1 are in the open LHP):

$$X_d(0) = -A_2^{-1} B_2 u \tag{3.19}$$

$$X_d(T) = -A_1^{-1} B_1 u \tag{3.20}$$

So we reduce the $(n+1)$ equations, (3.15) and (3.16), to one equation with one unknown d:

$$y(d) - h(d) = CX_d(d) + Du - h(d) = 0 \tag{3.21}$$

We have a sufficient condition for the existence of a fixed point in the sampled-data dynamics:

Theorem 3.1 *Assume that all of the eigenvalues of A_1 and A_2 are in the open LHP. If*

$$(CA_2^{-1}B_2u - Du + h(0))(CA_1^{-1}B_1u - Du + h(T^-)) < 0 \tag{3.22}$$

Then there exists a fixed point $(x_n, u_n, d_n) = (x^0(0), u, d)$ in the sampled-data dynamics (3.3)-(3.5).

Proof:

From Eq. (3.21), if

$$\begin{aligned}
&(CA_2^{-1}B_2u - Du + h(0))(CA_1^{-1}B_1u - Du + h(T^-)) \\
&= (CX_d(0) + Du - h(0))(CX_d(T) + Du - h(T^-)) \\
&< 0
\end{aligned}$$

then by the intermediate value theorem, there exists a solution d satisfying Eq. (3.21). Hence there exists a fixed point $(x_n, u_n, d_n) = (x^0(0), u, d)$ in the sampled-data dynamics (3.3)-(3.5).

After solving for $x^0(0)$ and d, we get a periodic solution $x^0(t)$,

$$x^0(t) = \begin{cases} e^{A_1 t}x^0(0) + \int_0^t e^{A_1(t-\sigma)}d\sigma B_1 u & \text{for } t \in [nT, nT+d) \\ e^{A_2(t-d)}x^0(d) + \int_d^t e^{A_2(t-\sigma)}d\sigma B_2 u & \text{for } t \in [nT+d, (n+1)T) \end{cases} \tag{3.23}$$

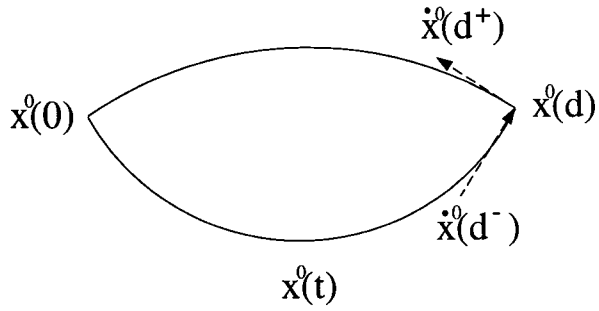

Figure 3.8: A typical periodic solution $x^0(t)$ in the DC-DC converter

A typical periodic solution $x^0(t)$ is shown Fig. 3.8.

So far, we tried to obtain the fixed point in the sampled-data dynamics, where we assumed the circuit is on and off once in a cycle. For the converter with voltage mode control, the periodic solution $x^0(t)$ obtained from Eq. (3.23) may not be the solution in Fig. 3.1.

For example, suppose we obtain a fixed point $(x_n, u_n, d_n) = (x^0(0), u, d)$. Then we can obtain the periodic solution $x^0(t)$ from Eq. (3.23). The signal $y^0(t) = Cx^0(t) + Du$ and $h(t)$ is shown in Fig. 3.9. It is periodic with $y^0(d) = h(d)$. The solution $y^0(t)$ (hence $x^0(t)$) is not eligible because $y^0(t)$ intersects with $h(t)$ more than once. So for the converter with voltage mode control, those conditions in Eqs. (3.10)-(3.12) need to be checked.

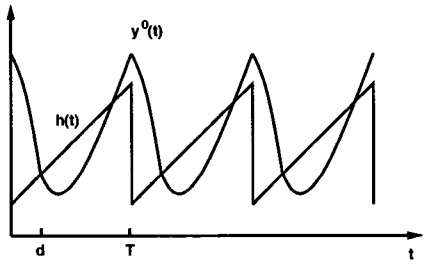

Figure 3.9: Ineligible signals $y^0(t)$ and $h(t)$ in voltage mode control

3.4 Analytical Linearized Sampled-Data Dynamics

Ths sampled-data dynamics (3.3)-(3.5) is constrained and nonlinear. The implicit function theorem allows us to linearize (3.3)-(3.5) at the fixed point $(x_n, u_n, d_n) = (x^0(0), u, d)$ to obtain an unconstrained linear sampled-data dynamics. Using the symbol $\hat{}$ to denote small perturbations (e.g. $\hat{x}_n = x_n - x^0(0)$), we have:

$$\begin{aligned} \hat{x}_{n+1} &\approx \Phi\hat{x}_n + \Gamma\hat{u}_n \\ \hat{v}_{on} &= E\hat{x}_n \end{aligned} \tag{3.24}$$

where

$$\begin{aligned} \Phi &= \frac{\partial f}{\partial x_n} - \frac{\partial f}{\partial d_n}\left(\frac{\partial g}{\partial d_n}\right)^{-1}\frac{\partial g}{\partial x_n}\bigg|_{(x_n,u_n,d_n)=(x^0(0),u,d)} \\ &= e^{A_2(T-d)}\left(I - \frac{((A_1-A_2)x^0(d)+(B_1-B_2)u)C}{C(A_1x^0(d)+B_1u)-\dot{h}(d)}\right)e^{A_1d} \\ &= e^{A_2(T-d)}\left(I - \frac{(\dot{x}^0(d^-)-\dot{x}^0(d^+))C}{C\dot{x}^0(d^-)-\dot{h}(d)}\right)e^{A_1d} \end{aligned} \tag{3.25}$$

$$\begin{aligned} \Gamma &= \frac{\partial f}{\partial u_n} - \frac{\partial f}{\partial d_n}\left(\frac{\partial g}{\partial d_n}\right)^{-1}\frac{\partial g}{\partial u_n}\bigg|_{(x_n,u_n,d_n)=(x^0(0),u,d)} \\ &= e^{A_2(T-d)}\Big(\int_0^d e^{A_1\sigma}d\sigma B_1 \\ &\quad - \frac{(A_1-A_2)x^0(d)+(B_1-B_2)u}{C(A_1x^0(d)+B_1u)-\dot{h}(d)}\Big(C\int_0^d e^{A_1\sigma}d\sigma B_1 + D\Big)\Big) + \int_0^{T-d} e^{A_2\sigma}d\sigma B_2 \\ &= e^{A_2(T-d)}\Big(\int_0^d e^{A_1\sigma}d\sigma B_1 \\ &\quad - \frac{\dot{x}^0(d^-)-\dot{x}^0(d^+)}{C\dot{x}^0(d^-)-\dot{h}(d)}\Big(C\int_0^d e^{A_1\sigma}d\sigma B_1 + D\Big)\Big) + \int_0^{T-d} e^{A_2\sigma}d\sigma B_2 \end{aligned} \tag{3.26}$$

To show the effects of v_{sn} and v_{rn} on the state x_n separately, let $u_n = (v_{sn}, v_{rn})'$, $D = [D_1, D_2]$, $\Gamma = [\Gamma_1, \Gamma_2]$, $B_1 = [B_{11}, B_{12}]$ and $B_2 = [B_{21}, B_{22}]$.

We have

$$\begin{aligned} \hat{x}_{n+1} &\approx \Phi\hat{x}_n + \Gamma_1\hat{v}_{sn} + \Gamma_2\hat{v}_{rn} \\ \hat{v}_{on} &= E\hat{x}_n \end{aligned} \tag{3.27}$$

where Γ_1 and Γ_2 are given by

$$\begin{aligned} \Gamma_1 &= e^{A_2(T-d)}\Big(\int_0^d e^{A_1\sigma}d\sigma B_{11} \\ &\quad - \frac{\dot{x}^0(d^-) - \dot{x}^0(d^+)}{C\dot{x}^0(d^-) - \dot{h}(d)}\Big(C\int_0^d e^{A_1\sigma}d\sigma B_{11} + D_1\Big)\Big) \\ &\quad + \int_0^{T-d} e^{A_2\sigma}d\sigma B_{21} \end{aligned} \tag{3.28}$$

$$\begin{aligned} \Gamma_2 &= e^{A_2(T-d)}\Big(\int_0^d e^{A_1\sigma}d\sigma B_{12} \\ &\quad - \frac{\dot{x}^0(d^-) - \dot{x}^0(d^+)}{C\dot{x}^0(d^-) - \dot{h}(d)}\Big(C\int_0^d e^{A_1\sigma}d\sigma B_{12} + D_2\Big)\Big) \\ &\quad + \int_0^{T-d} e^{A_2\sigma}d\sigma B_{22} \end{aligned} \tag{3.29}$$

3.5 Stability Analysis and Bifurcations

In the switching converter, the steady-state operating condition is a *periodic orbit*, not an equilibrium point. The relevant stability notion is *orbital stability* discussed in Sec. 2.1. In the power electronics literature, the circuit is generally said to be either stable or unstable, without mentioning orbital stability per se.

To determine the asymptotic orbital stability of the periodic solution $x^0(t)$, we have the following results:

Theorem 3.2 *[37] The fixed point $x^0(0)$ of the system (3.3-(3.5) is asymptotically stable, or equivalently the periodic solution $x^0(t)$ in the original continuous-time system of Fig. 3.1 is asymptotically orbitally stable if all of the eigenvalues of Φ are inside the unit circle of the complex plane.*

Theorem 3.3 *If the periodic solution $x^0(t)$ is asymptotically orbitally stable, then the following inequality holds:*

$$\left|\frac{C\dot{x}^0(d^+) - \dot{h}(d)}{C\dot{x}^0(d^-) - \dot{h}(d)}\right| \leq e^{\mathrm{tr}[A_2 - A_1]d - \mathrm{tr}[A_2]T} \tag{3.30}$$

Proof: Suppose the periodic solution $x^0(t)$ is asymptotically orbitally stable. Then all the eigenvalues of Φ have magnitude less than or equal than 1. Since $\det[\Phi]$ is the product of the eigenvalues of Φ, we have that

$$\begin{aligned} |\det[\Phi]| &= \left|\det[e^{A_1 d}e^{A_2(T-d)}]\det[I - \frac{(\dot{x}^0(d^-) - \dot{x}^0(d^+))C}{C\dot{x}^0(d^-) - \dot{h}(d)}]\right| \\ &= e^{-\mathrm{tr}[A_2 - A_1]d + \mathrm{tr}[A_2]T}\left|\frac{C\dot{x}^0(d^+) - \dot{h}(d)}{C\dot{x}^0(d^-) - \dot{h}(d)}\right| \\ &\leq 1 \end{aligned}$$

Then Eq. (3.30) follows. □

Remarks: (i) Generally the switching period is so small that the right side of (3.30) can be approximated as 1, resulting in a condition that resembles a well-known stability criterion in current mode control [111, for example]:

$$\left|\frac{m_2 - m_c}{m_1 - m_c}\right| < 1 \tag{3.31}$$

where m_1 and m_2 are the slopes of current trajectories during the on and off stages respectively using a *linear approximation* [61], and m_c is the slope of the compensating ramp. There are two main differences with Theorem 3.3, where the *instantaneous* slope is used and the statement is a necessary condition.

(ii) In current mode control, the closed-loop poles can be obtained approximately from Eq. (3.25) under the assumption $\omega_0 \ll \omega_s$. Both of the poles are real. One is slightly less than 1 (e.g. in the buck-boost converter, it is $e^{\frac{-d}{RC}}$.) Another is

$$\frac{i_L(d^+) - \dot{h}(d)}{i_L(d^-) - \dot{h}(d)} \approx \frac{m_2 - m_c}{m_1 - m_c} \tag{3.32}$$

which is consistent with [102], where the authors consider the case $m_c = 0$.

In stability or bifurcation analysis, we need to know the locations of the eigenvalues of Φ. We have the following two results. The first result gives a condition for λ to be an eigenvalue of Φ. This is then applied to check for the occurrence of period-doubling bifurcation and saddle-node bifurcation.

Theorem 3.4 *Suppose that λ is not an eigenvalue of $e^{A_2(T-d)}e^{A_1 d}$. Then λ is an eigenvalue of Φ if and only if*

$$1 + Ce^{A_1 d}(\lambda I - e^{A_2(T-d)}e^{A_1 d})^{-1}e^{A_2(T-d)}\frac{\dot{x}^0(d^-) - \dot{x}^0(d^+)}{C\dot{x}^0(d^-) - \dot{h}(d)} = 0 \tag{3.33}$$

Proof: Suppose λ is not an eigenvalue of $e^{A_2(T-d)}e^{A_1 d}$, then

$$\begin{aligned}
\det[\lambda I - \Phi] &= \det[\lambda I - e^{A_2(T-d)}e^{A_1 d}] \cdot \\
&\quad \det[I + (\lambda I - e^{A_2(T-d)}e^{A_1 d})^{-1}e^{A_2(T-d)}\frac{\dot{x}^0(d^-) - \dot{x}^0(d^+)}{C\dot{x}^0(d^-) - \dot{h}(d)}Ce^{A_1 d}] \\
&= \det[\lambda I - e^{A_2(T-d)}e^{A_1 d}] \cdot \\
&\quad (1 + Ce^{A_1 d}(\lambda I - e^{A_2(T-d)}e^{A_1 d})^{-1}e^{A_2(T-d)}\frac{\dot{x}^0(d^-) - \dot{x}^0(d^+)}{C\dot{x}^0(d^-) - \dot{h}(d)})
\end{aligned}$$

So λ is an eigenvalue of Φ if and only if

$$1 + Ce^{A_1 d}(\lambda I - e^{A_2(T-d)}e^{A_1 d})^{-1}e^{A_2(T-d)}\frac{\dot{x}^0(d^-) - \dot{x}^0(d^+)}{C\dot{x}^0(d^-) - \dot{h}(d)} = 0$$

□

Corollary 3.1

(i) If the system parameters correspond to an occurrence of period-doubling bifurcation, then

$$1 + Ce^{A_1 d}(-I - e^{A_2(T-d)}e^{A_1 d})^{-1}e^{A_2(T-d)}\frac{\dot{x}^0(d^-) - \dot{x}^0(d^+)}{C\dot{x}^0(d^-) - \dot{h}(d)} = 0 \tag{3.34}$$

(ii) If the system parameters correspond to an occurrence of saddle-node bifurcation, then

$$1 + Ce^{A_1 d}(I - e^{A_2(T-d)}e^{A_1 d})^{-1}e^{A_2(T-d)}\frac{\dot{x}^0(d^-) - \dot{x}^0(d^+)}{C\dot{x}^0(d^-) - \dot{h}(d)} = 0 \qquad (3.35)$$

3.6 Analytical Formulae for Audio-susceptibility and Output Impedance

The dynamic performance of a DC-DC converter is assessed in terms of stability, transient dynamics, line regulation and load regulation. The first two of these can be studied using the eigenvalues of Φ; this was pursued in the foregoing section. Evaluation of the line and load regulation is considered in this section.

Generally in a controlled switching converter, there are disturbances at the voltage source and the load. In DC-DC converters, the output voltage should be kept as close to the desired constant value as possible in the presence of these disturbances. There are two measures that are commonly used to assess the effect of disturbances at the voltage source and the load on the output voltage. The first is the small-signal source to output voltage transfer function, also called the audio-susceptibility, which is a measure of the effect of the line disturbance. The second is the small-signal output current to output voltage transfer function, also called the output impedance, which measures the effect of the load disturbance. These two measures are expressed in terms of transfer functions that show the effect of disturbances at various frequencies on the output voltage. In a good design, these two measures should be as low as possible.

More specifically, let the nominal source voltage be V_s and the nominal average output voltage and current be $V_{o,\text{ave}}$ and $I_{o,\text{ave}}$ respectively. Define

$\hat{v}_s = v_s - V_s$, $\hat{v}_o = v_o - V_{o,\text{ave}}$ and $\hat{i}_o = i_o - I_{o,\text{ave}}$. Assume the dynamics between $\hat{v}_o$ and $\hat{v}_s$ (or $\hat{i}_o$) can be approximated by a linear time-invariant continuous-time system. Then the audio-susceptibility is

$$\left.\frac{\hat{v}_o(s)}{\hat{v}_s(s)}\right|_{s=j\omega} \tag{3.36}$$

The output impedance is

$$\left.\frac{\hat{v}_o(s)}{\hat{i}_o(s)}\right|_{s=j\omega} \tag{3.37}$$

Next we develop two methods for calculating the audio-susceptibility and output impedance. In the first method, we use the sampled-data dynamic model. This approach was also used in [48, 103], except that here we derive the formulae for audio-susceptibility and output impedance *analytically*. In the second method, the sampled-data dynamics are "lifted" to give a continuous-time linear approximation that is valid locally.

3.6.1 Sampled-Data Method (S method)

In this method, we assume the source voltage and the load are constant within each switching period; this was also assumed for modeling in the sampled-data method.

Audio-susceptibility (small signal source to output voltage transfer function)

The audio-susceptibility is derived directly from the linearized sampled-data dynamic model, Eq. (3.27). It is

$$T_{os}(z) = \frac{\hat{v}_o(z)}{\hat{v}_s(z)} = E(zI - \Phi)^{-1}\Gamma_1 \tag{3.38}$$

Output impedance (small signal output current to output voltage transfer function)

To calculate the output impedance, we add a fictitious current source i_o (as perturbation) in parallel with the load. Then the state equations in Eqs. (3.1) and (3.2) are replaced by

$$S_1 : \dot{x} = A_1 x + B_{11} v_s + B_{12} v_r + B_{13} i_o \tag{3.39}$$

$$S_2 : \dot{x} = A_2 x + B_{21} v_s + B_{22} v_r + B_{23} i_o \tag{3.40}$$

Since i_o is used as perturbation, the nominal value of i_o is 0. Similar to the derivations in Sec. 3.2, the new linearized sampled-data dynamics is

$$\begin{aligned} \hat{x}_{n+1} &\approx \Phi \hat{x}_n + \Gamma_1 \hat{v}_{sn} + \Gamma_2 \hat{v}_{rn} + \Gamma_3 \hat{I}_{on} \\ \hat{v}_{on} &= E \hat{x}_n \end{aligned} \tag{3.41}$$

where

$$\begin{aligned} \Gamma_3 &= \frac{\partial f}{\partial i_{on}} - \frac{\partial f}{\partial d_n} \left(\frac{\partial g}{\partial d_n}\right)^{-1} \frac{\partial g}{\partial i_{on}} \Big|_{(x_n, u, d_n, i_{on}) = (x^0(0), u, d, 0)} \\ &= e^{A_2(T-d)} \Big(\int_0^d e^{A_1 \sigma} d\sigma B_{13} \\ &\quad - \frac{\dot{x}^0(d^-) - \dot{x}^0(d^+)}{C\dot{x}^0(d^-) - \dot{h}(d)} C \int_0^d e^{A_1 \sigma} d\sigma B_{13} \Big) \\ &\quad + \int_0^{T-d} e^{A_2 \sigma} d\sigma B_{23} \end{aligned} \tag{3.42}$$

and i_{on} is the sampled perturbed output current during the n-th cycle. So the output impedance is

$$T_{oo}(z) = \frac{\hat{v}_o(z)}{\hat{i}_o(z)} = E(zI - \Phi)^{-1} \Gamma_3 \tag{3.43}$$

From the discussion in Sec. 2.1.2, the frequency response of audio-susceptibility and output impedance are $T_{os}(e^{j\omega T})$ and $T_{oo}(e^{j\omega T})$ respectively. These frequency responses differ from those in Eqs. (3.36) and (3.37) respectively by the following arguments:

1. The nominal output voltage in sampled-data dynamics is $Ex^0(0)$, it differs from the nominal output voltage $V_{o,\text{ave}}$ in continuous-time dynamics.

2. In the sampled-data dynamics, we assume v_s, v_r and i_o are constant in a cycle, while they are time-varying in continuous-time dynamics.

3. Both $T_{os}(e^{j\omega T})$ and $T_{oo}(e^{j\omega T})$ are periodic in ω with period ω_s. Thus the aliasing effect discussed in 2.1.2 will occur. The frequency responses in Eqs. (3.36) and (3.37) are not periodic.

For small switching period T, $Ex^0(0) \approx V_{o,\text{ave}}$, and v_s, v_r and i_o can be assumed constant in a cycle. Also for small T, v_s and i_o are sampled more enough that aliasing effect will not be pronounced. Thus for small T, the frequency responses $T_{os}(e^{j\omega T})$ and $T_{oo}(e^{j\omega T})$ obtained from the sampled-data dynamics are close to the frequency responses in Eqs. (3.36) and (3.37) respectively.

3.6.2 "Lifting" the Sampled-Data Dynamics (SC method)

Assuming v_s (or i_o) is constant within each switching period is the same as assuming a sampler with a zero-order-hold (ZOH) being placed after v_s (or i_o). Thus the input v_s (or i_o) and output v_o relationship is similar to those in Fig. 2.1. In Sec. 2.1.3, we have shown that the continuous-time dynamics can be obtained from the discretized dynamics. To obtain the audio-susceptibility, we can convert the pair (Φ, Γ_1) to the continuous-time pair (Φ^c, Γ_1^c), using the method in Sec. 2.1.3. Then $E(j\omega I - \Phi^c)^{-1}\Gamma_1^c$ is the audio-susceptibility. Similarly, by converting the pair (Φ, Γ_3) to the continuous-time pair (Φ^c, Γ_3^c), then $E(j\omega I - \Phi^c)^{-1}\Gamma_3^c$ is the output impedance.

3.7 Stability Calculation for Period-Doubling Bifurcation in 1-Dimensional Switching Converters

If a period-doubling bifurcation occurs, it can be supercritical or subcritical. The stability type of the bifurcation cannot be discerned from the linearized dynamics. To determine which type of period-doubling bifurcation occurs, we need to analyze the nonlinear dynamics.

Switching converters are high dimensional, and the nonlinear dynamics are difficult to analyze. Generally some of the states are slowly varying so that the order of the system can be reduced. For example, the output voltage is kept at a DC value with a very small AC ripple. This allows us to approximate the load and capacitor by a constant voltage source, so that the dimension of the system dynamics is reduced.

Suppose we can perform approximate order reduction to result in a 1-dimensional reduced-order model. From this model we try to determine the stability of the bifurcated limit cycle. Here we analyze a 1-dimensional model of a switching converter in current mode control with 2 stages:

$$S_1 : \dot{x} = a_1 x + b_1 V_s \tag{3.44}$$

$$S_2 : \dot{x} = a_2 x + b_2 V_s \tag{3.45}$$

where $x \in \mathbf{R}$ is the system state (for example, the inductor current), V_s is the source voltage, and $a_1, a_2, b_1, b_2 \in \mathbf{R}$.

To be specific, we consider the we 1-dimensional converter in current mode control depicted in Fig. 3.10. Since the converter is in current mode control, the

reference signal in Fig. 3.10 is the current reference I_r (instead of V_r). The type of converter need not be specified.

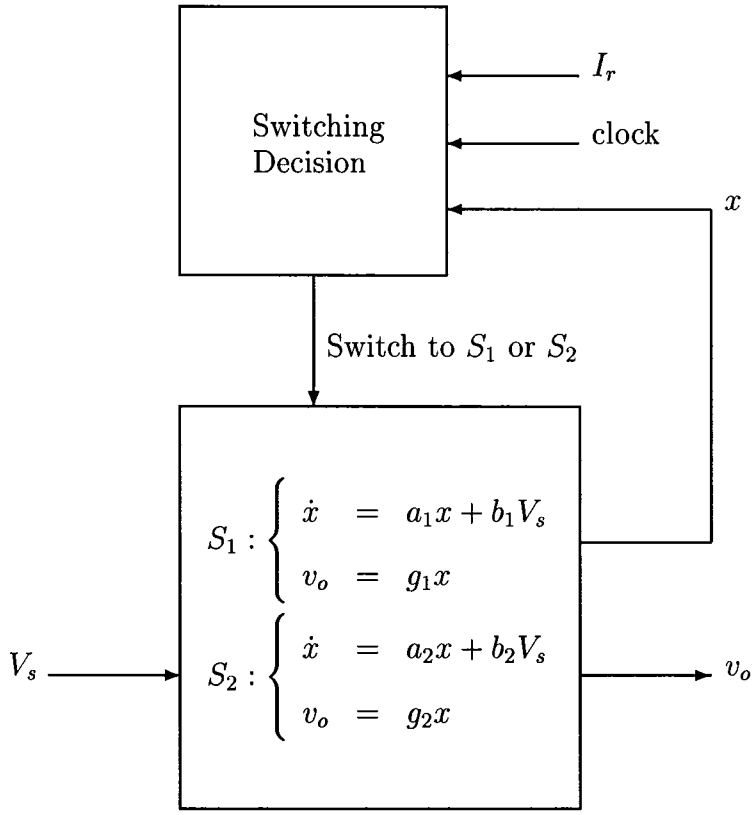

Figure 3.10: A 1-dimensional model of switching converter in current mode control

The current mode control is operated as follows: the operating condition is switched to S_1, when there is a clock pulse, and switched to S_2 when $x = I_r$.

Here V_s is used as the bifurcation variable. For the cases where other variables are used as the bifurcation variables, the analysis is similar. Similar to the Sec. 3.2, this system has the following sampled-data dynamics:

$$x_{n+1} = f(x_n, , d_n, V_s)$$

$$
\begin{aligned}
&= e^{a_2(T-d_n)}(e^{a_1 d_n}x_n + \int_0^{d_n} e^{a_1\sigma}d\sigma b_1 V_s) \\
&\quad + \int_{d_n}^{T} e^{a_2(T-\sigma)}d\sigma b_2 V_s \qquad (3.46)\\
g(x_n, d_n, V_s) &= e^{a_1 d_n}x_n + \int_0^{d_n} e^{a_1\sigma}d\sigma b_1 V_s - I_r \\
&= 0 \qquad (3.47)
\end{aligned}
$$

Suppose the period-doubling bifurcation occurs at $V_s = V_{s,*}$. Let the fixed point at bifurcation be $(x_n, d_n) = (x_*^0(0), d_*)$. This point satisfies

$$
\begin{aligned}
x_*^0(0) &= f(x_*^0(0), d_*, V_{s,*}) \qquad (3.48)\\
g(x_*^0(0), d_*, V_{s,*}) &= 0 \qquad (3.49)
\end{aligned}
$$

In the following, the nonlinear dynamics (3.46) will be analyzed in the neighborhood of this fixed point. From Eq. (3.47) and assuming $a_1 \neq 0$, we can express $\hat{d}_n = d_n - d_*$ in terms of $\hat{x}_n = x_n - x_*^0(0)$ using Taylor series:

$$
\begin{aligned}
\hat{d}_n &= \frac{1}{a_1}\ln(\frac{a_1 I_r + b_1 V_{s,*}}{a_1 x_n + b_1 V_{s,*}}) - d_* \\
&= -\frac{1}{a_1 x_*^0(0) + b_1 V_{s,*}}\hat{x}_n + \frac{a_1}{(a_1 x_*^0(0) + b_1 V_{s,*})^2}\hat{x}_n^2 \\
&\quad - \frac{2a_1^2}{(a_1 x_*^0(0) + b_1 V_{s,*})^3}\hat{x}_n^3 + O(\hat{x}_n^4) \\
&= -\frac{1}{\dot{x}_*^0(d_*^+)}\hat{x}_n + \frac{a_1}{(\dot{x}_*^0(d_*^+))^2}\hat{x}_n^2 \\
&\quad - \frac{2a_1^2}{(\dot{x}_*^0(d_*^+))^3}\hat{x}_n^3 + O(\hat{x}_n^4) \qquad (3.50)
\end{aligned}
$$

Similarly, expanding the nonlinear dynamics (3.46), we have

$$
\begin{aligned}
x_{n+1} &= f(x_*^0(0), d_*) + \left.\frac{\partial f}{\partial x_n}\right|_\diamond \hat{x}_n + \left.\frac{\partial f}{\partial d_n}\right|_\diamond \hat{d}_n + \left.\frac{\partial f}{\partial x_n \partial d_n}\right|_\diamond \hat{x}_n\hat{d}_n + \frac{1}{2}\left.\frac{\partial^2 f}{\partial d_n^2}\right|_\diamond \hat{d}_n^2 \\
&\quad + \frac{1}{2}\left.\frac{\partial^3 f}{\partial x_n \partial d_n^2}\right|_\diamond \hat{x}_n\hat{d}_n^2 + \frac{1}{6}\left.\frac{\partial^3 f}{\partial d_n^3}\right|_\diamond \hat{d}_n^3 + H.O.T. \qquad (3.51)
\end{aligned}
$$

where

$$\left.\frac{\partial f}{\partial x_n}\right|_{\diamond} = e^{a_2(T-d_*)}e^{a_1 d_*} \tag{3.52}$$

$$\left.\frac{\partial f}{\partial d}\right|_{\diamond} = e^{a_2(T-d_*)}(\dot{x}_*^0(d_*^-) - \dot{x}_*^0(d_*^+)) \tag{3.53}$$

$$\left.\frac{\partial f}{\partial x_n \partial d}\right|_{\diamond} = e^{a_2(T-d_*)}(a_1 - a_2)e^{a_1 d_*} \tag{3.54}$$

$$\left.\frac{\partial^2 f}{\partial d^2}\right|_{\diamond} = e^{a_2(T-d_*)}((a_1 - 2a_2)\dot{x}_*^0(d_*^-) + a_2\dot{x}_*^0(d_*^+)) \tag{3.55}$$

$$\left.\frac{\partial^3 f}{\partial x_n \partial d^2}\right|_{\diamond} = e^{a_2(T-d_*)}(a_1 - a_2)^2 e^{a_1 d_*} \tag{3.56}$$

$$\left.\frac{\partial^3 f}{\partial d^3}\right|_{\diamond} = e^{a_2(T-d_*)}((a_1^2 - 3a_1a_2 + 3a_2^2)\dot{x}_*^0(d_*^-) - a_2^2\dot{x}_*^0(d_*^+)) \tag{3.57}$$

and $\diamond$ indicates evaluation at $(x_n, d_n, V_s) = (x_*^0(0), d_*, V_{s,*})$.

Substituting Eq. (3.50) into Eq. (3.51), we have

$$\hat{x}_{n+1} = \Phi\hat{x}_n + \frac{1}{2}f_2\hat{x}_n^2 + \frac{1}{6}f_3\hat{x}_n^3 + O(\hat{x}_n^4) \tag{3.58}$$

where

$$\begin{aligned}
\Phi &= e^{a_2(T-d_*)}e^{a_1 d_*} - e^{a_2(T-d_*)}\frac{\dot{x}_*^0(d_*^-) - \dot{x}_*^0(d_*^+)}{\dot{x}_*^0(d_*^+)} \\
&= \frac{e^{a_2(T-d_*)}\dot{x}_*^0(d_*^+)}{\dot{x}_*^0(d_*^+)} \\
&= \frac{a_2 x_*^0(0) + b_2 V_{s,*}}{a_1 x_*^0(0) + b_1 V_{s,*}} \\
&= -1
\end{aligned} \tag{3.59}$$

$$f_2 = \frac{a_1 - a_2}{a_1 x_*^0(0) + b_1 V_{s,*}} \tag{3.60}$$

$$f_3 = \frac{(a_1 - a_2)(a_2 - 2a_1)}{(a_1 x_*^0(0) + b_1 V_{s,*})^2} \tag{3.61}$$

From Eq. (3.59), we have

$$x_*^0(0) = -\frac{(b_1 + b_2)V_{s,*}}{a_1 + a_2} \tag{3.62}$$

From Eq. (2.10), we have

$$\begin{aligned}\beta_2 &= -f_2^2 - \frac{2}{3}f_3 \\ &= \frac{a_1^2 - a_2^2}{3(a_1 x_*^0(0) + b_1 V_{s,*})^2} \\ &= \frac{a_1^2 - a_2^2}{3V_{s,*}^2}\left(\frac{a_1 + a_2}{b_1 a_2 - a_1 b_2}\right)^2 \end{aligned} \tag{3.63}$$

Thus, if $|a_1| < |a_2|$, then the period-doubling bifurcation of this reduced system is supercritical.

3.8 General Sampled-Data Model of the PWM Converter in DCM with FFC

Sampled-data model of PWM converter in CCM has bee derived in Sec. 3.2. In this section, Sampled-data model of PWM converter in discontinuous conduction mode (DCM) will be derived. When the load is light, the DC-DC converter is designed to operate in DCM. Take the $(n+1)$-th cycle for example, the inductor current reaches zero at $t = nT + d_{2n}$, where $0 < d_{2n} < T$. (Note: the switching instants are updated every cycle and denoted as d_{1n} and d_{2n}, instead of $d_{1,n}$ and $d_{2,n}$ to simplify the notations.)

So there are three stages in a cycle:

$$S_1 : \begin{cases} \dot{x} = A_1 x + B_1 u \\ v_o = E_1 x \end{cases} \quad \text{for } t \in [nT, nT + d_{1n}) \tag{3.64}$$

$$S_2 : \begin{cases} \dot{x} = A_2 x + B_2 u \\ v_o = E_2 x \end{cases} \quad \text{for } t \in [nT + d_{1n}, nT + d_{2n}) \tag{3.65}$$

$$S_3 \ : \ \begin{cases} \dot{x} &= A_3 x + B_3 u \\ v_o &= E_3 x \end{cases} \qquad \text{for } t \in [nT + d_{2n}, (n+1)T) \tag{3.66}$$

with two switching conditions:

$$Cx(nT + d_{1n}) + Du = h(nT + d_{1n}) \tag{3.67}$$

$$Fx(nT + d_{2n}) = i_L(nT + d_{2n}) = 0 \tag{3.68}$$

where $F \in \mathbf{R}^{1\times n}$ is chosen to have $Fx = i_L$.

Similar to Fig. 3.1, the circuit model for DCM is shown in Fig. 3.11. The associated switching decision for voltage mode and current mode control is shown in Fig. 3.12 and Fig. 3.13 respectively.

An illustrative figure about the mapping from $x_n = x(nT)$ to $x_{n+1} = x((n+1)T)$ is shown in Fig. 3.14.

Similar to the case in CCM, the output voltage in DCM can discontinuous at the clock time. we will use E to denote E_1, E_3, or $(E_1 + E_3)/2$ depending on which value of output voltage is of interest.

From Fig. 3.14, the PWM converter has the following sampled-data dynamics:

$$\begin{aligned} x_{n+1} &= f(x_n, u_n, d_n) \\ &= e^{A_3(T-d_{2n})}(e^{A_2(d_{2n}-d_{1n})}(e^{A_1 d_{1n}} x_n \\ &\quad + \int_0^{d_{1n}} e^{A_1(d_{1n}-\sigma)} d\sigma B_1 u_n) + \int_{d_{1n}}^{d_{2n}} e^{A_2(d_{2n}-\sigma)} d\sigma B_2 u_n) \\ &\quad + \int_{d_{2n}}^{T} e^{A_3(T-\sigma)} d\sigma B_3 u_n \end{aligned} \tag{3.69}$$

$$v_{on} = Ex_n \tag{3.70}$$

$g(x_n, u_n, d_n)$

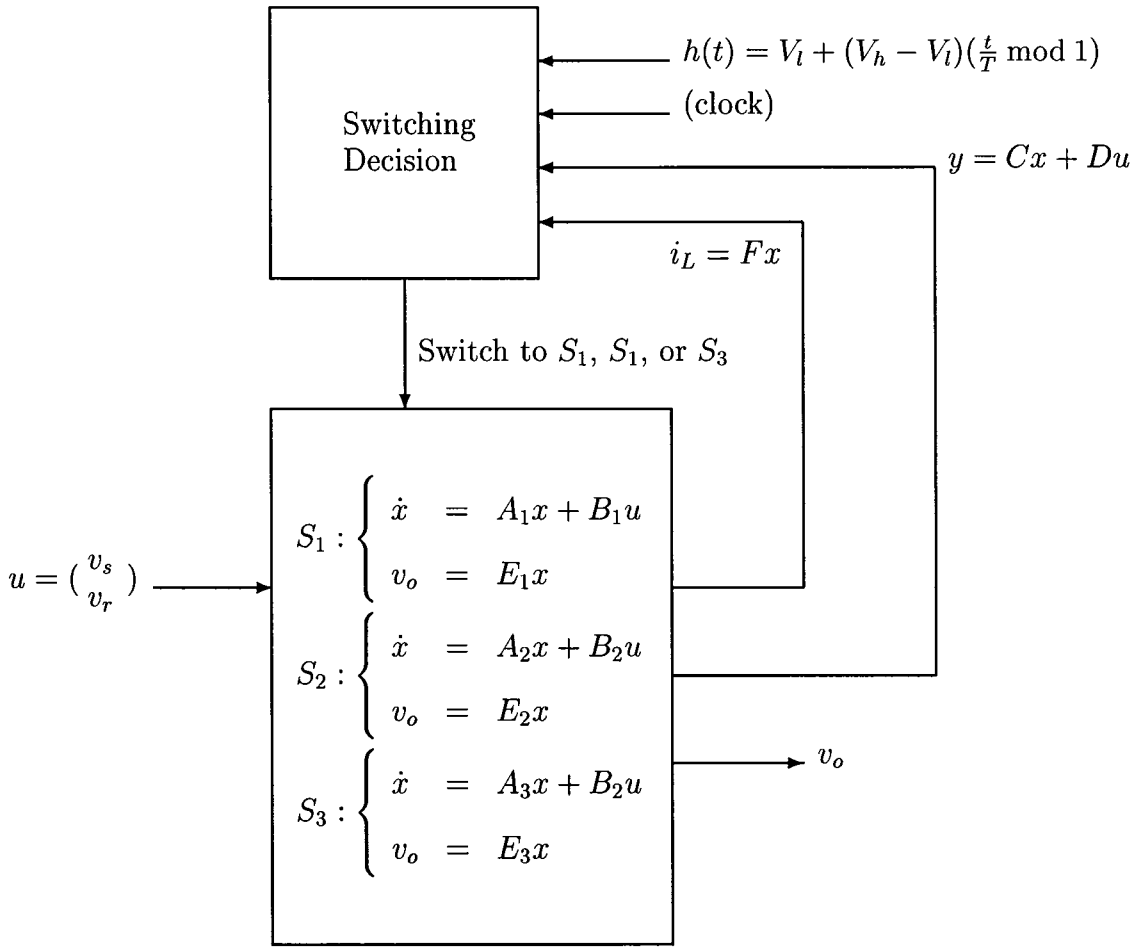

Figure 3.11: A general model for switching converters in DCM

$$
\begin{aligned}
&= \begin{bmatrix} Cx(nT + d_{1n}) + Du - h(nT + d_{1n}) \\ Fx(nT + d_{2n}) \end{bmatrix} \\
&= \begin{bmatrix} C(e^{A_1 d_{1n}} x_n + \int_0^{d_{1n}} e^{A_1 \sigma} d\sigma B_1 u_n) + Du_n - h(d_{1n}) \\ F(e^{A_2(d_{2n} - d_{1n})}(e^{A_1 d_{1n}} x_n + \int_0^{d_{1n}} e^{A_1 \sigma} d\sigma B_1 u_n) + \int_0^{d_{2n} - d_{1n}} e^{A_2 \sigma} d\sigma B_2 u_n) \end{bmatrix} \\
&= 0
\end{aligned}
\tag{3.71}
$$

where $d_n = (d_{1n}, d_{2n})'$. Since the inductor current always starts from 0 at the beginning of a cycle, another explicit constraint is $Fx_n = i_{Ln} = 0$, for *any* n. So

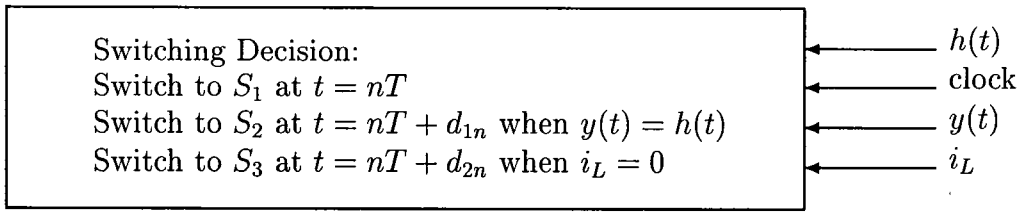

Figure 3.12: Switching decision in current mode control and DCM

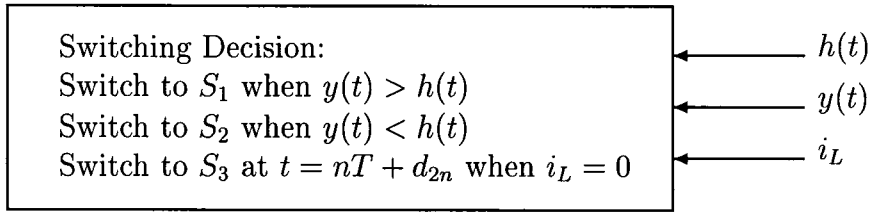

Figure 3.13: Switching decision in voltage mode control and DCM

the dynamics is $(n-1)$-dimensional instead of n-dimensional.

Linearizing Eqs. (3.69)-(3.71) and using the notation $\diamond$ to denote evaluation at the fixed point, $(x_n, u_n, d_n) = (x^0(0), u, (d_1, d_2)')$, we have

$$\begin{aligned} \hat{x}_{n+1} &\approx \Phi\hat{x}_n + \Gamma\hat{u}_n \\ \hat{v}_{on} &= E\hat{x}_n \end{aligned} \tag{3.72}$$

where

$$\Phi = \left.\frac{\partial f}{\partial x_n} - \frac{\partial f}{\partial d_n}\left(\frac{\partial g}{\partial d_n}\right)^{-1}\frac{\partial g}{\partial x_n}\right|_{\diamond} \tag{3.73}$$

$$\Gamma = \left.\frac{\partial f}{\partial u_n} - \frac{\partial f}{\partial d_n}\left(\frac{\partial g}{\partial d_n}\right)^{-1}\frac{\partial g}{\partial u_n}\right|_{\diamond} \tag{3.74}$$

$$\left.\frac{\partial f}{\partial x_n}\right|_{\diamond} = e^{A_3(T-d_2)}e^{A_2(d_2-d_1)}e^{A_1 d_1} \tag{3.75}$$

$$\left.\frac{\partial f}{\partial d_n}\right|_{\diamond} = e^{A_3(T-d_2)}\begin{bmatrix} e^{A_2(d_2-d_1)}(\dot{x}^0(d_1^-) - \dot{x}^0(d_1^+)) & \dot{x}^0(d_2^-) - \dot{x}^0(d_2^+) \end{bmatrix} \tag{3.76}$$

$$\left.\frac{\partial g}{\partial d_n}\right|_{\diamond} = \begin{bmatrix} C\dot{x}^0(d_1^-) - \dot{h}(d_1) & 0 \\ Fe^{A_2(d_2-d_1)}(\dot{x}^0(d_1^-) - \dot{x}^0(d_1^+)) & F\dot{x}^0(d_2^-) \end{bmatrix} \tag{3.77}$$

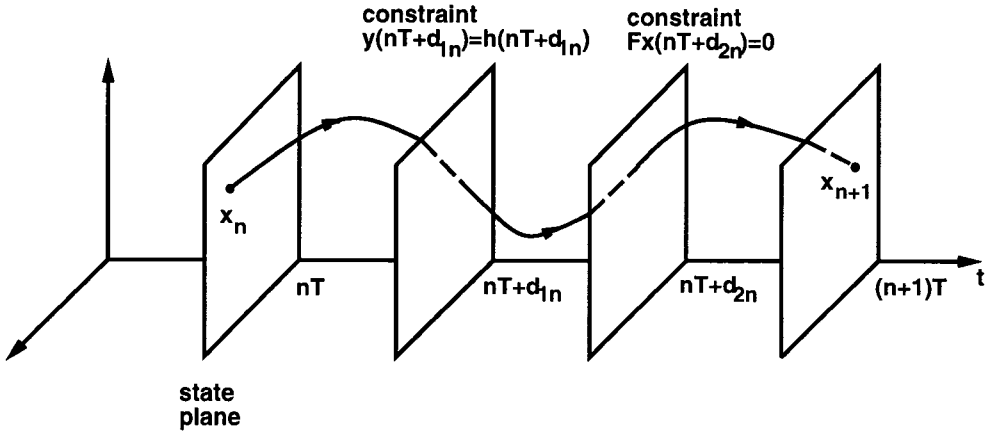

Figure 3.14: Illustration of sampled-data dynamics of PWM converter in DCM with FFC

$$\left.\frac{\partial g}{\partial x_n}\right|_{\diamond} = \begin{bmatrix} C \\ Fe^{A_2(d_2-d_1)} \end{bmatrix} e^{A_1 d_1} \tag{3.78}$$

$$\left.\frac{\partial f}{\partial u_n}\right|_{\diamond} = e^{A_3(T-d_2)}(e^{A_2(d_2-d_1)}\int_0^{d_1} e^{A_1\sigma}d\sigma B_1 + \int_0^{d_2-d_1} e^{A_2\sigma}d\sigma B_2) + \int_0^{T-d_2} e^{A_3\sigma}d\sigma B_3 \tag{3.79}$$

$$\left.\frac{\partial g}{\partial u_n}\right|_{\diamond} = \begin{bmatrix} C\int_0^{d_1} e^{A_1\sigma}d\sigma B_1 + D \\ F(e^{A_2(d_2-d_1)}\int_0^{d_1} e^{A_1\sigma}d\sigma B_1 + \int_0^{d_2-d_1} e^{A_2\sigma}d\sigma B_2) \end{bmatrix} \tag{3.80}$$

Since the inductor i_L starts at 0 and ends at 0 in a cycle, the eigenvalue of Φ associated with i_L is 0. This makes $\det[\Phi] = 0$. To prove this, we have

$$\begin{aligned} \det[\Phi] = \det[e^{A_3(T-d_2)}e^{A_2(d_2-d_1)} \cdot \\ (I - \begin{bmatrix} \dot{x}^0(d_1^-) - \dot{x}^0(d_1^+) & e^{-A_2(d_2-d_1)}(\dot{x}^0(d_2^-) - \dot{x}^0(d_2^+)) \end{bmatrix} \cdot \\ (\frac{\partial g}{\partial d_n})^{-1}\Big|_{\diamond} \begin{bmatrix} C \\ Fe^{A_2(d_2-d_1)} \end{bmatrix})e^{A_1 d_1}] \end{aligned}$$

$$
\begin{aligned}
&= \det[e^{A_1 d_1} e^{A_3(T-d_2)} e^{A_2(d_2-d_1)}] \det[I - \begin{bmatrix} C \\ Fe^{A_2(d_2-d_1)} \end{bmatrix} \cdot \\
&\quad \begin{bmatrix} \dot{x}^0(d_1^-) - \dot{x}^0(d_1^+) & e^{-A_2(d_2-d_1)}(\dot{x}^0(d_2^-) - \dot{x}^0(d_2^+)) \end{bmatrix} (\frac{\partial g}{\partial d_n})^{-1} \Big|_{\diamond}] \\
&= \det[e^{A_1 d_1} e^{A_3(T-d_2)} e^{A_2(d_2-d_1)}] \cdot \\
&\quad \det[I - \begin{bmatrix} C(\dot{x}^0(d_1^-) - \dot{x}^0(d_1^+)) & Ce^{-A_2(d_2-d_1)}(\dot{x}^0(d_2^-) - \dot{x}^0(d_2^+)) \\ Fe^{A_2(d_2-d_1)}(d_1^-) - \dot{x}^0(d_1^+)) & F\dot{x}^0(d_2^-) \end{bmatrix} \cdot \\
&\quad \frac{\begin{bmatrix} F\dot{x}^0(d_2^-) & 0 \\ -Fe^{A_2(d_2-d_1)}(\dot{x}^0(d_1^-) - \dot{x}^0(d_1^+)) & C\dot{x}^0(d_1^-) - \dot{h}(d_1) \end{bmatrix}}{(C\dot{x}^0(d_1^-) - \dot{h}(d_1))F\dot{x}^0(d_2^-)}] \\
&= \det[e^{A_1 d_1} e^{A_3(T-d_2)} e^{A_2(d_2-d_1)}] \cdot \\
&\quad \det[I - \begin{bmatrix} \text{(don't care)} & \text{(don't care)} \\ 0 & 1 \end{bmatrix}] \\
&= 0
\end{aligned}
$$

The stability, audio-susceptibility and output impedance analysis are similar to the case in CCM and are omitted.

3.9 General Sampled-Data Model of the PWM Converter in CCM with Hysteretic Control

In the previous sections, *fixed-frequency control* (FFC) was discussed. In this section, a case of *variable-frequency control* (VFC) will be presented. There are many ways to implement VFC, one of which is hysteretic control. Hysteretic control is also called ripple regulation in [9] because the voltage or current ripples can be regulated in a specified range. Other types of VFC (constant-on time or constant-off time control) are similar to hysteretic control, but only hysteretic

control is discussed here.

A general model of a switching converter with hysteretic control is shown in Fig. 3.15, where the associated switching decision box is shown in Fig. 3.16, and where v_r is the voltage or current reference (sometimes called control signal). The remaining notation is as in Fig. 3.1.

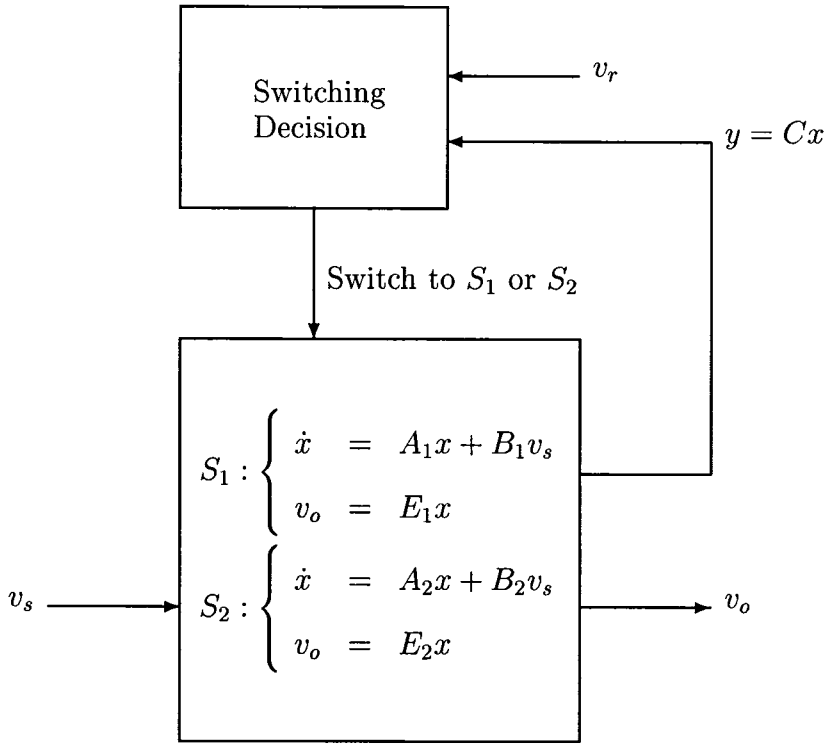

Figure 3.15: A general model for switching converters with hysteretic control

The hysteretic control operation is as follows: When $y < v_r$, the controlled switch is turned on. The switch is turned off when $y = v_r$, and it is turned on again when $y = v_r - \Delta V$. Thus the duration of an on-off cycle is variable. Let the duration of the n-th cycle be T_n and the time at the beginning of the n-th cycle be $t_n = \sum_{i=0}^{n-1} T_i$. Assuming v_r is constant in the n-th cycle with value v_{rn},

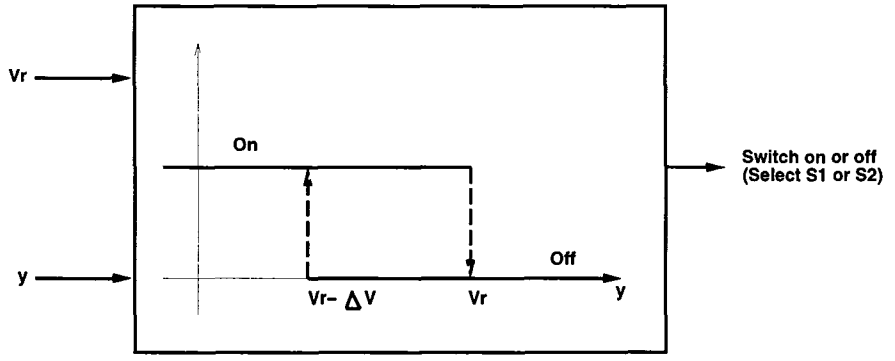

Figure 3.16: The switching decision box in Fig. 3.15

we have

$$y(t_n) = v_{rn} - \Delta V \tag{3.81}$$

$$y(t_n + d_{1n}) = v_{rn} \tag{3.82}$$

$$y(t_n + T_n) = v_{rn} - \Delta V \tag{3.83}$$

These equations place constraints on the sampled-data dynamics. An illustrative figure about the mapping from $x_n = x(t_n)$ to $x_{n+1} = x(t_n + T_n)$ is shown in Fig. 3.17.

The PWM converter in CCM with hysteretic control has the following sampled-data dynamics (letting $\tau_n = (d_n, T_n)'$):

$$\begin{aligned} x_{n+1} &= f(x_n, v_{sn}, \tau_n) \\ &= e^{A_2(T_n - d_n)}(e^{A_1 d_n} x_n + \int_0^{d_n} e^{A_1 \sigma} d\sigma B_1 v_{sn}) + \int_0^{T_n - d_n} e^{A_2 \sigma} d\sigma B_2 v_{sn} \\ v_o &= E x_n \end{aligned}$$

with the constraint equation

$g(x_n, v_{sn}, \tau_n, v_{rn})$

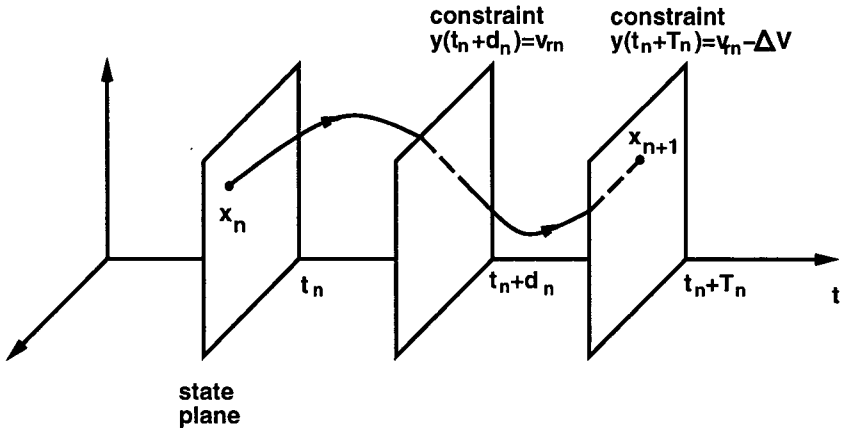

Figure 3.17: Illustration of sampled-data dynamics of PWM converter in CCM with hysteretic control

$$
\begin{aligned}
&= \begin{bmatrix} y(t_n + d_{1n}) - v_{rn} \\ y(t_n + T_n) - v_{rn} + \Delta V \end{bmatrix} \\
&= \begin{bmatrix} C(e^{A_1 d_n} x_n + \int_0^{d_n} e^{A_1 \sigma} d\sigma B_1 v_{sn}) - v_{rn} \\ C(e^{A_2(T_n - d_n)}(e^{A_1 d_n} x_n + \int_0^{d_n} e^{A_1 \sigma} d\sigma B_1 v_{sn}) + \int_0^{T_n - d_n} e^{A_2 \sigma} d\sigma B_2 v_{sn}) - v_{rn} + \Delta V \end{bmatrix} \\
&= 0 \qquad (3.84)
\end{aligned}
$$

Another explicit constraint is $Cx_n = v_{rn} - \Delta V$, for *any* n. Because of this constraint, the dynamics is $(n-1)$-dimensional.

The fixed point $(x_n, v_{sn}, \tau_n, v_{rn}) = (x^0(0), V_s, (d,T)', V_r)$ satisfies

$$x^0(0) = f(x^0(0), V_s, (d,T)') \qquad (3.85)$$

$$g(x^0(0), V_s, (d,T)', V_r) = 0 \qquad (3.86)$$

Linearizing the dynamics and using $\diamond$ to denote evaluation at the fixed point

$(x^0(0), V_s, (d,T)', V_r)$, we have

$$\begin{aligned} \hat{x}_{n+1} &\approx \Phi_h \hat{x}_n + \Gamma_{hv}\hat{v}_{sn} + \Gamma_{hr}\hat{v}_{rn} \\ \hat{v}_{on} &= E\hat{x}_n \end{aligned} \tag{3.87}$$

where

$$\Phi_h = \left.\frac{\partial f}{\partial x_n} - \frac{\partial f}{\partial \tau_n}\left(\frac{\partial g}{\partial \tau_n}\right)^{-1}\frac{\partial g}{\partial x_n}\right|_\diamond \tag{3.88}$$

$$\Gamma_{hv} = \left.\frac{\partial f}{\partial v_{sn}} - \frac{\partial f}{\partial \tau_n}\left(\frac{\partial g}{\partial \tau_n}\right)^{-1}\frac{\partial g}{\partial v_{sn}}\right|_\diamond \tag{3.89}$$

$$\Gamma_{hr} = \left.-\frac{\partial f}{\partial \tau_n}\left(\frac{\partial g}{\partial \tau_n}\right)^{-1}\frac{\partial g}{\partial v_{rn}}\right|_\diamond \tag{3.90}$$

$$\left.\frac{\partial f}{\partial x_n}\right|_\diamond = e^{A_2(T-d)}e^{A_1 d} \tag{3.91}$$

$$\left.\frac{\partial f}{\partial \tau_n}\right|_\diamond = \begin{bmatrix} e^{A_2(T-d)}(\dot{x}^0(d^-) - \dot{x}^0(d^+)) & \dot{x}^0(T^-) \end{bmatrix} \tag{3.92}$$

$$\left.\frac{\partial g}{\partial \tau_n}\right|_\diamond = \begin{bmatrix} C\dot{x}^0(d^-) & 0 \\ Ce^{A_2(T-d)}(\dot{x}^0(d^-) - \dot{x}^0(d^+)) & C\dot{x}^0(T^-) \end{bmatrix} \tag{3.93}$$

$$\left.\frac{\partial g}{\partial x_n}\right|_\diamond = \begin{bmatrix} C \\ Ce^{A_2(T-d)} \end{bmatrix} e^{A_1 d} \tag{3.94}$$

$$\left.\frac{\partial f}{\partial v_{sn}}\right|_\diamond = e^{A_2(T-d)}\int_0^d e^{A_1\sigma}d\sigma B_1 + \int_0^{T-d} e^{A_2\sigma}d\sigma B_2 \tag{3.95}$$

$$\left.\frac{\partial g}{\partial v_{sn}}\right|_\diamond = \begin{bmatrix} C\int_0^d e^{A_1\sigma}d\sigma B_1 \\ C(e^{A_2(T-d)}\int_0^d e^{A_1\sigma}d\sigma B_1 + \int_0^{T-d} e^{A_2\sigma}d\sigma B_2) \end{bmatrix} \tag{3.96}$$

$$\left.\frac{\partial f}{\partial v_{rn}}\right|_\diamond = 0 \tag{3.97}$$

$$\left.\frac{\partial g}{\partial v_{rn}}\right|_\diamond = \begin{bmatrix} -1 \\ -1 \end{bmatrix} \tag{3.98}$$

The system is $(n-1)$-dimensional, and we express the dynamics as if it is n-dimensional. Thus there is an eigenvalue of Φ_h at 0, which makes $\det[\Phi_h] = 0$.

To show this, we have

$$
\begin{aligned}
\det[\Phi_h] &= \det[e^{A_2(T-d)}(I - \left[\begin{array}{cc} \dot{x}^0(d^-) - \dot{x}^0(d^+) & \dot{x}^0(d^+) \end{array}\right] (\frac{\partial g}{\partial \tau_n})^{-1}\Big|_\diamond \cdot \\
&\quad \left[\begin{array}{c} C \\ Ce^{A_2(T-d)} \end{array}\right])e^{A_1 d}] \\
&= \det[e^{A_1 d}e^{A_2(T-d)}]\det[I - \left[\begin{array}{cc} \dot{x}^0(d^-) - \dot{x}^0(d^+) & \dot{x}^0(d^+) \end{array}\right] (\frac{\partial g}{\partial \tau_n})^{-1}\Big|_\diamond \cdot \\
&\quad \left[\begin{array}{c} C \\ Ce^{A_2(T-d)} \end{array}\right]] \\
&= \det[e^{A_1 d}e^{A_2(T-d)}]\det[I - \left[\begin{array}{c} C \\ Ce^{A_2(T-d)} \end{array}\right] \left[\begin{array}{cc} \dot{x}^0(d^-) - \dot{x}^0(d^+) & \dot{x}^0(d^+) \end{array}\right] \cdot \\
&\quad \frac{\left[\begin{array}{cc} C\dot{x}^0(T^-) & 0 \\ Ce^{A_2(T-d)}(\dot{x}^0(d^+) - \dot{x}^0(d^-)) & C\dot{x}^0(d^-) \end{array}\right]}{C\dot{x}^0(d^-)C\dot{x}^0(T^-)}] \\
&= \det[e^{A_1 d}e^{A_2(T-d)}]\det[\left[\begin{array}{cc} \frac{C\dot{x}^0(d^+)Ce^{A_2(T-d)}\dot{x}^0(d^-)}{C\dot{x}^0(d^-)C\dot{x}^0(T^-)} & \frac{C\dot{x}^0(d^+)}{C\dot{x}^0(T^-)} \\ 0 & 0 \end{array}\right]] \\
&= 0
\end{aligned}
$$

The local stability is determined by Φ_h. The audio-susceptibility and output impedance analysis is similar to those in Sec. 3.5 for the CCM case and is omitted. An example of a hysteretic current-programmed boost converter is in Sec. 3.11.

3.10 Bifurcation Analysis of Buck Converters by Harmonic Balance Method

In the buck converter as shown in Fig. 2.2, the switch and diode separate the source voltage from the components R, L and C. Due to this special structure,

the buck converter can be modeled as feedback system with a linear part and a nonlinear part.

Here a controlled buck converter with voltage mode control in leading-edge modulation will be analyzed. The other configurations, current-mode control and trailing-edge modulation, can be analyzed similarly. Let the voltage across the diode be v_d, the output of the error amplifier be y and the ramp function be

$$h(t) = V_l + (V_h - V_l)(\frac{t}{T} \bmod 1)$$

As mentioned in Sec. 3.1, when $h(t) < y(t)$, the switch is off and $v_d = 0$; when $h(t) \geq y(t)$, the switch is on and $v_d = V_s$, where V_s is assumed constant here. Thus $v_d(t)$ is a periodic square wave. Between v_d and v_o is the plant (power stage) which can be represented by a linear filter with transfer function

$$G_1(s) = \frac{1}{LCs^2 + Ls/R + 1} \tag{3.99}$$

Generally the error amplifier is linear and is driven by the signals V_r (assumed constant here) and v_o. So its output can be represented as

$$y(t) = gV_r + (G_2 \circ v_o)(t) \tag{3.100}$$

where g is a gain constant and G_2 is a linear transfer function. Since G_2 can vary depending on the control scheme, we place no further restriction on it.

Thus the buck converter can be modeled as system blocks shown in Fig. 3.18, which can be further simplified as Fig. 3.19, where $G(s) = G_1(s)G_2(s)$. So the system is a combination of a linear system $G(s)$ and a nonlinear one representing the switch.

Suppose the nominal operating condition is a T-periodic solution as studied in Sec. 3.1. Then the waveforms of $y(t)$ and $v_d(t)$ are as shown in Fig. 3.20.

When period-doubling bifurcation occurs, another $2T$-periodic solution arises, and the associated waveforms of $y(t)$ and $v_d(t)$ are shown in Fig. 3.21.

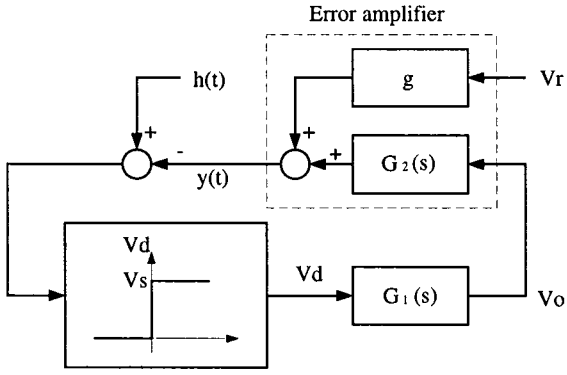

Figure 3.18: Dynamic model of controlled buck converter for applying harmonic balance method

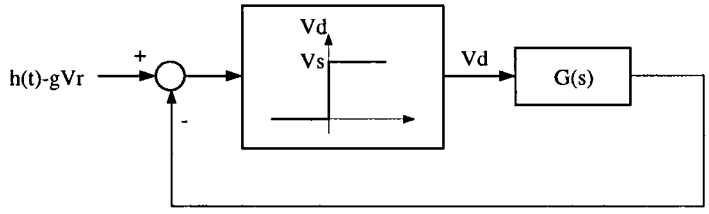

Figure 3.19: Simplified dynamic model of controlled buck converter for applying harmonic balance method

The harmonic balance method [27, 28, 69, 94] is a tool that can be used to analyze periodic solutions in nonlinear systems. In the buck converter, the nonlinearity is from the switch. The output signal of the switch, v_d, is periodic and can be represented by a Fourier series. By "balancing" the equations at the switching instant, we can derive a condition for existence of a periodic solution.

This method will be applied here to determine the period-doubling bifurca-

tion point. The basic idea is that at this bifurcation point (shown in Fig. 3.22), a period-one mode and a period-two mode coalesce. By determining the existence conditions for both modes, the period-doubling bifurcation point can be determined.

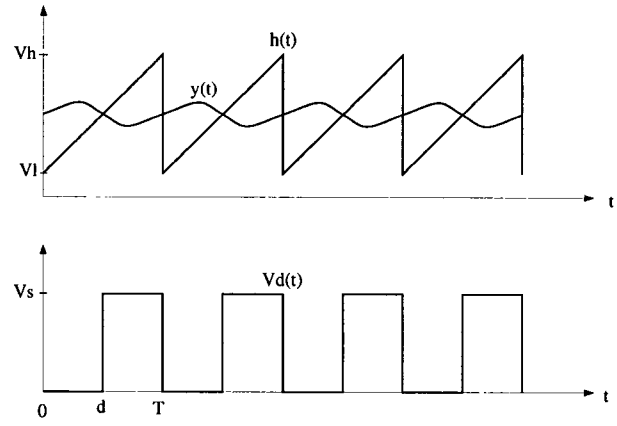

Figure 3.20: Waveforms of $y(t)$, $h(t)$ and $v_d(t)$ in period-one mode

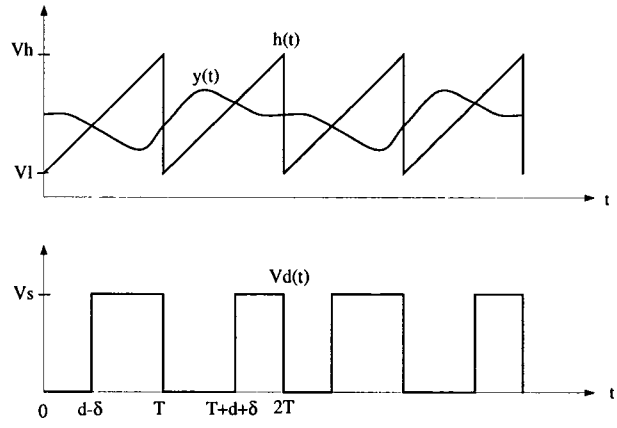

Figure 3.21: Waveforms of $y(t)$, $h(t)$ and $v_d(t)$ in period-two mode

In the period-one mode, $v_d(t)$ is periodic with angular frequency $\omega_s = 2\pi/T$,

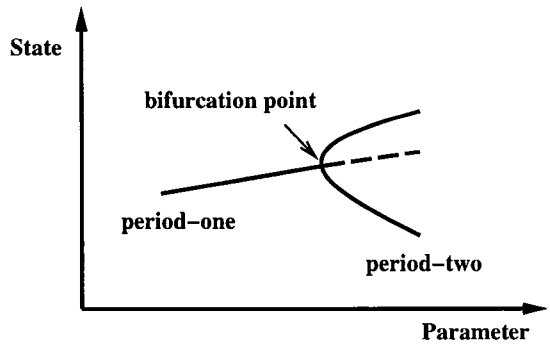

Figure 3.22: Period-doubling bifurcation.

and can be expressed as the Fourier series

$$V_d(t) = \sum_{n=-\infty}^{\infty} c_n e^{jn\omega_s t} \quad \text{where} \quad c_n = \frac{V_s}{j2n\pi}(e^{-jn\omega_s d} - 1) \tag{3.101}$$

Then the signal at the output of the error amplifier is

$$\begin{aligned} y(t) &= gV_r + \sum_{n=-\infty}^{\infty} c_n e^{jn\omega_s t} G(jn\omega_s) \\ &= gV_r + V_s((1 - \frac{d}{T})G(0) + (\frac{1}{\pi})\mathrm{Im}(\sum_{n=1}^{\infty} \frac{e^{-jn\omega_s d} - 1}{n} e^{jn\omega_s t} G(jn\omega_s)) \end{aligned}$$

Since in steady-state the system is operated periodically, we only consider $t \in [0, T]$. The switching happens at $t = d$, so

$$y(d) = h(d) \tag{3.102}$$

From Eqs. (3.101) and (3.102), we can write V_s in terms of d as

$$V_s = \frac{h(d) - gV_r}{(1 - \frac{d}{T})G(0) + (\frac{1}{\pi})\mathrm{Im}[\sum_{n=1}^{\infty} \frac{1 - e^{jn\omega_s d}}{n} G(jn\omega_s)]} \tag{3.103}$$

Similarly in the period-two mode, we can express $y(t)$ as the Fourier series

$$y(t) = gV_r + \sum_{n=-\infty}^{\infty} c_n e^{\frac{jn\omega_s t}{2}} G(\frac{jn\omega_s}{2}) \tag{3.104}$$

where

$$c_n = \begin{cases} (\frac{V_s}{n\pi})e^{-\frac{jn\omega_s d}{2}} \sin(\frac{n\omega_s\delta}{2}), & \text{if n is odd} \\ (\frac{V_s}{jn\pi})(e^{-\frac{jn\omega_s d}{2}} \cos(\frac{n\omega_s\delta}{2}) - 1), & \text{if n is even} \end{cases}$$

and we have two switching conditions

$$y(d-\delta) = h(d-\delta) \tag{3.105}$$

$$y(T+d+\delta) = h(T+d+\delta) \tag{3.106}$$

Subtracting (3.105) from (3.106), we obtain

$$\begin{aligned} \delta\frac{V_h - V_l}{T} = & \\ & (\frac{V_s}{\pi})\mathrm{Re}(-\sum_{k=1}^{\infty}\frac{1}{2k-1}G(j(k-\frac{1}{2})\omega_s)\sin((2k-1)\omega_s\delta) \\ & + \sum_{k=1}^{\infty}\frac{1}{2k}G(jk\omega_s)(\sin(2k\omega_s\delta) - 2e^{jk\omega_s d}\sin(k\omega_s\delta)) \end{aligned} \tag{3.107}$$

Solving for V_s, we have another expression for V_s in terms of d and δ,

$$V_s = \frac{\frac{\delta\pi(V_h-V_l)}{T}}{\mathrm{Re}(-\sum_{k=1}^{\infty}(\frac{1}{2k-1}G(j(k-\frac{1}{2})\omega_s)\sin((2k-1)\omega_s\delta) + \frac{1}{2k}G(jk\omega_s)(\sin(2k\omega_s\delta)) - 2e^{jk\omega_s d}\sin(k\omega_s\delta)))} \tag{3.108}$$

The period-doubling bifurcation happens at $\delta = 0$, so V_s at the bifurcation is

$$V_{s,*} = \frac{\frac{V_h-V_l}{2}}{\mathrm{Re}[-\sum_{k=1}^{\infty}G(j(k-\frac{1}{2})\omega_s) + (1-e^{jk\omega_s d})G(jk\omega_s)]} \tag{3.109}$$

The critical values $V_{s,*}$ and d_* can be obtained graphically by plotting Eqs. (3.103) and (3.109) together. The intersection ($V_{s,*}$, d_*) of these graphs is the period-doubling bifurcation point.

Generally $G(j\omega)$ is low-pass. The denominator of (3.109) can be approximated by the term that involves G with the smallest argument, namely, $-\mathrm{Re}[G(\frac{j\omega_s}{2})]$. So a good estimate for the critical value $V_{s,*}$ is

$$\frac{\frac{V_h-V_l}{2}}{-\mathrm{Re}[G(\frac{j\omega_s}{2})]} \tag{3.110}$$

which shows how the indicated system parameters affect the period-doubling bifurcation. This result also suggests that the operating range of the source voltage can be increased by increasing the magnitude of the ramp, $V_h - V_l$, or by increasing the switching frequency.

3.11 Illustrative Examples

In this section, we will illustrate the results of the preceding sections using examples taken from the literature. In particular, two examples of input filter instability are shown in Example 3.4 and 3.5. We will see that input filter instability can be determined easily by sampled-data analysis.

Example 3.1 (*Buck converter with voltage mode control*, [31]) Consider the buck converter with voltage mode control shown in Fig. 3.23. Let $T = 400\mu s$, $L = 20mH$, $C = 47\mu F$, $R = 22\Omega$, $V_r = 11.3V$, $g_1 = 8.4$, $V_l = 3.8V$, $V_h = 8.2V$, (then $h(t) = 3.8 + 4.4[\frac{t}{T} \bmod 1]$), and let V_s be the bifurcation parameter.

Let the state be $x = (i_L, v_C)$. In terms of the block diagram model in Fig. 3.1, we have

$$A_1 = A_2 = \begin{bmatrix} 0 & \frac{-1}{L} \\ \frac{1}{C} & \frac{-1}{RC} \end{bmatrix} \tag{3.111}$$

$$B_1 = \begin{bmatrix} 0 \\ 0 \end{bmatrix} \tag{3.112}$$

$$B_2 = \begin{bmatrix} \frac{1}{L} \\ 0 \end{bmatrix} \tag{3.113}$$

$$C = \begin{bmatrix} 0 & g_1 \end{bmatrix} \tag{3.114}$$

$$D = \begin{bmatrix} 0 & -g_1 \end{bmatrix} \tag{3.115}$$

$$E_1 = E_2 = \begin{bmatrix} 0 & 1 \end{bmatrix} \tag{3.116}$$

Fig. 3.24 shows the bifurcation diagram of the circuit. The circuit undergoes a series of period-doubling bifurcations beginning at $V_s = 24.5V$ approximately.

Fig. 3.25 shows $\sigma(\Phi)$ (the eigenvalues of Φ) as V_s varies from 13.1 to $25.068V$. They are calculated from Eq. (3.25), while [24] obtains the same graph by numerical estimation. One eigenvalue of Φ is -1 when $V_s = 24.527$, which agrees exactly with the numerical results in Fig. 3.24.

Another calculation of the period-doubling bifurcation point follows. V_s is the bifurcation parameter. From Eq. (3.21), we get the following equation relating V_s and d:

$$V_s = \frac{h(d) + g_1 V_r}{Ce^{A_2 d}(I - e^{A_2 T})^{-1} A_2^{-1}(e^{A_2(T-d)} - I)B_2} \tag{3.117}$$

From Eq. (3.34), we get another equation relating V_s and d at the period-doubling bifurcation:

$$V_s = \frac{\dot{h}(d)}{C[(I + e^{-A_2 T})^{-1} + (I - e^{A_2 T})^{-1}(e^{A_2 T} - e^{A_2 d})]B_2} \tag{3.118}$$

Fig. 3.26 shows the loci of these two equations. From the figure, we see that the period-doubling bifurcation occurs at around $V_{s,*} = 24.527V$ and $d_* = 2.039 \times 10^{-4}$.

A similar analysis can be done using the harmonic balance method. Representing the system by Fig. 3.18, we have $G_2(s) = g_1$, $g = -g_1$ and

$$G(s) = G_1(s)G_2(s) = \frac{g_1}{LCs^2 + Ls/R + 1} \tag{3.119}$$

The two functions, Eqs. (3.103) and (3.109), can be expressed as

$$V_s = \frac{h(d) + g_1 V_r}{(1 - \frac{d}{T})G(0) + (\frac{1}{\pi})\mathrm{Im}(\sum_{n=1}^{\infty} \frac{1 - e^{jn\omega_s d}}{n} G(jn\omega_s))} \tag{3.120}$$

$$V_{s,*} = \frac{\frac{V_h - V_l}{2}}{\mathrm{Re}(-\sum_{k=1}^{\infty} G(j(k - \frac{1}{2})\omega_s) + (1 - e^{jk\omega_s d})G(jk\omega_s))} \tag{3.121}$$

which are the same as Eq. (3.117) and Eq. (3.118) respectively.

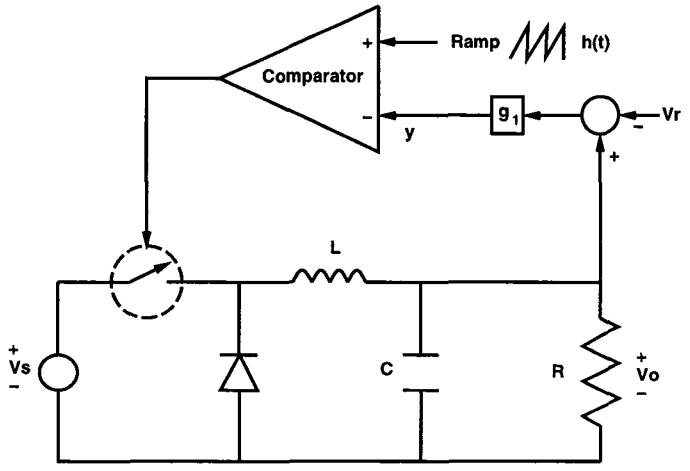

Figure 3.23: System diagram for Example 3.1

Example 3.2 (*Boost converter with current mode control*, [15]) Consider the boost converter with current mode control shown in Fig. 3.27, where $T = 100\mu s$, $V_s = 10V$, $L = 1mH$, $C = 12\mu F$, $R = 20\Omega$, and V_r (current reference) is taken to be the bifurcation parameter.

Let the state be $x = (i_L, v_C)$. In terms of the block diagram model in Fig. 3.1, we have

$$A_1 = \begin{bmatrix} 0 & 0 \\ 0 & \frac{-1}{RC} \end{bmatrix} \tag{3.122}$$

$$A_2 = \begin{bmatrix} 0 & \frac{-1}{L} \\ \frac{1}{C} & \frac{-1}{RC} \end{bmatrix} \tag{3.123}$$

$$B_1 = B_2 = \begin{bmatrix} \frac{1}{L} \\ 0 \end{bmatrix} \tag{3.124}$$

$$C = \begin{bmatrix} 1 & 0 \end{bmatrix} \tag{3.125}$$

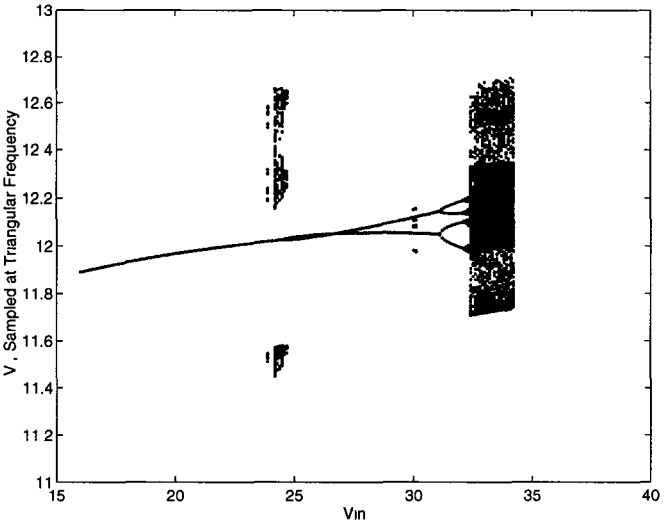

Figure 3.24: Bifurcation diagram of the circuit in Fig. 3.23 (V_{in} is the source voltage V_s).

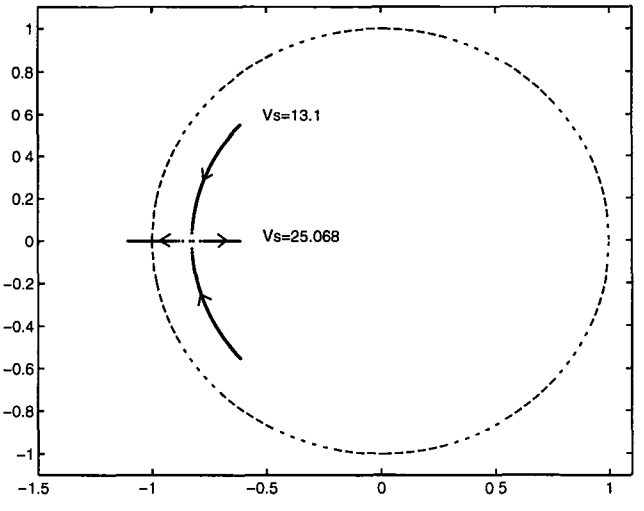

Figure 3.25: $\sigma(\Phi)$ as V_s varies from 13.1 to 25.068

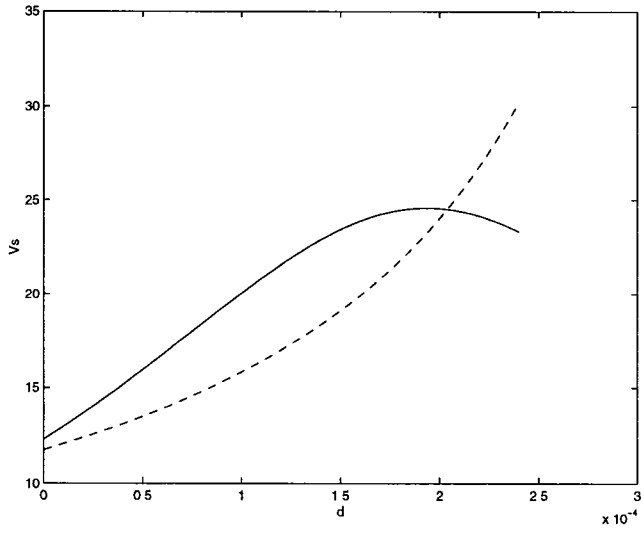

Figure 3.26: Plot of Eq. (3.117) (dashed line) and Eq. (3.118) (solid line). The intersection $(d, V_s) = (0.0002039, 24.527)$ is the period-doubling bifurcation point

$$D = \begin{bmatrix} 0 & -1 \end{bmatrix} \tag{3.126}$$

$$E_1 = E_2 = \begin{bmatrix} 0 & 1 \end{bmatrix} \tag{3.127}$$

$$h(t) = 0 \tag{3.128}$$

Fig. 3.28 shows the bifurcation diagram of the circuit.

Fig. 3.29 shows $\sigma(\Phi)$ as V_r varies from 0.6634 to 3.3759. One eigenvalue of Φ is -1 when $V_r = 1.7457$, which agrees exactly with the simulation in [15].

Example 3.3 (*Global and local orbital stability are sometimes not distinguished in the power electronics literature*, [51, p90]) Consider the boost converter shown in Fig. 3.30, where $T = 2\mu s$, $V_s = 4V$, $L = 5.24\mu H$, $C = 0.2\mu F$, $R = 16\Omega$, $k_1 = -0.1$, $k_2 = 0.01$, $V_r = 0.48V$, and $h(t) = ((\frac{t}{T}) \mod 1)$.

Let the state be $x = (i_L, v_C)$. In terms of the block diagram model in Fig. 3.1, the matrices A_1, A_2, B_1, B_2, E_1, and E_2 are the same as those in Example 3.2,

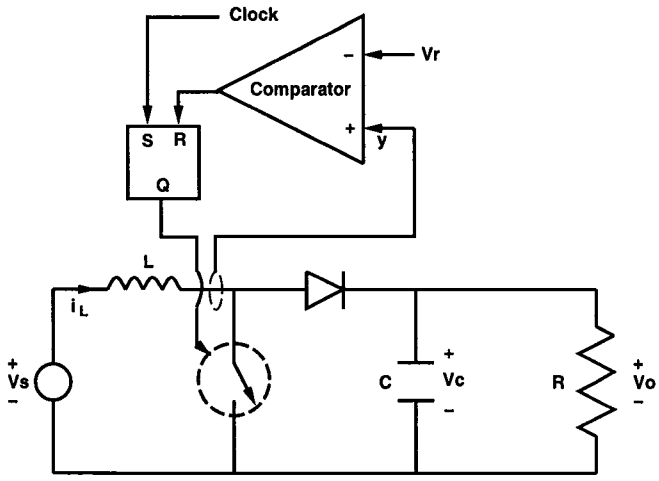

Figure 3.27: System diagram for Example 3.2

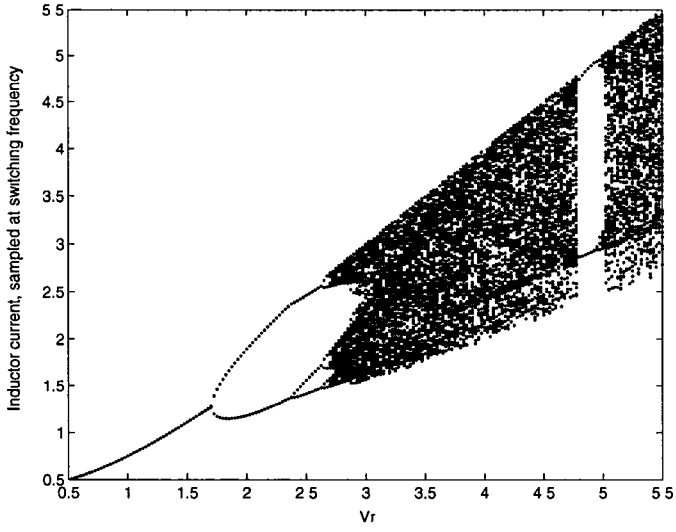

Figure 3.28: Bifurcation diagram of the circuit in Fig. 3.27

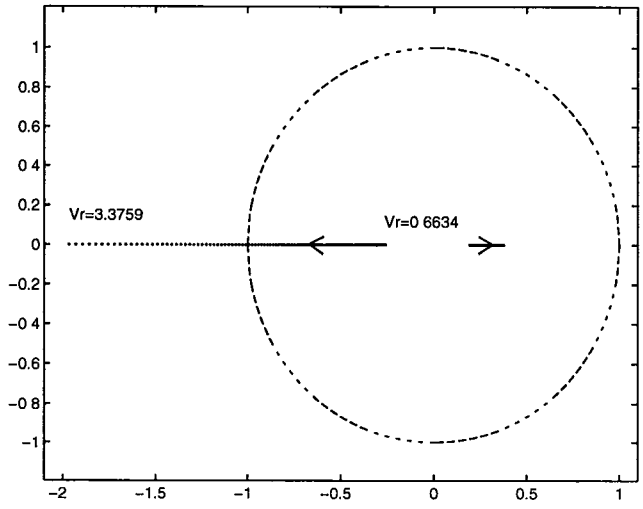

Figure 3.29: $\sigma(\Phi)$ as V_r varies from 0.6634 to 3.3759

which C and D are

$$C = \begin{bmatrix} -k_1 & -k_2 \end{bmatrix} \tag{3.129}$$

$$D = \begin{bmatrix} 0 & 1 \end{bmatrix} \tag{3.130}$$

From Eq. (3.23), we calculate the periodic solution and it is shown in Fig. 3.31. The closed-loop poles calculated from Eq. (3.25) are $\sigma(\Phi) = 0.8 \pm 0.45i$, which are inside the unit circle. So the periodic solution is *locally* orbitally stable. The magnitude of the eigenvalue is 0.9225 and we expect the settling time to the steady state will be long. For example, let the initial state starts from $(i_L, v_C) = (0.9, 8)$. The simulated output voltage is shown in Fig. 3.32. After the transient, the state trajectory goes to the periodic solution.

Then we use averaging method to see if it can predict the local stability. Let

$$A_{\text{ave}} = A_1 D_c + A_2(1 - D_c) \tag{3.131}$$

$$B_{\text{ave}} = B_1 D_c + B_2(1 - D_c) \tag{3.132}$$

$$x_{\text{ave}} = -A_{\text{ave}}^{-1} B_{\text{ave}} V_s \tag{3.133}$$

Then the close-loop poles predicted by the averaging method are [64]

$$\lambda = \sigma(A_{\text{ave}} + ((A_1 - A_2)x_{\text{ave}} + (B_1 - B_2)V_s)C) = (-0.2759 \pm 2.9276i) \times 10^5 \tag{3.134}$$

and $e^{\lambda T} = 0.7887 \pm 0.5230i$, which are close to the eigenvalues calculated by the sampled-data method. So in this example, the averaging method can predict the local stability.

The circuit is not globally stable and is described as being unstable in [51], without mentioning the local stability. Since the averaging method is for local (small-signal) analysis, it is not surprising that it cannot predict the global instability.

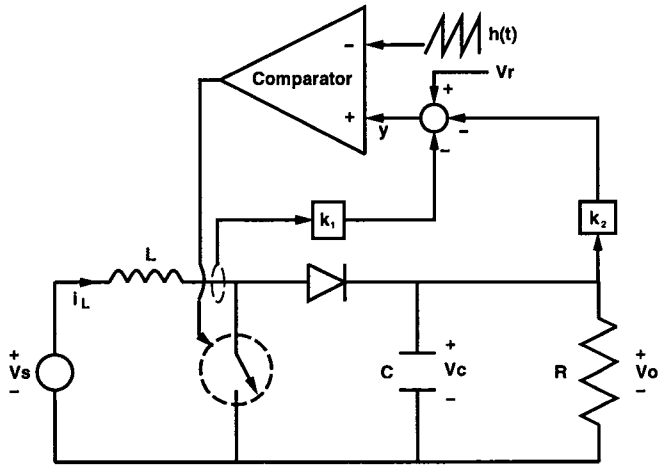

Figure 3.30: System diagram for Example 3.3

Example 3.4 (*Buck converter with input filter*) We add an input filter between the voltage source and the switch in the system of Example 3.1 with

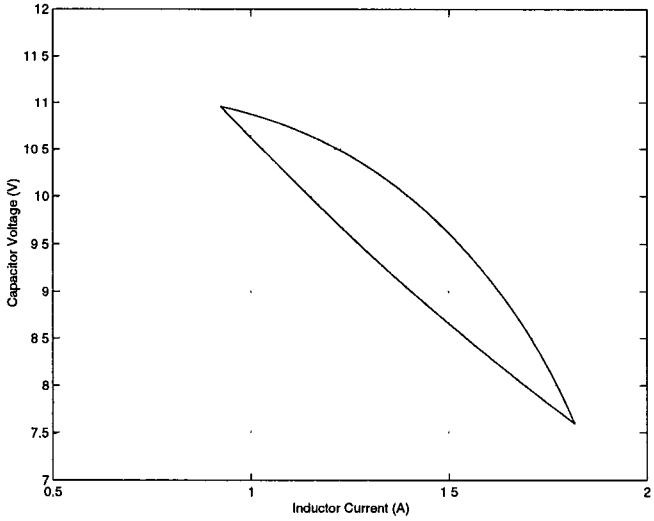

Figure 3.31: The periodic solution in Example 3.3

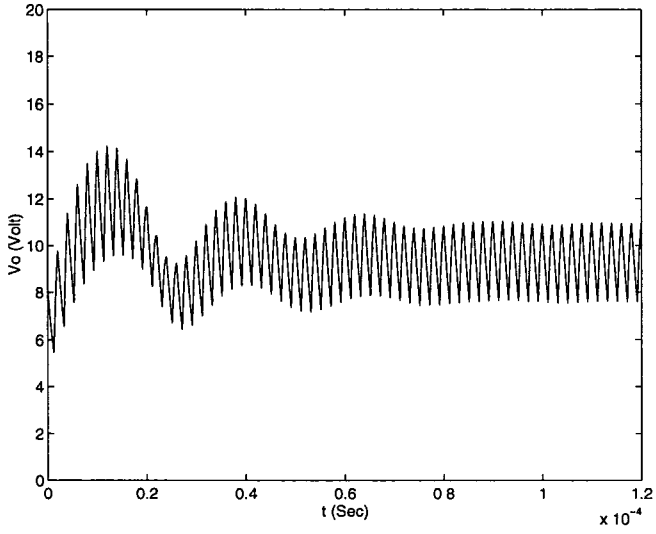

Figure 3.32: The output voltage trajectory in Example 3.3 when the system starts from $(i_L, v_C) = (0.9, 8)$

$V_s = 15.8V$. The system diagram is shown in Fig. 3.33. The input filter parameters are $L_f = 2.5mH$, $C_f = 160\mu F$ and R_p is added to adjust the damping.

Let the state be $x = (i_L, v_C, i_f, v_f)$, where i_f and v_f are the inductor current and capacitor voltage in the input filter respectively. In terms of the block diagram model in Fig. 3.1, we have

$$A_1 = \begin{bmatrix} 0 & \frac{-1}{L} & 0 & 0 \\ \frac{1}{C} & \frac{-1}{RC} & 0 & 0 \\ 0 & 0 & 0 & \frac{-1}{L_f} \\ 0 & 0 & \frac{1}{C_f} & \frac{-1}{R_p C_f} \end{bmatrix} \tag{3.135}$$

$$A_2 = \begin{bmatrix} 0 & \frac{-1}{L} & 0 & \frac{1}{L} \\ \frac{1}{C} & \frac{-1}{RC} & 0 & 0 \\ 0 & 0 & 0 & \frac{-1}{L_f} \\ \frac{-1}{C_f} & 0 & \frac{1}{C_f} & \frac{-1}{R_p C_f} \end{bmatrix} \tag{3.136}$$

$$B_1 = B_2 = \begin{bmatrix} 0 \\ 0 \\ \frac{1}{L_f} \\ \frac{1}{R_p C_f} \end{bmatrix} \tag{3.137}$$

$$C = \begin{bmatrix} 0 & g_1 & 0 & 0 \end{bmatrix} \tag{3.138}$$

$$D = \begin{bmatrix} 0 & -g_1 \end{bmatrix} \tag{3.139}$$

$$E_1 = E_2 = \begin{bmatrix} 0 & 1 & 0 & 0 \end{bmatrix} \tag{3.140}$$

The angular resonance frequency of input filter and output filter are respectively:

$$\omega_0 = \frac{1}{\sqrt{LC}} = 1031.4 \tag{3.141}$$

$$\omega_f = \frac{1}{\sqrt{L_f C_f}} = 1581.1 \tag{3.142}$$

Fig. 3.34 shows $\sigma(\Phi)$ as R_p varies. One pair of eigenvalues are almost fixed at $-0.5963 \pm 0.5301i$, while the other pair moves as R_p varies. A Neimark-Sacker bifurcation occurs when $R_p = 38.85$, where a pair of eigenvalues $0.8087 \pm 0.5883i$ crosses the unit circle. After the bifurcation, the steady-state trajectory is on a torus, as depicted in Fig. 3.35. The two angular frequency vectors of the trajectory are perpendicular to each other. One of them is the same as the angular switching frequency ω_s; the other is approximately $\angle(0.81 + 0.59i)/T$, ($\angle$ denotes the angle in radian,) which is ω_f. The state trajectory will be periodic (phase-locking) if these two frequencies are commensurate; otherwise it will be quasi-periodic.

Fig. 3.36 shows the output trajectory, (I_l, V_c), for $R_p = 20$, which is stable and periodic.

Fig. 3.37 shows the output trajectory, (I_l, V_c), for $R_p = 50$, which is quasi-periodic.

From Fig. 3.34, we can see that adding an input filter does not affect the eigenvalues of the original system without input filter, where the eigenvalues are around $-0.5963 \pm 0.5303i$. This motivates us to use the reduced model shown in Fig. 3.38, where I=0.5688A is a current source, and the switch is turned on and off periodically, with duty cycle 0.25.

We use sampled-data analysis and calculate the matrix Φ of this reduced system as $\Phi = e^{AT}$, where $A = \begin{bmatrix} 0 & -1/L_f \\ 1/C_f & -1/(R_p C_f) \end{bmatrix}$. Fig. 3.39 shows $\sigma(\Phi)$ as R_p varies. We can see the loci of the eigenvalues is very similar to the corresponding eigenvalue loci (Fig. 3.34) for the original system , except that in

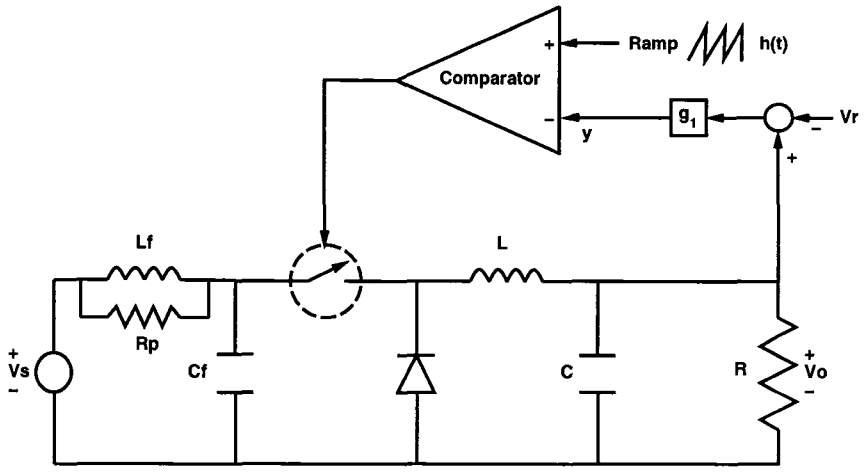

Figure 3.33: Buck converter with an input filter

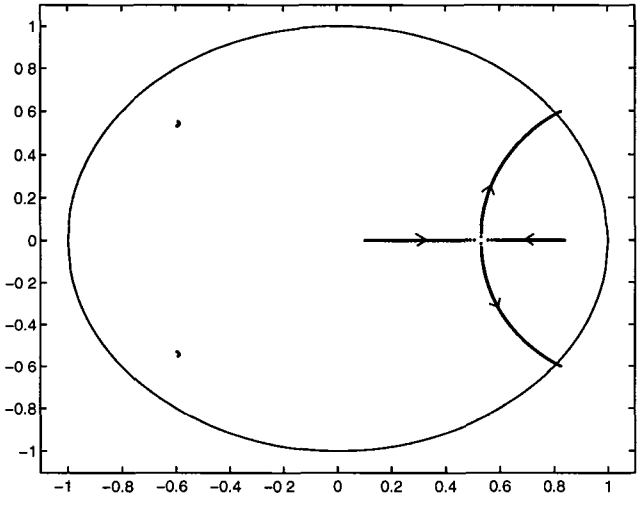

Figure 3.34: $\sigma(\Phi)$ as R_p varies from 1 to 100

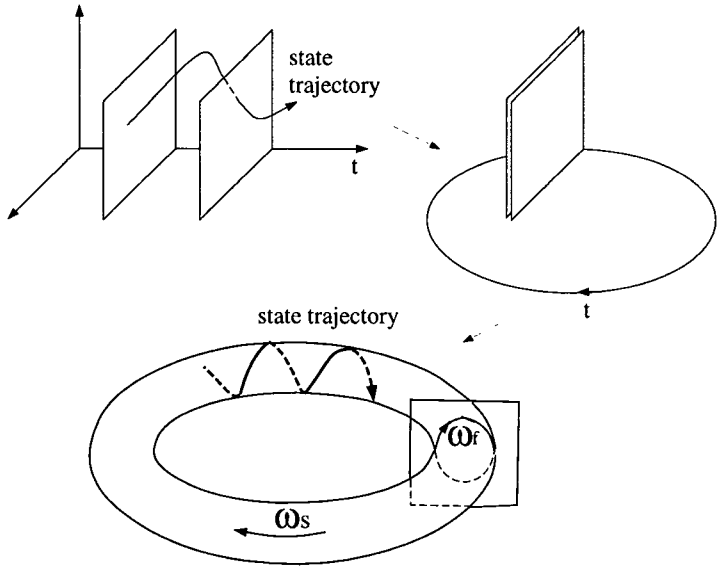

Figure 3.35: State trajectory after Niemark-Sacker bifurcation

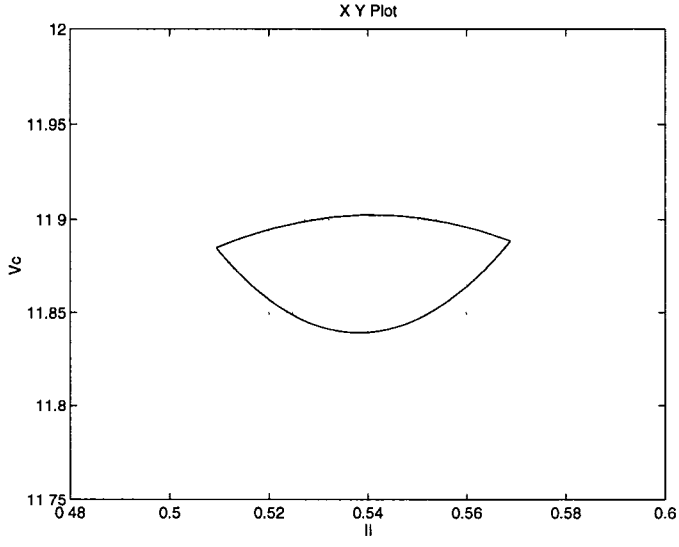

Figure 3.36: (I_l, V_c) trajectory when $R_p = 20$

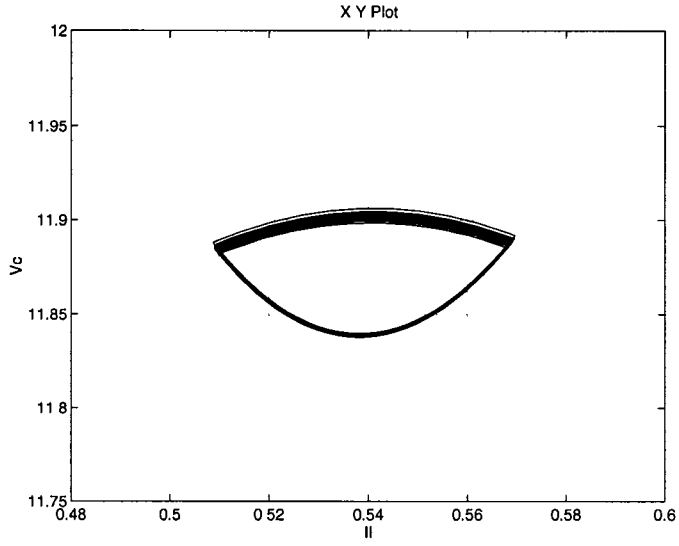

Figure 3.37: (I_l, V_c) trajectory when $R_p = 50$

Fig. 3.39 the eigenvalues don't cross the unit circle because A is a stable matrix for any R_p. A conservative criterion to prevent this buck converter with input filter from oscillation is to make the sytem to have real eigenvalues instead of complex ones, which requires $R_p < \sqrt{L_f/C_f}/2 = 1.9764$.

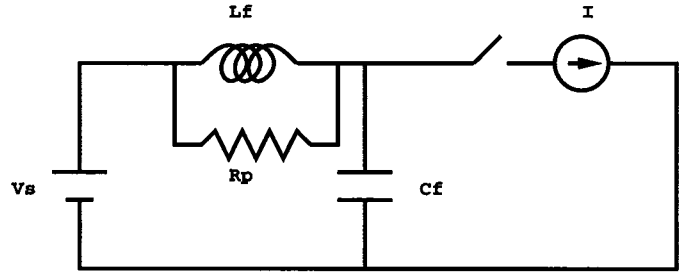

Figure 3.38: A reduced model for a buck converter with input filter

Then we use averaging method to see if it can predict the instability. First we calculate the duty cycle, which is determined by how the signals y and $h(t)$

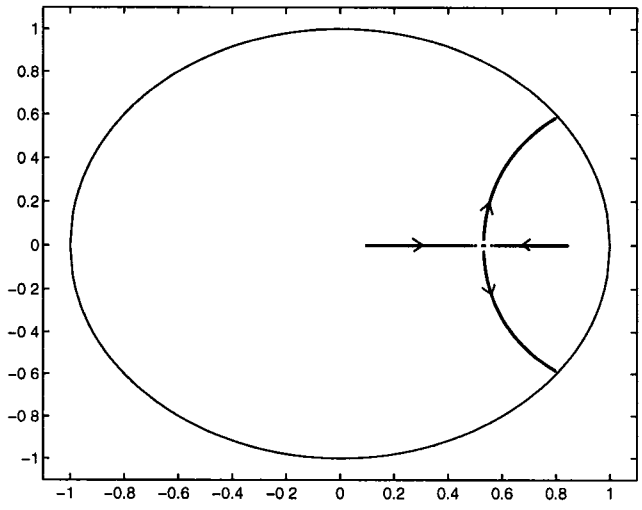

Figure 3.39: $\sigma(\Phi)$ of reduced buck converter as R_p varies from 1 to 100

intersect. We have

$$\begin{aligned} D_c &= \frac{V_h - y}{V_h - V_l} \\ &= \frac{V_h - g_1(V_o - V_r)}{V_h - V_l} \\ &= \frac{V_h - g_1(D_c V_s - V_r)}{V_h - V_l} \end{aligned}$$

Solving for D_c, we have

$$D_c = \frac{V_h + g_1 V_r}{V_h - V_l + g_1 V_s} = 0.7512 \tag{3.143}$$

Let

$$\begin{aligned} A_{\text{ave}} &= A_2 D_c + A_1(1 - D_c) \\ B_{\text{ave}} &= B_2 D_c + B_1(1 - D_c) \\ x_{\text{ave}} &= -A_{\text{ave}}^{-1} B_{\text{ave}} V_s \\ K &= \begin{bmatrix} 0 & -\frac{g_1}{V_h - V_l} & 0 & 0 \end{bmatrix} \end{aligned}$$

Then the close-loop poles predicted by the averaging method are [64]

$$\lambda = \sigma(A_{\text{ave}} + ((A_2 - A_1)x_{\text{ave}} + (B_2 - B_1)V_s)K) \tag{3.144}$$

The trajectories of the close-loop poles as R_p varies is shown in Fig. 3.40. One pair of poles are almost fixed, while the other pair of poles cross the imaginary axis when $R_p = 38.75$. Plot of $\sigma(e^{\lambda T})$ as R_p varies is shown in Fig. 3.41, which is very similar to Fig. 3.34.

In a continuous-time nonlinear system, the bifurcation associated with a pair of eigenvalues cross the imaginary axis is called a Hopt bifurcation, where the original equilibrium point evolves into limit cycle. In this converter system, the original operating condition is a stable periodic solution instead of an equilibrium as from averaging. But the averaging method can predict the instability very well in this example. There is also a close correspondence between the poles from the sampled-data method and those from the averaging method.

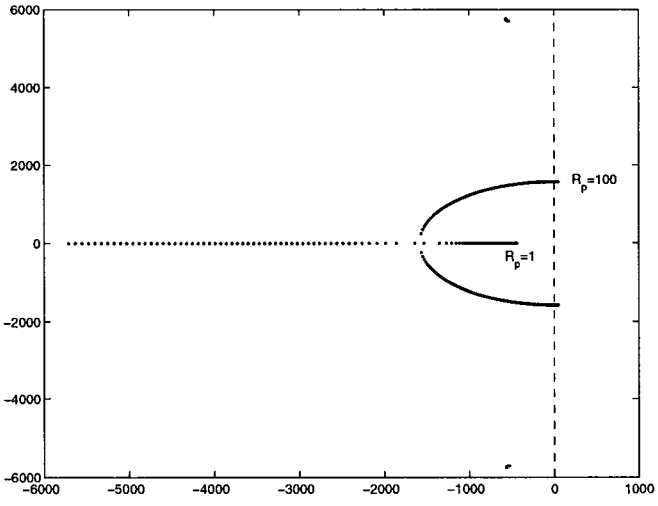

Figure 3.40: The trajectories of the close-loop poles as R_p varies

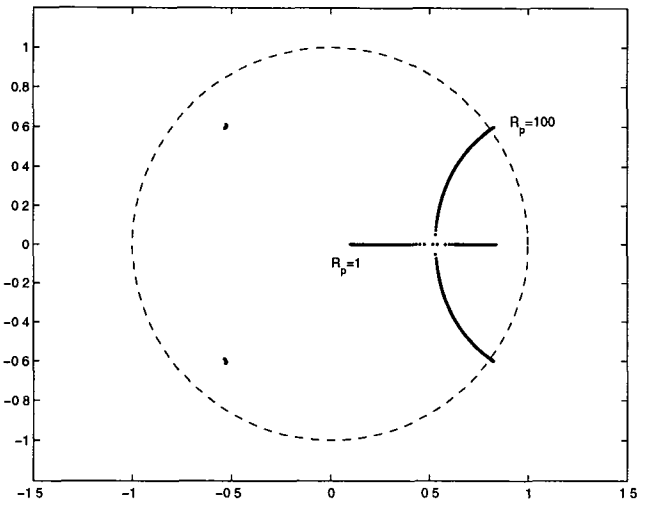

Figure 3.41: The trajectories of $\sigma(e^{\lambda T})$ as R_p varies

Then we look at those input filter design criteria proposed in [59]. Let

$$Z_s(s) = (R_p \| sL_f \| \frac{1}{sC_f}) \tag{3.145}$$

$$Z_{ii} = -\frac{R}{D_c^2} = -38.9869 \tag{3.146}$$

$$Z_{ei}(s) = \frac{sL + (\frac{1}{sC} \| R)}{D_c^2} \tag{3.147}$$

be the input filter output impedance, incremental input resistance, and effective output filter impedance respectively. Since our concern here is the stability, the design criteria [59] not to affect the control-to-output transfer function and also stability are

$$|Z_s| \ll |Z_{ii}| \tag{3.148}$$

$$|Z_s| \ll |Z_{ei}| \tag{3.149}$$

The plot of $Z_{ei}(j\omega)$ is shown in Fig. 3.42. $Z_s(j\omega)$ has a peak value of R_p (at $\omega = \omega_f$) and this peak increases as R_p increases. The inequality conditions,

(3.148) and (3.149), are violated when $R_p > |Z_{ii}| = 38.9869$, which is very close to the prediction from the sampled-data method.

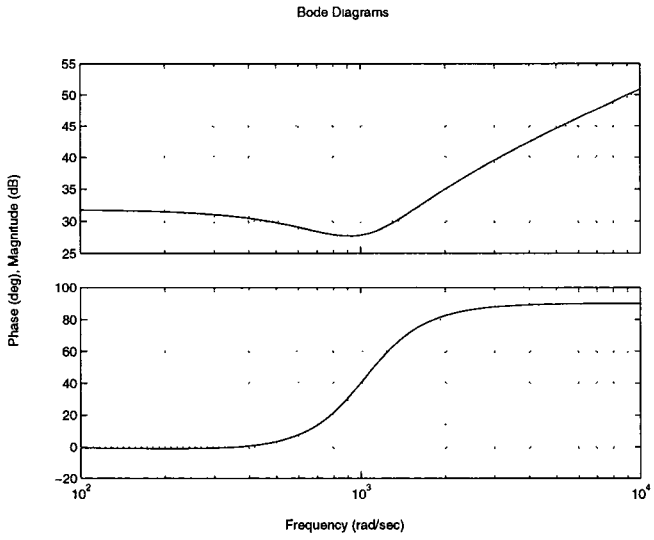

Figure 3.42: The effective output filter impedance $Z_{ei}(j\omega)$

Example 3.5 (*Buck converter with input filter in current mode control*) Traditionally, various stability criteria [20, 41, 33] have been given for a converter with an input filter in *current mode control.* Here we will show that a unified method can be applied to both voltage and current mode control. We take an example from [87, p96]. The system diagram is shown in Fig. 3.43, where $f_s = 30kHz$, $V_s = 15V$, $R = 10.4\Omega$, $L = 0.48mH$, $C = 30\mu F$, $R_L = 0.6\Omega$, with input filter parameters $R_{L1} = 0.25\Omega$, $L_f = 0.43mH$ and $C_f = 10.4\mu F$.

Let the state be $x = (i_L, v_C, i_f, v_f)$, where i_f and v_f are the inductor current and capacitor voltage in the input filter, respectively. In terms of the block

diagram model in Fig. 3.1, we have

$$A_1 = \begin{bmatrix} \frac{-R_L}{L} & \frac{-1}{L} & 0 & \frac{1}{L} \\ \frac{1}{C} & \frac{-1}{RC} & 0 & 0 \\ 0 & 0 & \frac{-R_{L1}}{L_f} & \frac{-1}{L_f} \\ \frac{-1}{C_f} & 0 & \frac{1}{C_f} & 0 \end{bmatrix} \tag{3.150}$$

$$A_2 = \begin{bmatrix} \frac{-R_L}{L} & \frac{-1}{L} & 0 & 0 \\ \frac{1}{C} & \frac{-1}{RC} & 0 & 0 \\ 0 & 0 & \frac{-R_{L1}}{L_f} & \frac{-1}{L_f} \\ 0 & 0 & \frac{1}{C_f} & 0 \end{bmatrix} \tag{3.151}$$

$$B_1 = B_2 = \begin{bmatrix} 0 \\ 0 \\ \frac{1}{L_f} \\ 0 \end{bmatrix} \tag{3.152}$$

$$C = \begin{bmatrix} 1 & 0 & 0 & 0 \end{bmatrix} \tag{3.153}$$

$$D = \begin{bmatrix} 0 & -1 \end{bmatrix} \tag{3.154}$$

$$E_1 = E_2 = \begin{bmatrix} 0 & 1 & 0 & 0 \end{bmatrix} \tag{3.155}$$

Fig. 3.44 shows $\sigma(\Phi)$ as the duty cycle D_c varies. An eigenvalue pair departs the unit circle for the parameter value $D_c = 0.2443$. In contrast, in reference [87] the circuit is said to become unstable when $D_c > 0.3$. Again as in the previous example, the bifurcated solution is on a torus, with angular frequencies, ω_s and $1/\sqrt{L_f C_f}$, which can be verified from the eigenvalue locus diagram in Fig. 3.44.

Example 3.6 (*Saddle-node bifurcation*) Saddle-node bifurcations in switching converters have not been reported explicitly to the author's knowledge. Here we will show one example of such a bifurcation. The system diagram is shown

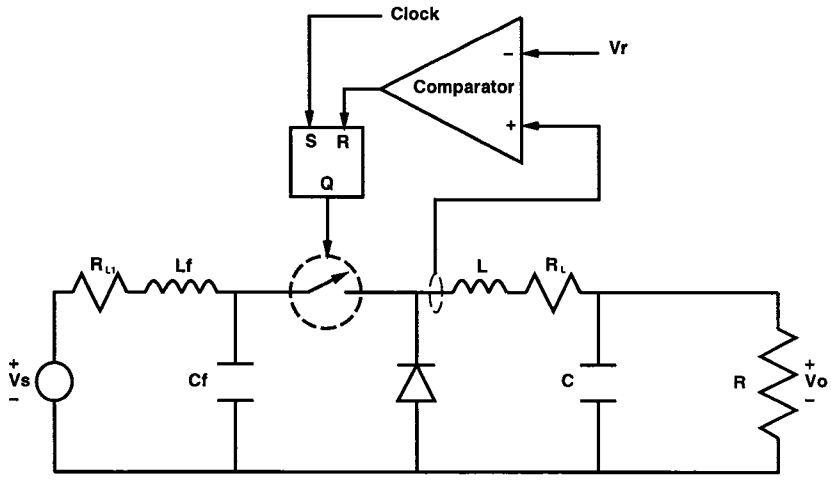

Figure 3.43: System diagram for Example 3.5

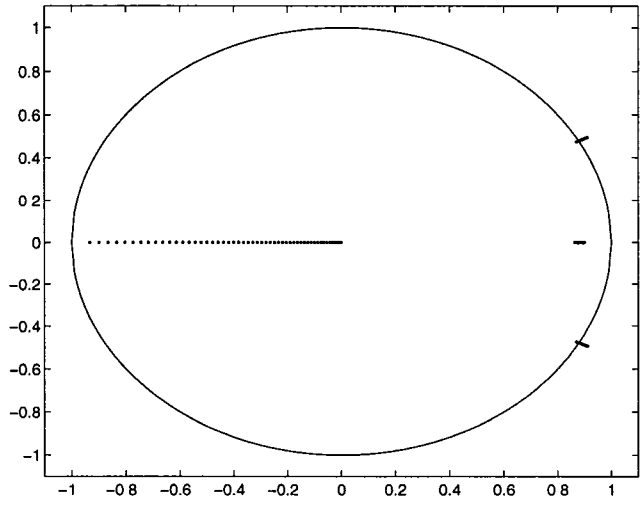

Figure 3.44: $\sigma(\Phi)$ for Example 3.5 as duty cycle D_c varies from 0 to 0.5, where the eigenvalue trajectories goes outward

in Fig. 3.45. The system parameters (the same as those in Example 3.1) are $T = 400\mu s$, $L = 20mH$, $C = 47\mu F$, $R = 22\Omega$, and $V_s = 20V$. The switching decision in the $(n+1)$-th cycle is as follows (similar to leading-edge modulation): the switch is turned off at $t = nT$ and turned on at $t = nT + d_n$. The switching instant d_n is updated by $d_n = \ell(0.3T + 8.574 \times 10^{-4}(i_n - 0.6785) - 5.53 \times 10^{-5}(v_n - 14.0263))$, where ℓ is a limiter:

$$\ell(t) = \begin{cases} 0 & \text{for } t < 0 \\ t & \text{for } t \in [0, T] \\ T & \text{for } t > T \end{cases} \tag{3.156}$$

Fig. 3.46 shows the bifurcation diagram of this circuit.

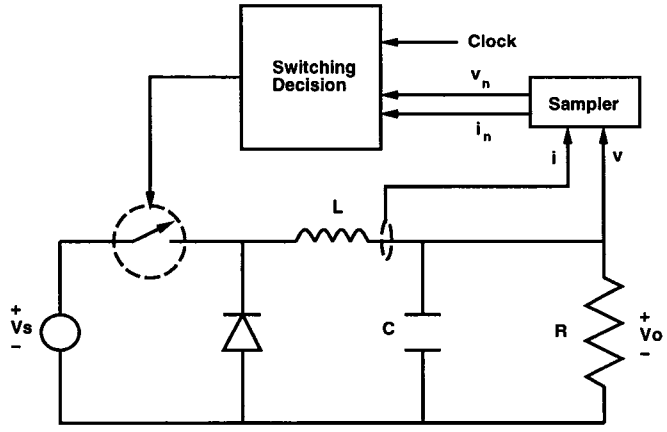

Figure 3.45: System diagram for Example 3.6

For V_s below $19.23V$, the output voltage is regulated below $11V$. For V_s between $19.23V$ and $20V$, there is a hysteresis loop. When $V_s = 20V$, the output voltage suddenly jumps to $20V$. For $V_s > 20V$, the circuit is always on, and the output voltage is the same as the input voltage. For V_s between $19.23V$ and $20V$, there actually exists another unstable periodic solution which collides

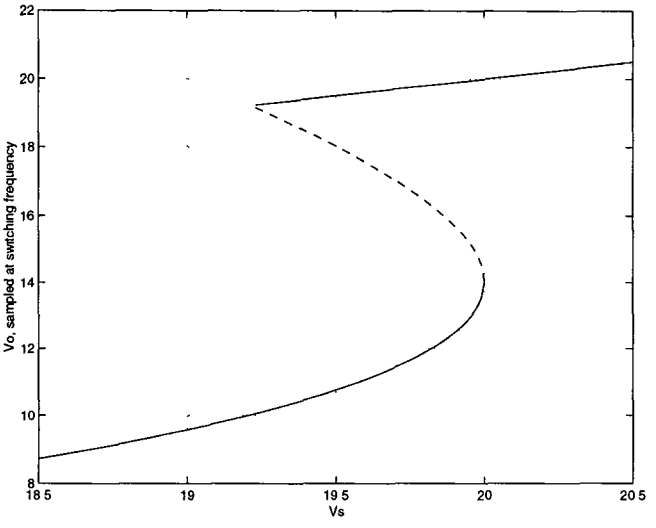

Figure 3.46: Bifurcation diagram of the buck converter in Example 3.6. The solid line is for stable solutions and the dashed line is for unstable solutions

with the stable one at $V_s = 20V$. Thus there is a saddle-node bifurcation at this point. When $V_s = 20V$, one eigenvalue of Φ is 1, which is in agreement with the basic result on saddle-node bifurcation, Corollary 3.1.

Example 3.7 (*Determination of direction of period-doubling bifurcation using* β_2) A 1-dimensional buck converter model is presented in [6]. The system diagram is shown in Fig. 3.47, where $T = 72\mu s$, $R = 26\Omega$, diode resistance $r_d = 0.5\Omega$, $L = 16mH$, $I_r = 0.5A$, and V_s is used as the bifurcation parameter.

Let the state be the inductor current i_L. In terms of the block diagram representation for the 1-dimensional switching converter in Fig. 3.10, we have

$$a_1 = -\frac{R}{L} \tag{3.157}$$

$$a_2 = -\frac{R + r_d}{L} \tag{3.158}$$

$$b_1 = \frac{V_s}{L} \tag{3.159}$$

$$b_2 = 0 \tag{3.160}$$

$$g_1 = g_2 = R \tag{3.161}$$

Since the diode resistance is always positive, we have $|a_1| < |a_2|$. From the conclusion in Sec. 3.7, we expect the period-doubling bifurcation to be supercritical. After solving Eq. (3.48), (3.49) and (3.59), we determine that the period-doubling bifurcation occurs at $V_{s,*} = 24.774$. From Eq. (3.63), we have $\beta_2 = -0.05595$ and the period-doubling bifurcation is supercritical. This agrees with the results in [6].

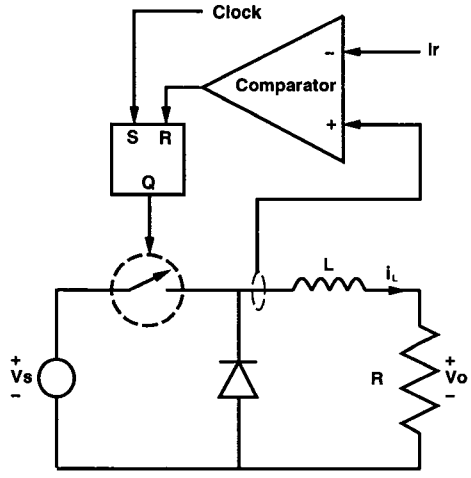

Figure 3.47: System diagram for Example 3.7

Example 3.8 (*Hysteretic current-programmed boost converter*, [57]) The system diagram is shown in Fig. 3.48, where $R = 10\Omega$, $L = 290\mu H$, $C = 760\mu F$, $V_s = 10V$, current reference $V_r = 4A$ and $\Delta V = 0.1A$.

Let the system state be $x = (i_L, v_C)$. In terms of the block diagram model in Fig. 3.15, the matrices A_1, A_2, B_1, B_2, C, E_1, and E_2 are the same as those in Example 3.2.

The fixed point is calculated as $(x^0(0), V_s, (d_n, T_n)', V_r) = ((3.9000; 19.8784)', 10, (2.9\times 10^{-6}, 5.8368 \times 10^{-6})', 4)$.

For the boost converter, the constraint equation (3.84) can be further simplified as

$$g(x_n, v_{sn}, \tau_n, v_{rn}) \tag{3.162}$$

$$= \begin{bmatrix} L\frac{\Delta V}{d_n} - v_{sn} \\ C(e^{A_2(T_n-d_n)}(e^{A_1 d_n}x_n + \int_0^{d_n} e^{A_1\sigma}d\sigma B_1 v_{sn}) + \int_0^{T_n-d_n} e^{A_2\sigma}d\sigma B_2 v_{sn}) - v_{rn} + \Delta V \end{bmatrix}$$

$$= 0 \tag{3.163}$$

From Eq. (3.88), we have

$$\Phi_h = e^{A_2(T-d)}(I - \frac{\dot{x}^0(d^+)Ce^{A_2(T-d)}}{Ce^{A_2(T-d)}\dot{x}^0(d^+)})e^{A_1 d} \tag{3.164}$$

so we have

$$\begin{aligned} \det[\Phi_h] &= \det[e^{A_1 d}e^{A_2(T-d)}](1 - \frac{Ce^{A_2(T-d)}\dot{x}^0(d^+)}{Ce^{A_2(T-d)}\dot{x}^0(d^+)}) \\ &= 0 \end{aligned}$$

Thus one pole is 0 and the system dynamics is 1-dimensional. The other pole can be analytically approximated (using a technique that will be discussed in Chapter 6) as

$$1 + \frac{(T-d)(R(V_r - \Delta V) - v_L^0(0))}{RC(V_s - v_L^0(0))} \tag{3.165}$$

Using this formula, the estimated pole is 0.9993, which is very close to 0.9985, calculated directly from $\sigma[\Phi_h]$.

By calculating the control (v_r) to output transfer function $E(zI - \Phi_h)^{-1}\Gamma_{hr}$, we have an unstable zero at 1.0537, which will cause an undershoot on the output voltage when v_r is step-changed. This transfer function is shown in Fig. 3.49. All of these results agree very well with [57].

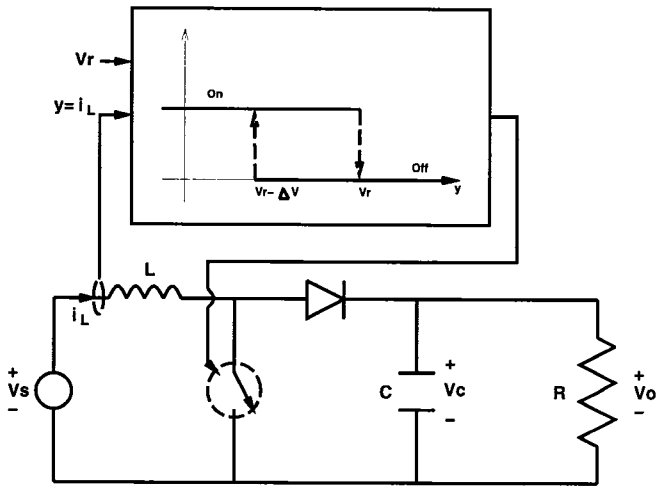

Figure 3.48: System diagram for Example 3.8

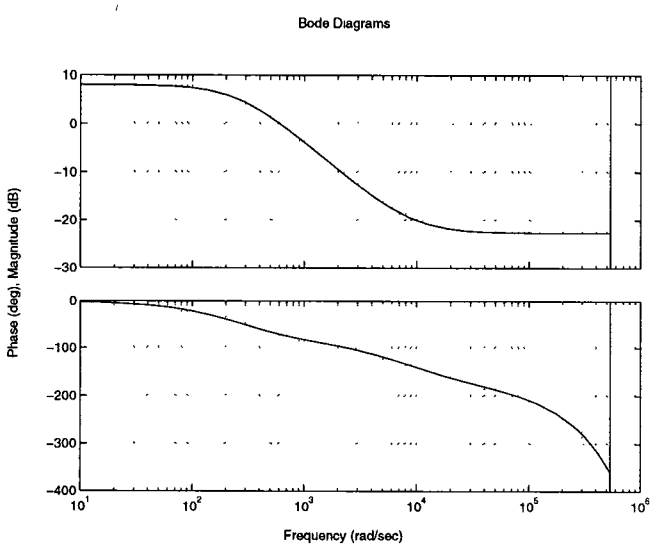

Figure 3.49: Control-to-output transfer function

Example 3.9 (*Analysis of a buck converter with voltage mode phase-lead control*, [21, p.346]) The system diagram is shown in Fig. 3.50.

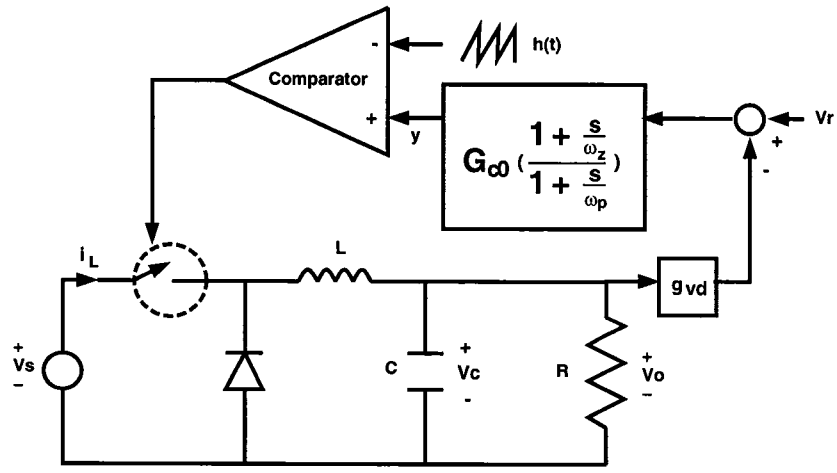

Figure 3.50: System diagram for Example 3.9

The system parameters are as follows: $T = 10\mu s$, $V_s = 28V$, $R = 3\Omega$, $L = 50\mu H$, $C = 500\mu F$, $g_{vd} = 1/3$ (voltage divider gain), $V_r = 5V$, $G_{c0} = 3.7$, $\omega_z = 10681\ rad/sec$, $\omega_p = 91106\ rad/sec$, and $h(t) = V_l + (V_h - V_l)[(\frac{t}{T}) \bmod 1]$ with $V_h = 4$ and $V_l = 0$.

The output voltage is designed to be $15V$. We will first show that this is not true by simple analysis, then we will apply sampled-data analysis to confirm this result.

Let the average output voltage be V_o. Then the DC value of the output of the error amplifier y can be calculated from as

$$G_{c0}(V_r - g_{vd}V_o) = V_h\frac{V_o}{V_s} \tag{3.166}$$

Solving this equation, we have $V_o = 13.44V$ instead of $15V$ as designed. So this circuit has poor steady-state regulation. To confirm this, a more detailed sampled-data analysis will be applied.

Let the state $x = (i_L, v_C, x_c)$, where x_c is the state of the error amplifier. In terms of the representation in Fig. 3.1, we have

$$A_1 = A_2 = \begin{bmatrix} 0 & \frac{-1}{L} & 0 \\ \frac{1}{C} & \frac{-1}{RC} & 0 \\ 0 & g_{vd}(\omega_p - \omega_z) & -\omega_p \end{bmatrix} \tag{3.167}$$

$$B_1 = \begin{bmatrix} \frac{1}{L} & 0 \\ 0 & 0 \\ 0 & \omega_z - \omega_p \end{bmatrix} \tag{3.168}$$

$$B_2 = \begin{bmatrix} 0 & 0 \\ 0 & 0 \\ 0 & \omega_z - \omega_p \end{bmatrix} \tag{3.169}$$

$$C = \frac{G_{c0}\omega_p}{\omega_z} \begin{bmatrix} 0 & -g_{vd} & 1 \end{bmatrix} \tag{3.170}$$

$$D = \begin{bmatrix} 0 & \frac{G_{c0}\omega_p}{\omega_z} \end{bmatrix} \tag{3.171}$$

$$E_1 = E_2 = \begin{bmatrix} 0 & 1 & 0 \end{bmatrix} \tag{3.172}$$

Solving Eqs. (3.17) and (3.21) by Newton's method, we have $x^0(0) = (3.7817, 13.4417, -0.4584)$ and $d = 4.8 \times 10^{-6}$. So the previous estimate $V_o = 13.44$ is correct. The steady-state orbit $x^0(t)$ calculated from Eq. (3.23) is shown in Fig. 3.51.

The reason why the output voltage is around $13.44V$ instead of $15V$ is because the error amplifier has finite DC gain G_{c0}. In [21], g_{vd} is chosen as V_r/V_o. But after solving Eq. (3.166), we have

$$g_{vd} = \frac{V_r}{V_o} - \frac{V_h}{V_s G_{c0}} \tag{3.173}$$

equals to V_r/V_o only when $G_{c0} = \infty$.

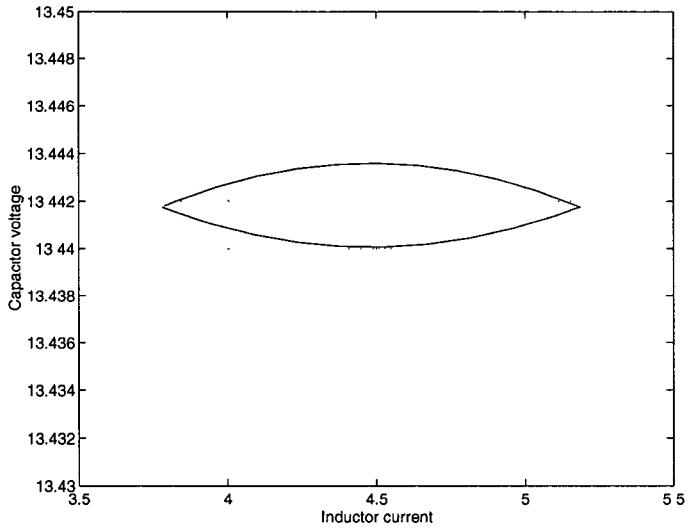

Figure 3.51: The steady-state orbit $x^0(t)$ of the buck converter with $g_{vd} = 1/3$

To achieve the output voltage at $15V$, we can either increase the DC loop gain by using PID control as shown in [21] or by adjusting g_{vd}. Here we will only illustrate adjusting g_{vd}. From Eq. (3.173) with $V_o = 15$, we have $g_{vd} = 0.29465$. Similar to the previous procedures, sampled-data analysis is applied and the steady-state orbit $x^0(t)$ is shown in Fig. 3.52. We can see that the output voltage is now around $15V$. The eigenvalues of the closed-loop system can be obtained from $\sigma[\Phi]$ and they are 0.8096 ± 0.1154 and 0.5973. So the closed-loop system is stable.

Example 3.10 (*Analysis of a boost converter in current mode control with outer voltage loop closed*, [111]) The system diagram is shown in Fig. 3.53, where $f_s = 25kHz$, $V_s = 28V$, $R = 11.2\Omega$, $L = 195\mu H$, $C = 2mF$, $R_1 = 47.5k\Omega$, $R_2 = 2.5k\Omega$, $R_s = 0.8125\Omega$, $R_f = 72.2\Omega$, and $C_f = 0.23\mu F$. The source voltage V_s and thus the duty cycle are varied. We will analyze this system in two configurations: without ramp compensation ($h(t) = 0$) and with ramp

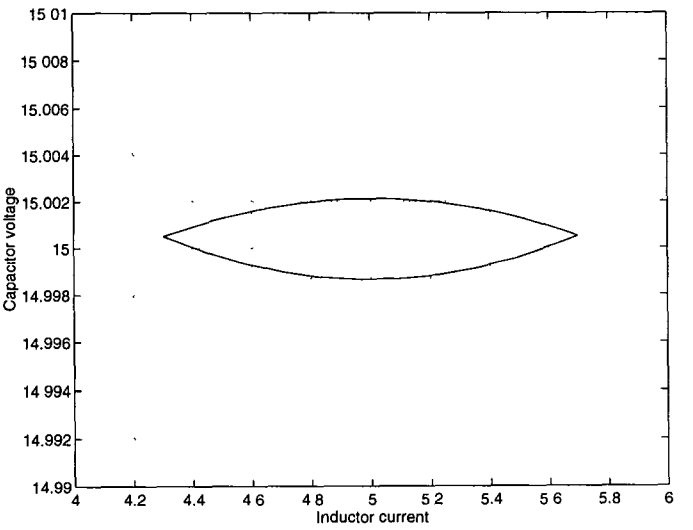

Figure 3.52: The steady-state orbit $x^0(t)$ of the buck converter with $g_{vd} = 0.29465$

compensation ($h(t) = (\frac{R_s V_s T}{5L})[\frac{t}{T} \bmod 1]$).

Let the state $x = (i_L, v_C, v_{cf})$. Those system matrices in Fig. 3.1 are

$$A_1 = \begin{bmatrix} 0 & 0 & 0 \\ 0 & \frac{-1}{RC} & 0 \\ 0 & \frac{-1}{C_f R_1} & 0 \end{bmatrix} \tag{3.174}$$

$$A_2 = \begin{bmatrix} 0 & \frac{-1}{L} & 0 \\ \frac{1}{C} & \frac{-1}{RC} & 0 \\ 0 & \frac{-1}{C_f R_f} & 0 \end{bmatrix} \tag{3.175}$$

$$B_1 = B_2 = \begin{bmatrix} \frac{1}{L} & 0 \\ 0 & 0 \\ 0 & \frac{1}{C_f R_1} + \frac{1}{C_f R_2} \end{bmatrix} \tag{3.176}$$

$$C = \begin{bmatrix} -R_s & \frac{-R_f}{R_1} & 1 \end{bmatrix} \tag{3.177}$$

$$D = \left[\begin{array}{ccc} 0 & 1+\frac{R_f}{R_1}+\frac{R_f}{R_2} \end{array} \right] \tag{3.178}$$

$$E_1 = E_2 = \left[\begin{array}{ccc} 0 & 1 & 0 \end{array} \right] \tag{3.179}$$

First we analyze the system without ramp compensation. The duty cycle is varied from 0.4 to 0.6 and $\sigma[\Phi]$ is plotted and shown in Fig. 3.54. One eigenvalue trajectory crosses the unit circle at $D_c = 0.498$. The other two are very close to 1. For $D_c > 0.498$, the system is unstable.

Then we analyze the system with ramp compensation. The duty cycle is varied from 0.4 to 0.7 and $\sigma[\Phi]$ is plotted and shown in Fig. 3.55. One eigenvalue trajectory crosses the unit circle at $D_c = 0.5845$. For $D_c > 0.5845$, the system is unstable.

For $D_c = 0.45$, the steady-state inductor currents are simulated with or without ramp compensation. These are plotted in Fig. 3.56 and Fig. 3.57 respectively.

These results are different to those in [111], where HSPICE is used to simulate this system. The difference may be that here we assume there is no voltage drop at the switch, while this is not assumed in [111].

3.12 Concluding Remarks

A general model of the PWM converter is developed by the sampled-data method. It is so general that most PWM converters can be modeled by this approach. Analytical conditions on existence of periodic solutions and asymptotic orbital stability have been derived. Analytical formulae for audio-susceptibility and output impedance have also been derived. The stability of bifurcated limit cycles has been investigated by an index β_2 of the reduced system. The results for CCM under FFC are extended to the cases of DCM and VFC. The buck

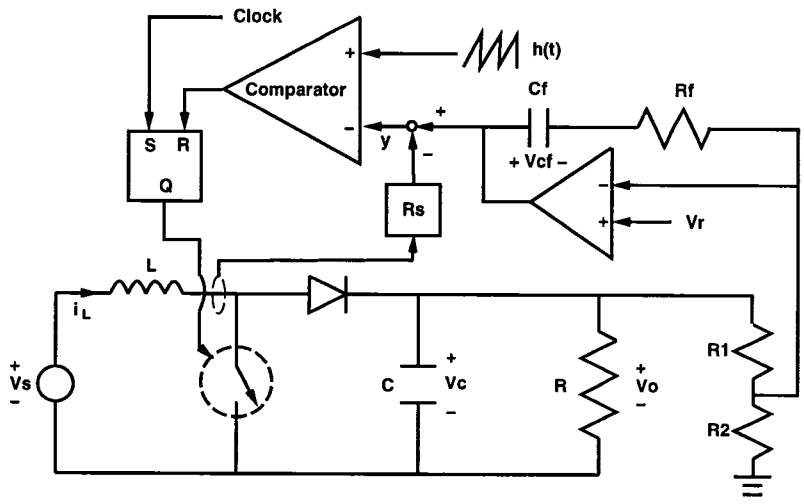

Figure 3.53: System diagram for Example 3.10

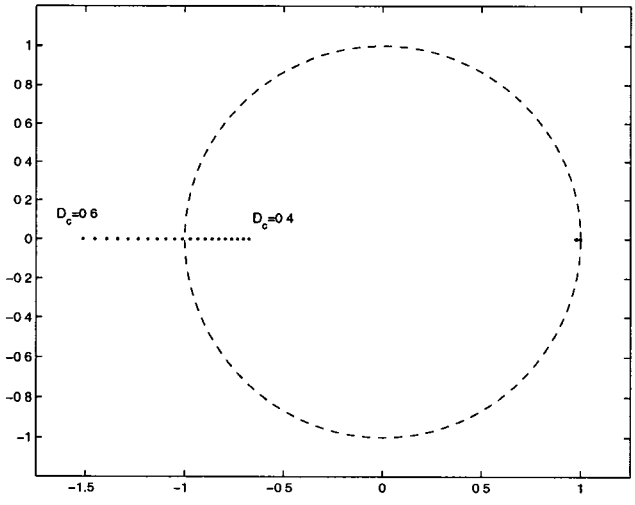

Figure 3.54: $\sigma(\Phi)$ as D_c varies from 0.4 to 0.6

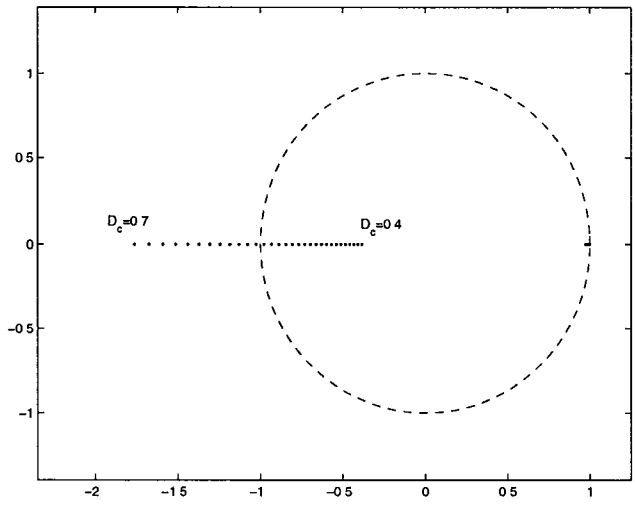

Figure 3.55: $\sigma(\Phi)$ as D_c varies from 0.4 to 0.7

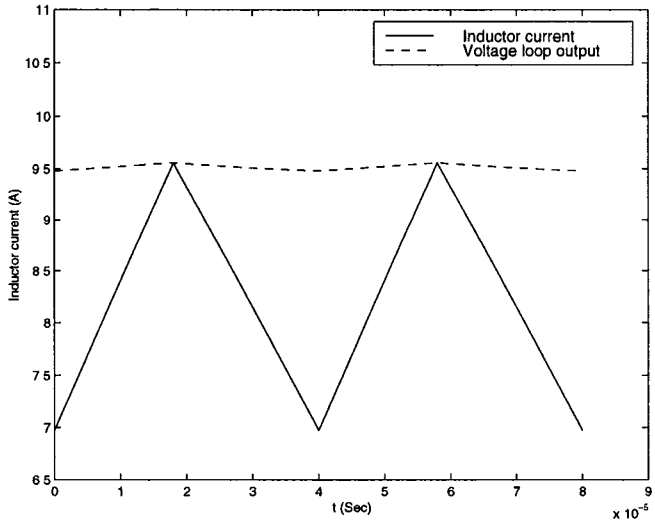

Figure 3.56: Steady-state inductor current without ramp compensation when $D_c = 0.45$

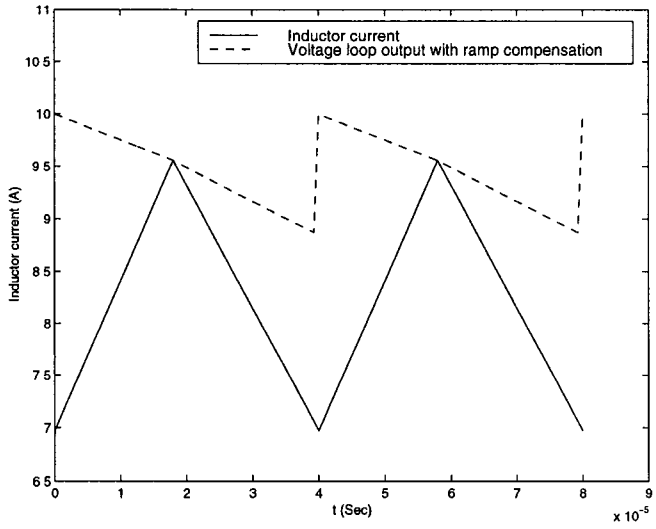

Figure 3.57: Steady-state inductor current with ramp compensation when $D_c = 0.45$

converter has also been studied by the harmonic balance method, which can determine the location of the period-doubling bifurcation. Many examples taken from the literature are given to illustrate this unified approach. In particular, the input filter instability is explained by Neimark-Sacker bifurcation.

Chapter 4

Stabilization of Unstable Periodic Orbits in PWM DC-DC Converters

In every controlled switching converter, stability is one of the basic requirements. In this chapter, we concentrate on stabilization of unstable periodic orbits in PWM converters. The issue of control to achieve good line and load regulation will be addressed in the next chapter. Generally when the switching converter undergoes period-doubling bifurcation or Neimark-Sacker bifurcation, the original periodic solution becomes unstable. To stabilize the system, we can either stabilize this unstable periodic orbit (UPO) or another periodic orbit. The advantage of stabilizing the nominal unstable periodic orbit is to smoothly extend the operating condition.

In this chapter, discrete-time feedback stabilization is employed. We will show two schemes for stabilization. Sufficient conditions for stabilization will be given. Then we will show how to maintain the original operating condition using washout filters. Stabilization of a segment of a bifurcated branch is also studied. Numerous examples are given.

To stabilize the switching circuits, we need information about the states of

the circuits. Generally these are capacitor voltages and inductor currents. Here we assume they are measurable, which is achievable with the existing technology. In Chapter 7, we investigate control using *partial* state information.

4.1 Stabilization by Adding a Discrete-Time Feedback Loop

Generally there are many unstable UPOs with different periods when the PWM converter is unstable. Here we only show stabilization of the T-periodic UPO. A similar approach can be applied to stablize a general nT-periodic UPO. We will show this through an example (for n=2) in Section 4.5.

There are many ways to design control laws to stabilize the UPO; here we illustrate two schemes.

4.1.1 Voltage Reference (v_r) Compensation

The system diagram is shown in Fig. 4.1, where the matrices B_1, B_2, D are decomposed into $[B_{11}, B_{12}]$, $[B_{21}, B_{22}]$, and $[D_1, D_2]$ respectively. As mentioned in Chapter 3, v_r can be either voltage or current reference. In this scheme, v_r is updated at the clock time and denoted as v_{rn}. In the linearized sampled-data dynamics (3.27), set $\hat{v}_{sn} = 0$ and let $\hat{v}_{rn}$ be controlled according to the law $\hat{v}_{rn} = -K\hat{x}_n$, where $K \in \mathbf{R}^{1\times n}$ is the linear feedback gain. Then $\hat{x}_n$ evolves according to

$$\hat{x}_{n+1} \approx (\Phi - \Gamma_2 K)\hat{x}_n \tag{4.1}$$

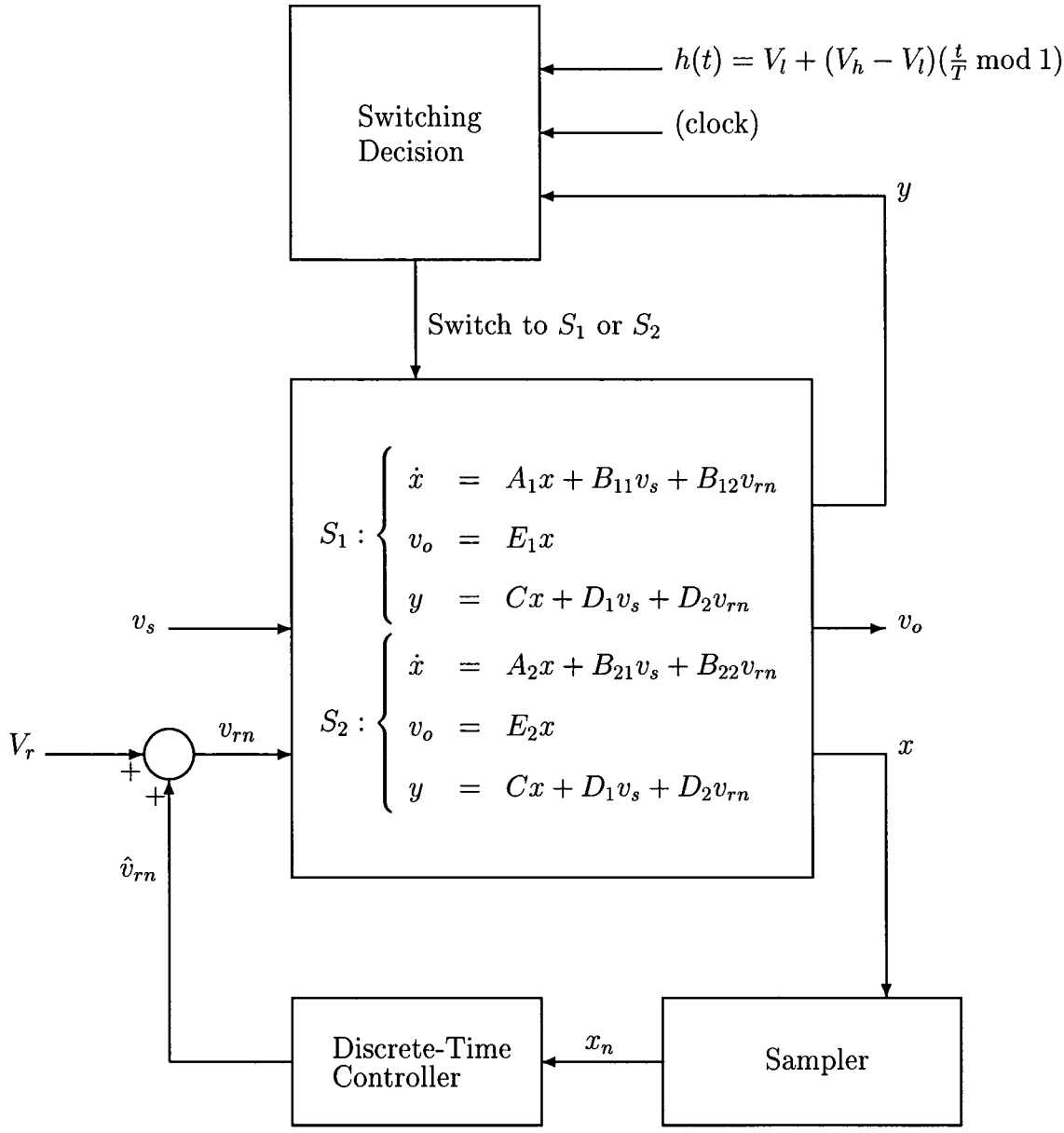

Figure 4.1: Stabilization by voltage reference (v_r) compensation

When the pair (Φ, Γ_2) is stabilizable, there exists a feedback gain K such that the eigenvalues of $\Phi - \Gamma_2 K$ are inside the unit circle. Thus under this condition the periodic solution $x^0(t)$ can be stabilized with such a feedback law.

4.1.2 Dynamic Ramp Compensation

The system diagram is shown in Fig. 4.2. In this approach, the slope of $h(t)$ is changed by state feedback. We call the signal $h(t)$ a *dynamic ramp*, to distinguish it from the traditional fixed-ramp compensating ramp.

Let $h(t) = V_l + (v_h - V_l)(\frac{t}{T} \bmod 1)$. Changing the slope is equivalent to changing v_h. Let v_h be updated in each cycle and denoted as $v_{hn} = V_h + \hat{v}_{hn}$. The switching constraint equation, Eq. (3.4), now becomes

$$\begin{aligned} g(x_n, u_n, d_n, v_{hn}) &= C(e^{A_1 d_n} x_n + \int_0^{d_n} e^{A_1(d_n-\sigma)} d\sigma B_1 u_n) \\ &\quad + Du_n - V_l - \frac{(v_{hn} - V_l)d_n}{T} \\ &= 0 \end{aligned} \tag{4.2}$$

Linearizing Eqs. (3.3) and (4.2), and setting $\hat{u}_n = 0$, we obtain

$$\hat{x}_{n+1} \approx \Phi \hat{x}_n + \Gamma_h \hat{v}_{hn} \tag{4.3}$$

where

$$\begin{aligned} \Phi &= \frac{\partial f}{\partial x_n} - \frac{\partial f}{\partial d_n}(\frac{\partial g}{\partial d_n})^{-1} \frac{\partial g}{\partial x_n}\bigg|_{(x_n,u_n,d_n,v_{hn})=(x^0(0),u,d,V_h)} \\ &= e^{A_2(T-d)}(I - \frac{(\dot{x}^0(d^-) - \dot{x}^0(d^+))C}{C\dot{x}^0(d^-) - \frac{V_h - V_d}{T}})e^{A_1 d} \end{aligned} \tag{4.4}$$

$$\begin{aligned} \Gamma_h &= -\frac{\partial f}{\partial d_n}(\frac{\partial g}{\partial d_n})^{-1} \frac{\partial g}{\partial v_{hn}}\bigg|_{(x_n,u_n,d_n,v_{hn})=(x^0(0),u,d,V_h)} \\ &= e^{A_2(T-d)} \frac{(\dot{x}^0(d^-) - \dot{x}^0(d^+))d}{(C\dot{x}^0(d^-) - \frac{V_h - V_d}{T})T} \end{aligned} \tag{4.5}$$

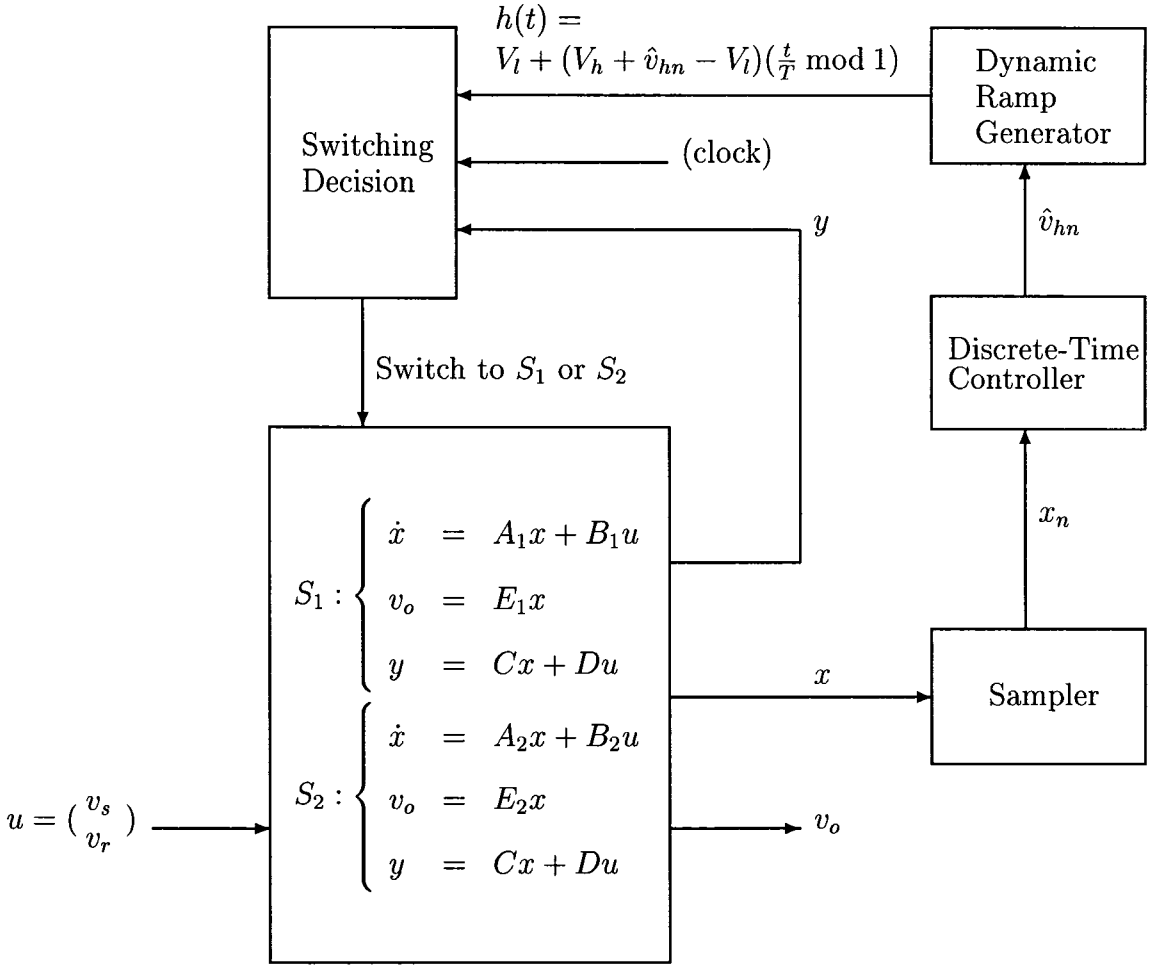

Figure 4.2: Stabilization by dynamic ramp compensation

Let the feedback law be $\hat{v}_{hn} = -K\hat{x}_n$. We have the following positive result on stabilizability by dynamic ramp compensation.

Theorem 4.1 *Assume that all of the eigenvalues of A_1 and A_2 are in the open LHP, or one of them may have eigenvalues on the imaginary axis. Then the periodic solution $x^0(t)$ is asymptotically stabilizable using dynamic ramp.*

Proof:

Let $K = -\frac{T}{d}Ce^{A_1 d}$, then $\Phi - \Gamma_h K = e^{A_2(T-d)}e^{A_1 d}$, the eigenvalues of which by

Lemma 3.1 lie inside the unit circle. □

4.2 Robust Stabilization Through Discrete-Time Washout Filter

In the feedback stabilization schemes presented in the previous section, we feed back $\hat{x}_n = x_n - x^0(0)$, which requires knowledge of the fixed point $x^0(0)$. Washout filters [49, 1] are generally introduced in a controller to preserve the original steady states without the need for precise knowledge of these steady states. We will add washout filters to the two stabilization schemes presented in the preceding section.

4.2.1 Washout Filter Aided Voltage Reference Control

The stabilization scheme using v_r as the control variable has the following dynamics

$$x_{n+1} = f(x_n, v_{sn}, V_r + \hat{v}_{rn}, d_n) \tag{4.6}$$

$$g(x_n, v_{sn}, V_r + \hat{v}_{rn}, d_n) = 0 \tag{4.7}$$

Recall that this model depends on matrices A_1, A_2, B_1, B_2, C, and D, which are not shown explicitly. (see Fig. 4.1)

We add a one-dimensional discrete-time washout filter, and the discrete-time controller in Fig. 4.1 is

$$w_{n+1} = -K_1 x_n + (1 - K_2) w_n \tag{4.8}$$

$$\hat{v}_{rn} = -K_1 x_n - K_2 w_n \tag{4.9}$$

where $w_n \in \mathbf{R}$ is the state of the washout filter, $K_1 \in \mathbf{R}^{1\times n}$, $K_2 \in \mathbf{R}$ are the feedback gains and $K_2 \neq 0$.

We can see that the fixed-point of the new closed-loop system by adding washout filter is $(x_n, w_n) = (x^0(0), -K_2^{-1}K_1x^0(0))$. Thus the original fixed point $x_n = x^0(0)$ is preserved.

From the results of Sec. 3.4, we see that the linearized dynamics of the closed-loop system is

$$\begin{bmatrix} \hat{x}_{n+1} \\ \hat{w}_{n+1} \end{bmatrix} \approx \left(\begin{bmatrix} \Phi & 0 \\ 0 & 1 \end{bmatrix} - \begin{bmatrix} \Gamma_2 \\ 1 \end{bmatrix} \begin{bmatrix} K_1 & K_2 \end{bmatrix} \right) \begin{bmatrix} \hat{x}_n \\ \hat{w}_n \end{bmatrix} \tag{4.10}$$

We have the following result.

Theorem 4.2 *The system (3.3, 3.4) is asymptotically stabilizable by using washout filter aided voltage reference control scheme if the following conditions are satisfied:*

(i) (Φ, Γ_2) *is stabilizable.*

(ii) $\begin{bmatrix} \Phi - I & \Gamma_2 \\ 0 & 1 \end{bmatrix}$ *is of full rank.*

Proof:

If the condition (ii) holds, then the eigenvalue at 1 is controllable. Let λ be any eigenvalue of Φ which lies outside the unit circle. This eigenvalue is controllable if $\begin{bmatrix} \Phi - \lambda I & 0 & \Gamma_2 \\ 0 & 1-\lambda & 1 \end{bmatrix}$ is of full rank. The last statement is true if condition (i) is satisfied. □

4.2.2 Washout Filter Aided Dynamic Ramp Scheme

Similarly, the washout filter aided dynamic ramp scheme has the following dynamics

$$w_{n+1} = -K_1 x_n + (1 - K_2) w_n \tag{4.11}$$

$$\hat{v}_{hn} = -K_1 x_n - K_2 w_n \tag{4.12}$$

Applying the results in Sec. 4.1.2, the linearized dynamics of the closed-loop system is

$$\begin{bmatrix} \hat{x}_{n+1} \\ \hat{w}_{n+1} \end{bmatrix} \approx \left(\begin{bmatrix} \Phi & 0 \\ 0 & 1 \end{bmatrix} - \begin{bmatrix} \Gamma_h \\ 1 \end{bmatrix} \begin{bmatrix} K_1 & K_2 \end{bmatrix} \right) \begin{bmatrix} \hat{x}_n \\ \hat{w}_n \end{bmatrix} \tag{4.13}$$

where Γ_h is as in Eq. (4.5).

Analogous to Theorem 4.2, we have

Theorem 4.3 *Assume that all of the eigenvalues of A_1 and A_2 are in the open LHP, or one of them may have eigenvalues on the imaginary axis. If the matrix* $\begin{bmatrix} \Phi - I & \Gamma_h \\ 0 & 1 \end{bmatrix}$ *is of full rank, the system (3.3, 3.4) is asymptotically stabilizable by using washout filter aided dynamic ramp scheme.*

Proof:

The pair (Φ, Γ_h) has been proved to be asymptotically stabilizable in Theorem 4.1. The rest of the proof is similar to Theorem 4.2. □

4.3 Stabilization of Bifurcated Branch

In the preceding sections, the stabilization law is designed for a specific operating condition, for example, for a specific nominal duty cycle, d/T. It would be better

if a circuit can be designed to work in broader operating conditions. In terms of the bifurcation diagram, we hope the circuit is not only stable at a specific operating *point*, but also stable on a segment of the operating *branch*.

Here we mention two linear stabilization methods that can be used to achieve this goal.

1. Gain Scheduling

Let a nominal duty cycle D_c, which is equivalent to a nominal switching time d, be given. Suppose the pair (Φ, Γ) is stabilizable, where Γ here could be either Γ_2 or Γ_h, depending on which variable v_r or v_h is used as the control variable is used. The stabilizing feedback gain K is a function of the nominal switching time d. By adjusting the feedback gain K according to this function in different operating conditions, we can stabilize the whole operating branch.

2. Fixed Gain Feedback Stabilization

Generally, linear feedback is robust to some extent. If we can find a fixed stabilizing gain K such that all of the eigenvalues of $\Phi - \Gamma K$ are inside the unit circle for all d, or for d in an interval $[d_1, d_2]$, then we can stabilize at least this segment of the operating branch.

4.4 Stabilization by Analog Feedback

From the structure of the controlled PWM converter shown in Fig. 3.1, a feedback loop using the measured variable $y = Cx + Du$ is already present. If the controlled converter is unstable for a given set of system parameters, we will show that stabilization of the original nominal periodic solution is possible through adjusting the gains C and D.

Theorem 4.4 *Assume $\dot{h}(t) \neq 0$. Then there exist $C \in \mathbf{R}^{1\times n}$ and $D \in \mathbf{R}^{1\times 2}$ that locally stabilize the periodic solution $x^0(t)$ in the system shown in Fig. 3.1.*

Proof:

A trivial solution, $C = 0$ and $D = [0, h(d)/V_r]$, satisfies the conditions (3.9)-(3.12) in voltage mode control or (3.6) in current mode control, and also

$$|\sigma[\Phi]| = |e^{A_2(T-d)}e^{A_1 d}| < 1$$

So the periodic solution $x^0(t)$ is locally stabilized. □

In the theorem above, the existence of C and D that stabilize the system is proved. Next a procedure to find $C \neq 0$ and D that locally stabilize the system is given.

Since all of the eigenvalues of $e^{A_1 d}e^{A_2(T-d)}$ are inside the unit circle, we can find a matrix $K \in \mathbf{R}^{1\times n}$ such that

$$\left|\sigma[e^{A_1 d}e^{A_2(T-d)} - e^{A_1 d}e^{A_2(T-d)}(\dot{x}^0(d^-) - \dot{x}^0(d^+))K]\right| < 1 \qquad (4.14)$$

$$K\dot{x}^0(d^-) - 1 \neq 0 \qquad (4.15)$$

Let

$$C = \frac{\dot{h}(d)K}{K\dot{x}^0(d^-) - 1} \qquad (4.16)$$

then $\frac{C}{C\dot{x}^0(d^-)-\dot{h}(d)} = K$. From Eq. (3.25), we have

$$\begin{aligned} |\sigma[\Phi]| &= \left|\sigma[e^{A_1 d}e^{A_2(T-d)}(I - \frac{(\dot{x}^0(d^-) - \dot{x}^0(d^+))C}{C\dot{x}^0(d^-) - \dot{h}(d)})]\right| \\ &= \left|\sigma[e^{A_1 d}e^{A_2(T-d)}(I - (\dot{x}^0(d^-) - \dot{x}^0(d^+))K)]\right| \\ &< 1 \end{aligned}$$

After C is chosen, we can find a matrix $D \in \mathbf{R}^{1\times 2}$ to satisfy

$$Cx^0(d) + Du = h(d) \qquad (4.17)$$

For voltage mode control, extra conditions are needed so that the switching condition is eligible. Similar to the discussion in Sec. 3.3.2, these conditions are (3.10)-(3.12).

4.5 Illustrative Examples

In this section, we give examples of stabilization of the UPO in PWM converters.

Example 4.1. (*Discrete-time stabilization of a UPO in a buck converter with voltage mode control*) The system in Example 3.1 has been shown to be chaotic for $V_s = 34.66V$. Here we will demonstrate stabilization of this system using voltage reference or dynamic ramp compensation, both with a washout filter.

The pairs $\left(\begin{bmatrix} \Phi & 0 \\ 0 & 1 \end{bmatrix}, \begin{bmatrix} \Gamma_2 \\ 1 \end{bmatrix}\right)$ (Eq. (4.10)) and $\left(\begin{bmatrix} \Phi & 0 \\ 0 & 1 \end{bmatrix}, \begin{bmatrix} \Gamma_h \\ 1 \end{bmatrix}\right)$ (Eq. (4.13)) for this example can be shown to be controllable, so we can assign all of the eigenvalues of the closed-loop system to the origin. In an n-dimensional linear time-invariant discrete system, assigning all of the poles of the closed-loop system to zero is called dead-beat control. This is because with such a control law, the system is driven to the origin in finitely many (n) steps. In the switching converter, the dynamics is nonlinear, so the dead-beat effect cannot be guaranteed to occur, but we still expect the stabilization to be fast if a linear dead-beat control is used.

Using v_r as the control variable, we stabilize the UPO by assigning all of the closed-loop eigenvalues to 0. The feedback gains achieving this are $K_1 = (-1.6622, -0.4655)$ and $K_2 = 0.2403$. Fig. 4.3 shows the effectiveness of the control law. Originally the system is chaotic. When the control scheme is applied

at $t = 0.0048$, the chaotic trajectory is stabilized to a period-one mode in around 3 switching periods. The stabilized period-one mode is shown in Fig. 4.4.

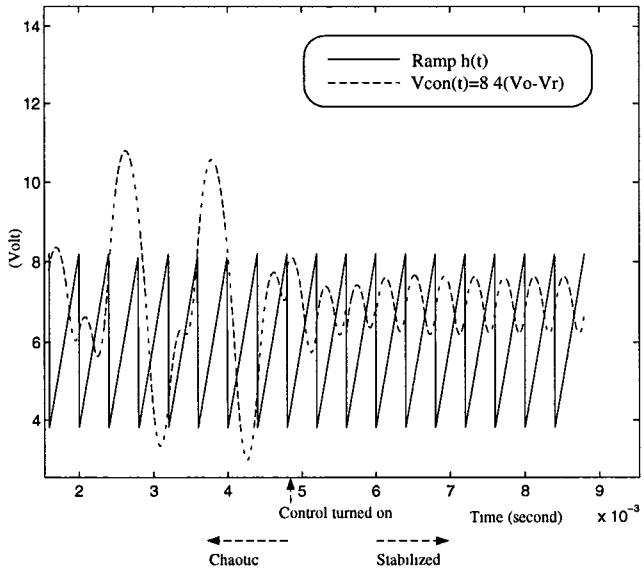

Figure 4.3: Stabilization of the buck converter in Fig. 3.23 using washout filter aided voltage reference compensation; control turned on at $t = 0.0048$

The effectiveness of dynamic ramp control in stabilizing the UPO is illustrated in Fig. 4.5. The feedback gains used in this illustration are $K_1 = (-21.4809, -6.0160)$ and $K_2 = 0.2403$, which also makes all of the closed-loop eigenvalues at 0. Similar to the result of using v_r as control variable, the periodic solution is stabilized in around 3 switching periods. Fig. 4.6 shows the bifurcation diagram with the same feedback gains. The stable operating range is now extended up to a source voltage of $V_s = 35V$.

In this example we have shown that a chaotic system can be stabilized by simple state feedback, which can be compared, for instance, with the complicated algorithm proposed in [72].

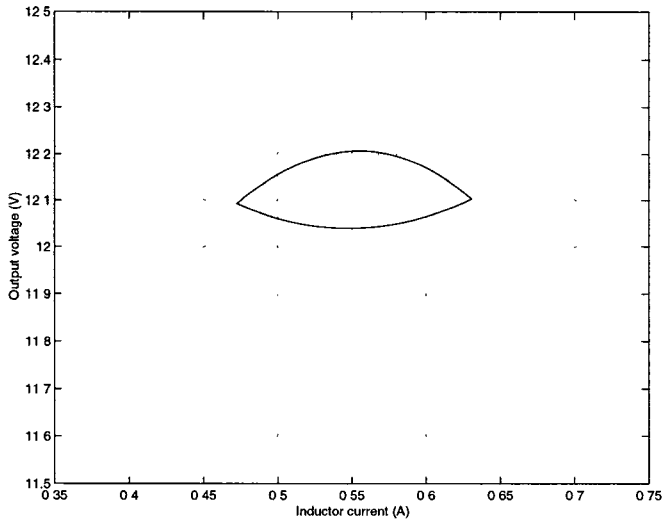

Figure 4.4: Stabilized period-one trajectory in state space for $V_s = 34.66V$

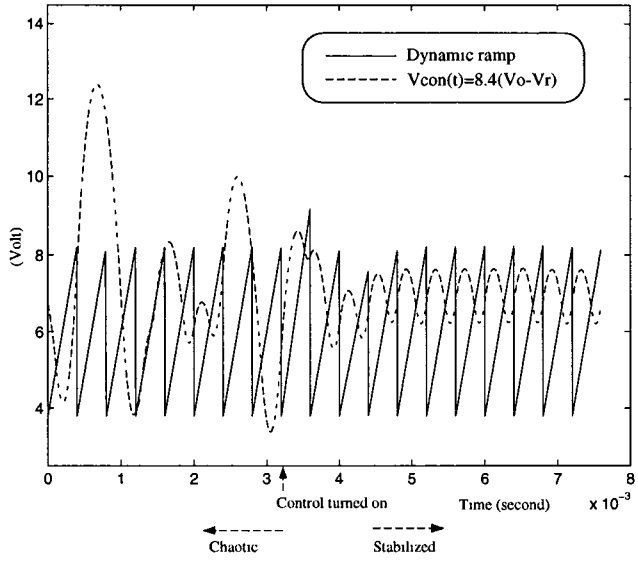

Figure 4.5: Stabilization of the buck converter in Fig. 3.23 using washout filter aided dynamic ramp compensation; control turned on at $t = 0.0032$

Generally switching converters are designed to operate in period-*one* mode, not in any higher periodic mode. It is known that in a chaotic system there are an infinite number of *unstable* periodic solutions embedded in the chaotic orbit. To show the flexibility of our control methods, we will demonstrate how to stabilize a period-two mode.

Similar to stabilization of the period-one mode, we first derive the period-two dynamics, linearize these dynamics, and calculate the feedback stabilization gain. We use v_r as the control variable. We assign all of the closed-loop poles to zero using feedback gains $K_1 = (0.006616, -0.59)$ and $K_2 = 0.23426$. The sampling rate for feedback stabilization is half of the switching frequency. A simulation showing stabilization of the period-two mode is given in Fig. 4.7, and the stabilized period-two mode is shown in Fig. 4.8.

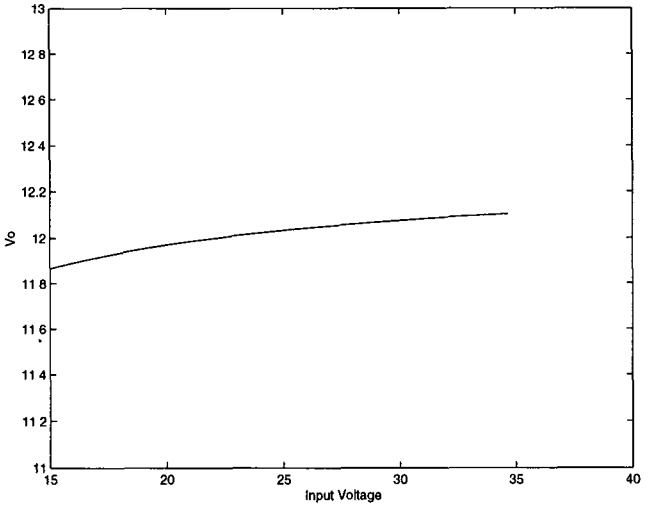

Figure 4.6: Bifurcation diagram for Example 4.1 using washout filter aided dynamic ramp compensation

Example 4.2 (*Analog stabilization of a UPO in a buck converter in voltage*

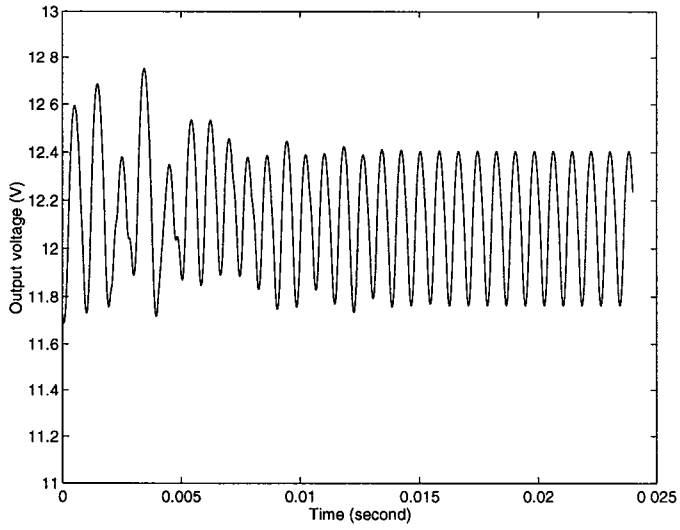

Figure 4.7: Stabilization of period-two mode; control turned on at $t = 4.8 \times 10^{-3}$

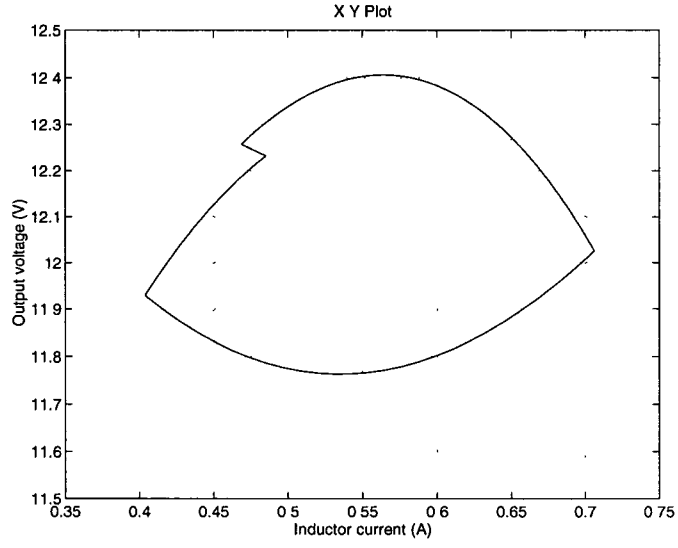

Figure 4.8: Stabilized period-two trajectory in state space for $V_s = 34.66V$

mode control) The system in Example 3.1 is chaotic when $V_s = 34.66V$. Here we try to stabilize the unstable period-one mode by adding a current feedback loop and adjusting the feedback gains from v_o and V_r. The system diagram is shown in Fig. 4.9. Expressing this system in terms of the model in Fig. 3.1, we have $C = g_1(g_3, g_4) = 8.4(g_3, g_4)$ and $D = g_1 g_2 = 8.4 g_2$. We will show how to find the gains g_2, g_3, and g_4.

We use Eq. (4.14) to assign both closed-loop poles to 0.5 (this value is chosen for illustration only). We have $K = (-3.646 \times 10^4, 3.8 \times 10^{-6})$. From Eq. (4.16), we have $C = (5.1044, -0.0531)$. So $g_3 = 0.6077$ and $g_4 = -0.0063$. The UPO $x^0(t)$ satisfies the constraint

$$Cx^0(d) + Du = h(d) \tag{4.18}$$

From this constraint, we have

$$g_1 g_2 V_r = Du = h(d) - Cx^0(d)$$

Solving this equation, we have $g_2 = 0.0515$.

With these feedback gains applied, the voltage during start-up (i.e., starting from $(i_L, v_C) = (0, 0)$) is shown in Fig. 4.10. After the transient, the state trajectory converges to $x^0(t)$, which is the same as in Fig. 4.4. The switching actions occur based on how the signals $h(t)$ and $y(t)$ intersect. The signals $h(t)$ and $y(t)$ in steady state are shown in Fig. 4.11.

Example 4.3 (*Discrete-time stabilization of UPO in Boost converter in current mode control*) The system of Example 3.2 was shown to be in period-two mode when $V_r = 1.85$. Here we will demonstrate stabilization using washout filter aided dynamic ramp compensation.

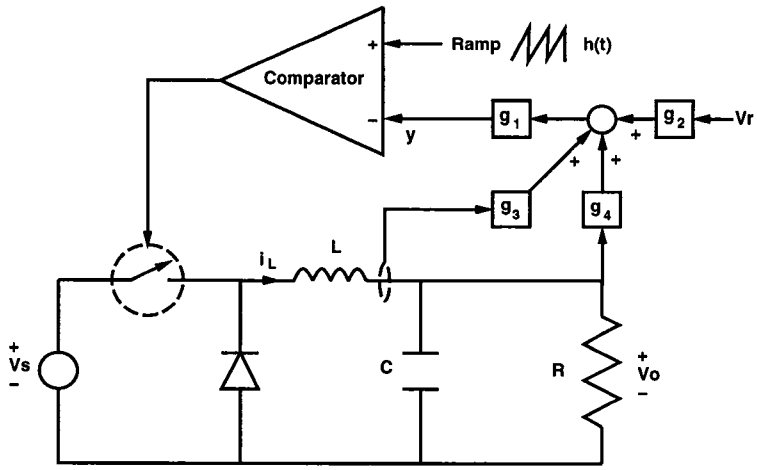

Figure 4.9: Buck converter with analog stabilization in Example 4.2

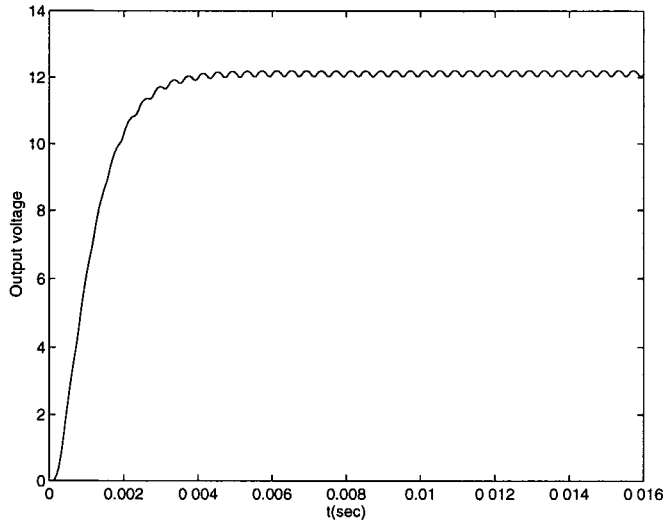

Figure 4.10: Output voltage during start-up after the stabilization scheme is applied

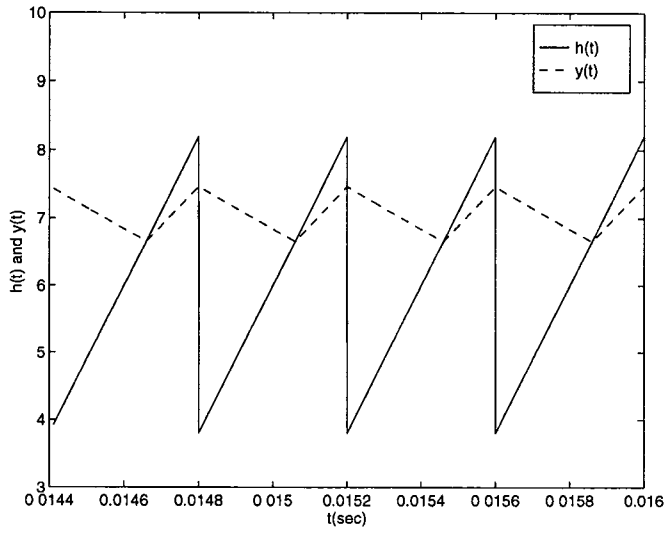

Figure 4.11: The signals $h(t)$ and $y(t)$ of Example 4.2 in steady state

It can be checked that the pair $(\begin{bmatrix} \Phi & 0 \\ 0 & 1 \end{bmatrix}, \begin{bmatrix} \Gamma_h \\ 1 \end{bmatrix})$ is controllable for this example. Therefore we can assign closed-loop eigenvalues so as to achieve dead-beat control, (similar to the approach in the preceding example).

Using dynamic ramp compensation, we can stabilize the period-one mode from the period-two mode as shown in Fig. 4.12.

Similarly for different conditions as V_r varies, the stabilizing gain is scheduled by Ackermann's formula [34]. We have the bifurcation diagram shown in Fig. 4.13

To compare the performance with that for the traditional method, we use fixed-ramp compensation with a slope 10000 Amp/sec, The bifurcation diagram is shown in Fig. 4.14. The fixed-ramp compensation is seen to just *delays* the period-doubling bifurcation, and it doesn't preserve the original equilibrium.

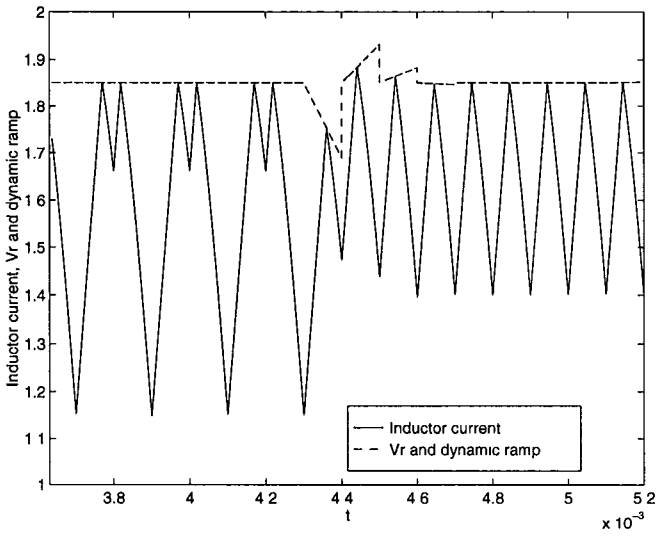

Figure 4.12: Stabilization of the boost converter in Fig. 3.27 using washout filter aided dynamic ramp compensation; control turned on at $t = 4.3 \times 10^{-3}$

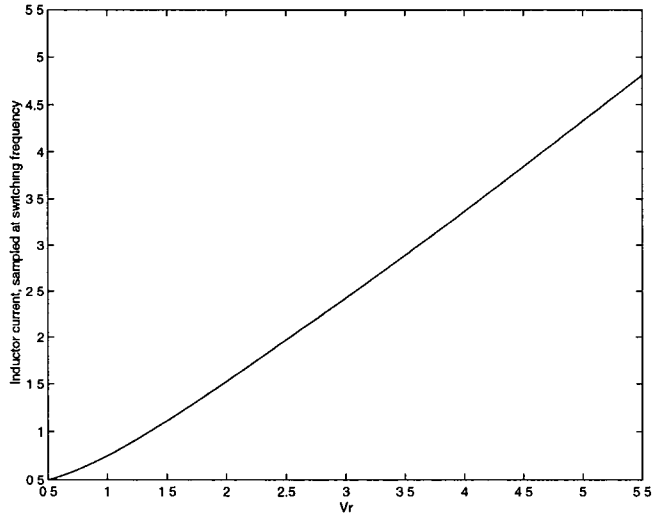

Figure 4.13: Bifurcation diagram for Example 4.3 using dynamic ramp compensation and gain scheduling

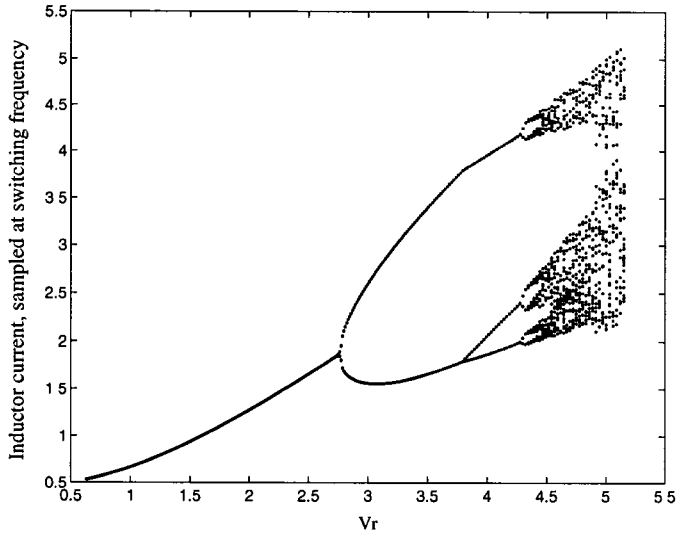

Figure 4.14: Bifurcation diagram using fixed-ramp compensation

4.6 Concluding Remarks

In this chapter, discrete-time and analog schemes to stabilize unstable periodic orbits in controlled switching converters have been developed. The same schemes can be used to stabilize an unstable period-two mode or a higher order mode. Washout filters are introduced to ensure that the nominal equilibrium is unaffected by the control, without the need for accurate knowledge of the equilibrium. Conditions for stabilizability have been derived. The operating range can be extended by the gain-scheduling or the fixed-gain method.

Chapter 5

Sampled-Data Modeling and Analysis of the Power Stage of the PWM DC-DC Converter

In Chapter 3, we analyzed the *controlled* PWM converter. Here we will analyze only the *power stage* of the PWM converter. Once this model of the power stage is derived, we will use it to derive the poles and zeros of the power stage in Chapter 6 and to design the controller (error amplifier) in Chapter 7.

Traditionally, the power stage is analyzed by the averaging method, and a frequency independent and continuous-time model of the power stage is derived. The poles and zeros of this model are also derived. Then the controller design is based on this model. We will show that the averaged model of power stage is not accurate, and the subsequent controller design will also result in inaccurate closed-loop performances.

In a PWM converter, the control variables are the duty cycle and switching frequency. In this chapter, we will first derive a sampled-data model of the power stage in continuous conduction mode (CCM) with the duty cycle as the control

variable. Then we will derive a new and better *continuous-time* model of power stage based on the sampled-data model. This continuous-time model will be useful for *analog* controller design. Then we will derive a sampled-data model of the power stage with the switching period as the control variable (i.e. variable frequency control (VFC)). We also investigate the sampled-data model of the power stage in discontinuous conduction mode (DCM).

5.1 Sampled-Data Modeling of the Power Stage of the PWM Converter in CCM with FFC

In a switching converter with fixed frequency control (FFC), the duration of each cycle is T, which is a fixed value. In the $(n+1)$-th cycle, the system switches from S_1 to S_2 at $t = nT + d_n$ and from S_2 to S_1 at $t = (n+1)T$. Here d_n is the switching instant in the $(n+1)$-th cycle and will be used as the control variable. This is equivalent to using the duty cycle d_n/T as the control variable.

A general model of the power stage of a PWM converter operated in CCM with FFC is shown in Fig. 5.1, where $A_1, A_2 \in \mathbf{R}^{n\times n}$, $B_1, B_2 \in \mathbf{R}^{n\times 1}$, $C, E_1, E_2 \in \mathbf{R}^{1\times n}$, are constant matrices, and v_s, $v_o \in \mathbf{R}$ are the source and output voltages respectively.

Compared with the sampled-data dynamics of the controlled PWM converter (3.3)-(3.5), the sampled-data dynamics of the power stage is simpler. It is because here the switching instant d_n is a control variable and no switching con-

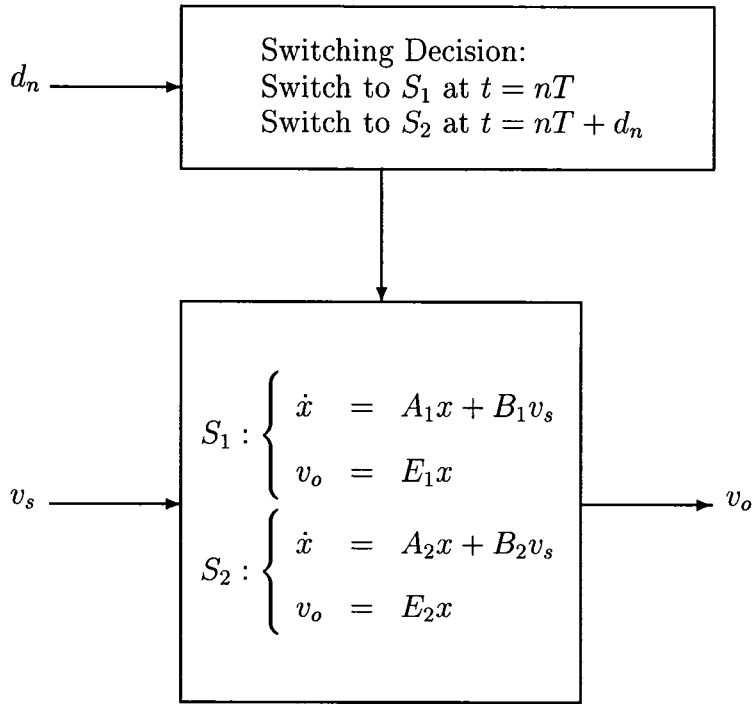

Figure 5.1: Power stage of PWM converter in CCM with FFC

straint like (3.4) exists. The sampled-data dynamics of the power stage is

$$\begin{aligned} x_{n+1} &= f(x_n, v_{sn}, d_n) \\ &= e^{A_2(T-d_n)}(e^{A_1 d_n}x_n + \textstyle\int_0^{d_n} e^{A_1\sigma}d\sigma B_1 v_{sn}) + \int_0^{T-d_n} e^{A_2\sigma}d\sigma B_2 v_{sn} \qquad (5.1) \\ \hat{v}_{on} &= E\hat{x}_n \end{aligned}$$

The fixed point $(x_n, v_{sn}, d_n) = (x^0(0), V_s, d)$, if it exists, must satisfy

$$\begin{aligned} x^0(0) &= f(x^0(0), V_s, d) \\ &= e^{A_2(T-d)}(e^{A_1 d}x^0(0) + \int_0^d e^{A_1\sigma}d\sigma B_1 V_s) + \int_0^{T-d} e^{A_2\sigma}d\sigma B_2 V_s \qquad (5.2) \end{aligned}$$

So we have

$$\begin{aligned} x^0(0) &= (I - e^{A_2(T-d)}e^{A_1 d})^{-1}(e^{A_2(T-d)}\int_0^d e^{A_1\sigma}d\sigma B_1 V_s \\ &\quad + \int_0^{T-d} e^{A_2\sigma}d\sigma B_2 V_s) \qquad (5.3) \end{aligned}$$

So, $x^0(0)$ is a function of A_1, A_2, B_1, B_2, T, V_s, and d. To save notation, we only express $x^0(0)$ as function of d and denote it as $X(d)$:

$$\begin{aligned} X(d) \;:=\; & (I - e^{A_2(T-d)}e^{A_1 d})^{-1}(e^{A_2(T-d)}\int_0^d e^{A_1\sigma}d\sigma B_1 V_s \\ & + \int_0^{T-d} e^{A_2\sigma}d\sigma B_2 V_s) \end{aligned} \tag{5.4}$$

Let the nominal (set-point) output voltage at the clock time be $V_{\rm SET}$, so in steady state we need to have

$$EX(d) = V_{\rm SET} \tag{5.5}$$

where, as mentioned in Chapter 3, $E = E_1$, or E_2, or $(E_1 + E_2)/2$ depending on which output voltage is of interest.

From Eqs. (5.3) and (5.5), we can express V_s as a function of d:

$$V_s(d) = \frac{V_{\rm SET}}{E(I - e^{A_2(T-d)}e^{A_1 d})^{-1}(e^{A_2(T-d)}\int_0^d e^{A_1\sigma}d\sigma B_1 + \int_0^{T-d} e^{A_2\sigma}d\sigma B_2)} \tag{5.6}$$

The meaning of this equation is: given the set-point output voltage $V_{\rm SET}$, the nominal switching instant d (or equivalently the nominal duty cycle D_c) and the source voltage should satisfy this equation.

The inverse of this function, $d(V_s)$, although it cannot be given analytically, specifies the right duty cycle, given the source voltage V_s. This function will be used in the feedforward design presented in Chapter 7.

Regarding the question of existence of a periodic solution achieving the nominal output voltage $V_{\rm SET}$, we have a result similar to Theorem 3.1.

Theorem 5.1 *Assume that all of the eigenvalues of A_1 and A_2 are in the open LHP. Given the nominal output voltage $V_{\rm SET}$, suppose*

$$(EA_2^{-1}B_2V_s + V_{\rm SET})(EA_1^{-1}B_1V_s + V_{\rm SET}) < 0 \tag{5.7}$$

Then there exists a periodic solution $x^0(t)$ in the PWM converter.

Proof:

$$X(0) = -A_2^{-1}B_2V_s \tag{5.8}$$

$$X(T) = -A_1^{-1}B_1V_s \tag{5.9}$$

From Eq. (5.5), if

$$\begin{aligned}
&(EX(0) - V_{\text{SET}})(EX(T) - V_{\text{SET}}) \\
&= (EA_2^{-1}B_2V_s + V_{\text{SET}})(EA_1^{-1}B_1V_s + V_{\text{SET}}) \\
&< 0
\end{aligned}$$

then by the intermediate value theorem, there exists a solution d satisfying Eq. (5.5). Hence there exists a periodic solution $x^0(t)$. □

When there exists a periodic solution $x^0(t)$, or equivalently a fixed point $(x^0(0), V_s, d)$, we can linearize the system at this fixed point (similar analysis has been done for the case in which A_1 and A_2 are invertible in [26]):

$$\begin{aligned}
\hat{x}_{n+1} &\approx \Phi_o\hat{x}_n + \Gamma_v\hat{v}_{sn} + \Gamma_d\hat{d}_n \\
\hat{v}_{on} &= E\hat{x}_n
\end{aligned} \tag{5.10}$$

where

$$\begin{aligned}
\Phi_o &= \left.\frac{\partial f}{\partial x_n}\right|_{(x_n,v_{sn},d_n)=(x^0(0),V_s,d)} \\
&= e^{A_2(T-d)}e^{A_1d} \qquad (5.11) \\
\Gamma_v &= \left.\frac{\partial f}{\partial v_{sn}}\right|_{(x_n,v_{sn},d_n)=(x^0(0),V_s,d)} \\
&= e^{A_2(T-d)}\int_0^d e^{A_1\sigma}d\sigma B_1 + \int_0^{T-d} e^{A_2\sigma}d\sigma B_2 \qquad (5.12) \\
\Gamma_d &= \left.\frac{\partial f}{\partial d_n}\right|_{(x_n,v_{sn},d_n)=(x^0(0),V_s,d)} \\
&= e^{A_2(T-d)}((A_1 - A_2)x^0(d) + (B_1 - B_2)V_s) \\
&= e^{A_2(T-d)}(\dot{x}^0(d^-) - \dot{x}^0(d^+)) \qquad (5.13)
\end{aligned}$$

5.2 Open-Loop Stability, Control-to-Output Transfer Function, Audio-Susceptibility, and Output Impedance

The matrix Φ_o determines the local open-loop stability. From Eq. (5.11) and Lemma 3.1, we have

Theorem 5.2 *Assume that all of the eigenvalues of at least one of A_1 and A_2 are in the open LHP, and that neither matrix has any eigenvalue in the open RHP. Then the PWM converter is locally open-loop asymptotically stable.*

This statement also implies the local stabilizability of PWM converters satisfying the stated conditions.

From the linearized dynamics (5.10), the control (d_n) to output voltage transfer function in the z-domain is

$$T_{oc}(z) = E(zI - \Phi_o)^{-1}\Gamma_d \tag{5.14}$$

In the case when v_o is discontinuous because $E_1 \neq E_2$, then this transfer function depends on which output point is chosen.

The open-loop audio-susceptibility is

$$T_{os}(z) = E(zI - \Phi_o)^{-1}\Gamma_v \tag{5.15}$$

To calculate the open-loop output impedance, we add a fictitious current source, i_o, in parallel with the load. Assume

$$S_1 : \dot{x} = A_1 x + B_1 v_s + B_{i1} i_o \tag{5.16}$$

$$S_2 : \dot{x} = A_1 x + B_2 v_s + B_{i2} i_o \tag{5.17}$$

Then the open-loop output impedance is

$$T_{oo}(z) = E(zI - \Phi_o)^{-1}\Gamma_i \tag{5.18}$$

where

$$\Gamma_i = e^{A_2(T-d)} \int_0^d e^{A_1\sigma} d\sigma B_{i1} + \int_0^{T-d} e^{A_2\sigma} d\sigma B_{i2} \tag{5.19}$$

Similar to Sec. 3.6, we can convert the pairs, (Φ_o, Γ_v) and (Φ_o, Γ_i), to the continuous-time pairs, (Φ_o^c, Γ_v^c) and (Φ_o^c, Γ_i^c). Then $E(j\omega I - \Phi_o^c)^{-1}\Gamma_v^c$ is the audio-susceptibility and $E(j\omega I - \Phi_o^c)^{-1}\Gamma_i^c$ is the output impedance.

5.3 A New Continuous-Time Model of Power Stage Derived from Sampled-Data Model

The most popular continuous-time model of the power stage of the PWM converter is the one derived from the averaging method. The averaged model is independent of the switching frequency. Here we propose a new linear time-invariant continuous-time model which is dependent of the switching frequency.

In the PWM converter, the switching instant d_n (or equivalently the duty cycle $D_{c,n} = d_n/T$) is updated in every cycle. So it is not a time-varying function like $d(t)$. The motivation to obtain a continuous-time model of the power stage is to facilitate the traditional analog control design which uses frequency response approach.

The linearized sampled-data dynamics of the power stage has been derived in Eq. (5.10). Transforming ("lifting") the sampled-data pair $(\Phi_o, [\Gamma_v, \Gamma_d])$ to the continuous-time pair $(\Phi_o^c, [\Gamma_v^c, \Gamma_d^c])$ by the techniques in Sec 2.1.3, we propose

the following continuous-time model of the power stage

$$\begin{aligned} \dot{\hat{x}} &= \Phi_o^c \hat{x} + \Gamma_v^c \hat{v}_s + \Gamma_d^c \hat{d} \\ \hat{v}_o &= E\hat{x} \end{aligned} \tag{5.20}$$

The control-to-output transfer function in the lifted dynamics (5.20) is

$$T_{oc}^c(s) = E(sI - \Phi_o^c)^{-1}\Gamma_d^c \tag{5.21}$$

5.4 Sampled-Data Modeling of the Power Stage of the PWM Converter in CCM with VFC

The output voltage of a PWM converter is determined by the duty cycle (d_n/T_n) and source voltage. In the previous sections, *fixed-frequency control* (FFC) was used and d_n was used as the control variable. Here will look at variable-frequency control (VFC) case. In VFC, T_n or both d_n and T_n can be used as the control variables to achieve the output voltage regulation.

1. Using T_n as control variable while fixing $d_n = d$, (Fig. 5.2)

This control method is called constant on-time control if S_1 is the on stage, or constant off-time control if S_1 is the off stage. The nonlinear and linearized sampled-data dynamics of the power stage are

$$\begin{aligned} x_{n+1} &= f(x_n, v_{sn}, T_n) \\ &= e^{A_2(T_n-d)}(e^{A_1 d}x_n + \int_0^d e^{A_1\sigma}d\sigma B_1 v_{sn}) + \int_0^{T_n-d} e^{A_2\sigma}d\sigma B_2 v_{sn} \\ \hat{x}_{n+1} &\approx \Phi_o \hat{x}_n + \Gamma_v \hat{v}_{sn} + \Gamma_T \hat{T}_n \end{aligned}$$

where Φ_o and Γ_v are the same as in case of the fixed-frequency control, and

$$\Gamma_T = \left.\frac{\partial f}{\partial T_n}\right|_{(x_n, v_{sn}, T_n)=(x^0(0), V_s, T)} = A_2 x^0(0) + B_2 = \dot{x}^0(0^-) \tag{5.22}$$

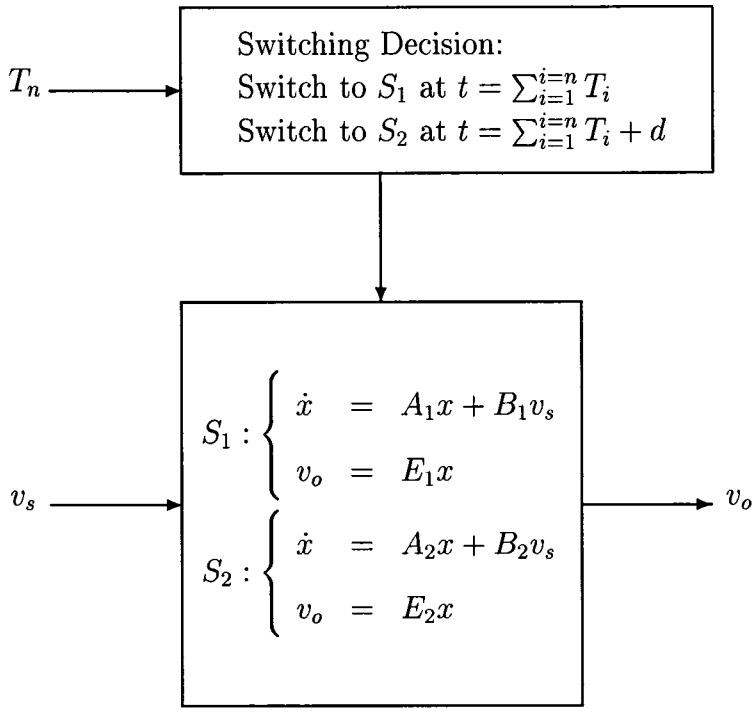

Figure 5.2: Power stage of PWM converter in CCM and VFC

2. Using d_n and T_n as control variables (Dual input control)

The sampled-data dynamics and its linearized dynamics are

$$\begin{aligned} x_{n+1} &= f(x_n, v_{sn}, d_n, T_n) \\ &= e^{A_2(T_n - d_n)}\left(e^{A_1 d_n} x_n + \int_0^{d_n} e^{A_1 \sigma} d\sigma B_1 v_{sn}\right) + \int_0^{T_n - d_n} e^{A_2 \sigma} d\sigma B_2 v_{sn} \\ \hat{x}_{n+1} &\approx \Phi_o \hat{x}_n + \Gamma_v \hat{v}_{sn} + \begin{bmatrix} \Gamma_d & \Gamma_T \end{bmatrix} \begin{bmatrix} \hat{d}_n \\ \hat{T}_n \end{bmatrix} \end{aligned}$$

The analysis of open-loop stability, audio-susceptibility, output impedance in VFC case is similar to FFC case and is omitted.

5.5 Sampled-Data Modeling of the Power Stage of the PWM Converter in DCM with FFC

In the foregoing sections, the power stage in CCM with either FFC or VFC are analyzed. In this section, the power stage in DCM with FFC will be analyzed. In DCM, there are three stages in one cycle. In the $(n+1)$-th cycle, for example, we have

$$S_1 : \dot{x} = A_1 x + B_1 v_s \quad \text{for } t \in [nT, nT + d_{1n}) \tag{5.23}$$

$$S_2 : \dot{x} = A_2 x + B_2 v_s \quad \text{for } t \in [nT + d_{1n}, nT + d_{2n}) \tag{5.24}$$

$$S_3 : \dot{x} = A_3 x + B_3 v_s \quad \text{for } t \in [nT + d_{2n}, (n+1)T) \tag{5.25}$$

The status of the switch and diode in S_1, S_2, and S_3 are on-off, off-on, and off-off respectively. In DCM with FFC, d_{1n} is used as the control variable to control the duty cycle. The system is switched from S_1 to S_2 at $t = nT + d_{1n}$. The system is switched from S_2 to S_3 at $t = nT + d_{2n}$ when the inductor current $i_L = 0$.

A general model of the power stage of a PWM converter operated in DCM and FFC is shown in Fig. 5.3, where $A_1, A_2, A_3 \in \mathbf{R}^{n\times n}$, $B_1, B_2, B_2 \in \mathbf{R}^{n\times 1}$, and $C, E_1, E_2, E_3 \in \mathbf{R}^{1\times n}$ are constant matrices, and v_s, $v_o \in \mathbf{R}$ are the source and output voltages respectively. The matrix $F \in \mathbf{R}^{1\times n}$ is chosen to have $Fx = i_L$.

Similar to CCM, the power stage in DCM has the following sampled-data dynamics:

$$\begin{aligned} x_{n+1} &= f(x_n, v_{sn}, d_{1n}, d_{2n}) \\ &= e^{A_3(T-d_{2n})}(e^{A_2(d_{2n}-d_{1n})}(e^{A_1 d_{1n}} x_n \\ &\quad + \int_0^{d_{1n}} e^{A_1(d_{1n}-\sigma)} d\sigma B_1 v_{sn}) + \int_{d_{1n}}^{d_{2n}} e^{A_2(d_{2n}-\sigma)} d\sigma B_2 v_{sn}) \end{aligned}$$

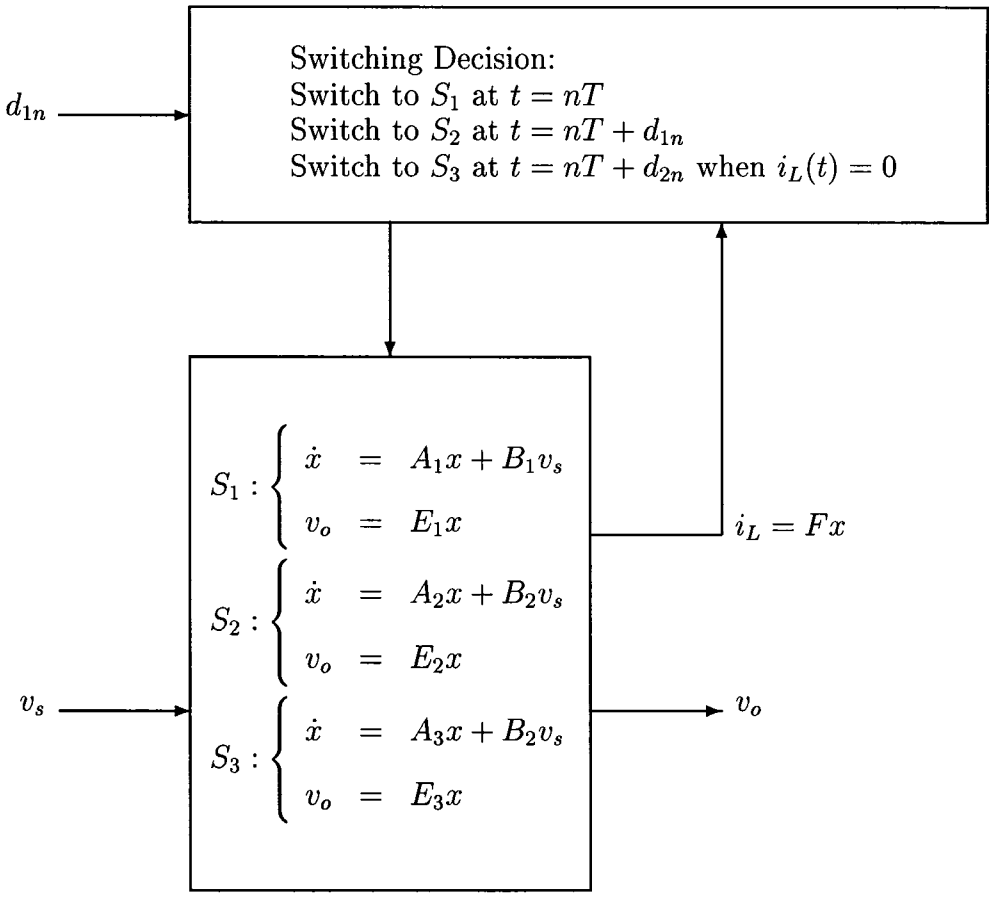

Figure 5.3: Power stage of PWM converter in DCM with FFC

$$+ \int_{d_{2n}}^{T} e^{A_3(T-\sigma)} d\sigma B_3 v_{sn} \tag{5.26}$$

$$\hat{v}_{on} = E\hat{x}_n \tag{5.27}$$

$$\begin{aligned} g(x_n, v_{sn}, d_{1n}, d_{2n}) &= Fx(nT + d_{2n}) \\ &= F(e^{A_2(d_{2n}-d_{1n})}(e^{A_1 d_{1n}} x_n + \int_0^{d_{1n}} e^{A_1\sigma} d\sigma B_1 v_{sn}) \\ &\quad + \int_0^{d_{2n}-d_{1n}} e^{A_2\sigma} d\sigma B_2 v_{sn}) \\ &= 0 \end{aligned} \tag{5.28}$$

The variable d_{2n} is constrained by Eq. (5.28) and is not a free variable. Another explicit constraint is $Fx_n = i_{Ln} = 0$, because the inductor current

always starts from 0 at the beginning of a cycle. So the dynamics is $(n-1)$-dimensional instead of n-dimensional.

Let the nominal (set-point) output voltage at the clock time be $V_{\rm SET}$, so the nominal values of $x^0(t)$, V_s, d_1, and d_2 should satisfy

$$
\begin{aligned}
x^0(d_1) &= e^{A_1 d_1} x^0(0) + \int_0^{d_1} e^{A_1 \sigma} d\sigma B_1 V_s && (5.29)\\
x^0(d_2) &= e^{A_2 (d_2 - d_1)} x^0(d_1) + \int_0^{d_2 - d_1} e^{A_2 \sigma} d\sigma B_2 V_s && (5.30)\\
x^0(0) &= x^0(T) = e^{A_3 (T - d_2)} x^0(d_2) + \int_0^{T - d_2} e^{A_3 \sigma} d\sigma B_3 V_s && (5.31)\\
E x^0(0) &= V_{\rm SET} && (5.32)\\
F x^0(d_2) &= 0 && (5.33)
\end{aligned}
$$

We have totally $(3n+2)$ equations and $(3n+2)$ unknowns ($x^0(0)$, $x^0(d_1)$, $x^0(d_2)$, d_1, d_2). Newton's method can be used to solve for these unknowns.

Once these unknowns are solved, we can linearize the dynamics around the fixed point $(x_n, v_{sn}, d_{1n}, d_{2n})$=$(x^0(0), V_s, d_1, d_2)$. Using the notation $\diamond$ to denote the evaluation at this fixed point, we have

$$
\hat{x}_{n+1} \approx \Phi_o \hat{x}_n + \Gamma_v \hat{v}_{sn} + \Gamma_d \hat{d}_{1n} \qquad (5.34)
$$

where

$$
\begin{aligned}
\Phi_o &= \frac{\partial f}{\partial x_n} - \frac{\partial f}{\partial d_{2n}} \left(\frac{\partial g}{\partial d_{2n}} \right)^{-1} \frac{\partial g}{\partial x_n} \bigg|_{\diamond} \\
&= e^{A_3 (T - d_2)} \left(I - \frac{(\dot{x}^0(d_2^-) - \dot{x}^0(d_2^+)) F}{F \dot{x}^0(d_2^-)} \right) e^{A_2 (d_2 - d_1)} e^{A_1 d_1} && (5.35)\\
\Gamma_v &= \frac{\partial f}{\partial v_{sn}} - \frac{\partial f}{\partial d_{2n}} \left(\frac{\partial g}{\partial d_{2n}} \right)^{-1} \frac{\partial g}{\partial v_{sn}} \bigg|_{\diamond} \\
&= e^{A_3 (T - d_2)} \left(e^{A_2 (d_2 - d_1)} \int_0^{d_1} e^{A_1 \sigma} d\sigma B_1 + \int_0^{d_2 - d_1} e^{A_2 \sigma} d\sigma B_2 \right) \\
&\quad + \int_0^{T - d_2} e^{A_3 \sigma} d\sigma B_3 - \frac{\dot{x}^0(d_2^-) - \dot{x}^0(d_2^+)}{F \dot{x}^0(d_2^-)} \, .
\end{aligned}
$$

$$F(e^{A_2(d_2-d_1)}\int_0^{d_1} e^{A_1\sigma}d\sigma B_1 + \int_0^{d_2-d_1} e^{A_2\sigma}d\sigma B_2) \tag{5.36}$$

$$\begin{aligned}\Gamma_d &= \frac{\partial f}{\partial d_{1n}} - \frac{\partial f}{\partial d_{2n}}(\frac{\partial g}{\partial d_{2n}})^{-1}\frac{\partial g}{\partial d_{1n}}\Big|_\diamond \\ &= e^{A_3(T-d_2)}(I - \frac{(\dot{x}^0(d_2^-) - \dot{x}^0(d_2^+))F}{F\dot{x}^0(d_2^-)})\cdot \\ &\quad e^{A_2(d_2-d_1)}(\dot{x}^0(d_1^-) - \dot{x}^0(d_1^+))\end{aligned} \tag{5.37}$$

The eigenvalues of Φ_o are the open-loop poles. Since the dynamics is $(n-1)$-dimensional, we expect the determinant of Φ_o will be 0. To show this, we have

$$\begin{aligned}\det[\Phi_o] &= \det[e^{A_2(d_2-d_1)}e^{A_1d_1}e^{A_3(T-d_2)}](1 - \frac{F(\dot{x}^0(d_2^-) - \dot{x}^0(d_2^+))}{F\dot{x}^0(d_2^-)}) \\ &= 0\end{aligned}$$

because $F\dot{x}^0(d_2^+) = \frac{d}{dt}i_L^0(d_2^+) = 0$.

The discussions for DCM case on open-loop stability, audio-susceptibility, output impedance, control-to-output transfer function and continuous-time model of the power stage are similar to those for CCM case and are omitted here.

5.6 Illustrative Examples

Example 5.1 (*Calculation of open-loop audio-susceptibility and output impedance*) In [99], the author used complicated analysis to calculate the open-loop audio-susceptibility of a boost converter and the output impedance of a buck converter. Here a simpler analysis will be shown.

The system parameters of the boost converter (Fig. 2.3) are $V_s = 15V$, $T = 25\mu s$, $D_c = 0.4$, $L = 58\mu H$, $C = 5.5\mu F$, $R_c = 0$, and $R = 18.6\Omega$. From Eq. (5.11) and (5.12), we have

$$(\Phi_o, \Gamma_v) = (\begin{bmatrix} 0.6831 & -0.1934 \\ 2.2490 & 0.5098 \end{bmatrix}, \begin{bmatrix} 0.3481 \\ 0.7047 \end{bmatrix}) \tag{5.38}$$

Convert this pair to the continuous-time pair

$$(\Phi_o^c, \Gamma_v^c) = (10^5 \begin{bmatrix} -0.0048 & -0.0984 \\ 1.1438 & -0.0929 \end{bmatrix}, 10^4 \begin{bmatrix} 1.6792 \\ 0.9187 \end{bmatrix}) \tag{5.39}$$

Then $E(jwI - \Phi_o^c)^{-1}\Gamma_v^c$ is the audio-susceptibility, shown in Fig .5.4.

The second example is that of a buck converter (Fig. 2.2). The system parameters are $f_s = 140kHz$, $D_c = 0.3$, $L = 100\mu H$, $C = 50\mu F$, $R_c = 0$,and $R = 3\Omega$. From Eqs. (5.11) and (5.19), we have

$$(\Phi_o, \Gamma_i) = (\begin{bmatrix} 0.9950 & -0.0696 \\ 0.1393 & 0.9486 \end{bmatrix}, \begin{bmatrix} -0.0050 \\ 0.1393 \end{bmatrix}) \tag{5.40}$$

Convert this pair to the continuous-time pair

$$(\Phi_o^c, \Gamma_i^c) = (10^4 \begin{bmatrix} -0.0000 & -1.0000 \\ 2.0000 & -0.6667 \end{bmatrix}, 10^4 \begin{bmatrix} -0.0000 \\ 2.0000 \end{bmatrix}) \tag{5.41}$$

Then $E(jwI - \Phi_o^c)^{-1}\Gamma_i^c$ is the output impedance, shown in Fig. 5.5.

Example 5.2 (*Sampled-data modeling of the power stage is more accurate than averaged modeling*) As mentioned at the beginning of this chapter, the traditional design of controller (error amplifier) in DC-DC converter is based on the averaged model of the power stage. We have shown in Chapter 3 that sampled-data modeling of the whole *closed-loop* system is more accurate. Here we will show that by modeling the *power stage* by sampled-data method, prediction of instability will be improved.

Take Example 3.1 for instance. We have shown that the system is unstable when $V_s = 24.527$. If the averaged model is used, it has been shown in [30] that the system is stable from $V_s = 15$ to $V_s = 40$. We will show that sampled-data modeling of the power stage provides a better prediction of instability.

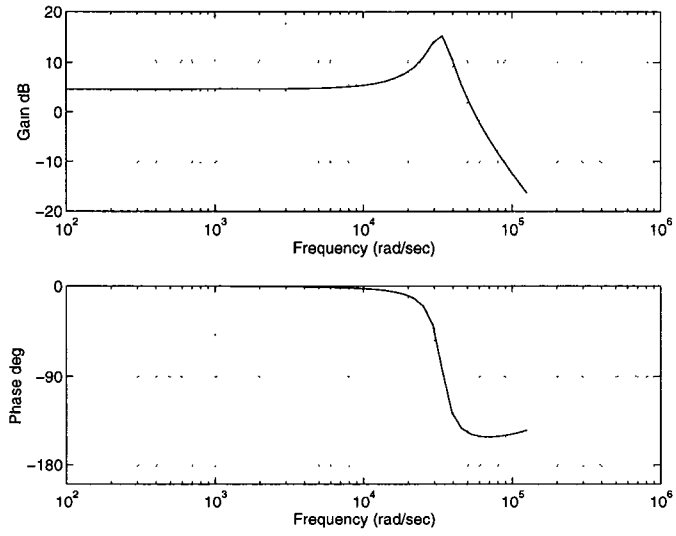

Figure 5.4: Open-loop audio-susceptibility of the boost converter in Example 5.1

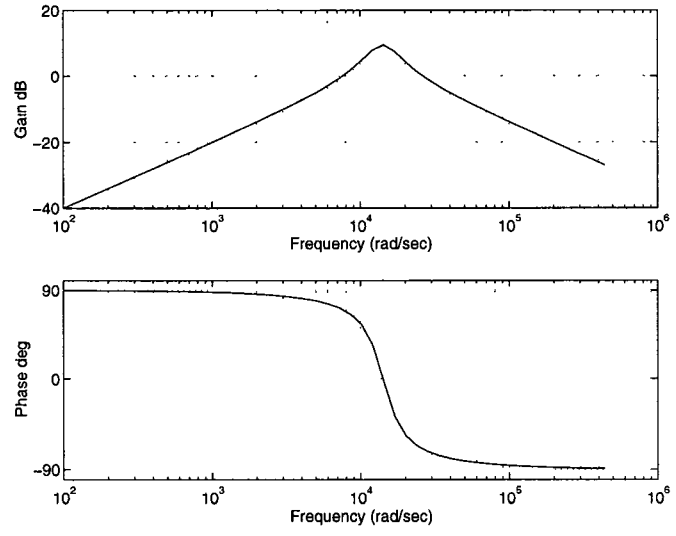

Figure 5.5: Open-loop output impedance of the buck converter in Example 5.1

We first apply the sampled-data method on the power stage to obtain the control-to-output transfer function $T_{oc}(z)$ as shown in Eq. (5.14). Then we transform this transfer function to the s-domain to obtain $T_{oc}^{c}(s)$. Letting $v_e = v_r - v_o$, then the open-loop transfer function including error amplifier and PWM modulator is

$$\frac{\hat{v}_o(s)}{\hat{v}_e(s)} = \frac{\hat{d}(s)}{\hat{v}_e(s)} \frac{\hat{v}_o(s)}{\hat{d}(s)} \tag{5.42}$$

$$= \frac{-g_1}{V_h - V_l} T_{oc}^{c}(s) \tag{5.43}$$

So basically the difference with the traditional averaging method is that here we use $T_{oc}^{c}(s)$, the continuous-time transfer function of the power stage derived from the lifted sampled-data model.

From this transfer function, we plot the Bode plot to determine stability. Following these procedures, we find out that the system is unstable for $V_s > 27.3494$. Although it is still not accurate according to the *closed-loop* sampled-data analysis in Chapter 3 (where we prove the system is unstable for $V_s > 24.527$), it has better prediction of instability than the traditional averaging method (which predicts that the system is always stable).

Take $V_s = 27.3494$, for example, we have from (5.43)

$$\frac{\hat{v}_o(s)}{\hat{v}_e(s)} = \frac{-966.8911s + 55931713.3528}{s^2 + 967.118s + 1063829.7872} \tag{5.44}$$

and the Bode plot is as shown in Fig. 5.6. Note that the phase margin is 0 degrees, so the system instability just occurs. Using the averaging method, the transfer function is obtained as [30]

$$\frac{52.2124}{9.4 \times 10^{-7} s^2 + 0.0009s + 1} \tag{5.45}$$

The corresponding Bode plot is shown in Fig. 5.7. From the figure, the phase margin is 7.5 degrees, which predicts stability.

The reason for the discrepancy is that the averaged model is a frequency independent model [51], and it works well only when the switching frequency is sufficiently high. On the other hand, the transfer function $T_{oc}^{c}(s)$ derived from the sampled-data method is frequency dependent. To confirm this, we plot the Bode plot of $\frac{\hat{v}_o(s)}{\hat{v}_e(s)}$ derived from the lifted sampled-data model for different switching frequencies and also the same transfer function derived from the averaging method when $V_s = 27.3494$ (the crossover frequency is around 7550 rad/sec). They are shown in Fig. 5.8 and Fig. 5.9 for frequency range from 10^3 to 10^5 to show the differences in detail. As the switching frequency increases, the transfer function derived from the lifted sampled-data model approaches the transfer function derived from the averaging method. For low switching frequency, the averaged model does not account for this difference in frequency and does not predict the closed-loop performances very well.

This example supports out belief that sampled-data modeling of the power stage is more accurate than modeling based on averaging. The design of the controller (error amplifier) based on this method will have better closed-loop performance.

Example 5.3 (*The effect of ESR on the output voltage ripple in the boost converter*, [42, p392]) The boost converter is shown in Fig. 2.3. The system parameters are $f_s = 100kHz$, $V_s = 10V$, $D_c = 0.8$, $R = 5\Omega$, $L = 8\mu H$, $C = 96\mu F$, and $R_c = 3.3m\Omega$.

Let the state be $x = (i_L, v_C)$. In terms of system representation in Fig. 5.1,

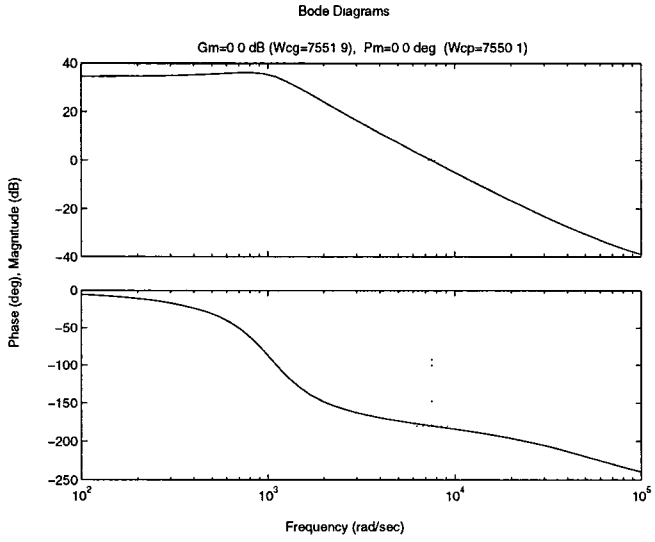

Figure 5.6: The Bode plot of the transfer function $\frac{\hat{v}_o(s)}{\hat{v}_e(s)}$ derived from lifted sampled-data model

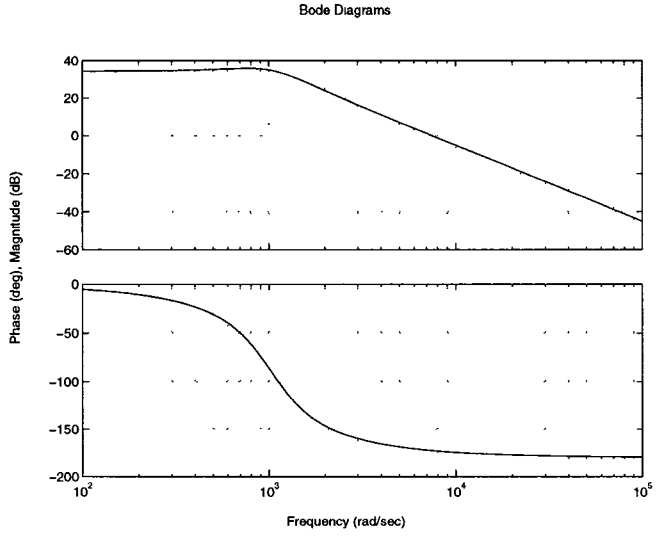

Figure 5.7: The Bode plot of the transfer function $\frac{\hat{v}_o(s)}{\hat{v}_e(s)}$ derived from averaging method

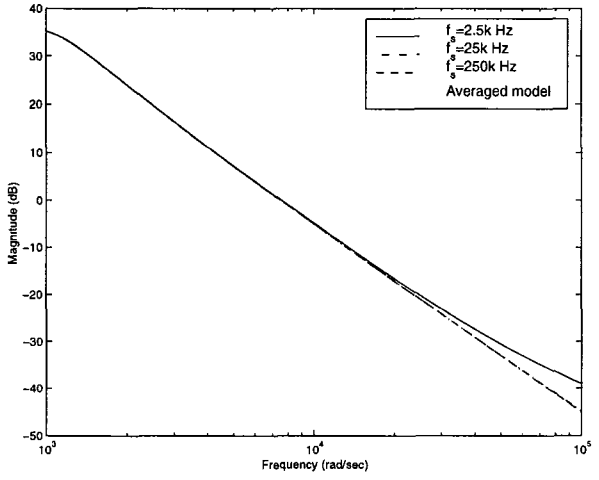

Figure 5.8: The open-loop magnitude response of $\frac{\hat{v}_o(s)}{\hat{v}_e(s)}$ derived from the lifted sampled-data model for different switching frequencies ($f_s = 2.5k, 25k$, and $250kHz$); also the same magnitude response derived from the averaging method

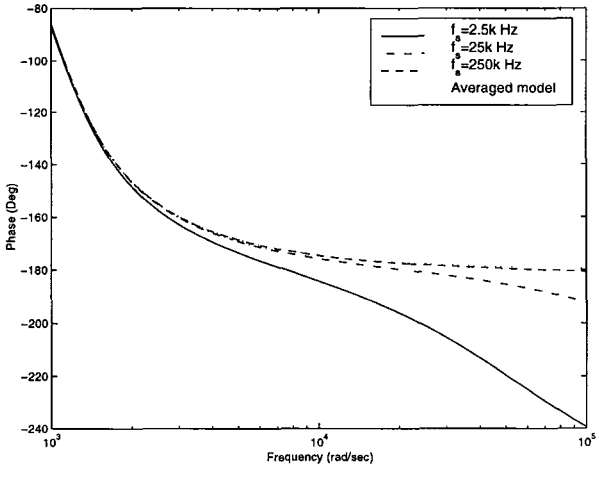

Figure 5.9: The open-loop phase response of $\frac{\hat{v}_o(s)}{\hat{v}_e(s)}$ derived from the lifted sampled-data model for different switching frequencies ($f_s = 2.5k, 25k$, and $250kHz$); also the same phase response derived from the averaging method

we have

$$A_1 = \begin{bmatrix} 0 & 0 \\ 0 & \frac{-1}{(R+R_c)C} \end{bmatrix} \tag{5.46}$$

$$A_2 = \begin{bmatrix} \frac{-RR_c}{(R+R_c)L} & \frac{-R}{(R+R_c)L} \\ \frac{R}{(R+R_c)C} & \frac{-1}{(R+R_c)C} \end{bmatrix} \tag{5.47}$$

$$B_1 = B_2 = \begin{bmatrix} \frac{1}{L} \\ 0 \end{bmatrix} \tag{5.48}$$

$$E_1 = \begin{bmatrix} 0 & \frac{R}{R+R_c} \end{bmatrix} \tag{5.49}$$

$$E_2 = \begin{bmatrix} \frac{RR_c}{R+R_c} & \frac{R}{R+R_c} \end{bmatrix} \tag{5.50}$$

Since $E_1 \neq E_2$ due to ESR, the output voltage is discontinuous.

From Eq. (5.3), we have $x^0(0) = (44.8355, 50.2646)$. The voltage jump at the clock time is $(E_2 - E_1)x^0(0) = 0.1494V$. Similar to the calculation in Eq. (3.23), the steady-state $x^0(t)$ can be calculated and is shown in Fig. 5.10.

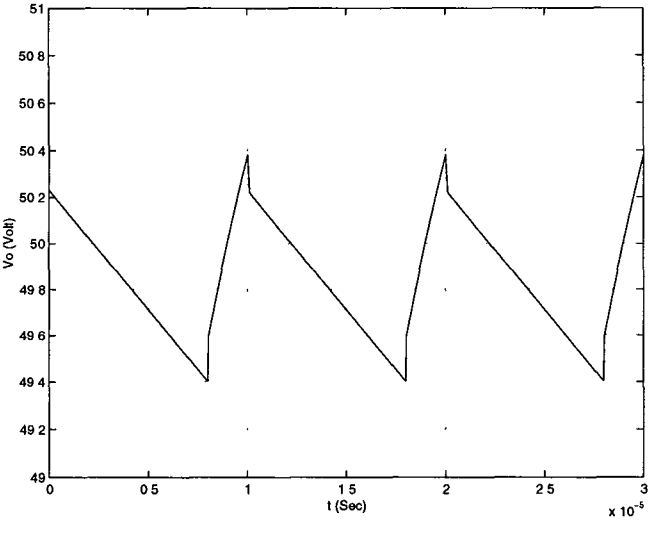

Figure 5.10: The effect of ESR on the output voltage ripple in the boost converter

5.7 Concluding Remarks

In this chapter, the power stages of the PWM converter in CCM/DCM and FFC/VFC are analyzed by the sampled-data method. Open-loop stability, audio–susceptibility and output impedance are also analyzed. A new continuous-time frequency-dependent model of the power stage is proposed.

Chapter 6

Poles and Zeros for Sampled-Data Control-to-Output Dynamics of the PWM Converter

In the preceding chapter, a sampled-data model of the power stage of a general PWM converter was derived. In this chapter, the poles and zeros of this model are determined. The results are compared with results in the literature that are based on averaged models. Some discrepancies are found and explained.

6.1 Introduction

In a continuous-time linear system, a zero in the RHP is called unstable. In the discrete-time linear system, a zero outside the unit circle is called unstable. The following statements reflect commonly held perceptions about the open-loop zeros of the averaged model in continuous-conduction mode:

1. The zeros are independent of the switching frequency [21, for example].

2. With the same duty cycle, the zeros in leading-edge modulation (LEM) and the zeros in trailing-edge modulation (TEM) are the same. (The zeros can differ in LEM and TEM if a discrete-average model [79] is used.)

3. A buck converter model without an equivalent series resistance (ESR) does not have a zero. If an ESR of value R_c is modeled, then the model has a a stable zero. The zero is at $-1/R_cC$, which is independent of the duty cycle. [64, for example]

4. The boost converter model always has an unstable zero at $V_s/(LI_L)$ [9]. If an ESR of value R_c is modeled, then an additional (stable) zero occurs at $-1/R_cC$ [63].

In this chapter, we will show that these conclusions are not valid for the sampled-data model. This deviation from the results for the averaged models is difficult to interpret because, as noted in Chapter 2, there is no simple correspondence between a continuous-time system and its sampled-data version about the zero locations and stability (minimum phase) property [2, 5].

The linearized sampled-data dynamics of the power stage has been derived in Eq. (5.10) for CCM and Eq. (5.34) for DCM. The control (d_n or d_{1n}) to output voltage transfer function in the z-domain is

$$E(zI - \Phi_o)^{-1}\Gamma_d \tag{6.1}$$

The zeros and poles are the roots of the numerator and denominator respectively of this transfer function. As mentioned in Chapter 3, the output voltage of interest in most applications is the peak, minimum, or average voltage. The matrix E here denotes E_1, E_2, or $(E_1 + E_2)/2$ depending which output voltage is of interest.

In this chapter, the zeros and poles of the buck (Fig. 2.2) and the boost (Fig. 2.3) converters in CCM or DCM will be derived. The following fact is useful for the derivations. It can be verified by the Cayley-Hamilton theorem.

Fact 6.1 *Let* $A = \kappa \begin{bmatrix} -\omega_l & -\omega_0 \\ \omega_0 & -\omega_c \end{bmatrix}$ *with* $\omega_0 > \frac{|\omega_c - \omega_l|}{2}$, *and let* $\omega = \sqrt{\omega_0^2 - (\frac{\omega_c - \omega_l}{2})^2}$.

Then

$$e^{At} = \frac{e^{\frac{-\kappa(\omega_c+\omega_l)t}{2}}}{\omega} \begin{bmatrix} (\frac{\omega_c-\omega_l}{2})\sin(\kappa\omega t) + \omega\cos(\kappa\omega t) & -\omega_0\sin(\kappa\omega t) \\ \omega_0\sin(\kappa\omega t) & (\frac{\omega_l-\omega_c}{2})\sin(\kappa\omega t) + \omega\cos(\kappa\omega t) \end{bmatrix} \tag{6.2}$$

6.2 Preliminaries about the Poles and Zeros in the CCM Case

The set of poles for the CCM case is given by

$$\sigma[\Phi_o] = \sigma[e^{A_2(T-d)}e^{A_1 d}] \tag{6.3}$$

In the two-dimensional cases (e.g., the standard buck, boost and buck-boost converter models), the transfer function (6.1) can be further simplified as

$$\begin{aligned} \frac{E(zI - \mathrm{tr}[\Phi_o]I + \Phi_o)\Gamma_d}{\det[zI - \Phi_o]} &= \frac{E(zI - \det[\Phi_o]\Phi_o^{-1})\Gamma_d}{\det[zI - \Phi_o]} \\ &= \frac{zE\Gamma_d - \det[\Phi_o]E\Phi_o^{-1}\Gamma_d}{\det[zI - \Phi_o]} \end{aligned}$$

Thus there always exists a zero (after substituting Φ_o and Γ_d from Eq. (5.11) and Eq. (5.13))

$$\begin{aligned} z_0 &= \frac{\det[\Phi_o]E\Phi_o^{-1}\Gamma_d}{E\Gamma_d} \\ &= e^{\mathrm{tr}[A_2](T-d)+\mathrm{tr}[A_1]d} \frac{Ee^{-A_1 d}((A_1 - A_2)x^0(d) + (B_1 - B_2)V_s)}{Ee^{A_2(T-d)}((A_1 - A_2)x^0(d) + (B_1 - B_2)V_s)} \end{aligned} \tag{6.4}$$

provided $Ee^{A_2(T-d)}((A_1 - A_2)x^0(d) + (B_1 - B_2)V_s) \neq 0$.

6.3 Buck Converter in CCM

For the buck converter (Fig. 2.2), the system matrices are given by

$$\begin{aligned} A_1 &= A_2 = A_{\text{ON}} \\ E &= E_{\text{ON}} \\ B_1 &= B_{\text{ON}}, \quad B_2 = 0 \quad \text{for trailing-edge modulation (TEM), while} \\ B_1 &= 0, \quad B_2 = B_{\text{ON}} \quad \text{for leading-edge modulation (LEM)} \end{aligned}$$

6.3.1 Poles of the Sampled-Data Model of Buck Converter in CCM

The set of poles of the sampled-data model of buck converter in CCM for either TEM or LEM is

$$\begin{aligned} \sigma[\Phi_o] &= \sigma[e^{A_{\text{ON}}T}] \\ &= e^{\kappa T(-\frac{\omega_c+\omega_l}{2} \pm j\omega)} \end{aligned}$$

6.3.2 Zero of the Sampled-Data Model of Buck Converter in CCM

From Eq. (6.4), the system zero for either TEM or LEM is

$$\begin{aligned} z_0 &= e^{-\kappa T(\omega_c+\omega_l)} \frac{Ee^{-A_{\text{ON}}d}B_{\text{ON}}V_s}{Ee^{A_{\text{ON}}(T-d)}B_{\text{ON}}V_s} \\ &= e^{\frac{-\kappa T(\omega_c+\omega_l)}{2}} \frac{-(\frac{\omega_c-\omega_l}{2}+\omega_e)\sin(\kappa\omega d)+\omega\cos(\kappa\omega d)}{(\frac{\omega_c-\omega_l}{2}+\omega_e)\sin(\kappa\omega(T-d))+\omega\cos(\kappa\omega(T-d))} \\ &= e^{\frac{-\kappa T(\omega_c+\omega_l)}{2}} \frac{\sin(\kappa\omega d-\theta)}{\sin(\kappa\omega(d-T)-\theta)} \end{aligned}$$

where

$$\theta = \arctan(\frac{2\omega}{\omega_c - \omega_l + 2\omega_e}) \tag{6.5}$$

Next we express the zero in terms of the duty cycle. In the case of TEM, $d = D_c T$, and we have

$$z_0 = e^{\frac{-\kappa T(\omega_c+\omega_l)}{2}} \frac{\sin(\kappa\omega T D_c - \theta)}{\sin(\kappa\omega T(D_c - 1) - \theta)} \tag{6.6}$$

In the case of LEM, $d = (1 - D_c)T$, and we have

$$z_0 = e^{\frac{-\kappa T(\omega_c+\omega_l)}{2}} \frac{\sin(\kappa\omega T(1 - D_c) - \theta)}{\sin(\kappa\omega T(-D_c) - \theta)} \tag{6.7}$$

So a the buck converter with duty cycle D^* in TEM has the same zero as the same converter with duty cycle $(1 - D^*)$ in LEM.

In the following, we focus on the TEM case. To show the effects of the duty cycle and the equivalent series resistance R_c on the location of the zero, the zero will be denoted as a function of D_c and R_c, viz. $z_0(D_c, R_c)$.

The following theorem applies to the function $z_0(D_c, R_c)$.

Theorem 6.1

(i) $z_0(0, 0) = 0$

(ii) $z_0(0.5, 0) \in (-1, 0)$

(iii) If $\kappa\omega T \in (0, \pi)$, *then* $\frac{\partial}{\partial D_c} z_0(D_c, R_c) < 0$.

Thus the zero moves to the left in the complex plane as the duty cycle increases.

(iv) If $(\kappa\omega T + \theta) \in (0, \pi/2)$ *and* $(2\omega_e + \omega_c - \omega_l) > 0$, *then*

(iv.a) $z_0(0, R_c) \in [0, 1)$

(iv.b) $z_0(D_c, R_c) < 1$

(iv.c) $z_0(D_c, R_c) \geq z_0(D_c, 0)$

(iv.d) $z_0(D_c, R_c) \in (-1, 1)$ *for* $D_c < 0.5$.

From (iv.c), the ESR results in moving the zero to the right in the complex plane. From (iv.d), a sufficient condition for the zero to be stable is $D_c < 0.5$.

(v) If $\omega_s \gg \omega_0$ *and* $2\omega_e \gg (\omega_c - \omega_l)$, *then*

$$z_0(D_c, R_c) \approx \frac{\kappa T D_c - R_c C}{\kappa T(D_c - 1) - R_c C} \tag{6.8}$$

(The approximation becomes exact as ω_s *and* ω_e *grows without bound.) Thus a sufficient condition for the zero to be stable that holds for sufficiently large* ω_s *and* ω_e *is*

$$D_c < \frac{R_c C}{\kappa T} + \frac{1}{2} \tag{6.9}$$

If $R_c = 0$, *the zero is given by the approximate formula*

$$z_0(D_c, 0) \approx \frac{D_c}{D_c - 1} \tag{6.10}$$

Proof:

(*i*) For $R_c = 0$, $\omega_e = \infty$ and $\theta = 0$. Then $z_0(0, 0) = 0$.

(*ii*) From Eq. (6.6),

$$z_0(0.5, 0) = -e^{\frac{-\kappa T(\omega_c + \omega_l)}{2}} \tag{6.11}$$

$$\in (-1, 0) \tag{6.12}$$

(*iii*) Differentiating Eq. (6.6) with respect to D_c and using a trigonometric identity to simplify the result yields

$$\frac{\partial}{\partial D_c} z_0(D_c, R_c) = -e^{\frac{-\kappa T(\omega_c + \omega_l)}{2}} \frac{\kappa\omega T \sin(\kappa\omega T)}{\sin^2(\kappa\omega T(D_c - 1) - \theta)}$$

$$< 0$$

(*iv.a*) From Eq. (6.5), if $(2\omega_e + \omega_c - \omega_l) > 0$, then $\theta \geq 0$. Now Eq. (6.6) gives

$$z_0(0, R_c) = e^{\frac{-\kappa T(\omega_c + \omega_l)}{2}} \frac{\sin(\theta)}{\sin(\kappa\omega T + \theta)}$$

$$\in [0, 1)$$

(*iv.b*) The condition in (*iv*) imply that $\kappa\omega T \in (0, \pi)$, so the conclusion of (*iii*) applies. Thus,

$$\begin{aligned} z_0(D_c, R_c) &< z_0(0, R_c) \quad (\text{from } (iii)) \\ &< 1 \quad (\text{from } (iv.a)) \end{aligned}$$

(*iv.c*) From Eq. (6.6),

$$\begin{aligned} & z_0(D_c, R_c) - z_0(D_c, 0) \\ &= e^{\frac{-\kappa T(\omega_c+\omega_l)}{2}} \left(\frac{\sin(\kappa\omega T D_c - \theta)}{\sin(\kappa\omega T(D_c-1) - \theta)} - \frac{\sin(\kappa\omega T D_c)}{\sin(\kappa\omega T(D_c-1))}\right) \\ &= e^{\frac{-\kappa T(\omega_c+\omega_l)}{2}} \frac{\cos(\kappa\omega T - \theta) - \cos(\kappa\omega T + \theta)}{2\sin(\kappa\omega T(D_c-1) - \theta)\sin(\kappa\omega T(D_c-1))} \\ &= e^{\frac{-\kappa T(\omega_c+\omega_l)}{2}} \frac{\sin(\kappa\omega T)\sin(\theta)}{\sin(\kappa\omega T(1-D_c) + \theta)\sin(\kappa\omega T(1-D_c))} \\ &\geq 0 \end{aligned}$$

(*iv.d*) For $D_c < 0.5$,

$$\begin{aligned} z_0(D_c, R_c) &> z_0(0.5, R_c) \quad (\text{from } (iii)) \\ &\geq z_0(0.5, 0) \quad (\text{from } (iv.c)) \\ &> -1 \quad (\text{from } (ii)) \end{aligned}$$

(*v*) Under the stated conditions, Eq. (6.5) implies $\theta \approx \omega/\omega_e$, and

$$\begin{aligned} z_0(D_c, R_c) &\approx \frac{\kappa\omega T D_c - \theta}{\kappa\omega T(D_c-1) - \theta} \\ &\approx \frac{\kappa\omega T D_c - \frac{\omega}{\omega_e}}{\kappa\omega T(D_c-1) - \frac{\omega}{\omega_e}} \\ &= \frac{\kappa T D_c - R_c C}{\kappa T(D_c-1) - R_c C} \end{aligned}$$

□

Summarizing, we have that the zero of the buck converter is a real number that depends on the switching frequency and the duty cycle. The quantity is always less than 1, but the zero can be unstable (if it is less than -1). The effect of the ESR is to move the zero to the right in the complex plane.

In TEM, the zero moves to the left in the complex plane as the duty cycle increases. It lies within the unit circle if the duty cycle is less than 0.5. In LEM, the zero moves to the right in the complex plane as the duty cycle increases. The zero lies within the unit circle if the duty cycle is greater than 0.5.

In the sampled-data domain, it has been shown that the buck converter can have an unstable zero. However, no experimental observation of undershoot has, to the author's knowledge, been reported for a buck converter. In a linear discrete-time system, an initial undershoot will occur if and only if the system has an odd number of real positive unstable zeros [17, 14]. Since any unstable zero of the buck converter sampled-data model will be real and negative, this explains why undershoot has never been observed in the buck converter.

6.4 Boost Converter in CCM

6.4.1 Poles of the Sampled-Data Model of Boost Converter in CCM

The set of poles of the boost converter for either TEM or LEM is

$$\begin{aligned} \sigma[\Phi_o] &= \sigma[e^{A_{\text{OFF}}T(1-D_c)}e^{A_{\text{ON}}TD_c}] \\ &:= p_0, p_0^* \end{aligned} \tag{6.13}$$

where we use the notation p_0 and p_0^*, since the system is 2-dimensional and usually the eigenvalues occur in complex conjugate pair. The poles can be calculated numerically from this equation. In the following, the poles will be estimated in compact forms.

For $\omega_s \gg \omega_0$, then $e^{A_{\rm ON}TD_c} \approx I$. From Eqs. (6.13) and (6.2), we have

$$\begin{aligned} p_0 &\approx \sigma[e^{A_{\rm OFF}T(1-D_c)}] \\ &= e^{\kappa T(1-D_c)(-\frac{\omega_c+\omega_l}{2}\pm j\omega)} \\ &:= p_{e1} \end{aligned} \tag{6.14}$$

From Eqs. (6.13) and (6.14), the estimated pole p_{e1} and the true pole p_0 are related by

$$\begin{aligned} \frac{|p_0|}{|p_{e1}|} &= \sqrt{\det[e^{A_{\rm ON}TD_c}]} \\ &= e^{\frac{-\kappa\omega_c TD_c}{2}} \\ &< 1 \end{aligned}$$

From Fig. 6.1, we can prove $|p_{e2} - p_0| < |p_{e1} - p_0|$ by geometric arguments. So a better estimate of the pole is

$$\begin{aligned} p_{e2} &= e^{\frac{-\kappa\omega_c TD_c}{2}} p_{e1} \\ &= e^{\frac{-\kappa\omega_c TD_c}{2}+\kappa T(1-D_c)(-\frac{\omega_c+\omega_l}{2}\pm j\omega)} \\ &= e^{\frac{-\kappa T\omega_c}{2}+\kappa T(1-D_c)(-\frac{\omega_l}{2}\pm j\omega)} \end{aligned}$$

which has the same magnitude as the true pole p_0.

In the following, we transform the pole p_{e2} to the continuous-time domain and compare with the traditional results. For simplicity, we only show the case $R_c = 0$ (hence $\kappa = 1$, $\omega_l = 0$). In this case, the poles in the continuous-time

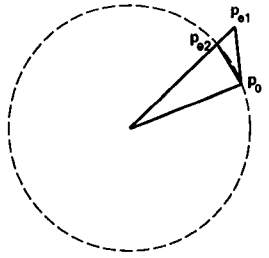

Figure 6.1: The relationship between the true pole p_0 and the estimated poles p_{e1} and p_{e2}

domain are

$$\begin{aligned} p_{e2}^c &= \frac{1}{T}\ln[p_{e2}] \\ &= -\frac{\omega_c}{2} \pm j(1-D_c)\omega \\ &= -\frac{\omega_c}{2} \pm j\sqrt{(1-D_c)^2\omega_0^2 - (1-D_c)^2\frac{\omega_c^2}{4}} \end{aligned} \tag{6.15}$$

From [21, p293], the continuous-time poles calculated from averaging method are

$$-\frac{1}{2RC} \pm j\sqrt{\frac{(1-D_c)^2}{LC} - \frac{1}{4R^2C^2}} = -\frac{\omega_c}{2} \pm j\sqrt{(1-D_c)^2\omega_0^2 - \frac{\omega_c^2}{4}} \tag{6.16}$$

The poles calculated from the sampled-data method and averaging method, Eqs. (6.15) and (6.16), are very close. Experimental work is needed to verify which one is more accurate.

6.4.2 Zero of the Sampled-Data Model of Boost Converter in CCM

Next, we derive the zero of the boost converter model (Fig. 2.3) exactly for the case $R_c = 0$, and then we get an approximate result for the zeros for the case $R_c \neq 0$.

For the case $R_c = 0$, $\omega_e = 0$ and $\kappa = 0$. From Eqs. (2.39)-(2.47), we have

$$A_{\text{ON}} = \begin{bmatrix} 0 & 0 \\ 0 & -\omega_c \end{bmatrix} \tag{6.17}$$

$$B_{\text{ON}} = \begin{bmatrix} \frac{1}{\sqrt{L}} \\ 0 \end{bmatrix} \tag{6.18}$$

$$E_{\text{ON}} = \begin{bmatrix} 0 & 1 \end{bmatrix} \tag{6.19}$$

$$A_{\text{OFF}} = \begin{bmatrix} 0 & -\omega_0 \\ \omega_0 & -\omega_c \end{bmatrix} \tag{6.20}$$

$$B_{\text{OFF}} = B_{\text{ON}} \tag{6.21}$$

$$E_{\text{OFF}} = E_{\text{ON}} \tag{6.22}$$

Since $E_{\text{ON}} = E_{\text{OFF}}$, the output voltage is continuous.

From Eq. (6.4) the zero of the boost converter model in TEM is

$$\begin{aligned} z_0 &= e^{\text{tr}[A_{\text{OFF}}](T-d)+\text{tr}[A_{\text{ON}}]d} \frac{E_{\text{ON}} e^{-A_{\text{ON}}d}(A_{\text{ON}} - A_{\text{OFF}})x^0(d)}{E_{\text{ON}} e^{A_{\text{OFF}}(T-d)}(A_{\text{ON}} - A_{\text{OFF}})x^0(d)} \\ &= \frac{e^{\frac{-\omega_c T(1-D_c)}{2}}}{\cos(\omega T(1-D_c)) - \frac{\sin(\omega T(1-D_c))}{\omega}(\frac{\omega_c}{2} + \frac{v_c(TD_c)}{Li_L(TD_c)})} \end{aligned}$$

The value of $\frac{v_c(TD_c)}{i_L(TD_c)}$ can be approximated by $(1-D_c)R$. Then for $\omega_s \gg \omega_0$,

$$z_0 \approx \frac{1}{1 - \frac{T(1-D_c)^2 R}{L}} \tag{6.23}$$

Based on this approximation, the zero is stable if $D_c < 1 - \sqrt{\frac{2L}{TR}}$ and is positive if $D_c > 1 - \sqrt{\frac{L}{TR}}$.

Similarly, the zero of the boost converter with $R_c = 0$ in LEM is

$$\begin{aligned} & e^{\frac{-\omega_c T(1-D_c)}{2}}(\cos(\omega T(1-D_c)) + \frac{\sin(\omega T(1-D_c))}{\omega}(\frac{\omega_c}{2} + \frac{v_c(T(1-D_c))}{Li_L(T(1-D_c)})) \\ & \approx 1 + \frac{T(1-D_c)^2 R}{L} \quad \text{for } \omega_s \gg \omega_0 \end{aligned} \tag{6.24}$$

which is positive and unstable.

In the case $R_c \neq 0$, the output voltage is discontinuous. We use $Ex = \frac{1}{2}(E_{\text{ON}} + E_{\text{OFF}})x$ to approximate the average output voltage. Similar to previous analysis, the zero of the boost converter with $R_c \neq 0$ in TEM is approximately

$$\frac{\frac{R_c}{2}\sqrt{\frac{C}{L}}\frac{R(1-D_c)}{L} - \omega_0}{\frac{R_c}{2}\sqrt{\frac{C}{L}}(\frac{R(1-D_c)}{L} + \omega_0^2 T(1-D_c)) + \frac{\omega_0 TR(1-D_c)^2}{L} - \omega_0} \tag{6.25}$$

and the zero of the boost converter with $R_c \neq 0$ in LEM is approximately

$$\frac{\frac{R_c}{2}\sqrt{\frac{C}{L}}\frac{R(1-D_c)}{L} - \frac{\omega_0 TR(1-D_c)^2}{L} - \omega_0}{\frac{R_c}{2}\sqrt{\frac{C}{L}}\frac{R(1-D_c)}{L} - \omega_0} \tag{6.26}$$

6.5 Buck and Boost Converters in DCM

From the discussion in Sec. 5.5, the sampled-data dynamics of the buck or boost converter in DCM is 1-dimensional. Although we express the state as x_n=($\sqrt{L}i_{L,n}$, $\sqrt{C}v_{C,n}$), the state $\sqrt{L}i_{L,n}$ is always 0. We have no zero and one pole, which corresponds to the state $v_{C,n}$. This pole is $\Phi_o(2,2)$, the component in the second column and second row of Φ_o.

The system matrices of the buck converter and boost converter are shown in Eqs. (2.30)-(2.38) and Eqs. (2.39)-(2.47) respectively. Let F=[1, 0], so $Fx_n = \sqrt{L}i_{L,n}$. As shown in Eq. (5.35), the matrix Φ_o consists of 4 parts multiplied together. The first 2 parts are the same for the buck and boost converter. They are

$$\begin{aligned} e^{A_3(T-d_2)} &= \begin{bmatrix} 1 & 0 \\ 0 & e^{-\kappa\omega_c(T-d_2)} \end{bmatrix} \\ I - \frac{(\dot{x}^0(d_2^-) - \dot{x}^0(d_2^+))F}{F\dot{x}^0(d_2^-)} &= I + \begin{bmatrix} -1 & 0 \\ \frac{\sqrt{C}(\dot{v}_C(d_2^+) - \dot{v}_C(d_2^-))}{\sqrt{L}i_L(d_2^-)} & 0 \end{bmatrix} \end{aligned} \tag{6.27}$$

$$= \begin{bmatrix} 0 & 0 \\ 0 & 1 \end{bmatrix} \tag{6.28}$$

because $\dot{v}_C(d_2^+) - \dot{v}_C(d_2^-) = -\omega_c(v_C(d_2) - v_C(d_2)) = 0$.

From Eqs. (5.35), (6.27) and (6.28), we have

$$\Phi_o(2,2) = e^{-\kappa\omega_c(T-d_2)} \cdot (\text{the (2,2) component of } e^{A_2(d_2-d_1)}e^{A_1 d_1}) \tag{6.29}$$

We will further calculate the pole, $\Phi_o(2,2)$, of the buck and boost converters in the following two subsections.

6.5.1 Pole of the sampled-data model of the Buck Converter in DCM

From Eqs. (6.29) and (6.2), the pole of the buck converter is

$$e^{-\kappa\omega_c(T-\frac{d_2}{2})}e^{-\kappa\omega_l(\frac{d_2}{2})}((\frac{\omega_l-\omega_c}{2\omega})\sin(\kappa\omega d_2) + \cos(\kappa\omega d_2)) \tag{6.30}$$

If this pole in the discrete-time domain is transformed by the function $\frac{1}{T}\ln[\cdot]$, then the pole in the continuous-time domain is

$$-\kappa\omega_c(1-\frac{d_2}{2T}) - \kappa\omega_l(\frac{d_2}{2}) + \frac{1}{T}\ln[(\frac{\omega_l-\omega_c}{2\omega})\sin(\kappa\omega d_2) + \cos(\kappa\omega d_2)] \tag{6.31}$$

6.5.2 Pole of the sampled-data model of the Boost Converter in DCM

From Eqs. (6.29) and (6.2), the pole of the boost converter is

$$e^{-\kappa\omega_c(T-\frac{d_2-d_1}{2})}e^{-\kappa\omega_l(\frac{d_2-d_1}{2})}((\frac{\omega_l-\omega_c}{2\omega})\sin(\kappa\omega(d_2-d_1)) + \cos(\kappa\omega(d_2-d_1))) \tag{6.32}$$

If this pole in the discrete-time domain is transformed by the function $\frac{1}{T}\ln[\cdot]$, then the pole in the continuous-time domain is

$$-\kappa\omega_c(1-\frac{d_2-d_1}{2T})-\kappa\omega_l(\frac{d_2-d_1}{2T})+\frac{1}{T}\ln[(\frac{\omega_l-\omega_c}{2\omega})\sin(\kappa\omega(d_2-d_1))+\cos(\kappa\omega(d_2-d_1))] \tag{6.33}$$

6.6 Illustrative Examples

Example 6.1 (*Zero of the buck converter in CCM*, [64, p326]) The power stage of the buck converter is shown in Fig. 2.2. The system parameters are $f_s = 200kHz$, $V_s = 8V$, $R = 0.2\Omega$, $L = 5\mu H$, and $C = 2mF$. Eqs. (6.6) and (6.7) are used to plot the location of the zero for TEM and LEM respectively as the duty cycle varies. The plot is shown in Fig. 6.2 for the case in which an ESR of value $R_c = 0.01\Omega$ is included. If the ESR is not included in the model (i.e.,$R_c = 0$), the location of the zero is as shown in Fig. 6.3. We can see the effect of ESR: for the same duty cycle, the zero in case $R_c \neq 0$ lies to the right in the complex plane of the zero in case $R_c = 0$.

Example 6.2 (*Zero of the boost converter in CCM*, [74]) The system parameters are $f_s = 25kHz$, $V_s = 20V$, $R = 17\Omega$, $L = 350\mu H$, $C = 660\mu F$, and $R_c = 0.075\Omega$. It is claimed in [74] that if, instead of TEM, LEM is used and if the condition

$$D_c < 1 - \frac{L}{RR_cC} \tag{6.34}$$

is satisfied, then the unstable zero of the boost converter in TEM is removed.

Let $D_c = 0.3$, which satisfies this condition. Since the output voltage is discontinuous, we use $Ex = \frac{1}{2}(E_{\text{ON}} + E_{\text{OFF}})x$ to approximate the average output voltage. From Eq. (6.4), the zero in TEM and LEM, respectively, is calculated

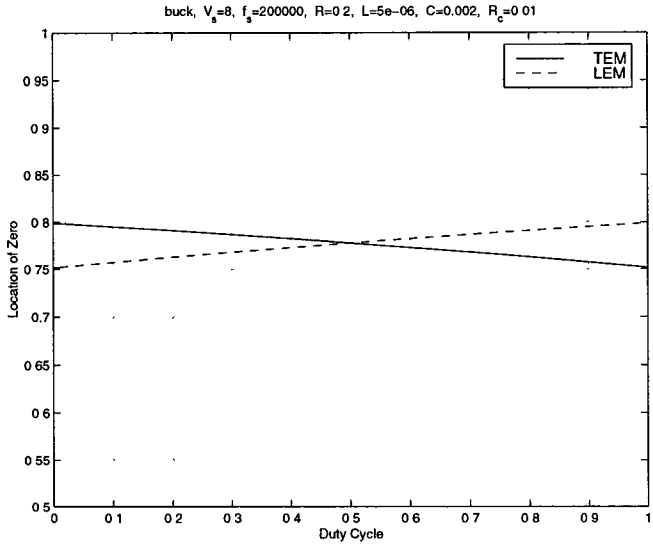

Figure 6.2: Zero of the buck converter in TEM and LEM as the duty cycle varies when $R_c = 0.01\Omega$

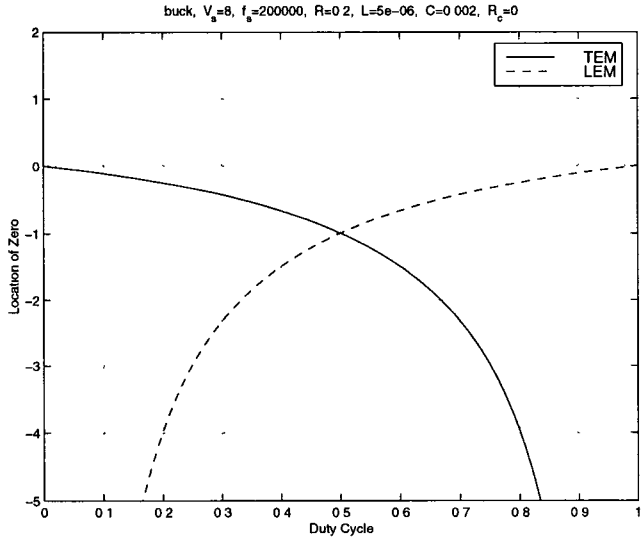

Figure 6.3: Zero of the buck converter in TEM and LEM as the duty cycle varies when $R_c = 0$

as -0.4495 and 99.4607 respectively. We therefore we expect that if there is a step increase in the duty cycle, the time response of average output voltage will not undergo undershoot in TEM, while it will in LEM. This result is the exact opposite of that in [74]. Not only can LEM not remove the unstable zero, but it also does not result in a better performance than TEM. Fig. 6.4 and Fig. 6.5 show the output voltage in TEM and LEM respectively when the duty cycle is changed from 0.3 to 0.45. In these figures, undershoot arises both in TEM and LEM. If we concentrate on the average output voltage, then it exhibits a small undershoot in LEM while it exhibits no undershoot in TEM. The undershoot of average output voltage in LEM is very small because the unstable positive zero (99.4607) is far from 1.

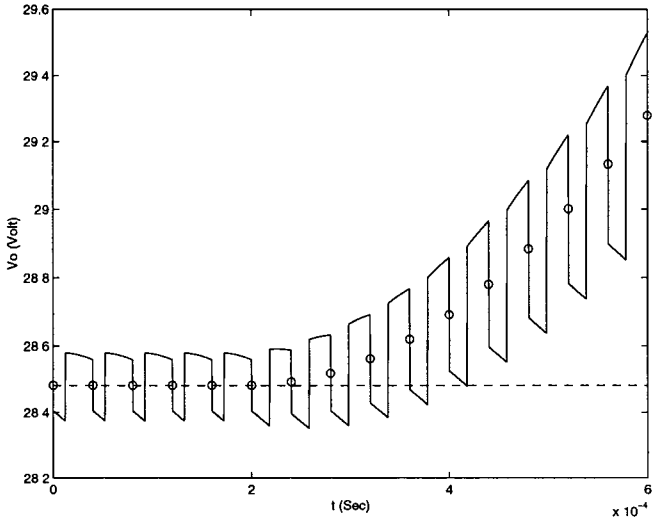

Figure 6.4: Transient output voltage response in TEM when the duty cycle is changed from 0.3 to 0.45 at $t = 2 \times 10^{-4}$

Example 6.3 (*Unstable zeros in a buck converter with input filter*, [87]) In [87], the zeros of a buck converter model with input filter were studied. The

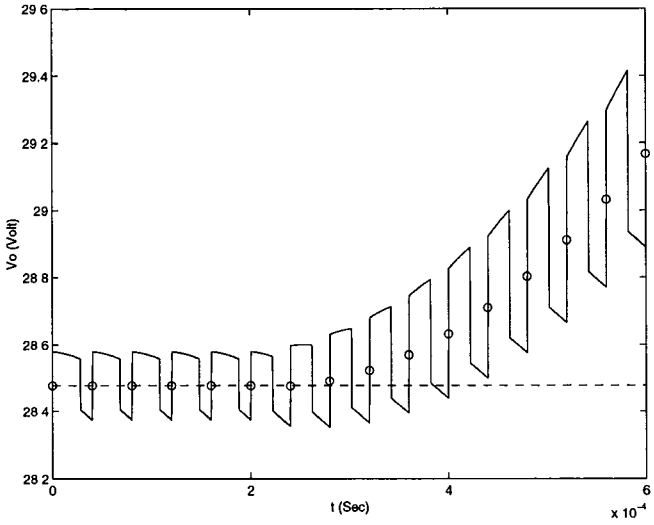

Figure 6.5: Transient output voltage response in LEM when the duty cycle is changed from 0.3 to 0.45 at $t = 2 \times 10^{-4}$

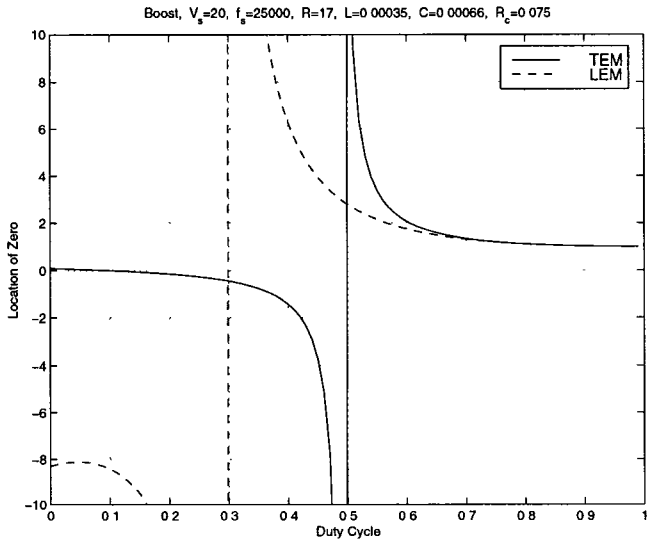

Figure 6.6: Zero location in TEM and LEM as the duty cycle varies

circuit parameters of the power stage are the same as in Example 3.5. Unstable zeros are predicted for the duty cycle greater than 0.24 by using flow-graph model [87]. Using Eq. (5.14), unstable zeros are predicted when the duty cycle is greater than 0.275.

Example 6.4 (*Boost converter in DCM*, [21, p389]) The power stage is shown in Fig. 2.3, where the system parameters are $f_s = 100kHz$, $V_s = 24V$, $R = 12\Omega$, $L = 5\mu H$, $C = 470\mu F$, $R_c = 0$ and $V_{SET} = 36V$.

Solving Eqs. (5.29)-(5.33) by Newton's method, we have $d_1 = 2.5 \times 10^{-6}$ (hence $D_c = 0.25$) and $d_2 = 7.4978 \times 10^{-6}$.

From Eq. (6.32), the pole in the discrete-time domain is 0.9929. From Eq. (6.33), the pole in the continuous-time domain is -709.6926, which agrees very well with [13, 21].

After obtaining (Φ_o, Γ_d) from Eqs. (5.35) and (5.37), we convert this pair to the continuous-time pair (Φ_o^c, Γ_d^c). Similar to Eq. (5.14), the duty-cycle-to-output frequency responses by the S and SC method are

$$T_{oc}(e^{j2\pi fT})T = E(e^{j2\pi fT}I - \Phi_o)^{-1}\Gamma_d T \tag{6.35}$$

$$T_{oc}^c(j2\pi f)T = E(j2\pi fI - \Phi_o^c)^{-1}\Gamma_d^c T \tag{6.36}$$

respectively and they are shown in Fig. 6.7 (magnitude) and Fig. 6.8 (phase). Although there is only one pole in the sampled-data modeling, the phase goes beyond -90 degree. The result from the S method agrees with [105], while the result from the SC method agrees very well with [13, 21].

We make the following remarks to resolve the issue on how many poles in a converter operating in DCM. There is only one pole and no zero in the *sampled-data* dynamics of the boost converter in DCM. Since the switching instant is a discrete-time variable, we expect the control-to-output transfer function using

the S method is more accurate than that using the SC method. The phase of the control-to-output transfer function by the S method can go beyond -90 degree, although there is only one pole. This agrees with the experimental observation in [105].

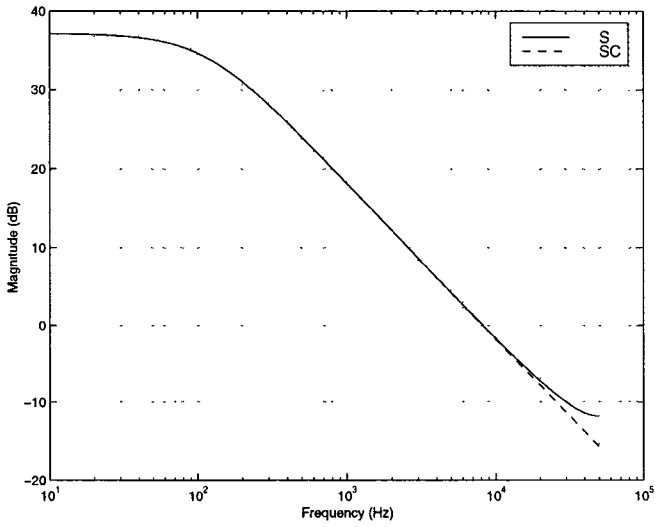

Figure 6.7: Magnitude response of duty-cycle-to-output transfer function by the S and SC method

6.7 Concluding Remarks

In the sampled-data model of the PWM converter, the open-loop zero differs from that obtained for the averaged model. The zero derived from the sampled-data model is dependent on the switching frequency and duty cycle, as well as on the modulation scheme (viz., TEM or LEM).

For the buck converter in CCM, a zero exists even if the ESR is not modeled. Inclusion of the ESR in the model results in shifting the zero to the right in

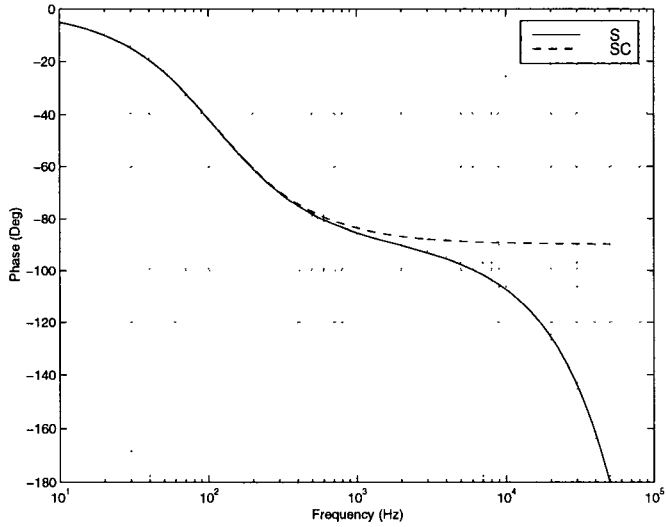

Figure 6.8: Phase response of duty-cycle-to-output transfer function by the S and SC method

the complex plane. The zero can be unstable with or without the ESR being modeled. Undershoot is not observed because the zero is less than 1.

For the boost converter in CCM, only one zero exists and this zero can be stable when the duty cycle is small. LEM does not necessarily result in better performance than TEM even if the condition (6.34) guaranteeing a stable zero is satisfied.

For the buck or boost converter in DCM, only one pole exists and there is no system zero. The phase of frequency response can go beyond -90 degree.

Chapter 7

Discrete-Time Control of PWM DC-DC Converters

In Chapter 3, we analyzed the PWM converters operated using conventional control methods (voltage or current mode control). When these traditional control methods cannot stabilize the circuits, we developed alternative stabilization schemes in Chapter 4. Sometimes the stabilized periodic orbits may not be desirable. In this chapter, we develop other control methods to achieve other objectives besides stabilization of unstable periodic orbits.

Traditional control methods for DC-DC converters are generally based on either heuristic averaging models or approximate sampled-data models. In Chapter 3, we showed that sampled-data models are more accurate. This motivates the use of discrete-time control. The discrete-time control algorithm can be implemented by digital ICs or DSP chips (e.g. the TMS320 series).

There are various control objectives depending on the applications for which the converter is used. The four main objectives are:

1. Stability

2. Fast transient dynamics

3. Good line regulation

4. Good load regulation

As mentioned in Chapter 3, stability and transient dynamics can be assessed using the closed-loop poles. The line and load regulation can be assessed using the audio-susceptibility and output impedance.

It is known that operating in fixed-frequency mode results in less EMI problems [63], so we concentrate on fixed-frequency mode. The design for variable-frequency control is similar and we will only illustrate it by an example.

The discrete-time control structure is presented in Sec. 7.1. Then we will gradually develop control methods directed toward the four objectives above in Sec. 7.2 and Sec. 7.3. These are state feedback control methods. A state observer is implemented for the case $A_1 = A_2$ in Sec. 7.4. We develop integral control with dynamic output feedback in Sec. 7.5 and Sec. 7.6, and with static output feedback in Sec. 7.7. For the case $A_1 = A_2$, we can guarantee the state of closed-loop system to be bounded and this is presented in Sec. 7.8. A new analog control design for the PWM converter is presented in Sec. 7.9. Numerous examples are given in Sec. 7.10.

Here we concentrate on switching circuits operated in continuous-conduction mode. The results can be easily extended to discontinuous-conduction mode.

There is a natural constraint that applies when using d as the control variable, because d must be between 0 and T. To implement the controller, we need to add a limiter (Eq. (3.156)) on d. Since here we emphasize the local dynamics, the limiter is not shown explicitly.

7.1 Closed-Loop Structure of Discrete-Time Control and the Controlled Output

The sampled-data block diagram model of a power stage (Fig. 5.1) and has been analyzed in Chapter 5. The implementation of discrete-time control is done by closing the feedback loop and, in some cases, feedforwarding v_s. The resulting system diagram is shown in Fig. 7.1.

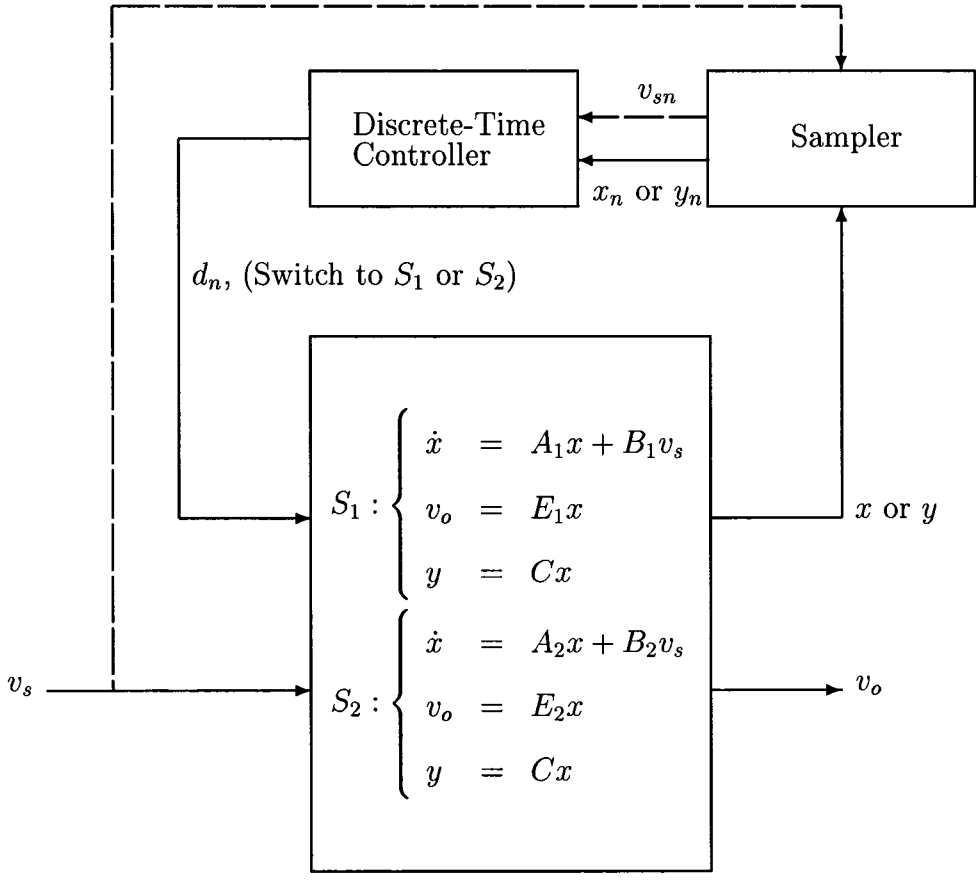

Figure 7.1: Power stage of PWM converter and digital controller

In discrete-time control, the system state or the output is sampled at the clock time, i.e., at multiples of of the switching period T. So only the clock-time

value of the state is controlled. The value could be the maximum, minimum or in-between in a cycle. For example, Fig. 4.4 shows a steady-state trajectory. In leading-edge modulation (i.e., off first in a cycle), the sampled current at the clock time is the maximum (around $0.63A$) in the cycle. In trailing-edge modulation (i.e., on first in a cycle), the sampled current is the minimum (around $0.475A$) in the cycle. In either case, the sampled voltage at the clock time is around the average value. Generally either the maximum or the average of a state is controlled depending on the requirements of the application at-hand. Sometimes it is desired that the *average* of a state is controlled, but the sampled state at the clock time is the *maximum* value (for example, the signal on the left hand side of Fig. 7.2). In this case, an *analog* low-pass filter can be applied to that state. This filter can be considered to be part of the power stage and augment its dimension. The effect of such a low-pass filter is shown in Fig. 7.2. The filter reduces the ripple, filters out the average value, and shifts the phase. When this filtered signal is sampled and fed back, the average value of the state can be controlled, at the expense of needing an additional measurement. An example of average current control will be given in Sec. 7.10.

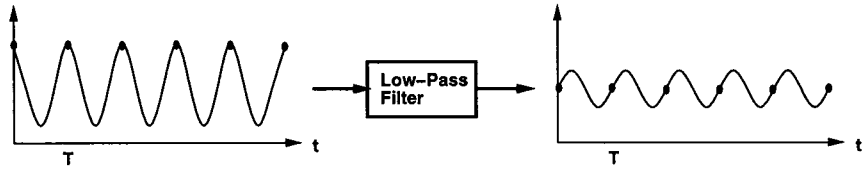

Figure 7.2: Adding a low-pass filter to reduce the ripple, filter out the average value and shift the phase

7.2 Discrete-Time State Feedback Control

Given the power stage dynamics in Eq. (5.1), we develop four control methods. The first two are good when there is little variation in source voltage and load. The next two improve the line regulation. We will further improve the load regulation in Sec. 7.3.

7.2.1 Constrained State Feedback (CSF)

The CSF is a static state feedback that does not involve explicit reference to the nominal limit cycle. The control law is

$$d_n = -Kx_n \tag{7.1}$$

where $K \in \mathbf{R}^{1\times n}$ is the feedback gain. Note that the gain K is not applied to the difference $x_n - x^0(0)$. A fixed point $(x^0(0), V_s, d)$ of the closed-loop dynamics, (5.1) and (7.1), satisfies

$$x^0(0) = f(x^0(0), V_s, d) \tag{7.2}$$

$$d = -Kx^0(0) \tag{7.3}$$

To stabilize the circuit using this method, we need to choose the feedback gain K so that

$$|\text{eig}[\Phi_o - \Gamma_d K]| < 1 \tag{7.4}$$

This relation defines an n-dimensional region in K-parameter space, while Eq. (7.3) corresponds to an $(n-1)$-dimensional hyperplane in K-parameter space. For a stabilizing gain K to exist, it is necessary and sufficient that these two geometric regions intersect. Any K lying in the intersection is a stabilizing feedback gain.

Using CSF, the linearized dynamics is

$$x_{n+1} = (\Phi_o - \Gamma_d K)x_n + \Gamma_v v_{sn} + \Gamma_i i_{on} \tag{7.5}$$

The audio-susceptibility becomes

$$T_{os}(z) = E(zI - (\Phi_o - \Gamma_d K))^{-1}\Gamma_v \tag{7.6}$$

The output impedance is

$$T_{oo}(z) = E(zI - (\Phi_o - \Gamma_d K))^{-1}\Gamma_i \tag{7.7}$$

7.2.2 Local State Feedback (LSF)

In the foregoing method, the feedback gain has constraints so that it cannot be chosen freely. To circumvent this and also to improve the transient performance, we use the following control law

$$d_n = d - K(x_n - x^0(0)) \tag{7.8}$$

where d and $x^0(0)$ are the nominal switching instant and equilibrium respectively. This controller has the same structure as that for the resonant converter in [19].

Since the nominal limit cycle is intrinsically preserved by this controller, the only constraint on K is

$$|\text{eig}[\Phi_o - \Gamma_d K]| < 1 \tag{7.9}$$

The linearized dynamics for LSF is the same as that for CSF, so the formulae for audio-susceptibility and output impedance are the same as in the CSF method.

Both CSF and LSF are designed for the nominal source voltage and load. When the line or the load changes, the output voltage deviates from the nominal

value. This motivates the two feedforward designs presented in the next two subsection, where the appropriate duty cycle is determined by feedforwarding the source voltage value. Then line regulation can be achieved.

7.2.3 Local State Feedback with Feedforward (LSFF)

The operating conditions changes as the source voltages changes. From Eq. (5.3), the nominal equilibrium $x^0(0)$ is a function of d and V_s. Denoted this equilibrium as $x_0(d, V_s)$. From the discussion in Sec. 5.1, the nominal switching instant d is also a function of the source voltage, which we denote as $d(V_s)$. So we propose the following control law:

$$\begin{aligned} d_n &= d(v_{sn}) - K(x_n - x_0(d(v_{sn}), v_{sn})) \\ &= -Kx_n + d(v_{sn}) + Kx_0(d(v_{sn}), v_{sn}) \end{aligned} \tag{7.10}$$

This is a modification of LSF that involves both a a feedback term and a feedforward term from the source voltage. This controller improves line regulation.

7.2.4 Local State Feedback with Feedforward and Washout Filter (LSFFW)

Here we propose another method to improve the line regulation. From the discussion in the foregoing subsection, the nominal switching instant d is a function $d(V_s)$ of the source voltage. As the source voltage changes, the line regulation can be improved if the switching instant is adjusted according to this function. In Sec. 4.2, the washout filter was used to preserve the original equilibrium point. Here the washout filter is used to preserve the switching instant. The washout

filter aided controller is

$$w_{n+1} = -K_1 x_n + (1 - K_2) w_n \tag{7.11}$$

$$d_n = -K_1 x_n - K_2 w_n + d(v_{sn}) \tag{7.12}$$

where $w_n \in \mathbf{R}$ is the washout state, and $K_1 \in \mathbf{R}^{1\times n}$, $K_2 \in \mathbf{R}$ are the feedback gains. This control law is designed to achieve good *line* regulation. When the switching frequency is high, the output voltage depends only on the duty cycle and source voltage, as shown in Table 2.2. Since this control law automatically adjusts the system to have the right duty cycle (or equivalently the right switching instant d), the *load* regulation is also good when the switching frequency is high.

The linearized closed-loop dynamics at the fixed point, $(x^0(0), V_s, d)$ is

$$\begin{bmatrix} \hat{x}_{n+1} \\ \hat{w}_{n+1} \end{bmatrix} \approx \begin{bmatrix} \Phi_o & 0 \\ 0 & 1 \end{bmatrix} \begin{bmatrix} \hat{x}_n \\ \hat{w}_n \end{bmatrix} + \begin{bmatrix} \Gamma_d \\ 1 \end{bmatrix} \hat{d}_n + \begin{bmatrix} \Gamma_v \\ 0 \end{bmatrix} \hat{v}_{sn} \tag{7.13}$$

To guarantee that such a controller exists, a sufficient condition is that the matrix $\begin{bmatrix} \Phi_o - I & \Gamma_d \\ 0 & 1 \end{bmatrix}$ is of full rank. The proof is similar to that in Theorem 4.3 and is omitted here.

7.3 Discrete-Time Integral Control

Integral control is commonly used to reduce steady-state errors. In DC-DC conversion, one of the main objectives is to regulate the output voltage, which motivates the use of integral control (IC) in this system.

The discrete-time integral controller proposed for the PWM converter is a

dynamic controller with input x_n and output d_n:

$$v_{n+1} = v_n + V_{\text{SET}} - Ex_n \tag{7.14}$$

$$d_n = -K_1 x_n - K_2 v_n \tag{7.15}$$

Here, $v_n \in \mathbf{R}$ is the integrator state, and $K_1 \in \mathbf{R}^{1\times n}$, $K_2 \in \mathbf{R}$ are the feedback gains.

The fixed point $(x_n, v_{sn}, d_n, v_n) = (x^0(0), V_s, d, v)$ of the system satisfies

$$x^0(0) = f(x^0(0), V_s, d) \tag{7.16}$$

$$V_{\text{SET}} = Ex \tag{7.17}$$

$$d = -K_1 x - K_2 v \tag{7.18}$$

So the controller automatically drives the output Ex to V_{SET} if the feedback gains are chosen to ensure stability.

Linearizing at the fixed point, we have

$$\begin{bmatrix} \hat{x}_{n+1} \\ \hat{v}_{n+1} \end{bmatrix} \approx \begin{bmatrix} \Phi_o & 0 \\ -E & 1 \end{bmatrix} \begin{bmatrix} \hat{x}_n \\ \hat{v}_n \end{bmatrix} + \begin{bmatrix} \Gamma_d \\ 0 \end{bmatrix} \hat{d}_n + \begin{bmatrix} \Gamma_v \\ 0 \end{bmatrix} \hat{v}_{sn} \tag{7.19}$$

Thus the audio-susceptibility is

$$T_{os}(z) = \begin{bmatrix} E & 0 \end{bmatrix} (zI - \begin{bmatrix} \Phi_o & 0 \\ -E & 1 \end{bmatrix} + \begin{bmatrix} \Gamma_d \\ 0 \end{bmatrix} \begin{bmatrix} K_1 & K_2 \end{bmatrix})^{-1} \begin{bmatrix} \Gamma_v \\ 0 \end{bmatrix} \tag{7.20}$$

The output impedance is

$$T_{oo}(z) = \begin{bmatrix} E & 0 \end{bmatrix} (zI - \begin{bmatrix} \Phi_o & 0 \\ -E & 1 \end{bmatrix} + \begin{bmatrix} \Gamma_d \\ 0 \end{bmatrix} \begin{bmatrix} K_1 & K_2 \end{bmatrix})^{-1} \begin{bmatrix} \Gamma_i \\ 0 \end{bmatrix} \tag{7.21}$$

Similar to Theorem 4.3, we have

Theorem 7.1 *Assume that all of the eigenvalues of A_1 and A_2 are in the open LHP, or one of them may have eigenvalues on the imaginary axis. If the matrix* $\begin{bmatrix} \Phi_o - I & \Gamma_d \\ E & 0 \end{bmatrix}$ *is of full rank, then the system (5.1) is asymptotically stabilizable by using discrete-time integral control.*

Proof:

It follows from Theorem 5.2 that the system (5.1) is open-loop stable. So we just need to prove that the eigenvalue at 1, which is introduced by the integral control, is controllable. By the PBH rank test [34], this is true if the matrix $\begin{bmatrix} \Phi_o - I & \Gamma_d \\ E & 0 \end{bmatrix}$ is of full rank. □

7.4 Discrete-Time State Observer Design in the Case $A_1 = A_2$

In the previous stabilizer and controller designs, we assume all of the states are measurable. The states are either voltages or currents. Generally current measurement is noiser than voltage measurement [8, page 3.153]. It is desired that only voltage is measured and fed back for compensation while maintaining the performance level achievable with full state feedback. In this section, we will demonstrate that in some types of converters we can asymptotically track the other states from the measurable states.

In [35], the authors designed a state observer from an averaged model, which is an approximate model. Here we design the state observer from the sampled-data model, which is a highly accurate model. In [62], an extra measurement of the inductor voltage is used to get the inductor current.

Some converters, like buck converters (Fig. 2.2), have been shown in Sec. 2.3 to have $A_1 = A_2 \stackrel{\text{def}}{=} A$. Then the sampled-data dynamics of the buck converter power stage is

$$\begin{aligned} x_{n+1} &= e^{AT}x_n + e^{A(T-d_n)}\int_0^{d_n} e^{A\sigma}d\sigma B_1 v_{sn} + \int_0^{T-d_n} e^{A\sigma}d\sigma B_2 v_{sn} \\ &\stackrel{\text{def}}{=} \Theta x_n + \Lambda(d_n, v_{sn}) \qquad (7.22) \\ y_n &= Cx_n \qquad (7.23) \end{aligned}$$

where $\Theta = e^{AT}$ and $y_n \in \mathbf{R}^m$ is the measured output.

7.4.1 Full-Order State Observer

We design a full-order observer with the following dynamics

$$z_{n+1} = \Theta z_n + \Lambda(d_n, v_{sn}) + G(y_n - Cz_n) \qquad (7.24)$$

where $z \in \mathbf{R}^n$ is the state of the observer and $G \in \mathbf{R}^{n\times m}$ is a feedback gain.

Letting $e_n = x_n - z_n$ be the error between the real state and the observer state, and subtracting Eq. (7.24) from Eq. (7.22), we have

$$e_{n+1} = (\Theta - GC)e_n \qquad (7.25)$$

Thus the error dynamics is linear.

Generally all of the eigenvalues of A are in open LHP, so all of the eigenvalues of $\Theta = e^{AT}$ are inside the unit circle. Thus the pair (Θ', C') is stabilizable and there exists an observer which asymptotically tracks the state in the system (7.22).

7.4.2 Reduced-Order State Observer

In the previous design, we estimate not only the unmeasured states but also the measured states, which are already available. To estimate just the unmeasured states, we can use a reduced-order state observer. To simplify the analysis, here we assume the first m states of the output are measurable, so we have $C = [I, 0]$, where I is an $m \times m$ identity matrix. Then from Eq. (7.22), we have

$$\begin{bmatrix} y_{n+1} \\ w_{n+1} \end{bmatrix} = \begin{bmatrix} \Theta_{11} & \Theta_{12} \\ \Theta_{21} & \Theta_{22} \end{bmatrix} \begin{bmatrix} y_n \\ w_n \end{bmatrix} + \begin{bmatrix} \Lambda_1(d_n, v_{sn}) \\ \Lambda_2(d_n, v_{sn}) \end{bmatrix} \tag{7.26}$$

where $y_n \in \mathbf{R}^m$ is the measured output and $w_n \in \mathbf{R}^{n-m}$ is the unmeasured state.

Here we design a reduced-order observer with the dynamics

$$z_{n+1} = (\Theta_{22} - G\Theta_{12})z_n + \Theta_{21}y_n + \Lambda_2(d_n, v_{sn}) + G(y_{n+1} - \Theta_{11}y_n - \Lambda_1(d_n, v_{sn}))$$

where $z \in \mathbf{R}^{n-m}$ is the state of the reduced-order observer and $G \in \mathbf{R}^{(n-m)\times m}$ is a feedback gain.

Letting $e_n = w_n - z_n$, we have

$$e_{n+1} = (\Theta_{22} - G\Theta_{12})e_n \tag{7.27}$$

So if the pair $(\Theta'_{22}, \Theta'_{12})$ is stabilizable, then there exists a reduced-order observer which asymptotically tracks the unmeasurable state in the system (7.22).

7.5 Output Feedback Integral Control (OFIC)

In the previous section, we constructed observers to recover unmeasurable states for some special converters. For other types of converters, we will show that given only the partial measured states we still can control the system.

We design an n-dimensional dynamic controller with output d_n and input $y_n \in \mathbf{R}^n$, v_{sn}, and also d_n. Here we assume y_n include the sampled output $v_{on} = Ex_n$. The structure of this controller is similar to an integrator plus an observer in order to achieve line/load regulation and to reduce the number of state measurements. The dynamics of the controller is

$$v_{n+1} = v_n + V_{\text{SET}} - Ex_n \tag{7.28}$$

$$z_{n+1} = \Phi_o z_n + \Gamma_d \hat{d}_n + G(y_n - Cx^0(0) - Cz_n) + \Gamma_v \hat{v}_{sn} \tag{7.29}$$

$$d_n = -K_1 z_n - K_2 v_n \tag{7.30}$$

where $v \in \mathbf{R}$ and $z_n \in \mathbf{R}^n$ are the states of the dynamic controller and $G \in \mathbf{R}^{n\times 1}$, $C \in \mathbf{R}^{1\times n}$ are constant matrices.

The fixed point $(x_n, v_{sn}, d_n, v_n, z_n) = (x^0(0), V_s, d, v, 0)$ of the closed-loop system satisfies

$$x^0(0) = f(x^0(0), V_s, d) \tag{7.31}$$

$$V_{\text{SET}} = Ex^0(0) \tag{7.32}$$

$$d = -K_2 v \tag{7.33}$$

Linearizing at this fixed point, we have

$$\begin{bmatrix} \hat{x}_{n+1} \\ \hat{v}_{n+1} \\ z_{n+1} \end{bmatrix} \approx \begin{bmatrix} \Phi_o & 0 & 0 \\ -E & 1 & 0 \\ GC & 0 & \Phi_o - GC \end{bmatrix} \begin{bmatrix} \hat{x}_n \\ \hat{v}_n \\ z_n \end{bmatrix} + \begin{bmatrix} \Gamma_d \\ 0 \\ \Gamma_d \end{bmatrix} \hat{d}_n + \begin{bmatrix} \Gamma_v \\ 0 \\ \Gamma_v \end{bmatrix} \hat{v}_{sn} \tag{7.34}$$

From the separation property [34] of controller-observer design, we can prove that the eigenvalues λ of the closed-loop linearized system satisfy

$$(\lambda I - \begin{bmatrix} \Phi_o & 0 \\ -E & 1 \end{bmatrix} + \begin{bmatrix} \Gamma_d \\ 0 \end{bmatrix} \begin{bmatrix} K_1 & K_2 \end{bmatrix})(\lambda I - \Phi_o + GC) = 0 \tag{7.35}$$

So the system is asymptotically stabilizable using the OFIC method if both of the pairs $\left(\begin{bmatrix} \Phi_o & 0 \\ -E & 1 \end{bmatrix}, \begin{bmatrix} \Gamma_d \\ 0 \end{bmatrix}\right)$ and (Φ_o', C') are stabilizable. This is generally possible because the power stage is open-loop stable and all of the eigenvalues of Φ_o are inside the unit circle.

The feedforward term $\hat{v}_{sn}$ can be omitted in this dynamic controller without affecting stability. Adding the feedforward term improves the transient performance.

7.6 Reduced-Order Output Feedback Integral Control (ROFIC)

Similar to Sec. 7.4, we can reduce the order of the dynamic controller. To simplify the analysis, here we assume the first m states of the output are measurable. So we have $C = [I, 0]$ and we can partition the state x_n into $[y_n, w_n]$, where w_n is not measured. We also partition the matrix Φ_o, Γ_d and Γ_v accordingly as $\begin{bmatrix} \Phi_{o11} & \Phi_{o12} \\ \Phi_{o21} & \Phi_{o22} \end{bmatrix}$, and $\begin{bmatrix} \Gamma_{d1} \\ \Gamma_{d2} \end{bmatrix}$ and $\begin{bmatrix} \Gamma_{v1} \\ \Gamma_{v2} \end{bmatrix}$ respectively. The $(n-m)$-dimensional dynamic controller with output d_n and input y_n, v_{sn}, and d_n is

$$
\begin{aligned}
v_{n+1} &= v_n + V_{\text{SET}} - E \begin{bmatrix} y_n \\ z_n \end{bmatrix} \\
z_{n+1} &= \Phi_{o22} z_n + \Phi_{o21} \hat{y}_n + \Gamma_{d2} \hat{d}_n \\
&\quad + G(y_{n+1} - Gx^0(0) - \Phi_{o11} \hat{y}_n - \Phi_{o12} z_n - \Gamma_{d1} \hat{d}_n) + \Gamma_{v2} \hat{v}_{sn} \\
d_n &= -K_1 \begin{bmatrix} y_n \\ z_n \end{bmatrix} - K_2 v_n
\end{aligned}
$$

Here $z_n \in \mathbf{R}^{(n-m)}$ is the state of the dynamic controller, and $G \in \mathbf{R}^{(n-m)\times m}$ is a constant matrix.

The fixed point $(x_n, v_{sn}, d_n, v_n, z_n) = (x^0(0), V_s, d, v, 0)$ of the closed-loop system satisfies

$$x^0(0) = f(x^0(0), V_s, d) \tag{7.36}$$

$$V_{\text{SET}} = Ex^0(0) \tag{7.37}$$

$$d = -K_1 \begin{bmatrix} Cx^0(0) \\ 0 \end{bmatrix} - K_2 v \tag{7.38}$$

Similar to the OFIC method, we can prove the eigenvalue λ of the linearized closed-loop system satisfies

$$(\lambda I - \begin{bmatrix} \Phi_o & 0 \\ -E & 1 \end{bmatrix} + \begin{bmatrix} \Gamma_d \\ 0 \end{bmatrix} \begin{bmatrix} K_1 & K_2 \end{bmatrix})(\lambda I - \Phi_{o22} + G\Phi_{o12}) = 0 \tag{7.39}$$

7.7 Design of Output Feedback Integral Control by Root-Locus Method

The proposed control law abbreviated as OFICR is:

$$v_{n+1} = v_n + V_{\text{SET}} - Ex_n \tag{7.40}$$

$$d_n = K_p(V_{\text{SET}} - Ex_n) + K_i v_n \tag{7.41}$$

where K_p, $K_i \in \mathbf{R}$. This controller is equivalent to a discrete-time PI controller, which would have transfer function $K_p + \frac{K_i}{z-1}$.

This controller introduces an open-loop zero at

$$z_0 = 1 - \frac{K_i}{K_p} \tag{7.42}$$

This zero is generally chosen to be close to 1 [44], which is the pole introduced by the integrator. After the zero is chosen, we have only one degree of freedom to choose the feedback gains. We can use the root-locus method to determine K_p. Then from Eq. (7.42), we have $K_i = K_p(1 - z_0)$.

7.8 Boundedness of the Closed-Loop State Trajectory in the Case $A_1 = A_2$

In the previous sections, we designed control laws to locally stabilize the periodic solution. Here we will show that these control laws also ensure boundedness of the state trajectories in the case $A_1 = A_2 \stackrel{\text{def}}{=} A$.

A dynamics of a general controlled converter with $A_1 = A_2$ has the following basic form:

$$\begin{aligned} \xi_{n+1} &= f(\xi_n, d_n) \\ &= \Omega\xi_n + \Psi_1 d_n + \Psi_2(d_n) \qquad (7.43) \\ \hat{d}_n &= -K\hat{\xi}_n \qquad (7.44) \end{aligned}$$

Here $\xi_n \in \mathbf{R}^p$ is the system state, $\Omega \in \mathbf{R}^{p\times p}$, $\Psi_1 \in \mathbf{R}^{p\times 1}$ $K \in \mathbf{R}^{1\times p}$ are constant matrices, and $\Psi_2(\cdot) : \mathbf{R} \to \mathbf{R}^{p\times 1}$ is a nonlinear function.

For example, in a PWM converter with integral control, we have $p = n + 1$, $\xi_n = (x_n, v_n)'$, $\Omega = \begin{bmatrix} \Phi_o & 0 \\ -E & 1 \end{bmatrix}$, $\Psi_1 = \begin{bmatrix} \Gamma_d \\ 0 \end{bmatrix}$ and $K = [K_1, K_2]$.

Denote the fixed point of the system by (ξ^0, d). Then

$$\xi^0 = \Omega\xi^0 + \Psi_1 d + \Psi_2(d) \qquad (7.45)$$

Subtracting this equation from Eq. (7.43), we have

$$\begin{aligned}\hat{\xi}_{n+1} &= \xi_{n+1} - \xi^0 \\ &= (\Omega - \Psi_1 K)\hat{\xi}_n + (\Psi_2(d_n) - \Psi_2(d))\end{aligned}$$

When (Ω, Ψ_1) is stabilizable, we can find a feedback gain K such that the eigenvalues of $\Omega - \Psi_1 K$ are inside the unit circle. From matrix theory, there exists a matrix norm $\| \ \|$ such that $\|\Omega - \Psi_1 K\| < 1$. Since the function Ψ_2 is continuous and d_n is in the compact set $[0, T]$, the function $\| \ \Psi_2(d_n) - \Psi_2(d) \ \|$ attains its maximum. Let Ψ_{max} denote this maximum. Then

$$\begin{aligned}\| \ \hat{\xi}_{n+1} \ \| &\leq \| \ \Omega - \Psi_1 K \ \| \| \ \hat{\xi}_n \ \| + \Psi_{max} \\ &< \| \ \hat{\xi}_n \ \|\end{aligned}$$

provided $\| \ \hat{\xi}_n \ \| > \frac{\Psi_{max}}{1 - \|\Omega - \Psi_1 K\|} \stackrel{\text{def}}{=} r^*$.

So the dynamics (7.43) is a contraction mapping. For initial states outside the region $\{\xi : \| \ \xi - \xi^0 \ \| < r^*\}$, the state trajectory will move into this region as time goes to infinity, thus boundedness is proved.

7.9 New Analog Control Design by a State-Space Approach

Most DC-DC converter controllers used in practice are analog controllers designed using averaged models and frequency response methods. In order to guarantee good performance of the closed-loop system, large gain margins and phase margins are needed.

Here we propose a new approach to design an analog controller, where good closed-loop performance can be guaranteed. Without loss of generality, we use

a buck converter in leading-edge design as an example to demonstrate this approach. The system diagram is shown in Fig. 7.3, where a filter $1/(s+p_f)$ is used to approximate an integrator to achieve line and load regulation.

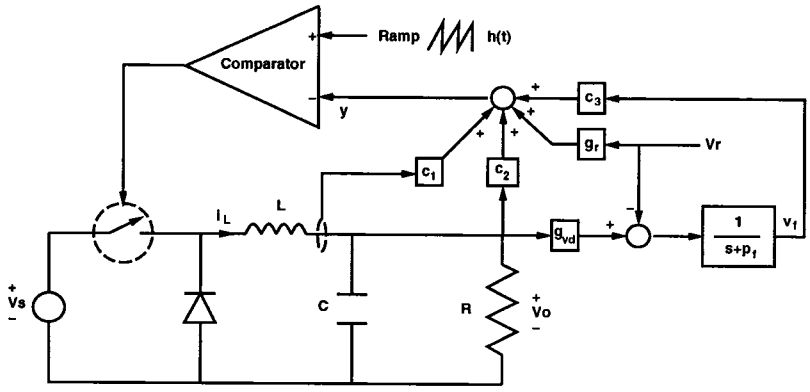

Figure 7.3: The system diagram of a buck converter with analog control

Let the state be $x = (i_L, v_C, v_f)$, where v_f is the state of the integrating filter. In terms of the representation in Fig. 3.1, we have

$$A_1 = A_2 = \begin{bmatrix} 0 & \frac{-1}{L} & 0 \\ \frac{1}{C} & \frac{-1}{RC} & 0 \\ 0 & g_{vd} & 0 \end{bmatrix} \tag{7.46}$$

$$B_1 = \begin{bmatrix} 0 & 0 \\ 0 & 0 \\ 0 & -1 \end{bmatrix} \tag{7.47}$$

$$B_2 = \begin{bmatrix} \frac{1}{L} & 0 \\ 0 & 0 \\ 0 & -1 \end{bmatrix} \tag{7.48}$$

$$C = \begin{bmatrix} c_1 & c_2 & c_3 \end{bmatrix} \tag{7.49}$$

$$D = \begin{bmatrix} 0 & g_r \end{bmatrix} \tag{7.50}$$

$$E_1 = E_2 = \begin{bmatrix} 0 & 1 & 0 \end{bmatrix} \tag{7.51}$$

Following the same procedures in Sec. 4.4, we can find matrices C and D to result in a stable system.

7.10 Illustrative Examples

We use the *power stage* of the buck converter in [31] as a benchmark example. The control methods proposed in this chapter will be illustrated in Examples 7.1-7.12. Then we will take another circuit to compare other control methods from the literature with the IC method. This will be illustrated in Example 7.13.

The circuit in this benchmark example is shown in Fig. 2.2. The system parameters are $T = 400\mu s$, $L = 20mH$, $C = 47\mu F$, $R = 22\Omega$, $R_c = 0$ and $V_s = 20V$. Here our concern is controller design, although the switching frequency is low. We choose S_1 as the off stage and S_2 as the on stage (as in the case of leading-edge design). The nominal duty cycle is 0.7, which corresponds to $d = 0.00012s$. For this duty cycle, the nominal output voltage is $14.026V$.

Example 7.1 (*Open-loop control*) For later comparison, we first show a buck converter with open-loop control, where the switch is turned on and off at a fixed duty cycle 0.7. Calculating the eigenvalues of Φ_o, we obtain the open-loop poles $0.7700 \pm 0.2937i$, so we expect the dynamics to be slow.

Fig. 7.4 shows the output voltage response during start-up.

Fig. 7.5 shows the normalized audio-susceptibility. The normalizing factor is V_s/V_o. Based on this figure we would expect an unsatisfactory output response when the source voltage undergoes a step change. We can estimate this effect by examining at the figure. For example, when there is a 25% change of source

voltage, we expect a $25\% \times 0\text{dB} = 25\%$ change in the output voltage.

Fig. 7.6 shows the normalized output impedance. The normalizing factor is $1/R$. From this figure we expect a good output response when the load is changed suddenly. The reason why load regulation is good is that the ratio $\omega_0/\omega_s = 0.0657$ is low (i.e., the relative switching frequency is high). Then from Table 2.2, the output voltage depends on the duty cycle and the source voltage only, but not on the load.

Fig. 7.7 shows the output voltage response when the source voltage changes to $25V$ (a 25% variation from the nominal source voltage). We can see that the change of the output voltage is very close to the value predicted by the approximation above, $14 \times 25\% = 3.5V$.

Fig. 7.8 shows the output voltage response when the load jumps to 16.5Ω (a 25% variation from the nominal load). There is little change of steady-state output voltage, which would be expected from the plot of the output impedance.

We can see that with open-loop control the dynamics is slow and the steady-state output voltage changes subject to the disturbances on the source voltage (and sometimes also the load).

Example 7.2 (*Constrained State Feedback*, CSF) To find the feedback gain K, we plot the constraints (7.3) and (7.4) in K-parameter space (Fig. 7.9). In Fig. 7.9, the straight line corresponds to Eq. (7.3) and the triangular region corresponds to Eq. (7.4). These two constraints intersect, so the circuit is stabilizable. Here we choose $K = (0, -8.555 \times 10^{-6})$ to implement only voltage feedback. We have $\text{eig}[\Phi_o - K\Gamma_d] = 0.748 \pm 0.368i$, so the expected settling time is long.

Fig. 7.10 shows the output voltage response during start-up.

Fig. 7.11 shows the normalized audio-susceptibility. From this figure we expect an unsatisfactory output response when the source voltage changes. We can estimate this by looking at the figure. For example, for a 25% jump in source voltage, we would expect a $25\% \times (-3)\text{dB} = 17.7\%$ change in the output voltage.

Fig. 7.12 shows the normalized output impedance. From this figure we expect a good output response when the load changes.

Fig. 7.13 shows the output voltage response when the source voltage changes to $25V$. We can see that the change of the output voltage is very close to the predicted value, $14 \times 17.7\% = 2.48V$.

Fig. 7.14 shows the output voltage response when the load changes to 16.5Ω. There is little change of steady-state output voltage, which is to be expected from the plot of the output impedance.

Example 7.3 (*Local State Feedback*, LSF) In this case, the system is controllable, so we can freely assign the eigenvalues, here we choose all of the eigenvalues at the origin. Using Ackermann's formula [34], we get $K = (-0.0012, -0.00007343)$.

Fig. 7.15 shows the output voltage response during start-up. As expected, the settling time is less than with the CSF method, because we assign the eigenvalues of the closed-loop system at the origin.

Fig. 7.16 shows the output voltage response when the source voltage changes to $25V$. As expected, the change of the output voltage is less than with the CSF method.

Fig. 7.17 shows the output voltage response when the load changes to 16.5Ω. The load regulation is unsatisfactory.

To check boundedness of the state trajectory by this control method, we have $\Psi_{max} = 0.6827$, $\|\Omega - \Psi_1 K\|_2 = 0.7296$ and $r^* = 2.5253$. So those initial states

whose distance (in Euclidean norm) to the fixed point $x^0(0) = (0.6785, 14.0263)$ is greater than r^* will eventually enter the region $\{x : \|x - x^0(0)\|_2 < r^*\}$ and the state trajectory is bounded.

Example 7.4 (*Local State Feedback with Feedforward*, LSFF) The feedback gain is the same as in Example 7.2, $K = (-0.0012, -0.00007343)$. The feedforward term is changed according to the nonlinear function $d(V_s)$, which can be obtained from Eq. (5.6).

Fig. 7.18 shows the output voltage response when the source voltage jumps to $25V$. As expected, the line regulation is better than with the LSF method in Example 7.3.

Example 7.5 (*Local State Feedback with Feedforward and Washout Filter*, LSFFW) We choose the eigenvalues of the closed-loop system at 0.5, 0.2 and 0.2. We have $K_1 = (0.0011, -0.000081)$ and $K_2 = 2.3$.

Fig. 7.19 shows the output voltage response during start-up.

Fig. 7.20 shows the output voltage response when the source voltage changes to $25V$. The line regulation is very good.

Fig. 7.21 shows the output voltage response when the load changes to 16.5Ω. The load regulation is also good.

Example 7.6 (*Integral Control*, IC) Since the pair $\left(\begin{bmatrix} \Phi_o & 0 \\ -E & 1 \end{bmatrix}, \begin{bmatrix} \Gamma_d \\ 0 \end{bmatrix}\right)$ is controllable, we can freely assign the eigenvalues. The magnitude of the control signal depends on the distance between the closed-loop poles and the open-loop poles [34], which are $0.77 \pm 0.2937i$ and 1. To prevent the control signal from being too large, here we assign the eigenvalues all at 0.3 and we have $K_1 = (-0.00113, -0.0001078)$ and $K_2 = 0.000491$.

Fig. 7.22 shows the output voltage response during start-up.

Fig. 7.23 shows the output voltage response when the source voltage changes to $25V$. As expected, the integral controller reacts promptly and the line regulation is very good.

Fig. 7.24 shows the output voltage response when the load changes to 16.5Ω. Again as expected, the load regulation is very good.

To show how much this method improves over open-loop control, we compare the audio-susceptibility and output impedance of this method with those in open-loop control in Fig. 7.25 and Fig. 7.26 respectively. The frequency response is obtained by the SC method.

Example 7.7 (*Constant current supply: peak inductor current, average inductor current, or peak load current regulations using the IC method*) Typical applications of constant current supplies are in battery charging [92], power factor correcting circuits [92], electron microscopes [9] and gas spectrometry [9]. Similar to the regulation of the output voltage by the IC method, we can use the same method to regulate either the inductor current or the load current. Suppose the peak inductor current is desired to be regulated at $0.7A$, so we set $V_{\text{SET}} = 0.7$. The inductor current is measured and compared with V_{SET}. Here we choose $K_1 = (-0.002, 4.9 \times 10^{-5})$, $K_2 = 0.0011$ and assign the eigenvalues at 0.2, 0.2 and 0.5. We regulate maximum inductor current in *steady state*. This differs from the traditional current mode control, where the maximum inductor current is *always* below the prescribed limit.

Fig. 7.27 shows the inductor current response during start-up. The peak inductor current is regulated at $0.7A$.

Fig. 7.28 shows the inductor current response when the source voltage changes to $25V$. Fig. 7.29 shows the inductor current response when the load changes to

16.5Ω. Under the line or load disturbances, the peak inductor current is always regulated at $0.7A$.

Average current can be controlled by adding a low-pass filter (as indicated in Sec. 7.1). The system diagram is shown in Fig. 7.30. A simple analog low-pass filter, $\frac{1000}{s+1000}$, is added to filter the signal of the inductor current. This filter augments the dimension of the power stage from 2 to 3. Then the states (inductor current, capacitor voltage, and filter state) are sampled and the IC method is applied. The feedback gains are $K_1 = (-0.00102, -0.000029, -0.00105)$ and $K_2 = 0.0007247$, which assign the closed-loop poles at 0.4, 0.4, 0.3 and 0.7.

Fig. 7.31 shows the inductor current response during start-up. The average inductor current is regulated at $0.7A$.

Fig. 7.32 shows the inductor current response when the source voltage changes to $25V$. Fig. 7.33 shows the inductor current response when the load changes to 16.5Ω. Under the line or load disturbances, the average inductor current is always regulated at $0.7A$.

If the load current is available, then we can use the IC method to regulate it. Here the load current is measured and compared with $V_{\text{SET}} = 0.7$. We assign the closed-loop eigenvalues at 0.2, 0.2, and 0.5. We have $K_1 = (-0.0011, -0.0001)$ and $K_2 = 0.001$.

Fig. 7.34 shows the load current response when the source voltage changes to $25V$.

Fig. 7.35 shows the load current response when the load changes to 16.5Ω.

Example 7.8 (*Output Feedback Integral Control*, OFIC) The system diagram is shown in Fig. 7.36. Here we measure only the output voltage and the source voltage, and input these information to a sampler and the dynamic

controller. The dimension of the dynamic controller is 3. We choose $K_1 = (-1.06 \times 10^{-3}, -8.16 \times 10^{-5})$, $K_2 = 3.61 \times 10^{-5}$, and $G = (0.0833, 1.34)$ to place the eigenvalues of the closed-loop system at 0.4, 0.4, 0.3, 0.1 and 0.1.

Fig. 7.37 shows the output voltage response during start-up. The settling time is long because the eigenvalues are away from the origin.

Fig. 7.38 shows the output voltage response when the source voltage changes to $25V$. Without the feedforward term from the source voltage, we still can regulate the output voltage and expect longer settling time as shown in Fig. 7.39.

Fig. 7.40 shows the output voltage response when the load changes to 16.5Ω.

Example 7.9 (*Reduced-Order Output Feedback Integral Control*, ROFIC) As in the previous example, we measure the output voltage and the source voltage. The dimension of the dynamic controller is now reduced to 2. Here we choose $K_1 = (-1.06 \times 10^{-3}, -8.16 \times 10^{-5})$, $K_2 = 3.61 \times 10^{-5}$, and $G = 0.135$ to place the eigenvalues of the closed-loop system at 0.4, 0.4, 0.3, and 0.

Fig. 7.41 shows the output voltage response during start-up. The settling time is shorter than with the OFIC method.

Fig. 7.42 shows the output voltage response when the source voltage changes to $25V$. Without the feedforward term from the source voltage, we still can regulate the output voltage and expect a longer settling time, as shown in Fig. 7.43.

Fig. 7.44 shows the output voltage response when the load changes to 16.5Ω.

Example 7.10 (*Design of Output Feedback Integral Control by Root-Locus Method*, OFICR) As in the previous example, we measure the output voltage, compare it with the reference voltage, and input the error signal into the PI controller. We choose the zero of the controller at 0.8. Using the root-locus method, we choose $K_p = -1.084 \times 10^{-5}$ and this corresponds to an integrator

gain $K_i = -2.17 \times 10^{-6}$.

Fig. 7.45 shows the output voltage response during start-up. The settling time is long because the closed-loop poles are far from the origin.

Fig. 7.46 shows the output voltage response when the source voltage changes to $25V$.

Fig. 7.47 shows the output voltage response when the load changes to 16.5Ω.

Example 7.11 (*The IC method with constant-off time control*) Here we keep $d = 0.00012s$ and use T_n as the control variable. Fig. 7.48 shows the output voltage response during start-up. Fig. 7.49 shows the output voltage response when the source voltage changes to $25V$. Fig. 7.50 shows the output voltage response when the load changes to 16.5Ω.

Example 7.12 (*Analog control*) The system diagram is shown in Fig. 7.3, where $V_r = 5V$ and $g_{vd} = 5/14$. We choose $p_f = 1$ so that the filter approximates an integrator. Here we need to design the values of $C = (c_1, c_2, c_3)$ and g_r. Let all of the closed-loop eigenvalues be at 0.6. Following the procedures in Sec. 4.4, we have $C = (1.33 \times 10^{-2}, 2.11 \times 10^{-4}, 1.2534)$ and $g_r = -1.93$.

Fig. 7.51 shows the output voltage response during start-up. One thing interesting about this control design is how the signals $y(t)$ and $h(t)$ intersects to adjust the duty cycle. The signals $y(t)$ and $h(t)$ in steady state are shown in Fig. 7.52. The output signal $y(t)$ is almost a straight line here, different from the sinusoidal waveform of output signal in the traditional PWM controller. Fig. 7.53 shows the output voltage response when the source voltage changes to $25V$. Fig. 7.54 shows the output voltage response when the load changes to 16.5Ω.

Example 7.13 (*The IC method compared with other control methods*) Here

we take the example from [53], where the authors compare the performances of μ-based control and classical optimal control [75]. The system parameters are $f_s = 40kHz$, $C = 330\mu F$, $L = 476\mu H$, ESR $R_c = 0.8\Omega$, $V_s = 15V$, and desirable output voltage $V_o = 5V$.

Here we use the IC method and assign the eigenvalues at 0.78, 0.78 and 0.8 for the system when $R = 5\Omega$. We have $K_1 = (-1.757, -6.097) \times 10^{-5}$ and $K_2 = 4.82 \times 10^{-6}$. Those different operating conditions in [53] ($R = 2.5\Omega$, 5Ω and 10Ω) are simulated in Fig. 7.55, Fig. 7.56, and Fig. 7.57 respectively. We can see that the peaking is only $14mV$ and the settling time is $1ms$. The performance is better than that under μ-based control (peaking, $20mV$; settling time, $3ms$) and that under classical optimal control (peaking, $50mV$; settling time, $4ms$).

7.11 Concluding Remarks

In this chapter, both discrete-time and analog control methods for PWM converters have been developed. We summarize the relative performance of these methods in Table 7.1, where general tendencies are given. Each control method achieves different control objectives. The performance of the CSF or LSF method is satisfactory when there is no variation in load and line. LSFF or LSFFW can achieve good line regulation. All the integral control methods have very good line and load regulations.

For the buck converter, we have shown how to estimate the unobservable states. We have also shown that these control methods have some global properties that we can guarantee that the state trajectories of the controlled system are bounded.

	Stability	Transient Performance	Line Regulation	Load Regulation
CSF	Yes	Fair	No	No
LSF	Yes	Good	No	No
LSFF	Yes	Good	Yes	No
LSFFW	Yes	Good	Yes	Fair
IC	Yes	Good	Yes	Yes
IC +observer	Yes	Good	Yes	Yes
OFIC	Yes	Fair	Yes	Yes
ROFIC	Yes	Fair	Yes	Yes
OFICR	Yes	Fair	Yes	Yes
Analog	Yes	Fair	Yes	Yes

Table 7.1: Comparison of performance tendencies for the control applications to the buck converter example as in text

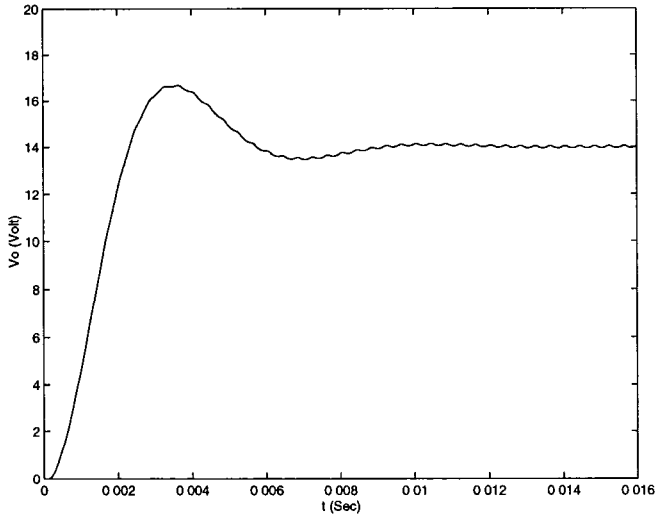

Figure 7.4: Output voltage response in Example 7.1 during start-up

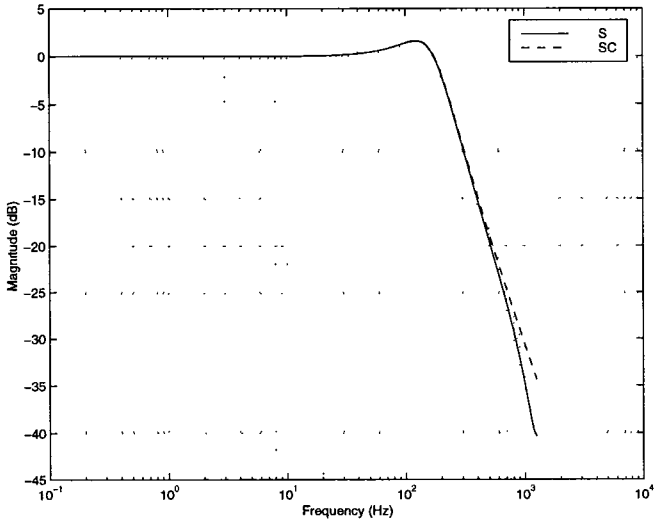

Figure 7.5: Normalized audio-susceptibility obtained by the S and SC methods

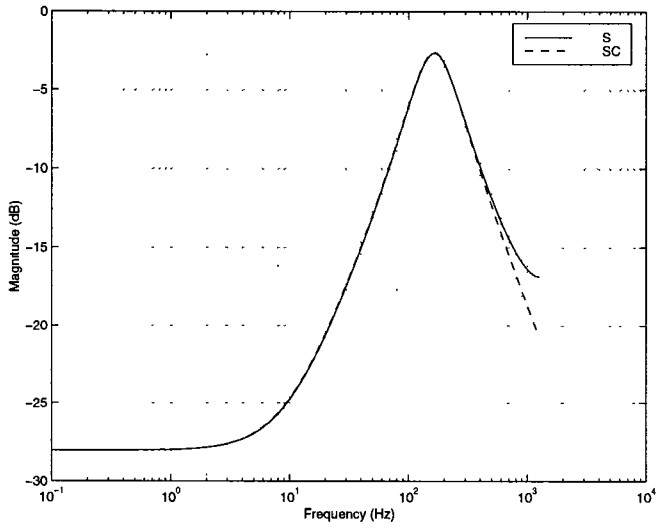

Figure 7.6: Normalized output impedance obtained by the S and SC methods

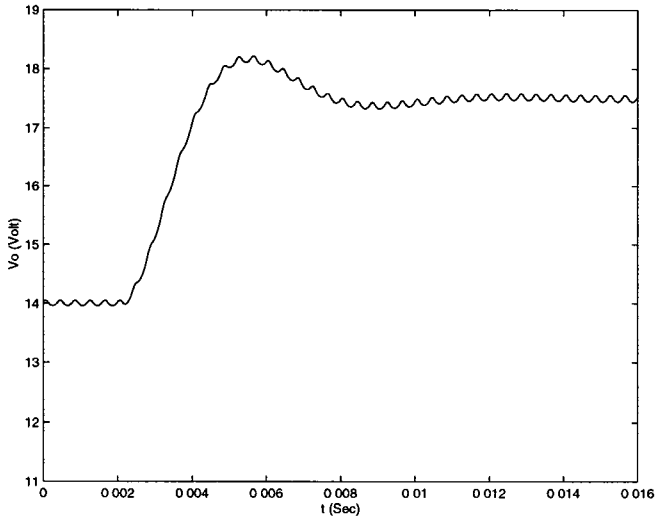

Figure 7.7: Output voltage response in Example 7.1 when the source voltage is changed from $20V$ to $25V$ at $t = 0.002s$

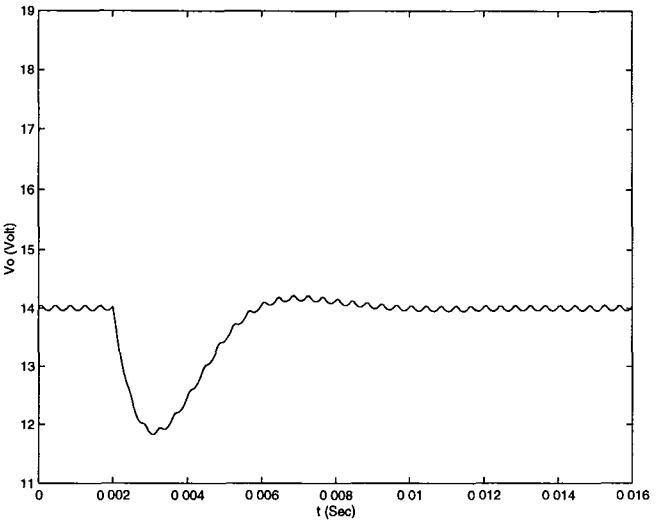

Figure 7.8: Output voltage response in Example 7.1 when the load is changed from 25Ω to 16.5Ω at $t = 0.002s$

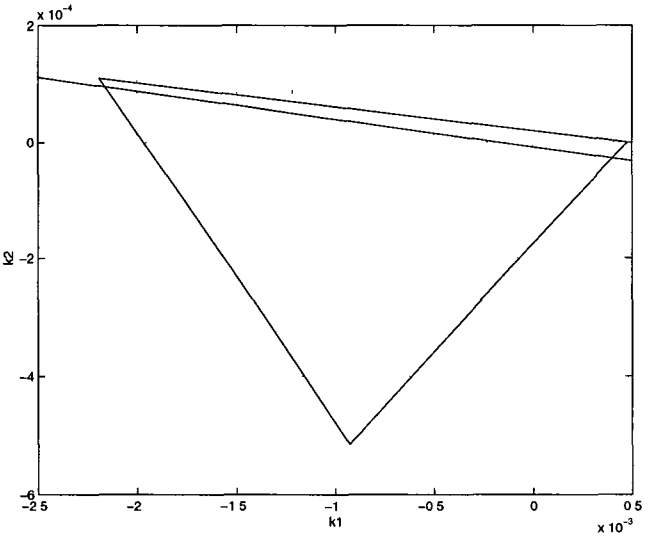

Figure 7.9: The triangular region corresponds to Eq. (7.4), which places a constraint on the feedback gain vector. The straight line constraint is Eq. (7.3).

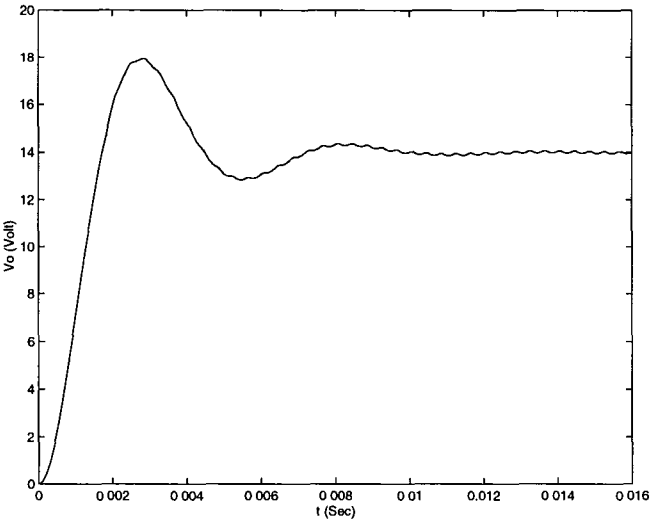

Figure 7.10: Output voltage response in Example 7.2 during start-up, (CSF method)

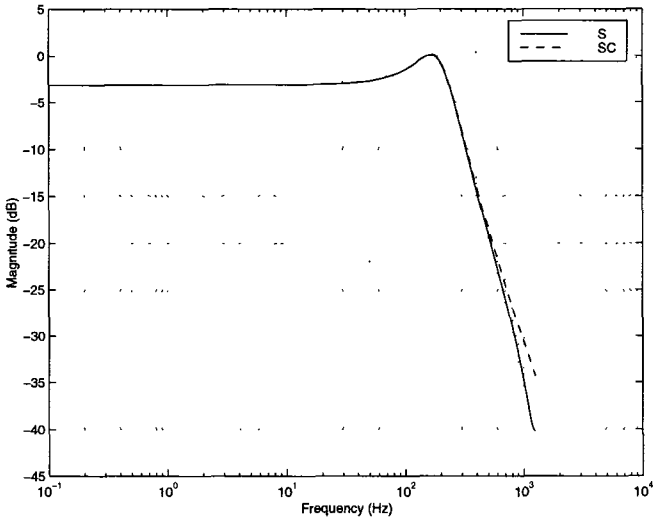

Figure 7.11: Normalized audio-susceptibility obtained by the S and SC methods

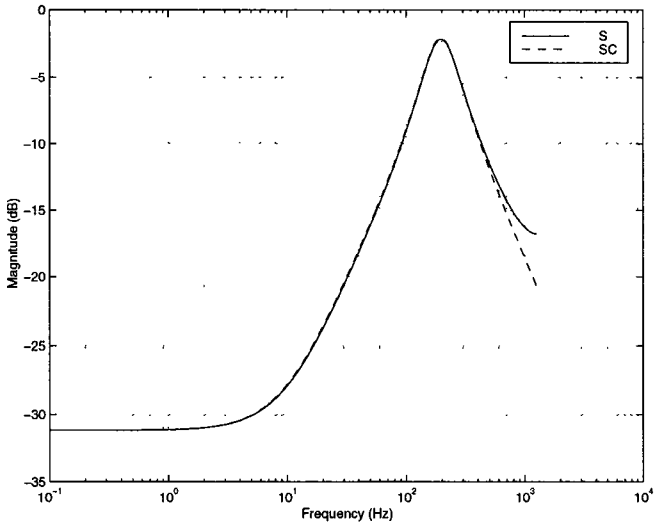

Figure 7.12: Normalized output impedance obtained by the S and SC methods

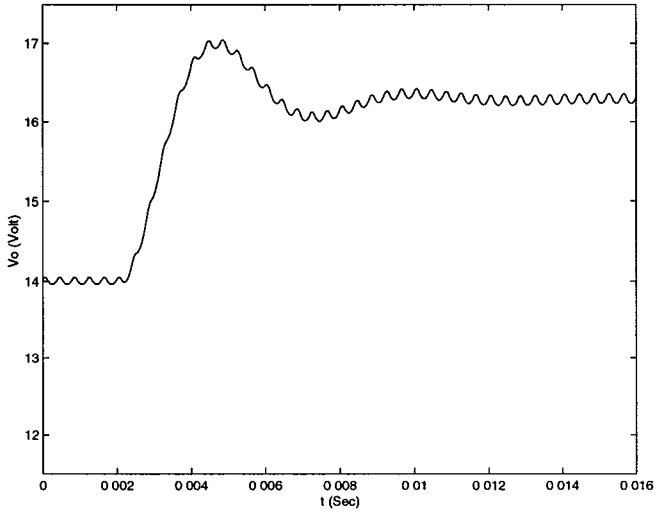

Figure 7.13: Output voltage response in Example 7.2 when the source voltage is changed from $20V$ to $25V$ at $t = 0.002s$ (CSF method)

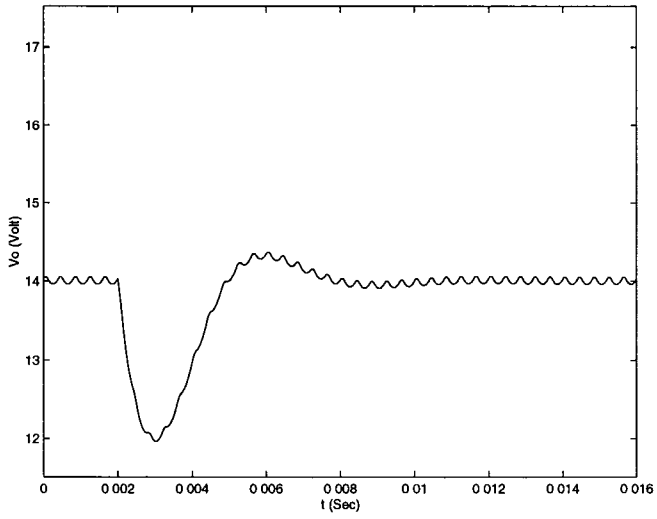

Figure 7.14: Output voltage response in Example 7.2 when the load is changed from 22Ω to 16.5Ω at $t = 0.002s$ (CSF method)

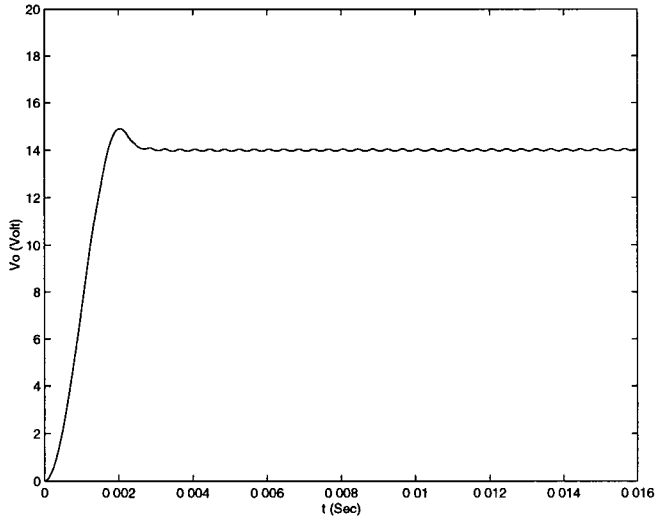

Figure 7.15: Output voltage response in Example 7.3 during start-up (LSF method)

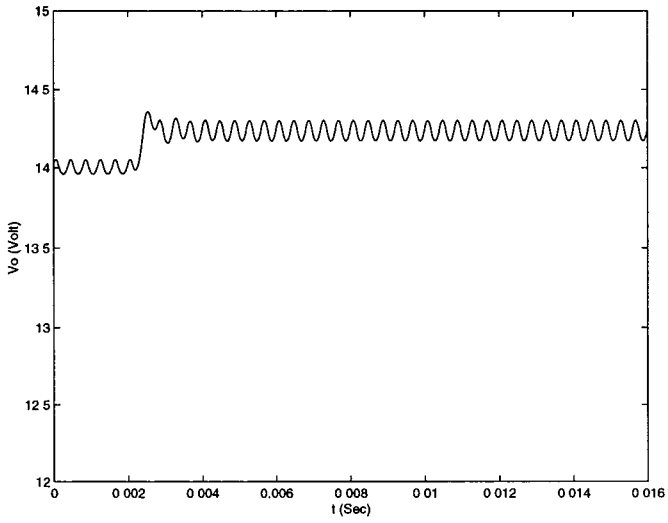

Figure 7.16: Output voltage response in Example 7.3 when the source voltage is changed from $20V$ to $25V$ at $t = 0.002s$ (LSF method)

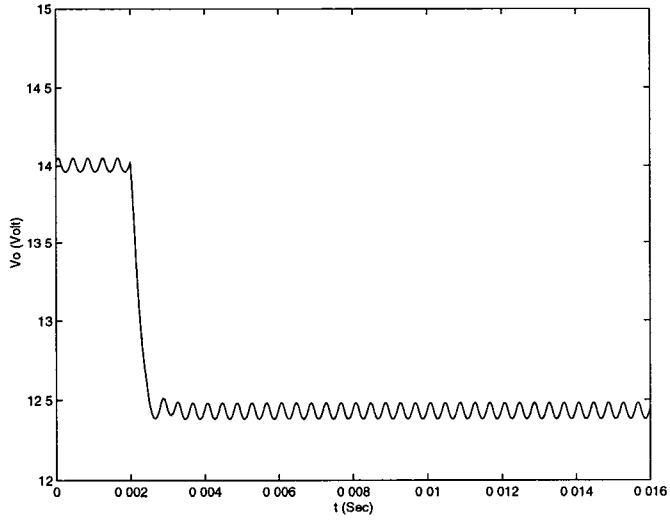

Figure 7.17: Output voltage response in Example 7.3 when the load is changed from 22Ω to 16.5Ω at $t = 0.002s$ (LSF method)

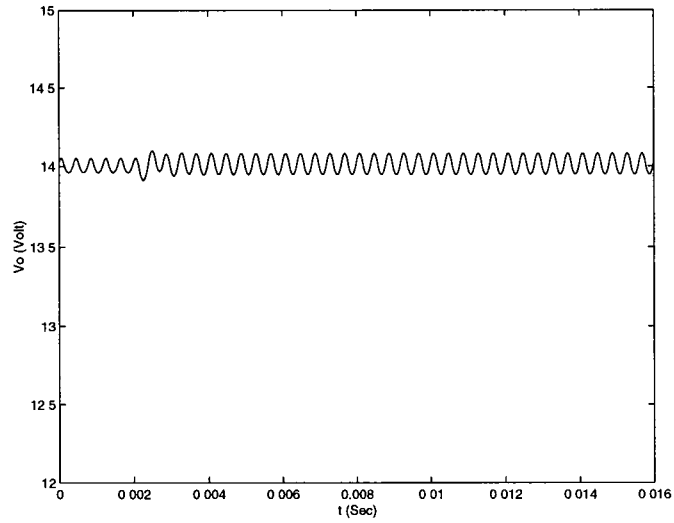

Figure 7.18: Output voltage response in Example 7.4 when the source voltage is changed from $20V$ to $25V$ at $t = 0.002s$, LSFF method

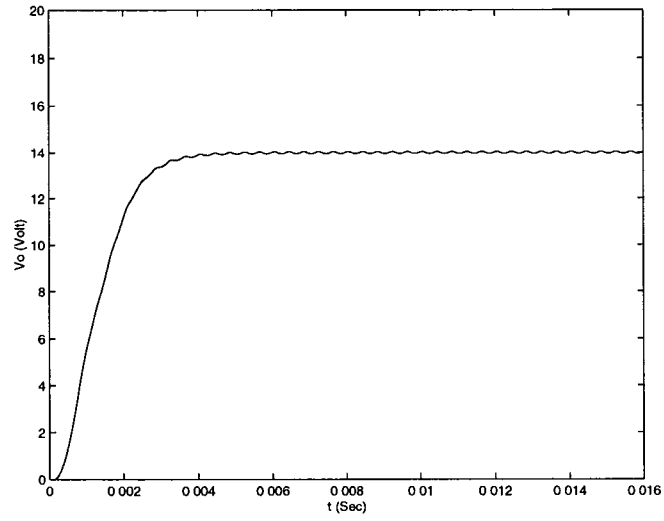

Figure 7.19: Output voltage response in Example 7.5 during start-up (LSFFW method)

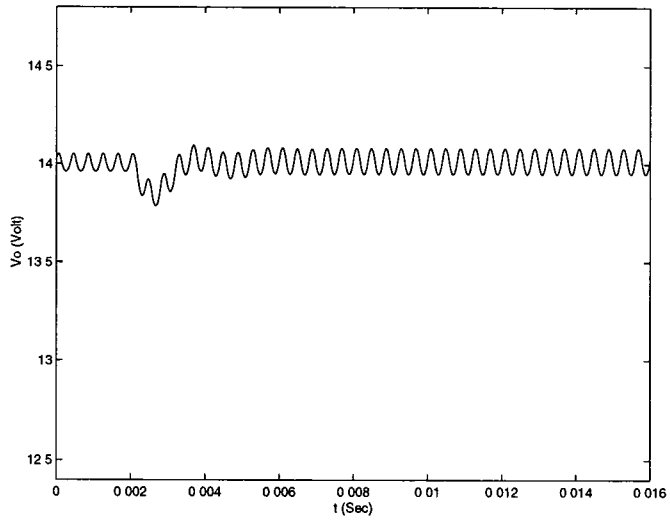

Figure 7.20: Output voltage response in Example 7.5 when the source voltage is changed from $20V$ to $25V$ at $t = 0.002s$ (LSFFW method)

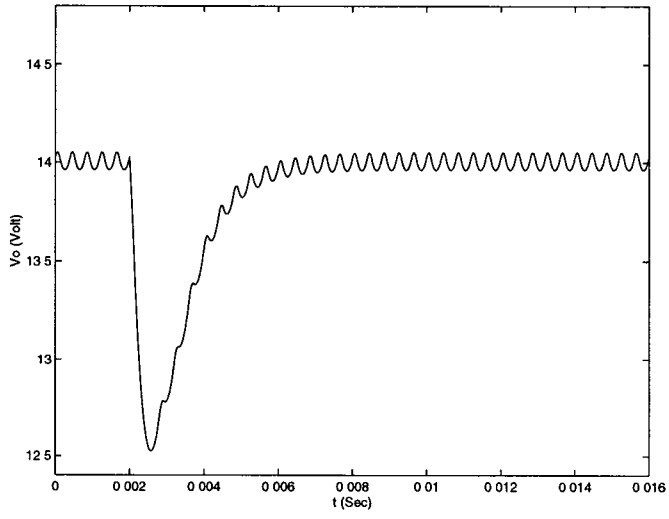

Figure 7.21: Output voltage response in Example 7.5 when the load is changed from 22Ω to 16.5Ω at $t = 0.002s$ (LSFFW method)

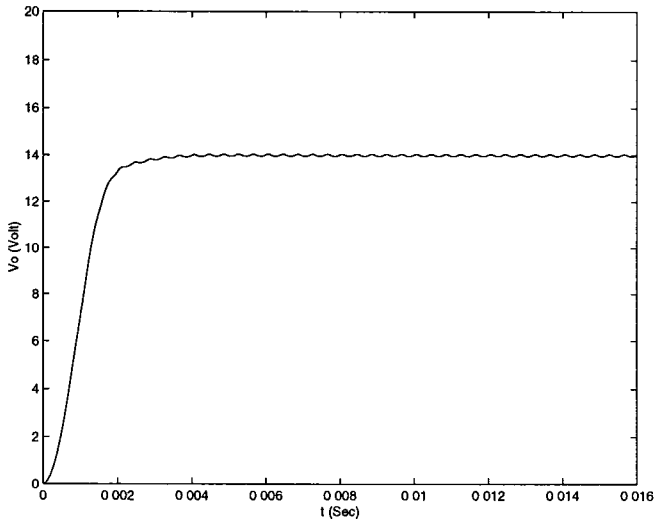

Figure 7.22: Output voltage response in Example 7.6 during start-up (IC method)

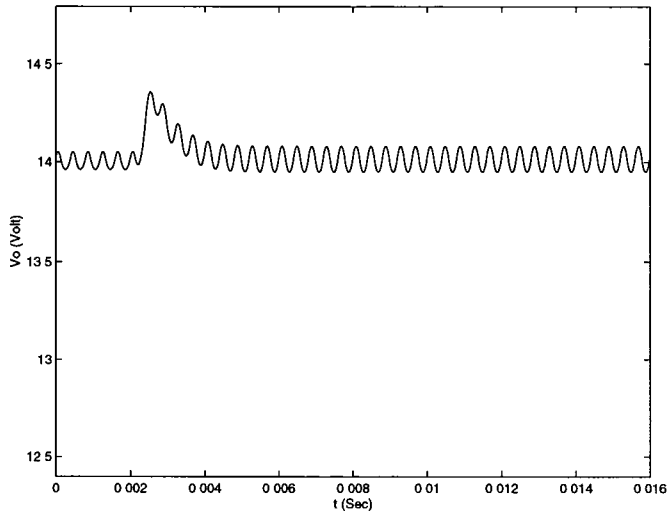

Figure 7.23: Output voltage response in Example 7.6 when the source voltage is changed from $20V$ to $25V$ at $t = 0.002s$ (IC method)

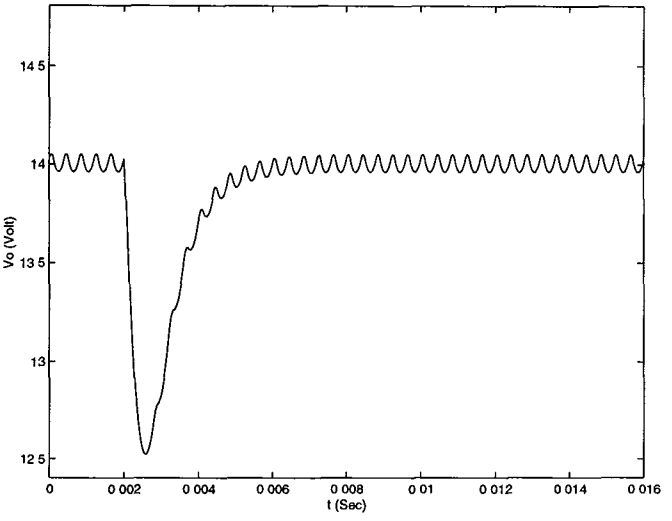

Figure 7.24: Output voltage response in Example 7.6 when the load is changed from 22Ω to 16.5Ω at $t = 0.002s$ (IC method)

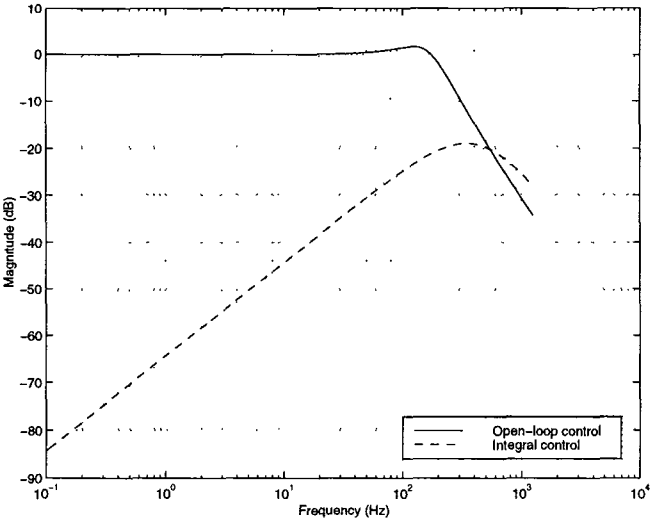

Figure 7.25: Comparison of normalized audio-susceptibility under open-loop control and integral control (IC method)

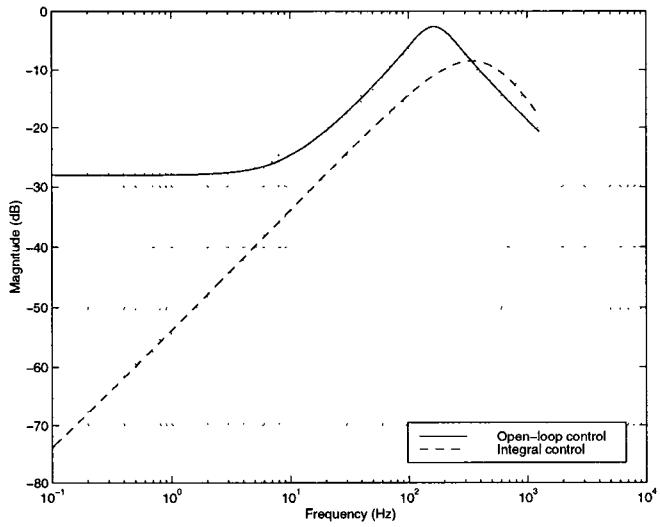

Figure 7.26: Comparison of normalized output impedance under open-loop control and integral control (IC method)

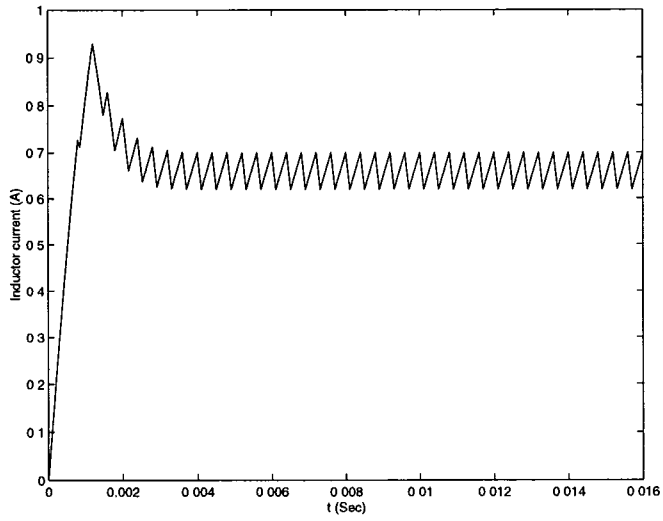

Figure 7.27: Inductor current response in Example 7.7 during start-up (IC method)

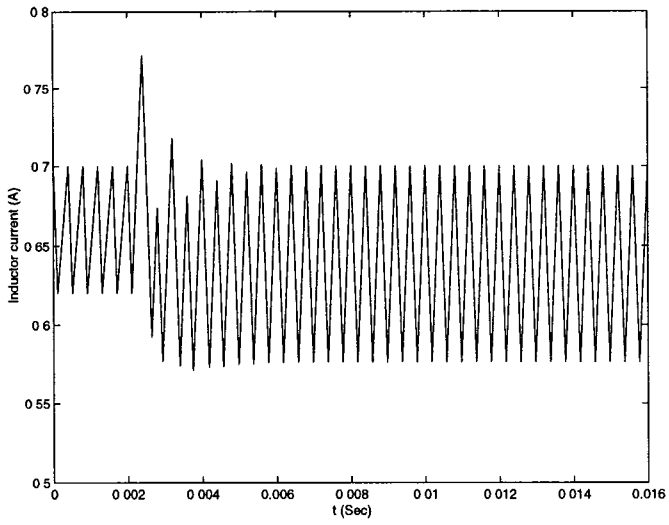

Figure 7.28: Inductor current response in Example 7.7 when the source voltage is changed from $20V$ to $25V$ at $t = 0.002s$ (IC method)

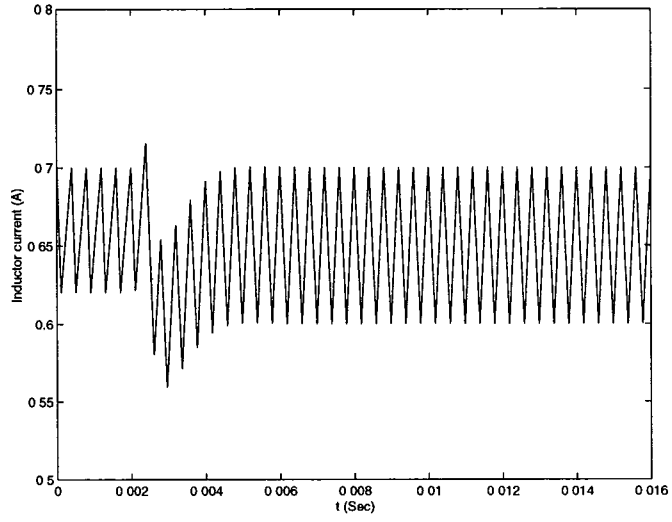

Figure 7.29: Inductor current response in Example 7.7 when the load is changed from 22Ω to 16.5Ω at $t = 0.002s$ (IC method)

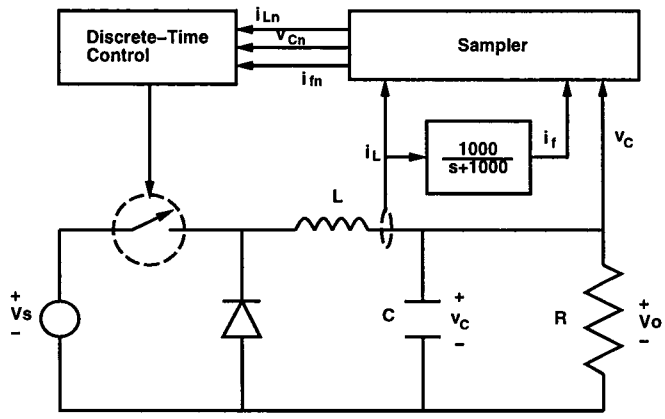

Figure 7.30: System diagram of average inductor current control in Example 7.7

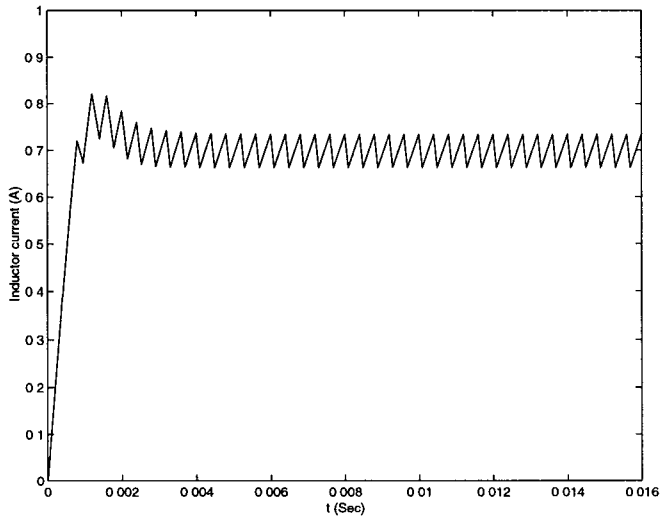

Figure 7.31: Inductor current response in Example 7.7 during start-up (IC method)

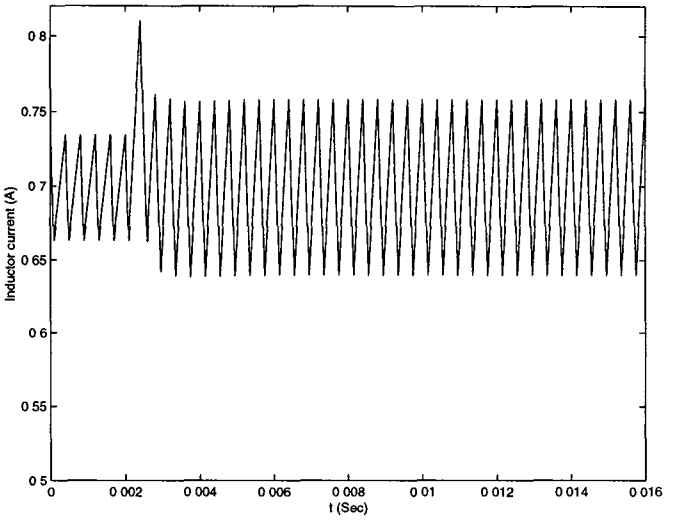

Figure 7.32: Inductor current response in Example 7.7 when the source voltage is changed from $20V$ to $25V$ at $t = 0.002s$ (IC method)

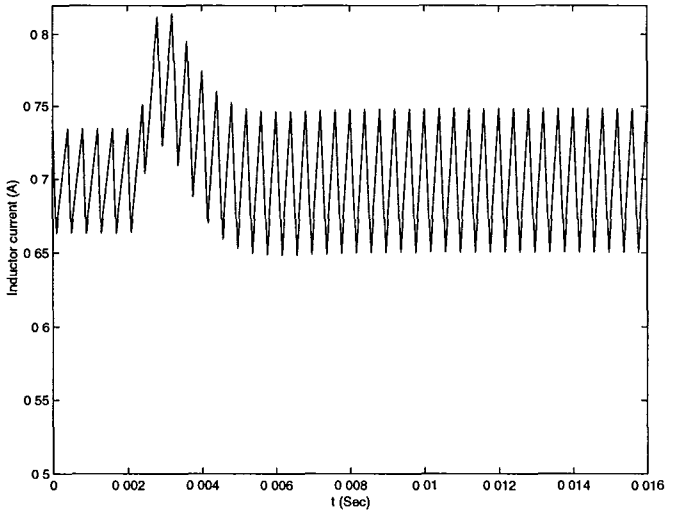

Figure 7.33: Inductor current response in Example 7.7 when the load is changed from 22Ω to 16.5Ω at $t = 0.002s$ (IC method)

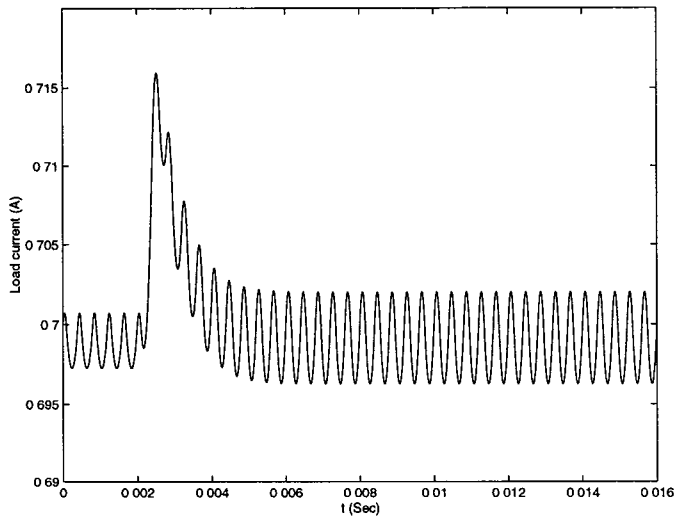

Figure 7.34: Load current response in Example 7.7 when the source voltage is changed from $20V$ to $25V$ at $t = 0.002s$ (IC method)

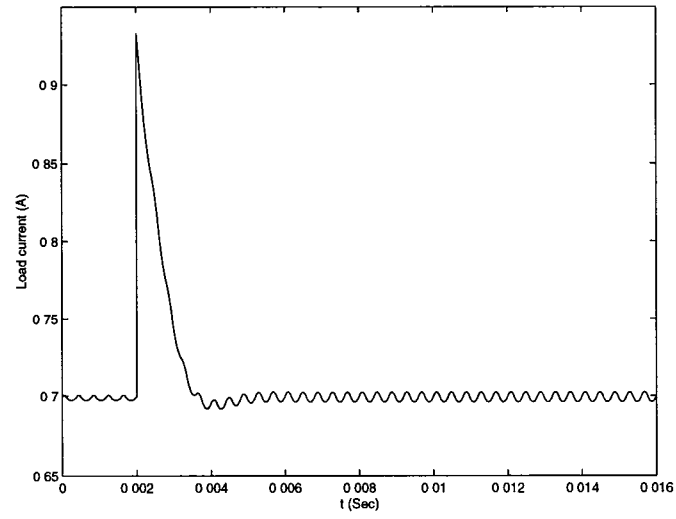

Figure 7.35: Load current response in Example 7.7 when the load is changed from 22Ω to 16.5Ω at $t = 0.002s$ (IC method)

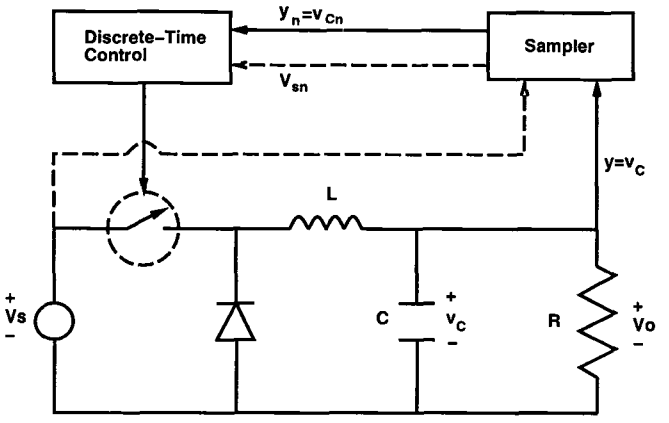

Figure 7.36: System diagram for Example 7.8

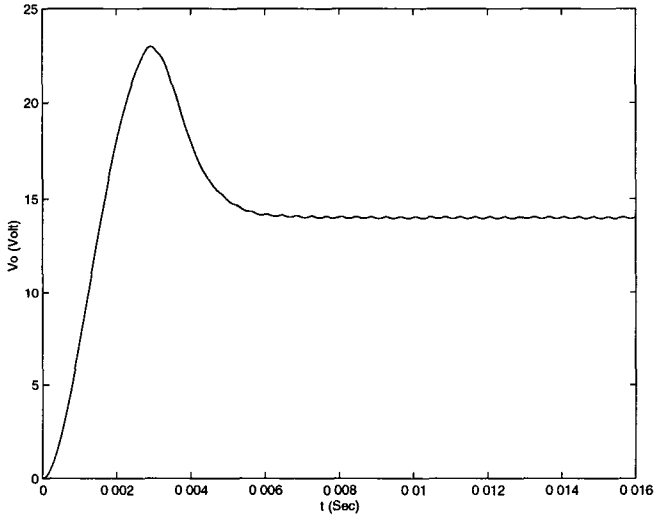

Figure 7.37: Output voltage response in Example 7.8 during start-up (OFIC method)

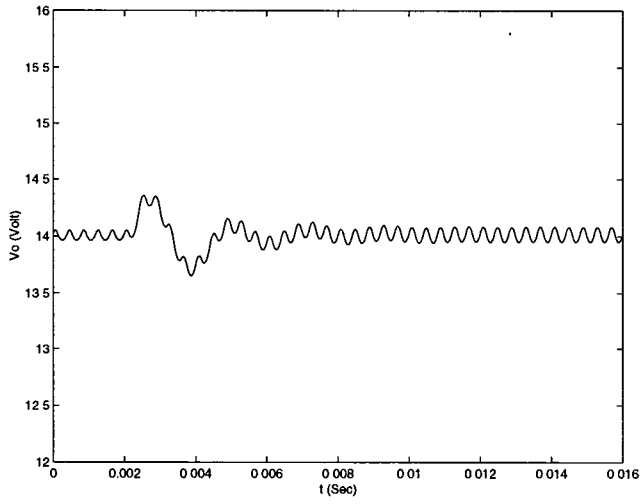

Figure 7.38: Output voltage response in Example 7.8 when the source voltage is changed from $20V$ to $25V$ at $t = 0.002s$ (OFIC method)

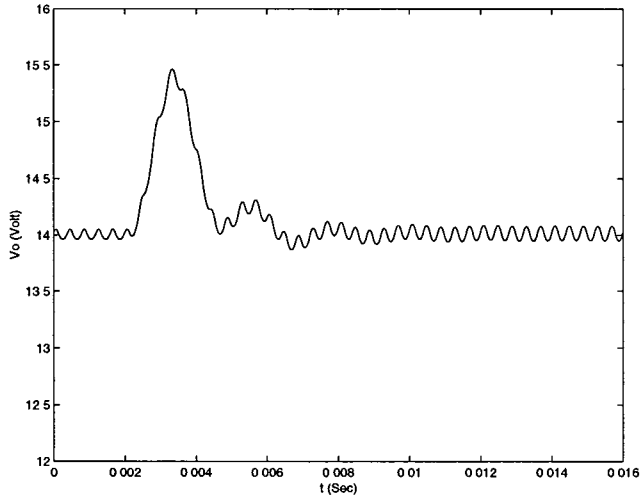

Figure 7.39: Output voltage response in Example 7.8 when the source voltage is changed from $20V$ to $25V$ at $t = 0.002s$ (OFIC method without source voltage feedforward)

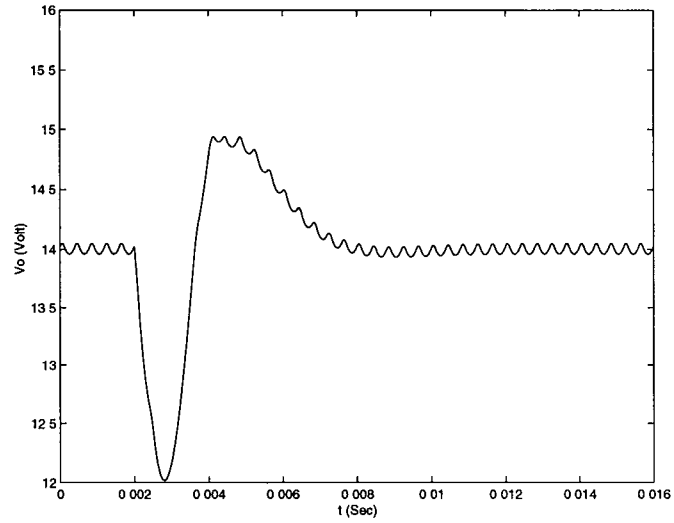

Figure 7.40: Output voltage response in Example 7.8 when the load is changed from 22Ω to 16.5Ω at $t = 0.002s$ (OFIC method)

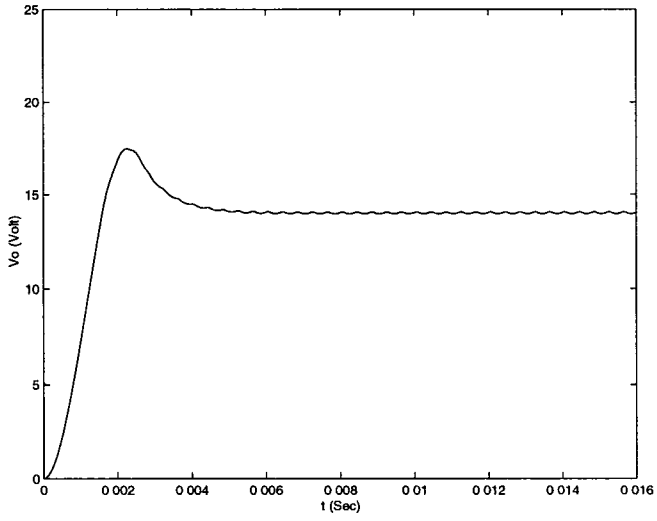

Figure 7.41: Output voltage response in Example 7.9 during start-up (ROFIC method)

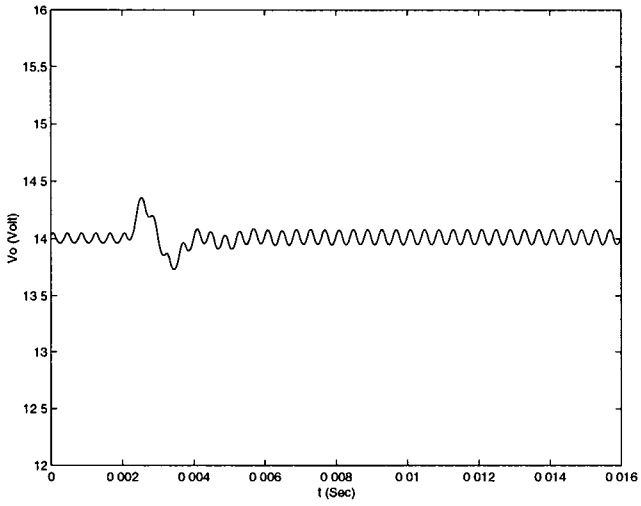

Figure 7.42: Output voltage response in Example 7.9 when the source voltage is changed from $20V$ to $25V$ at $t = 0.002s$ (ROFIC method)

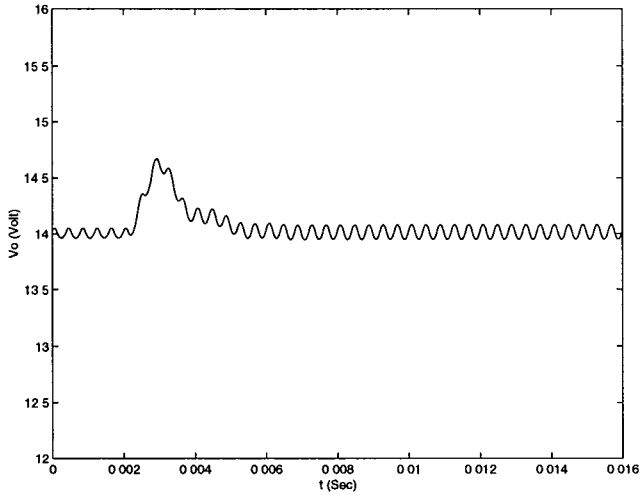

Figure 7.43: Output voltage response in Example 7.9 when the source voltage is changed from $20V$ to $25V$ at $t = 0.002s$ (ROFIC method without source voltage feedforward)

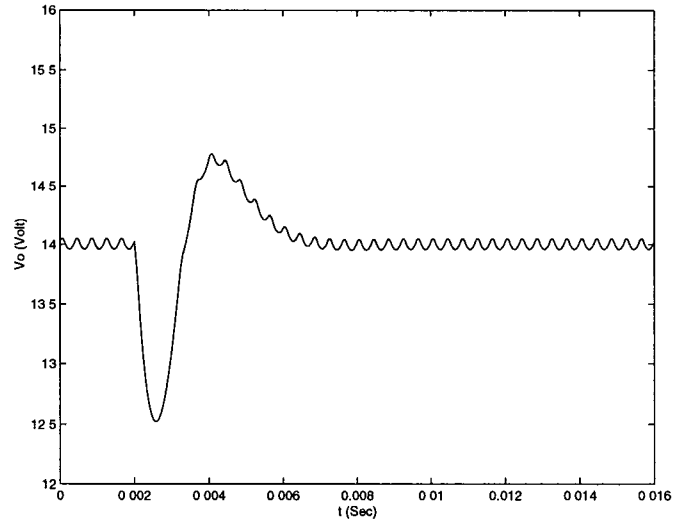

Figure 7.44: Output voltage response in Example 7.9 when the load is changed from 22Ω to 16.5Ω at $t = 0.002s$ (ROFIC method)

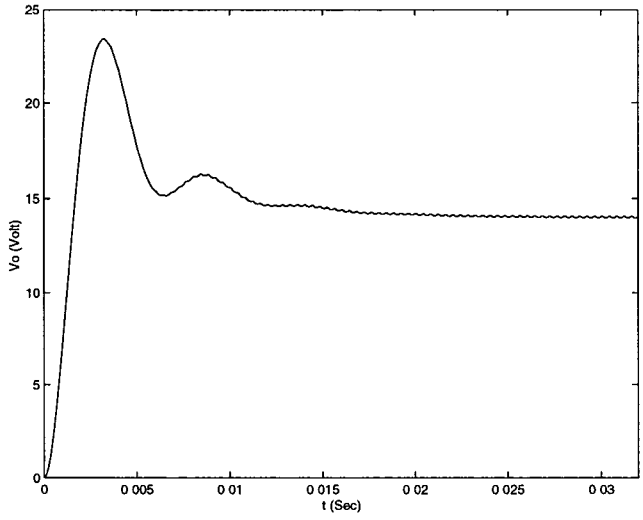

Figure 7.45: Output voltage response in Example 7.10 during start-up (OFICR method)

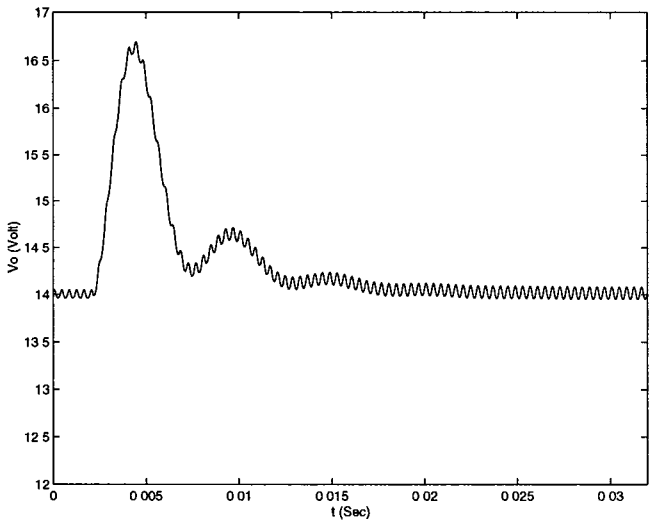

Figure 7.46: Output voltage response in Example 7.10 when the source voltage is changed from $20V$ to $25V$ at $t = 0.002s$ (OFICR method)

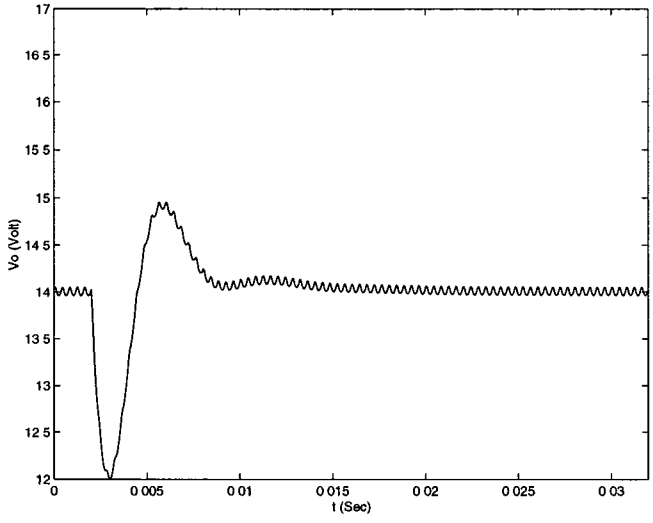

Figure 7.47: Output voltage response in Example 7.10 when the load is changed from 22Ω to 16.5Ω at $t = 0.002s$ (OFICR method)

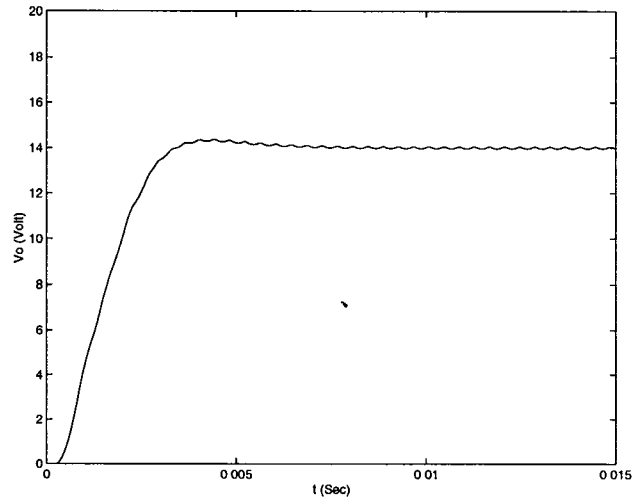

Figure 7.48: Output voltage response during start-up in Example 7.11 (The IC method with constant-off time)

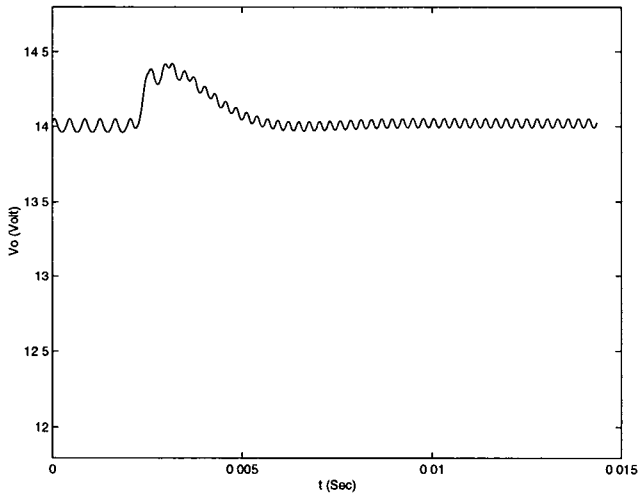

Figure 7.49: Output voltage response in Example 7.11 when the source voltage is changed from $20V$ to $25V$ at $t = 0.002s$ (The IC method with constant-off time)

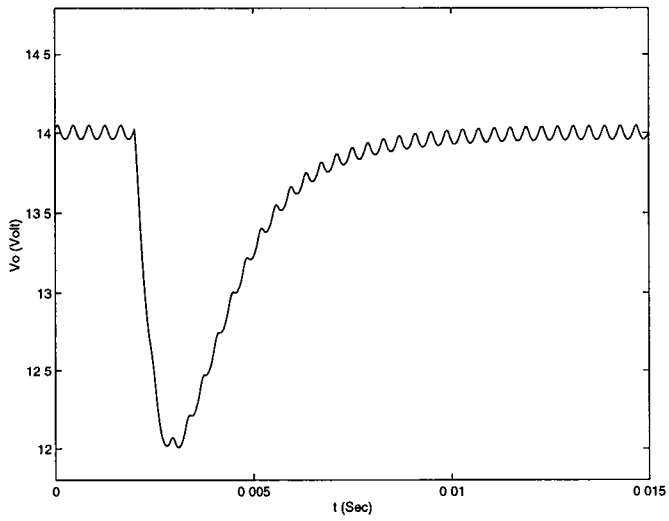

Figure 7.50: Output voltage response in Example 7.11 when the load is changed from 22Ω to 16.5Ω at $t = 0.002s$ (The IC method with constant-off time)

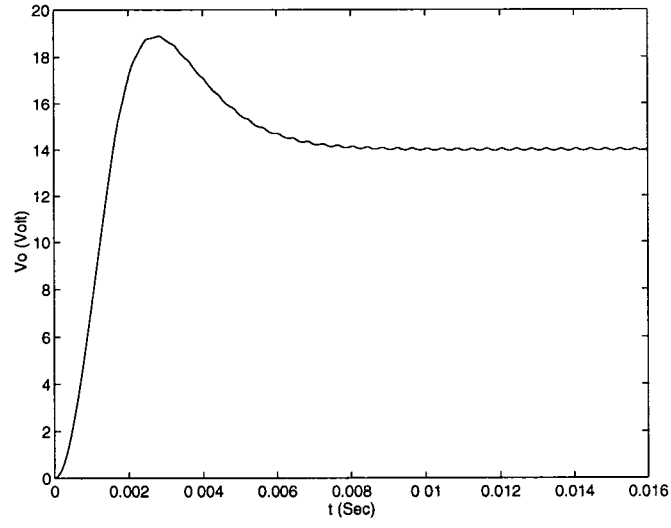

Figure 7.51: Output voltage response during start-up in Example 7.12

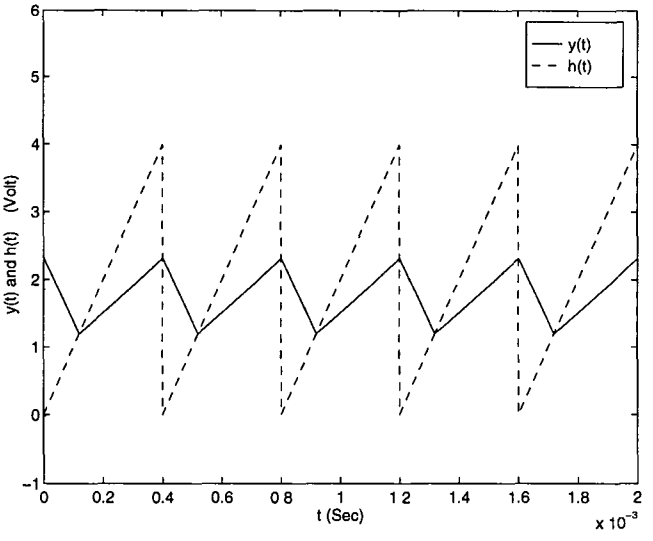

Figure 7.52: The signals $y(t)$ and $h(t)$ in steady state

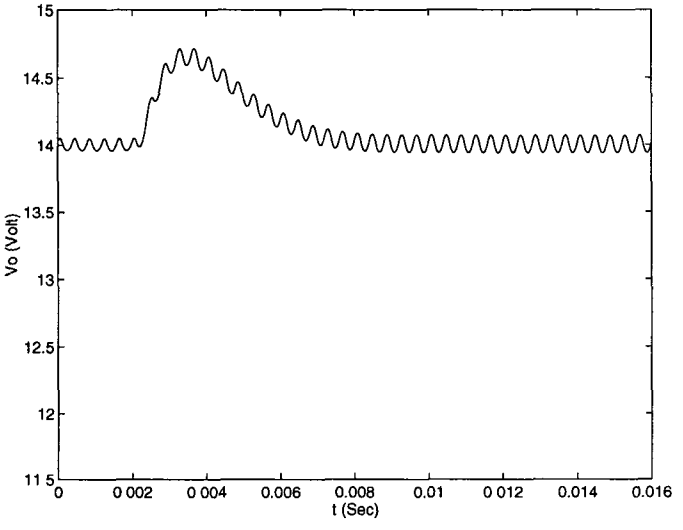

Figure 7.53: Output voltage response in Example 7.12 when the source voltage is changed from $20V$ to $25V$ at $t = 0.002s$

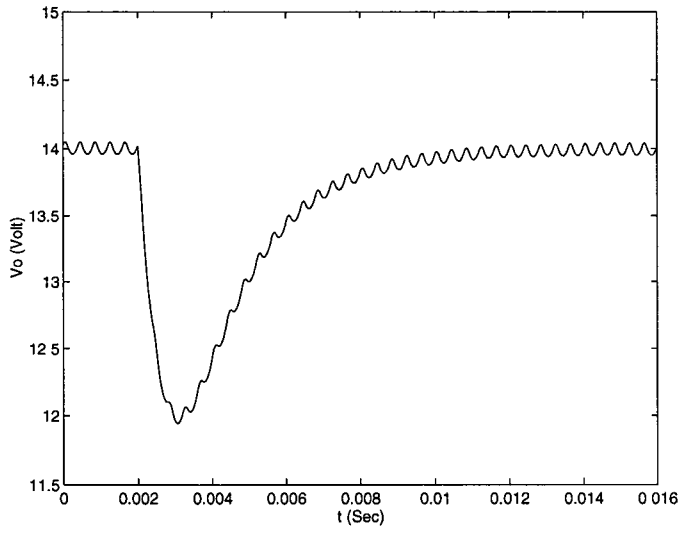

Figure 7.54: Output voltage response in Example 7.12 when the load is changed from 22Ω to 16.5Ω at $t = 0.002s$

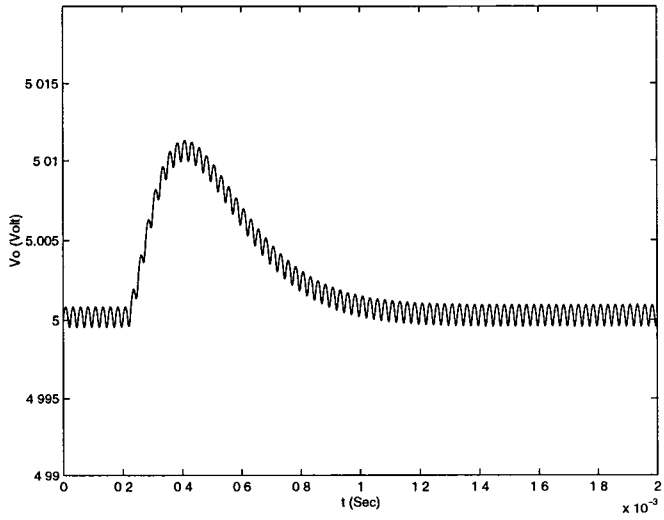

Figure 7.55: Output voltage response in Example 7.13 when the source voltage is changed from $15V$ to $17V$ at $t = 2 \times 10^{-4}s$; load $R = 2.5\Omega$

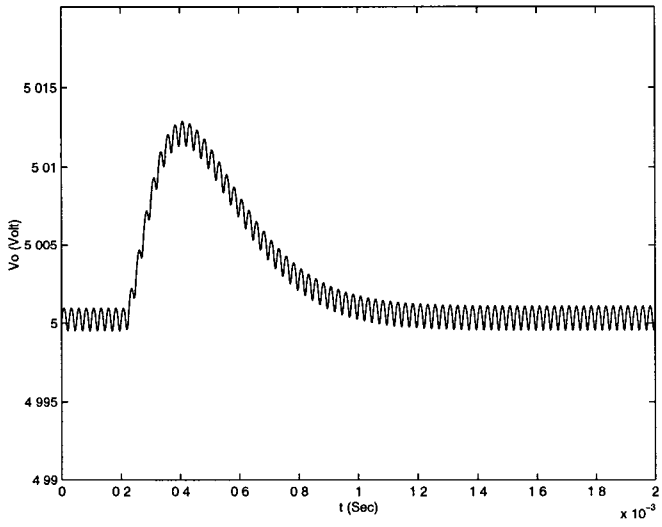

Figure 7.56: Output voltage response in Example 7.13 when the source voltage is changed from $15V$ to $17V$ at $t = 2 \times 10^{-4}s$; load $R = 5\Omega$

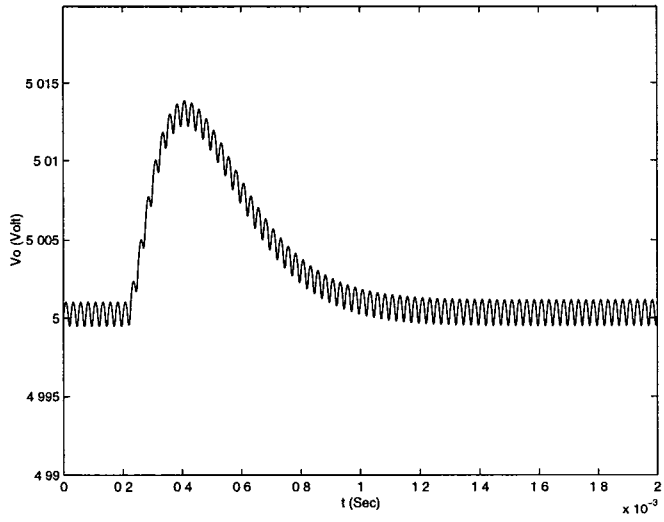

Figure 7.57: Output voltage response in Example 7.13 when the source voltage is changed from $15V$ to $17V$ at $t = 2 \times 10^{-4}s$; load $R = 10\Omega$

Chapter 8

Dynamic Analysis and Control of Load-Resonant DC-DC Converters

In the preceding chapters, PWM converters were analyzed. Similar approaches will be extended to the load-resonant converters in this chapter. Load-resonant converters generally have more states than PWM converters, so they are high dimensional. They also have more switches, so there are more stages in one cycle. These make load-resonant converters more difficult to analyze than PWM converters. Analysis has been done in a complicated way and separately for SRC, PRC and SPRC [40, 39, 86, 3, 4, 7]. Other methods such as extended describing function method [110] are prone to be inaccurate when the system approaches the discontinuous mode [23]. By expressing the system state in a matrix form and exploiting the symmetry property of these converters, we develop a more concise and unified method of analysis than the previous works.

To analyze this type of converter, we follow the same methodology as for PWM converters. First, by exploiting the symmetry property of this type of converter, we can simplify the analysis and derive a sampled-data model. Then we study the existence of periodic solutions, stability conditions, stabilizability,

and control design.

8.1 Modeling and Analysis of the Power Stage of Load-Resonant Converters

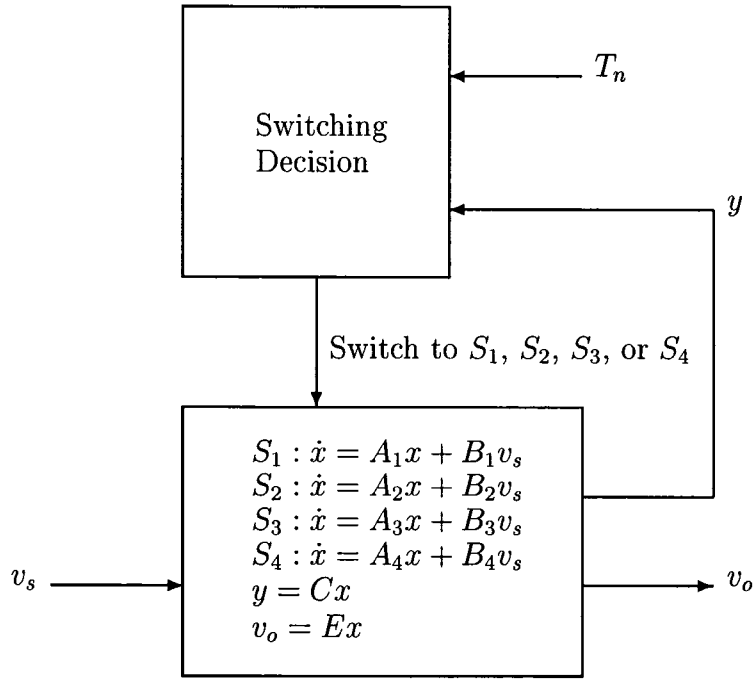

Figure 8.1: A general power stage model for load-resonant converters

In a PWM converter, the nominal duty cycle determines the nominal output voltage; while in a load-resonant converter, the nominal switching frequency determines the nominal output voltage. Thus in a load-resonant converter, the switching frequency, or equivalently the switching period, is used as the control variable and the circuit is operated in a variable frequency mode. By using phase-shift modulation [70, 96, 8, 46], the load-resonant converter can be operated in a fixed frequency mode and have more stages. Here we only concentrate on

the variable frequency mode. The same analysis can be extended to the fixed frequency mode.

A general model of the power stage of load-resonant converters (SRC, PRC, and SPRC) in a variable frequency mode is shown in Fig. 8.1, where T_n is the switching period in the n-th cycle, $A_i \in \mathbf{R}^{n\times n}$, $B_i \in \mathbf{R}^{n\times 1}$, $C, E \in \mathbf{R}^{1\times n}$, are constant matrices, v_s and v_o are the source and output voltages respectively, $y \in \mathbf{R}$ is the particular state determining switching (this will be mentioned again later). There are generally four stages per switching cycle in this class of converter. For example in the n-th cycle, we have (note that the switching instants are updated every cycle and denoted as d_{1n} and d_{2n}, instead of $d_{1,n}$ and $d_{2,n}$ to simplify notation):

$$S_1 : \dot{x} = A_1 x + B_1 v_s \quad \text{for } t \in [\sum_{i=0}^{n-1} T_i, \sum_{i=0}^{n-1} T_i + d_{1n}) \tag{8.1}$$

$$S_2 : \dot{x} = A_2 x + B_2 v_s \quad \text{for } t \in [\sum_{i=0}^{n-1} T_i + d_{1n}, \sum_{i=0}^{n-1} T_i + \frac{T_n}{2}) \tag{8.2}$$

$$S_3 : \dot{x} = A_3 x + B_3 v_s \quad \text{for } t \in [\sum_{i=0}^{n-1} T_i + \frac{T_n}{2}, \sum_{i=0}^{n-1} T_i + \frac{T_n}{2} + d_{2n}) \tag{8.3}$$

$$S_4 : \dot{x} = A_4 x + B_4 v_s \quad \text{for } t \in [\sum_{i=0}^{n-1} T_i + \frac{T_n}{2} + d_{2n}, \sum_{i=0}^{n} T_i) \tag{8.4}$$

The matrices A_i and B_i are related by

$$\begin{aligned} A_3 &= WA_1W & B_3 &= WB_1 \\ A_4 &= WA_2W & B_4 &= WB_2 \end{aligned} \tag{8.5}$$

here W is a projection matrix ($WW = I$) and satisfies $CW = \pm C$.

Actually in this class of converter, it can be shown that

$$\begin{aligned} A_2 &= WA_1W & B_2 &= B_1 \\ A_3 &= WA_1W & B_3 &= WB_1 \\ A_4 &= A_1 & B_4 &= WB_1 \end{aligned} \tag{8.6}$$

Indeed, it can be proved that (8.6) is a subset of (8.5). Here we will study the general case (8.5).

For example, let the state of the SPRC (Fig. 2.10) be $x = (i_{ls}, v_{cs}, v_{cp}, i_L, v_C)'$. The system matrices of the SPRC are

$$A_1 = \begin{bmatrix} 0 & \frac{-1}{L_s} & \frac{-1}{L_s} & 0 & 0 \\ \frac{1}{C_s} & 0 & 0 & 0 & 0 \\ \frac{1}{C_p} & 0 & 0 & \frac{1}{C_p} & 0 \\ 0 & 0 & \frac{-1}{L} & 0 & \frac{-1}{L} \\ 0 & 0 & 0 & \frac{1}{C} & \frac{-1}{RC} \end{bmatrix} \tag{8.7}$$

$$B_1 = \begin{bmatrix} \frac{1}{2L_s} \\ 0 \\ 0 \\ 0 \\ 0 \end{bmatrix} \tag{8.8}$$

$$C = \begin{bmatrix} 0 & 0 & 1 & 0 & 0 \end{bmatrix} \tag{8.9}$$

$$E = \begin{bmatrix} 0 & 0 & 0 & 0 & 1 \end{bmatrix} \tag{8.10}$$

$$W = \begin{bmatrix} -I_{3\times 3} & 0_{3\times 2} \\ 0_{2\times 3} & I_{2\times 2} \end{bmatrix} \tag{8.11}$$

In the load-resonant converter, switching from S_2 to S_3 occurs at half of the switching period $T_n/2$, and from S_4 to S_1 at the switching period T_n; while from S_1 to S_2 and from S_3 to S_4 are determined by the state y being zero:

$$y(\sum_{i=0}^{n-1} T_i + d_{1n}) = 0 \tag{8.12}$$

$$y(\sum_{i=0}^{n-1} T_i + \frac{T_n}{2} + d_{2n}) = 0 \tag{8.13}$$

By exploiting the symmetry property, (8.5), we will gradually simplify this 4-stage converter model. Let

$$\phi_i(x,t) = e^{A_i t}x + \int_0^t e^{A_i \sigma} d\sigma B_i v_s \tag{8.14}$$

where $i = 1, 2, 3, 4$.

We have

Lemma 8.1

$$\phi_1(x,t) = W\phi_3(Wx,t) \tag{8.15}$$

$$\phi_2(x,t) = W\phi_4(Wx,t) \tag{8.16}$$

Proof:

$$\begin{aligned}
\phi_1(x,t) &= e^{A_1 t}x + \int_0^t e^{A_1 \sigma} d\sigma B_1 v_s \\
&= We^{A_3 t}Wx + W\int_0^t e^{A_3 \sigma} d\sigma WWB_3 v_s \\
&= W\phi_3(Wx,t)
\end{aligned}$$

Similarly, we can prove $\phi_2(x,t) = W\phi_4(Wx,t)$ □

The next lemma shows that stage-1 started at x will have the same duration as stage-3 started at Wx.

Lemma 8.2 *If* $C\phi_1(x,d) = 0$, *then* $C\phi_3(Wx,d) = 0$.

Proof: If $C\phi_1(x,d) = 0$, then

$$\begin{aligned}
C\phi_3(Wx,d) &= CW\phi_1(x,d) \qquad \text{(from Lemma 8.1)} \\
&= \pm C\phi_1(x,d) \\
&= 0
\end{aligned}$$

□

Theorem 8.1 *If there exists a constant T and an initial state $x(0)$ such that $x(\frac{T}{2}) = Wx(0)$, then there exists a T-periodic solution $x^0(t)$ starting from $x(0)$.*

Proof:

If $x(\frac{T}{2}) = Wx(0)$, then

$$\begin{aligned} x(T) &= \phi_4(\phi_3(x(\frac{T}{2}), d), T-d) \\ &= W\phi_2(WW\phi_1(Wx(\frac{T}{2}), d), T-d) \qquad \text{(from Lemma 8.1)} \\ &= Wx(\frac{T}{2}) \\ &= x(0) \end{aligned}$$

□

Similar to Sec. 3.2, and using Lemma 8.1 and Lemma 8.2, the original system is equivalent to the following sampled-data system:

$$\begin{aligned} x_{n+\frac{1}{2}} &= f_1(x_n, v_{sn}, d_{1n}, T_n) \\ &= e^{A_2(\frac{T_n}{2}-d_{1n})}(e^{A_1 d_{1n}}x_n + \int_0^{d_{1n}} e^{A_1(d_{1n}-\sigma)}d\sigma B_1 v_{sn}) \\ &\quad + \int_{d_{1n}}^{\frac{T_n}{2}} e^{A_2(\frac{T_n}{2}-\sigma)}d\sigma B_2 v_{sn} \qquad (8.17) \\ x_{n+1} &= Wf_1(Wx_{n+\frac{1}{2}}, v_{sn}, d_{2n}, T_n) \qquad (8.18) \end{aligned}$$

$$\begin{aligned} g_1(x_n, v_{sn}, d_{1n}, T_n) &= C(e^{A_1 d_{1n}}x_n + \int_0^{d_{1n}} e^{A_1(d_{1n}-\sigma)}d\sigma B_1 v_{sn}) \\ &= 0 \qquad (8.19) \\ g_1(Wx_{n+\frac{1}{2}}, v_{sn}, d_{2n}, T_n) &= 0 \qquad (8.20) \end{aligned}$$

First we need to find the fixed point, $(x^0(0), V_s, d, T)$. Given the nominal source voltage V_s and the nominal switching period T, $x^0(0)$ and d satisfy

$$\begin{aligned} Wx^0(0) &= f_1(x^0(0), V_s, d, T) \qquad (8.21) \\ g_1(x^0(0), V_s, d, T) &= 0 \qquad (8.22) \end{aligned}$$

This set of nonlinear equations can be solved by Newton's method.

Similar to Sec. 3.3, we can express $x^0(d)$ as function of d, denoted as $X_d(d)$, (the invertibility of $W - e^{A_3 d}e^{A_2(\frac{T}{2}-d)}$ can be proved similarly as in Sec. 3.3)

$$\begin{aligned} X_d(d) &= (W - e^{A_3 d}e^{A_2(\frac{T}{2}-d)})^{-1}(e^{A_3 d}\int_0^{\frac{T}{2}-d} e^{A_2\sigma}d\sigma B_2 \\ &\quad + \int_0^d e^{A_3\sigma}d\sigma B_3)V_s \end{aligned} \tag{8.23}$$

Here the function $X_d(\cdot)$ satisfies

$$X_d(0) = (W - e^{A_2\frac{T}{2}})^{-1}\int_0^{\frac{T}{2}} e^{A_2\sigma}d\sigma B_2 V_s \tag{8.24}$$

$$X_d(\frac{T}{2}) = (W - e^{A_3\frac{T}{2}})^{-1}\int_0^{\frac{T}{2}} e^{A_3\sigma}d\sigma B_3 V_s \tag{8.25}$$

In this case, we have a sufficient condition regarding existence of periodic solutions.

Theorem 8.2 *There exists a T-periodic solution $x^0(t)$ for the load-resonant converter model (Fig. 8.1) if*

$$C(W - e^{A_2\frac{T}{2}})^{-1}\int_0^{\frac{T}{2}} e^{A_2\sigma}d\sigma B_2 C(W - e^{A_3\frac{T}{2}})^{-1}\int_0^{\frac{T}{2}} e^{A_3\sigma}d\sigma B_3 < 0 \tag{8.26}$$

Proof: From Eq. (8.22), if

$$\begin{aligned} & C(W - e^{A_2\frac{T}{2}})^{-1}\int_0^{\frac{T}{2}} e^{A_2\sigma}d\sigma B_2 C(W - e^{A_3\frac{T}{2}})^{-1}\int_0^{\frac{T}{2}} e^{A_3\sigma}d\sigma B_3 \\ = \; & CX_d(0)CX_d(\frac{T}{2})/(V_s^2) \\ < \; & 0 \end{aligned}$$

then from the intermediate-value theorem, there exists a solution d satisfying Eq. (8.22). Hence there exists a periodic solution $x^0(t)$. □

After getting the fixed point (or the periodic solution in continuous-time), we can study the local dynamics around the fixed point. Assuming $\frac{\partial g_1}{\partial d_n} = C\dot{x}^0(d^-)$

is not zero, then from the implicit function theorem, we can linearize at this fixed point. We obtain

$$\hat{x}_{n+\frac{1}{2}} \approx \Phi_{o1}\hat{x}_n + \Gamma_1\hat{v}_{sn} + \Gamma_{T1}\hat{T}_n \tag{8.27}$$

$$\hat{x}_{n+1} \approx \Phi_{o2}\hat{x}_{n+\frac{1}{2}} + \Gamma_2\hat{v}_{sn} + \Gamma_{T2}\hat{T}_n \tag{8.28}$$

where

$$\Phi_{o1} = e^{A_2(\frac{T}{2}-d)}(I - \frac{((A_1-A_2)x^0(d)+(B_1-B_2)V_s)C}{C(A_1x^0(d)+B_1V_s)})e^{A_1d} \tag{8.29}$$

$$= e^{A_2(\frac{T}{2}-d)}(I - \frac{(\dot{x}^0(d^-)-\dot{x}^0(d^+))C}{C\dot{x}^0(d^-)})e^{A_1d} \tag{8.30}$$

$$\Phi_{o2} = W\Phi_{o1}W \tag{8.31}$$

$$\Gamma_1 = e^{A_2(\frac{T}{2}-d)}(I - \frac{(\dot{x}^0(d^-)-\dot{x}^0(d^+))C}{C\dot{x}^0(d^-)})\int_0^d e^{A_1\sigma}d\sigma B_1 + \int_0^{\frac{T}{2}-d} e^{A_2\sigma}d\sigma B_2 \tag{8.32}$$

$$\Gamma_2 = W\Gamma_1 \tag{8.33}$$

$$\Gamma_{T1} = \frac{1}{2}(A_2x^0(\frac{T}{2}) + B_2V_s) \tag{8.34}$$

$$= \frac{1}{2}\dot{x}^0(\frac{T^-}{2}) \tag{8.35}$$

$$\Gamma_{T2} = W\Gamma_{T1} \tag{8.36}$$

So we have

$$\begin{aligned}\hat{x}_{n+1} &\approx \Phi_{o2}(\Phi_{o1}\hat{x}_n + \Gamma_1\hat{v}_{sn} + \Gamma_{T1}\hat{T}_n) + \Gamma_2\hat{v}_{sn} + \Gamma_{T2}\hat{T}_n \\ &= \Phi_{o2}\Phi_{o1}\hat{x}_n + (\Phi_{o2}\Gamma_1 + \Gamma_2)\hat{v}_{sn} + (\Phi_{o2}\Gamma_{T1} + \Gamma_{T2})\hat{T}_n \\ &\stackrel{\text{def}}{=} \Phi_o\hat{x}_n + \Gamma\hat{v}_{sn} + \Gamma_T\hat{T}_n \end{aligned} \tag{8.37}$$

where

$$\Phi_o = \Phi_{o2}\Phi_{o1}$$

$$
\begin{aligned}
&= (W\Phi_{o1})^2 \\
\Gamma &= \Phi_{o2}\Gamma_1 + \Gamma_2 \\
&= (W\Phi_{o1} + I)W\Gamma_1 \\
\Gamma_T &= \Phi_{o2}\Gamma_{T1} + \Gamma_{T2} \\
&= (W\Phi_{o1} + I)W\Gamma_{T1}
\end{aligned}
$$

Similar to Theorem 3.2, we have

Theorem 8.3 *The periodic solution $x^0(t)$ of the load-resonant converter is asymptotically orbitally stable for the open-loop system if all of the eigenvalues of Φ_o are inside the unit circle of the complex plane.*

Instead of checking the eigenvalues of Φ_o, we can check those of $W\Phi_{o1}$.

Theorem 8.4 $|\sigma[\Phi_o]| < 1$ *if and only if* $|\sigma[W\Phi_{o1}]| < 1$

Proof:

$$
\begin{aligned}
\Phi_o &= \Phi_{o2}\Phi_{o1} \\
&= (W\Phi_{o1})^2
\end{aligned}
$$

□

We also have a necessary condition for the open-loop load-resonant converter to be asymptotically orbitally stable

Theorem 8.5 *Suppose the periodic solution $x^0(t)$ is orbitally stable for the open-loop system. Then the following inequality holds:*

$$
\left|\frac{C\dot{x}^0(d^+)}{C\dot{x}^0(d^-)}\right| \leq e^{\mathrm{tr}[A_2 - A_1]d - \mathrm{tr}[A_2]\frac{T}{2}} \tag{8.38}
$$

Proof:

$$\begin{aligned} |\det[W\Phi_{o1}]| &= \left|\det[e^{A_1 d}e^{A_2(\frac{T}{2}-d)}]\det[I - \frac{(\dot{x}^0(d^-) - \dot{x}^0(d^+))C}{C\dot{x}^0(d^-)}]\right| \\ &= e^{-\mathrm{tr}[A_2-A_1]d+\mathrm{tr}[A_2]\frac{T}{2}}\left|\frac{C\dot{x}^0(d^+)}{C\dot{x}^0(d^-)}\right| \\ &\leq 1 \end{aligned}$$

□

8.2 Analytical Formulae for Open-Loop Audio-Susceptibility, Output Impedance and Control-to-Output Transfer Function

Open-loop audio-susceptibility (source to output voltage transfer function) From Eq. (8.37), we have

$$T_{os}(z) = E(zI - \Phi_o)^{-1}\Gamma \tag{8.39}$$

Open-loop output impedance (output current to output voltage transfer function)

To calculate the output impedance, we add a fictitious current source, i_o, in parallel with the load. The model is then

$$S_1 : \dot{x} = A_1 x + B_1 v_s + B_{i1} i_o \tag{8.40}$$

$$S_2 : \dot{x} = A_2 x + B_2 v_s + B_{i2} i_o \tag{8.41}$$

$$S_3 : \dot{x} = A_3 x + B_3 v_s + B_{i3} i_o \tag{8.42}$$

$$S_4 : \dot{x} = A_4 x + B_4 v_s + B_{i4} i_o \tag{8.43}$$

Similar to the discussion on output impedance of PWM converters (see Sec. 3.6), we have the output impedance

$$T_{oo}(z) = E(zI - \Phi_o)^{-1}\Gamma_i \tag{8.44}$$

where

$$\Gamma_i = (W\Phi_{o1} + I)W\Gamma_{i1} \tag{8.45}$$

$$\Gamma_{i1} = e^{A_2(\frac{T}{2}-d)}(I - \frac{(\dot{x}^0(d^-) - \dot{x}^0(d^+))C}{C\dot{x}^0(d^-)})\int_0^d e^{A_1\sigma}d\sigma B_{i1} + \int_0^{\frac{T}{2}-d} e^{A_2\sigma}d\sigma B_{i2} \tag{8.46}$$

Control-to-output transfer function

If we use the switching period T as the control variable, the control-to-output transfer function is

$$T_{co1}(z) = E(zI - \Phi_o)^{-1}\Gamma_T \tag{8.47}$$

If we use the switching frequency $1/T$ as the control variable, the control-to-output transfer function is

$$T_{co2}(z) = -T_{co1}(z)\frac{1}{f_s^2} = -E(zI - \Phi_o)^{-1}\Gamma_T\frac{1}{f_s^2} \tag{8.48}$$

where f_s is the nominal switching frequency.

8.3 Half-Cycle Sampled-Data Dynamics of the Power Stage of the Load-Resonant Converter

Motivated by [103], we can exploit the symmetry property of the load-resonant converter and simplify the dynamics. From Eqs. (8.17)-(8.20) and letting $w_{2k} =$

x_n and $w_{2k+1} = Wx_{n+\frac{1}{2}}$, we have the following simpler dynamics

$$w_{k+1} = Wf_1(w_k, v_{sk}, d_k, T_k) \tag{8.49}$$

$$g_1(w_k, v_{sk}, d_k, T_k) = 0 \tag{8.50}$$

We call this the half-cycle dynamics to distinguish it from the full-cycle dynamics derived in the previous sections.

The linearized half-cycle dynamics are given by

$$\hat{w}_{k+1} \approx W(\Phi_{o1}\hat{w}_k + \Gamma_1\hat{v}_{sk} + \Gamma_{T1}\hat{T}_k) \tag{8.51}$$

From the linearized dynamics, we derive the following transfer functions.

Open-loop audio-susceptibility (source to output voltage transfer function)

$$T_{os}(z) = E(zI - W\Phi_{o1})^{-1}W\Gamma_1 \tag{8.52}$$

Open-loop output impedance (output current to output voltage transfer function)

$$T_{oo}(z) = E(zI - W\Phi_{o1})^{-1}W\Gamma_{i1} \tag{8.53}$$

Control-to-output transfer function (using T as control variable)

$$T_{co1}(z) = E(zI - W\Phi_{o1})^{-1}W\Gamma_{T1} \tag{8.54}$$

Using the half-cycle dynamics has many advantages: firstly, it is more accurate because it has less stringent assumptions (we assume the source voltage is constant for *half* of the switching period); secondly, it is accurate up to the switching frequency while the full-cycle dynamics is accurate up to *half* of the switching frequency; thirdly, it is simpler than the full-cycle dynamics.

8.4 Discrete-Time Control of Load-Resonant Converters

After analyzing the power stage of load-resonant converters, we can study the control design. Here we use the switching period T as the control variable. The next result addresses the possibility of using this control variable to stabilize the system.

Theorem 8.6 *If the pair* (Φ_o, Γ_T) *or* $(W\Phi_{o1}, W\Gamma_{T1})$ *is stabilizable, then the periodic solution* $x^0(t)$ *is stabilizable using the switching period* T*, or equivalently the switching frequency, as the control variable.*

In Chapter 7, we designed various control methods for PWM converters. We also showed that integral control gives good load/line regulation. Similarly, we pursue integral control for load-resonant converters in this section. We design the control law based on the half-cycle dynamics of the power stage. The state sampling period in the n-th cycle is $T_n/2$. To ensure that the system is in the proper mode, we need to add a limiter on T, which is not shown explicitly in the control design.

The half-cycle dynamics of the power stage are

$$w_{n+1} = Wf_1(w_n, v_{sn}, d_n, T_n) \tag{8.55}$$

$$g_1(w_n, v_{sn}, d_n, T_n) = 0 \tag{8.56}$$

We propose the integral control

$$v_{n+1} = v_n + V_{\text{SET}} - Ew_{n+1} \tag{8.57}$$

$$T_n = -K_1 w_n - K_2 v_n \tag{8.58}$$

where v_n is the state of integral controller, and $V_{\rm SET}$ is the set-point output voltage.

The fixed point $(w_n, v_{sn}, d_n, T_n, v_n) = (w, V_s, d, T, v)$ of the system satisfies

$$w = W f_1(w, V_s, d, T) \tag{8.59}$$

$$V_{\rm SET} = Ew \tag{8.60}$$

$$T = -K_1 w - K_2 v \tag{8.61}$$

$$g_1(w, V_s, d, T) = 0 \tag{8.62}$$

So if the closed-loop system is stabilized, the output voltage will be driven to $V_{\rm SET}$.

Linearizing at this fixed point, we have

$$\begin{bmatrix} \hat{w}_{n+1} \\ \hat{v}_{n+1} \end{bmatrix} \approx \begin{bmatrix} W\Phi_{o1} & 0 \\ -E & 1 \end{bmatrix} \begin{bmatrix} \hat{w}_n \\ \hat{v}_n \end{bmatrix} + \begin{bmatrix} W\Gamma_{T1} \\ 0 \end{bmatrix} \hat{T}_n + \begin{bmatrix} W\Gamma_1 \\ 0 \end{bmatrix} \hat{v}_{sn}$$

To stabilize the system, we need to have the pair $(\begin{bmatrix} W\Phi_{o1} & 0 \\ -E & 1 \end{bmatrix}, \begin{bmatrix} W\Gamma_{T1} \\ 0 \end{bmatrix})$ to be stabilizable. This is equivalent to the pair $(W\Phi_{o1}, W\Gamma_{T1})$ being stabilizable and the matrix $\begin{bmatrix} W\Phi_{o1} - I & W\Gamma_{T1} \\ E & 0 \end{bmatrix}$ being of full rank.

From the linearized dynamics, the audio-susceptibility for the power stage with integral control is

$$T_{os}(z) = \begin{bmatrix} E & 0 \end{bmatrix} (zI - (\begin{bmatrix} W\Phi_{o1} & 0 \\ -E & 1 \end{bmatrix} - \begin{bmatrix} W\Gamma_{T1} \\ 0 \end{bmatrix} \begin{bmatrix} K_1 & K_2 \end{bmatrix}))^{-1} \begin{bmatrix} W\Gamma_1 \\ 0 \end{bmatrix}$$

The output impedance for the power stage with the integral control is

$$T_{oo}(z) = \begin{bmatrix} E & 0 \end{bmatrix} (zI - (\begin{bmatrix} W\Phi_{o1} & 0 \\ -E & 1 \end{bmatrix} - \begin{bmatrix} W\Gamma_{T1} \\ 0 \end{bmatrix} \begin{bmatrix} K_1 & K_2 \end{bmatrix}))^{-1} \begin{bmatrix} W\Gamma_{i1} \\ 0 \end{bmatrix}$$

8.5 Illustrative Examples

Example 8.1 *(Control-to-output frequency response of SPRC), [23]* The power stage is shown in Fig. 2.10, where $V_s = 100V$, $L_s = 5.2\mu H$, $C_s = C_p = 5.5nF$, $L_f = 13\mu H$, $C_f = 1\mu F$, $R = 26.507\Omega$, and the nominal switching frequency $f_s = 1.6713MHz$.

Using the the switching frequency as control variable, the control-to-output frequency response using the half-cycle dynamics is

$$T_{co}(e^{jw\frac{T}{2}}) = -E(e^{jw\frac{T}{2}}I - W\Phi_{o1})^{-1}W\Gamma_T(\frac{1}{f_s^2})(\frac{1}{2\pi\sqrt{L_sC_s}}) \tag{8.63}$$

where $1/(2\pi\sqrt{L_sC_s})$ is a normalizing factor. If we transform the pair $(W\Phi_{o1}, -W\Gamma_T/(2\pi\sqrt{L_sC_s}f_s^2))$ to the continuous-time pair (Φ^c, Γ^c), then the control-to-output frequency response (by the SC method) is

$$T(jw) = E(jwI - \Phi^c)^{-1}\Gamma^c \tag{8.64}$$

Fig. 8.2 and Fig. 8.3 show the control-to-output frequency response using the S and SC methods, which agree very well with the results in [23]. The plots using S or SC methods are similar for the load-resonant converter because of the high switching frequency.

Example 8.2 *(Integral Control of SPRC)* Here we try to regulate a SPRC with parameters the same as Example 8.1. The goal of this control design is to regulate the output voltage at $24V$, under the disturbances at the source voltage or load.

This circuit has open-loop poles at -0.6949, $0.6915\pm0.68i$, 0.5731 and 0.9808. Because of the complex poles which are close to the unit circle, we expect the dynamics to be slow.

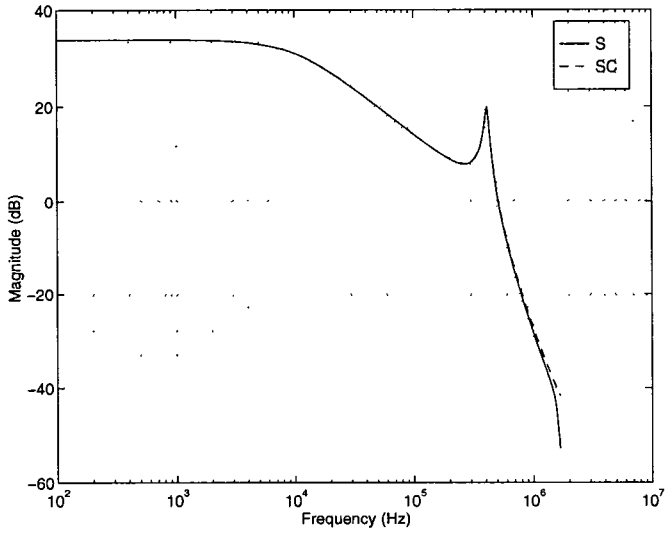

Figure 8.2: Control-to-output magnitude response obtained by the S and SC methods

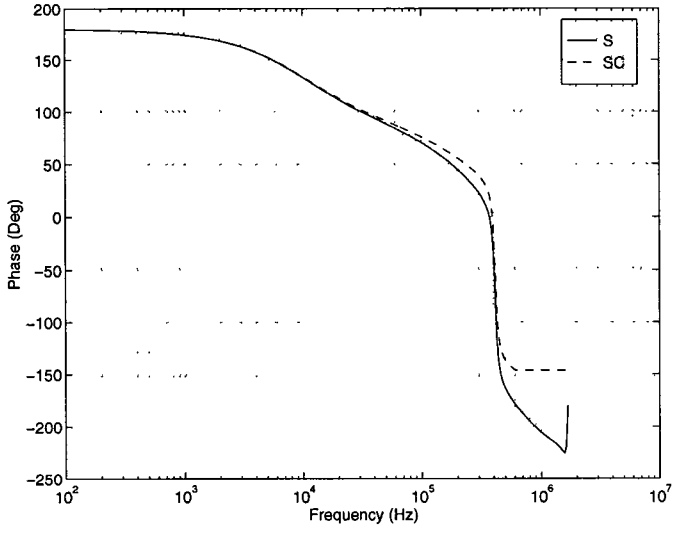

Figure 8.3: Control-to-output phase response obtained by the S and SC methods

Fig. 8.4 and Fig. 8.5 show the output voltage response subject to the disturbances at the source voltage and the load respectively. We can see that the response is slow and the line and load regulation are not good.

Next we apply integral control to this system. To prevent the control signal from being too large, we assign the closed loop poles at 0, 0, 0, 0, 0.5, and 0.5.

Fig. 8.6 and Fig. 8.7 show the output voltage response subject to the disturbances on the source voltage and the load respectively under integral control. We can see the response is fast and the output voltage is regulated at $24V$.

Fig. 8.8 and Fig. 8.9 show the audio-susceptibility and output impedance respectively, with and without control. We observe a significant improvement achieved with integral control.

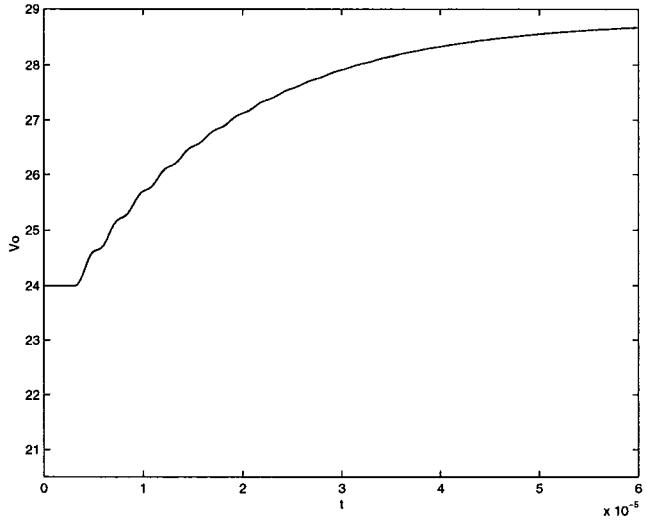

Figure 8.4: Output voltage response without control when the source voltage changes from $100V$ to $120V$ at $t = 2.7 \times 10^{-6}s$

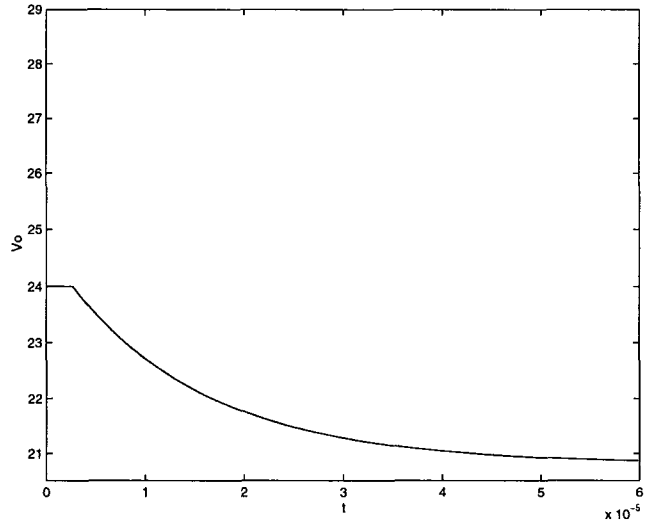

Figure 8.5: Output voltage response without control when the load changes from 26.5Ω to 21.2Ω at $t = 2.7 \times 10^{-6}s$

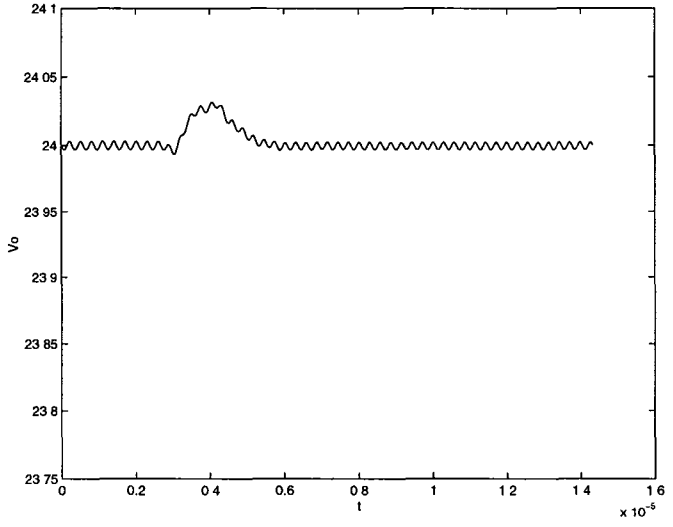

Figure 8.6: Output voltage response with control when the source voltage changes from $100V$ to $120V$ at $t = 2.7 \times 10^{-6}s$

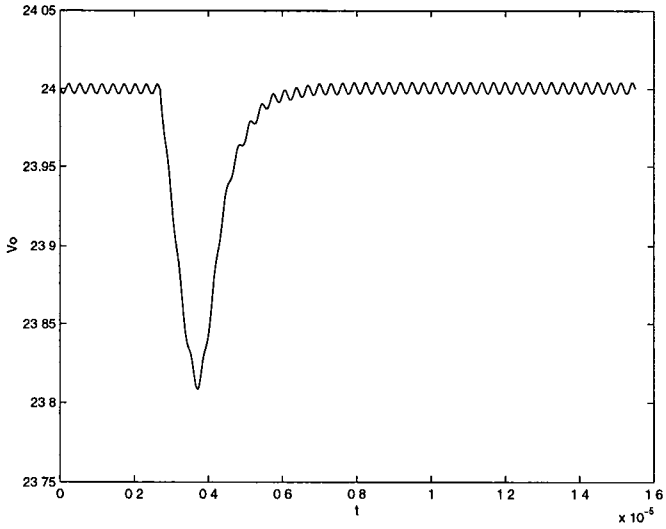

Figure 8.7: Output voltage response with control when the load changes from 26.5Ω to 21.2Ω at $t = 2.7 \times 10^{-6}s$

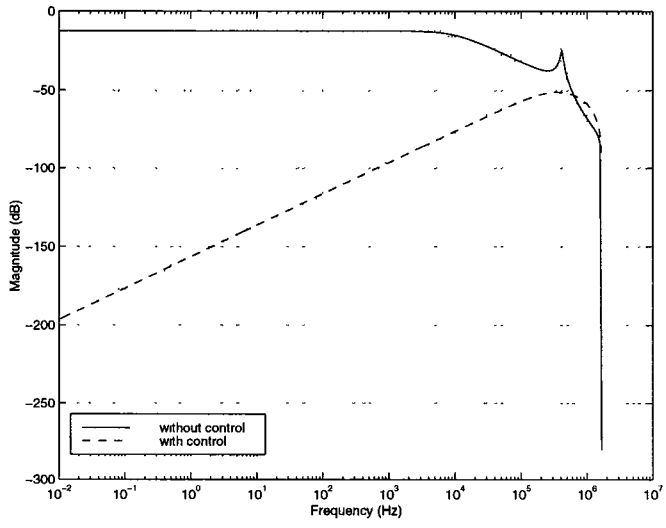

Figure 8.8: Audio-susceptibility of uncontrolled and controlled SPRC

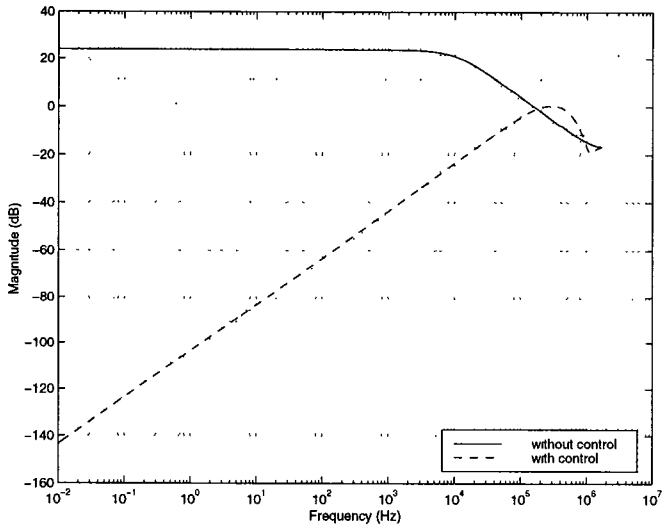

Figure 8.9: Output impedance of uncontrolled and controlled SPRC

8.6 Concluding Remarks

The methods and results for PWM converters developed in the previous chapters were extended to the load-resonant converters. By exploiting the symmetry property of this type of converter, methods that are more concise and unified than traditional ones have been developed. Analytical conditions on existence for periodic solutions and open-loop asymptotic orbital stability have been derived. Analytical formulae of open-loop audio-susceptibility, output impedance and half-cycle dynamics have also been derived. Integral control is applied to this type of converter and is shown to yield very good line/load regulation.

Chapter 9

Conclusion and Suggestions for Future Research

9.1 Conclusion

DC-DC switching converters are becoming popular in industrial, aerospace and consumer products. Methods for analyzing and controlling these converters are needed. The traditional methods like the state space averaging method have their limitations. In this dissertation, a unified method for analysis and control of PWM and load-resonant converters was presented. Because of the analytical and unified nature of this research, many unsolved instability problems have been solved. Control and stabilization of DC-DC converters are facilitated by a more complete understanding the dynamics of these converters.

Specifically, a unified method for different issues/classes/configurations of DC-DC converters has been proposed. Analytical conditions for stability and bifurcation of limit cycles arising in DC-DC converters were derived. Input filter instability was discussed using the Neimark-Sacker bifurcation. The possibility of saddle-node bifurcation in DC-DC converters was discovered. Stabilizability

conditions and stabilizers for PWM converters were derived. Better models of power stages of PWM converters were derived. Some discoveries about the locations of open-loop zeros in PWM converters were made. Analysis of load-resonant converters was simplified. Many new control methods for both PWM and resonant converters were proposed. A state observer for the buck converter was derived.

9.2 Suggestions for Future Research

Several possible directions for further research follow:

1. Local orbital stability with a large enough domain of attraction is necessary for every switching converter. In this study, only local stability is investigated. The size of the obtained stability region is an issue that merits investigation.

2. Since the switching frequency is generally very high, the signal delay will be pronounced and cannot be ignored. This should be addressed in future work.

3. The results in the dissertation should be extended to distributed system containing several sources, converters and loads.

4. Extension of the work to inverters, cylcoconverters, multiple output DC-DC converters, and power factor correcting (PFC) circuits should be pursued.

BIBLIOGRAPHY

[1] E.H. Abed, H.O. Wang, and R.C. Chen. Stabilization of period doubling bifurcations and implications for control of chaos. *Physica D*, 70(1-2):154–164, 1994.

[2] J. Ackermann. *Sampled-Data Control Systems: Analysis and Synthesis, Robust System Design.* Springer-Verlag, Berlin, 1985.

[3] V. Agarwal and A.K.S. Bhat. Large signal analysis of the LCC-type parallel resonant converter using discrete time domain modeling. *IEEE Transactions on Power Electronics*, 10(2):222–238, 1995.

[4] V. Agarwal and A.K.S. Bhat. Small signal analysis of the LCC-type parallel resonant converter using discrete time domain modeling. *IEEE Transactions on Industrial Electronics*, 42(6):604–614, 1995.

[5] K.J. Astrom. *Computer-Controlled Systems: Theory and Design.* Prentice Hall, Upper Saddle River, NJ, Third edition, 1997.

[6] S. Banerjee, E. Ott, J. A. Yorke, and G. H. Yuan. Anomalous bifurcations in DC-DC converters: Borderline collisions in piecewise smooth maps. In *IEEE Power Electronics Specialists Conf. Rec.*, pages 1337–1344, 1997.

[7] I. Batarseh, C. Megalemos, and M. Sznaier. Small signal analysis of the LCC-type parallel resonant converter. *IEEE Transactions on Aerospace and Electronic Systems*, 32(2):702–713, 1996.

[8] A.K.S. Bhat. Fixed frequency PWM series-parallel resonant converter. In *Conference Record of the IEEE Industry Applications Society Annual Meeting*, pages 1115–1121, 1989.

[9] K.H. Billings. *Switchmode Power Supply Handbook.* McGraw-Hill, New York, 1989.

[10] A.R. Brown and R.D. Middlebrook. Sampled-data modelling of switching regulators. In *IEEE Power Electronics Specialists Conf. Rec.*, pages 349–369, 1981.

[11] W.W. III Burns and T.G. Wilson. Analytic derivation and evaluation of a state-trajectory control law for DC-to-DC converters. In *IEEE Power Electronics Specialists Conf. Rec.*, pages 70–85, 1977.

[12] C. Collomb, M. Fadel, and Y. Cheron. Series resonant converter control: complete tuning of an IP regulator. In *Proceedings of International Conference on Industrial Electronics, Control, and Instrumentation*, pages 147–152, 1994.

[13] S. Ćuk and R.D. Middlebrook. A general unified approach to modelling switching DC-to-DC converters in discontinuous conduction mode. In *IEEE Power Electronics Specialists Conf. Rec.*, pages 36–57, 1977.

[14] B.L. de La Barra, M. El-Khoury, and M. Fernandez. On undershoot in scalar discrete-time systems. *Automatica*, 32(2):255–259, 1996.

[15] J.H.B. Deane. Chaos in a current-mode controlled boost DC-DC converter. *IEEE Transactions on Circuits and Systems-I: Fundamental Theory and Applications*, 39(8):680–683, 1992.

[16] J.H.B. Deane and D.C. Hamill. Instability, subharmonics, and chaos in power electronics circuits. *IEEE Transactions on Power Electronics*, 5(3):260–268, 1990.

[17] G. Deodhare and M. Vidyasagar. Control system design via infinite linear programming. *International Journal of Control*, 55(6):1351–1380, 1992.

[18] J.L. Duarte and J.M.A. Willaert. A fully digitized phase-shift modulated LCC resonant converter. In *IEEE Power Electronics Specialists Conf. Rec.*, pages 1303–1308, 1994.

[19] M.E. Elbuluk, G.C. Verghese, and J.G. Kassakian. Sampled-data modeling and digital control of resonant converters. *IEEE Transactions on Power Electronics*, 3(3):344–354, 1988.

[20] S.Y. Erich and W.M. Polivka. Input filter filter design criteria for current-programmed regulators. *IEEE Transactions on Power Electronics*, 7(1):143–151, 1992.

[21] R.W. Erickson. *Fundamentals of Power Electronics.* Chapman and Hall, New York, 1997.

[22] A.J. Forsyth and Y.K.E. Ho. Dynamic characteristics and closed-loop performance of the series-parallel resonant converter. *IEE Proceedings-Electric Power Applications*, 143(5):345–353, 1996.

[23] A.J. Forsyth, Y.K.E. Ho, and H.M. Ong. Comparison of small-signal modelling techniques for the series-parallel resonant converter. In *Proceedings of 5th International Conference on Power Electronics and Variable-Speed Drives*, pages 268–273, 1994.

[24] E. Fossas and G. Olivar. Study of chaos in the buck converter. *IEEE Transactions on Circuits and Systems-I: Fundamental Theory and Applications*, 43(1):13–25, 1996.

[25] G.F. Franklin, D. Powell, and M.L. Workman. *Digital control of dynamic systems.* Addison-Wesley, Reading, Mass., Second edition, 1990.

[26] F. Garofalo, P. Marino, S. Scala, and F. Vasca. Control of DC-DC converters with linear optimal feedback and nonlinear feedforward. *IEEE Transactions on Power Electronics*, 9(6):607–615, 1994.

[27] R. Genesio and A. Tesi. A harmonic balance approach for chaos prediction: Chua's circuit. *International Journal of Bifurcation and Chaos in Applied Sciences and Engineering*, 2(1):61–79, 1992.

[28] R. Genesio and A. Tesi. Harmonic balance methods for the analysis of chaotic dynamics in nonlinear systems. *Automatica*, 28(3):531–548, 1992.

[29] J. Guckenheimer and P. Holmes. *Nonlinear Oscillations, Dynamical Systems, and Bifurcations of Vector Fields.* Springer-Verlag, New York, 1983.

[30] D.C. Hamill. Power electronics: A field rich in nonlinear dynamics. In *Nonlinear Dynamics of Electronic Systems*, Dublin, 1995.

[31] D.C. Hamill, J.H.B. Deane, and J. Jefferies. Modeling of chaotic DC-DC converters by iterated nonlinear mappings. *IEEE Transactions on Power Electronics*, 7(1):25–36, 1992.

[32] S. Hiti and D. Borojevic. Robust nonlinear control for boost converter. *IEEE Transactions on Power Electronics*, 10(6):651–658, 1995.

[33] Y. Jang and R.E. Erickson. Physical origins of input filter oscillations in current programmed converters. *IEEE Transactions on Power Electronics*, 7(4):725–733, 1992.

[34] T. Kailath. *Linear Systems.* Prentice-Hall, Englewood Cliffs, NJ., 1980.

[35] L.A. Kamas and S.R. Sanders. Parameter and state estimation in power electronic circuits. *IEEE Transactions on Circuits and Systems-I: Fundamental Theory and Applications*, 40(12):920–928, 1993.

[36] N. Kawasaki, H. Nomura, and M. Masuhiro. A new control law of bilinear DC-DC converters developed by direct application of Lyapunov. *IEEE Transactions on Power Electronics*, 10(3):318–325, 1995.

[37] H.K. Khalil. *Nonlinear Systems.* Macmillan, New York, 1992.

[38] M.G. Kim, D.S. Lee, and M.J. Youn. A new state feedback control of resonant converters. *IEEE Transactions on Industrial Electronics*, 38(3):173–179, 1991.

[39] M.G. Kim and M.J. Youn. A discrete time domain modeling and analysis of controlled parallel resonant converter. *IEEE Transactions on Industrial Electronics*, 38(1):32–40, 1991.

[40] R.J. King and T.A. Stuart. Small-signal model for the series resonant converter. *IEEE Transactions on Aerospace and Electronic Systems*, AES-21(3):301–319, 1985.

[41] C.R. Kohut. Input filter design criteria for switching regulators using current mode control. *IEEE Transactions on Power Electronics*, 7(3):469–479, 1992.

[42] P.T. Krein. *Elements of Power Electronics.* Oxford University Press, New York, 1997.

[43] P.T. Krein, J. Bentsman, R.M. Bass, and B.L. Lesieutre. On the use of averaging for the analysis of power electronic systems. *IEEE Transactions on Power Electronics*, 5(2):182–190, 1990.

[44] B.C. Kuo. *Digital Control Systems.* Saunders, Philadelphia, Second edition, 1992.

[45] Y.A. Kuznetsov. *Elements of Applied Bifurcation Theory.* Springer-Verlag, New York, 1995.

[46] C.Q. Lee, S. Sooksatra, and R. Liu. Constant frequency controlled full-bridge LCC-type parallel resonant converter. In *Sixth Annual Applied Power Electronics Conference and Exposition. Conference Proceedings*, pages 587–593, 1991.

[47] F.C. Lee and Y. Yu. Input-filter design for switching regulators. *IEEE Transactions on Aerospace and Electronic Systems*, AES-15(5):627–634, 1979.

[48] F.C.Y. Lee, R.P. Iwens, Yuan Yu, and J.E. Triner. Generalized computer-aided discrete time-domain modeling and analysis of DC-DC converters. *IEEE Transactions on Industrial Electronics and Control Instrumentation*, IECI-26(2):58–69, 1979.

[49] H.-C. Lee. *Robust Control of Bifurcating Nonlinear Systems with Applications.* PhD thesis, University of Maryland, College Park, 1991.

[50] B. Lehman and R.M. Bass. Extensions of averaging theory for power electronic systems. *IEEE Transactions on Power Electronics*, 11(4):542–553, 1996.

[51] B. Lehman and R.M. Bass. Switching frequency dependent averaged models for PWM DC-DC converters. *IEEE Transactions on Power Electronics*, 11(1):89–98, 1996.

[52] F.H.F. Leung, P.K.S. Tam, and C.K. Li. The control of switching DC-DC converters-A general LQR problem. *IEEE Transactions on Industrial Electronics*, 38(1):65–71, 1991.

[53] J.L. Lin and S.J. Chen. μ-Based controller design for a DC-DC switching power converter with line and load variations. In *Proceedings of International Conference on Industrial Electronics, Control, and Instrumentation*, pages 1029–1034, 1996.

[54] J.L. Lin and J.S. Lew. Analysis, modeling and robust controller design for a series resonant converter. In *Proceedings of International Conference on Industrial Electronics, Control, and Instrumentation*, pages 665–670, 1996.

[55] Y.-F. Liu and P.C. Sen. Function control-a novel strategy to achieve improved performance of the DC-to-DC switching regulators. *IEEE Transactions on Industrial Electronics*, 42(2):186–191, 1995.

[56] Y.-F. Liu and P.C. Sen. A novel method to achieve zero-voltage regulation in buck converter. *IEEE Transactions on Power Electronics*, 10(3):292–301, 1995.

[57] Y.-F. Liu and P.C. Sen. Large-signal modeling of hysteretic current-programmed converters. *IEEE Transactions on Power Electronics*, 11(3):423–430, 1996.

[58] R. Lutz and M. Grotzbach. Straightforward discrete modelling for power converter systems. In *IEEE Power Electronics Specialists Conf. Rec.*, pages 761–770, 1986.

[59] R.D. Middlebrook. Input filter considerations in design and application of switching regulators. In *IEEE Industry Applications Society Annual Meeting*, pages 11–14, 1976.

[60] R.D. Middlebrook. Design techniques for preventing input-filter oscillations in switched-mode regulators. In *Proceedings of Powercon 5. Fifth National Solid-State Power Conversion Conference*, pages A3/1–16, 1978.

[61] R.D. Middlebrook and S. Ćuk. A general unified approach to modelling switching-converter power stages. In *IEEE Power Electronics Specialists Conf. Rec.*, pages 18–34, 1976.

[62] P. Midya. *Nonlinear Control and Operation of DC to DC Switching Power Converters.* PhD thesis, University of Illinois, Urbana-Champaign, 1995.

[63] D.M. Mitchell. *DC-DC Switching Regulator Analysis.* McGraw-Hill, New York, 1988.

[64] N. Mohan, T.M. Undeland, and W.P. Robbins. *Power Electronics: Converters, Applications, and Design.* Wiley, New York, 1995.

[65] R. Munzert and P.T. Krein. Issues in boundary control. In *IEEE Power Electronics Specialists Conf. Rec.*, pages 810–816, 1996.

[66] R. Oruganti and F.C. Lee. Resonant power processors. Part I. State plane analysis. *IEEE Transactions on Industry Applications*, IA-21(6):1453–1460, 1985.

[67] R. Oruganti and F.C. Lee. Resonant power processors, Part II. Methods of control. *IEEE Transactions on Industry Applications*, IA-21(6):1461–1471, 1985.

[68] S. Pavljasevic and D. Maksimovic. Subharmonic oscillations in converters with current-mode programming under large parameter variations. In *IEEE Power Electronics Specialists Conf. Rec.*, pages 1323–1329, 1997.

[69] C. Piccardi. Bifurcations of limit cycles in periodically forced nonlinear systems: the harmonic balance approach. *IEEE Transactions on Circuits and Systems-I: Fundamental Theory and Applications*, 41(4):315–320, 1994.

[70] I.J. Pitel. Phase-modulated, resonant power conversion techniques for high-frequency link inverters. *IEEE Transactions on Industry Applications*, IA-22(6):1044–1051, 1986.

[71] G. Podder, K. Chakrabarty, and S. Banerjee. Control of chaos in the boost converter. *Electronics Letters (IEE)*, 31(11):25, 1995.

[72] G. Podder, K. Chakrabarty, and S. Banerjee. Experimental control of chaotic behavior of buck converter. *IEEE Transactions on Circuits and Systems-I: Fundamental Theory and Applications*, 42(8):100–101, 1995.

[73] R.B. Ridley. A new, continuous-time model for current-mode control. *IEEE Transactions on Power Electronics*, 6(2):271–280, 1991.

[74] D.M. Sable, B.H. Cho, and R.B. Ridley. Elimination of the positive zero in fixed frequency boost and flyback converters. In *Fifth Annual Applied Power Electronics Conference and Exposition*, pages 205–211, 1990.

[75] D.M. Sable, R.B. Ridley, and B.H. Cho. Comparison of performance of single-loop and current-injection-control for PWM converters which operate in both continuous and discontinuous modes of operation. In *IEEE Power Electronics Specialists Conf. Rec.*, pages 74–79, 1990.

[76] S.R. Sanders, J.M. Noworolski, X.Z. Liu, and G.C. Verghese. Generalized averaging method for power conversion circuits. *IEEE Transactions on Power Electronics*, 6(2):251–259, 1991.

[77] S.R. Sanders and G.C. Verghese. Lyapunov-based control for switched power converters. *IEEE Transactions on Power Electronics*, 7(1):17–24, 1992.

[78] D.J. Shortt and F.C. Lee. Improved switching converter model using discrete and averaging techniques. *IEEE Transactions on Aerospace and Electronic Systems*, 19(2):190–202, 1983.

[79] D.J. Shortt and F.C. Lee. Extensions of the discrete average models for converter power stages. *IEEE Transactions on Aerospace and Electronic Systems*, 20(3):279–289, 1984.

[80] H. Sira-Ramirez. Nonlinear P-I controller design for switchmode DC-to-DC power converters. *IEEE Transactions on Circuits and Systems*, 38(4):410–417, 1991.

[81] H. Sira-Ramirez, M. Garcia-Esteban, and A.S.I. Zinober. Dynamical adaptive pulse-width-modulation control of DC-to-DC power converters: a backstepping approach. *International Journal of Control*, 65(2):205–222, 1996.

[82] H. Sira-Ramirez and L. Lischinsky-Arenas. Differential algebraic approach in nonlinear dynamical compensator design for DC-to-DC power converters. *International Journal of Control*, 54(1):111–133, 1991.

[83] H. Sira-Ramirez, R.A. Perez-Moreno, R. Ortega, and M. Garcia-Esteban. Passivity-based controllers for the stabilization of DC-to-DC power converters. *Automatica*, 33(4):499–513, 1997.

[84] H. Sira-Ramirez and M. Rios-Bolivar. Sliding mode control of DC-to-DC power converters via extended linearization. *IEEE Transactions on Circuits and Systems I: Fundamental Theory and Applications*, 41(10):652–661, 1994.

[85] H. Sira-Ramirez, R. Tarantino-Alvarado, and O. Llanes-Santiago. Adaptive feedback stabilization in PWM-controlled DC-to-DC power supplies. *International Journal of Control*, 57(3):599–625, 1993.

[86] K. Siri. *Small Signal Analysis of Resonant Converters and Control Approaches for Parallel Connected Converter Systems.* PhD thesis, University of Illinois at Chicago, 1991.

[87] K.M. Smedley. *Control Art of Switching Converters.* PhD thesis, California Institute of Technology, 1990.

[88] K.M. Smedley and S Ćuk. One-cycle control of switching converters. *IEEE Transactions on Power Electronics*, 10(6):625–633, 1995.

[89] R.L. Steigerwald. A comparison of half-bridge resonant converter topologies. *IEEE Transactions on Power Electronics*, 3(2):174–182, 1988.

[90] F.D. Tan and R.D. Middlebrook. A unified model for current-programmed converters. *IEEE Transactions on Power Electronics*, 10(4):397–408, 1995.

[91] P.T. Tang and C.K. Tse. Design and implementation of novel quasi-linear DSP-based control for power converters. *International Journal of Electronics*, 82(4):415–426, 1997.

[92] W. Tang, F.C. Lee, and R.B. Ridley. Small-signal modeling of average current-mode control. *IEEE Transactions on Power Electronics*, 8(2):112–119, 1993.

[93] W. Tang, F.C. Lee, R.B. Ridley, and I. Cohen. Charge control: Modeling, analysis, and design. *IEEE Transactions on Power Electronics*, 8(4):396–403, 1993.

[94] A. Tesi, E.H. Abed, R. Genesio, and H.O. Wang. Harmonic balance analysis of period-doubling bifurcations with implications for control of nonlinear dynamics. *Automatica*, 32(9):1255–1271, 1996.

[95] F.E. Thau. A feedback compensator design procedure for switching regulators. *IEEE Transactions on Industrial Electronics and Control Instrumentation*, IECI-26(2):104–110, 1979.

[96] F.-S. Tsai and F.C. Lee. Constant-frequency phase-controlled resonant power processor. In *Conference Record of the 1986 IEEE Industry Applications Society Annual Meeting*, pages 617–622, 1986.

[97] C.K. Tse. Flip bifurcation and chaos in three-state boost switching regulators. *IEEE Transactions on Circuits and Systems-I: Fundamental Theory and Applications*, 41(1):16–23, 1994.

[98] C.K. Tse and K.M. Adams. Quasi-linear modeling and control of DC-DC converters. *IEEE Transactions on Power Electronics*, 7(2):315–323, 1992.

[99] R. Tymerski. Sampled-data modelling of switched circuits, revisited. In *IEEE Power Electronics Specialists Conf. Rec.*, pages 395–401, 1993.

[100] R. Tymerski, V. Vorperian, F.C.Y. Lee, and W.T. Baumann. Nonlinear modeling of the PWM switch. *IEEE Transactions on Power Electronics*, 4(2):225–233, 1989.

[101] R. Venkataramanan, A. Sabanovic, and S. Ćuk. Sliding mode control of DC-to-DC converters. In *International Conference on Industrial Electronics, Control and Instrumentation*, pages 251–258, 1985.

[102] G.C. Verghese, C.A. Bruzos, and K.N. Mahabir. Averaged and sampled-data models for current mode control: a re-examination. In *IEEE Power Electronics Specialists Conf. Rec.*, pages 484–491, 1989.

[103] G.C. Verghese, M. Elbuluk, and J.G. Kassakian. A general approach to sample-data modeling for power electronic circuits. *IEEE Transactions on Power Electronics*, 1(2):76–89, 1986.

[104] V. Vorperian. Simplified analysis of PWM converters using model of PWM switch. I. Continuous conduction mode. *IEEE Transactions on Aerospace and Electronic Systems*, 26(3):490–496, 1990.

[105] V. Vorperian. Simplified analysis of PWM converters using model of PWM switch. II. Discontinuous conduction mode. *IEEE Transactions on Aerospace and Electronic Systems*, 26(3):497–505, 1990.

[106] V. Vorperian, R. Tymerski, and F.C.Y. Lee. Equivalent circuit models for resonant and PWM switches. *IEEE Transactions on Power Electronics*, 4(2):205–214, 1989.

[107] Z.-Q. Wang, I. Sznaier, I. Batarseh, and J. Bu. Robust controller design for a series resonant converter. *IEEE Transactions on Aerospace and Electronic Systems*, 32(1):221–233, 1996.

[108] S. Wiggins. *Introduction to Applied Nonlinear Dynamical Systems and Chaos.* Springer-Verlag, New York, 1990.

[109] E.X. Yang, B. Choi, F.C. Lee, and B.H. Cho. Dynamic analysis and control design of LCC resonant converter. In *IEEE Power Electronics Specialists Conf. Rec.*, pages 362–369, 1992.

[110] E.X. Yang, F.C. Lee, and M. M. Jovanovic. Small-signal modeling of LCC resonant converter. In *IEEE Power Electronics Specialists Conf. Rec.*, pages 941–950, 1992.

[111] I. Zafrany and S. Ben-Yaakov. A chaos model of subharmonic oscillations in current mode PWM boost converters. In *IEEE Power Electronics Specialists Conf. Rec.*, pages 1111–1117, 1995.